

Society of Automotive Engineers  
of China (SAE-China)  
International Federation  
of Automotive Engineering Societies (FISITA)  
*Editors*

# Proceedings of the FISITA 2012 World Automotive Congress

Volume 4: Future Automotive  
Powertrains (II)



# Lecture Notes in Electrical Engineering

Volume 192

For further volumes:  
<http://www.springer.com/series/7818>

Society of Automotive Engineers of China  
(SAE-China) · International Federation of  
Automotive Engineering Societies (FISITA)  
Editors

# Proceedings of the FISITA 2012 World Automotive Congress

Volume 4: Future Automotive  
Powertrains (II)



 Springer

The Springer logo, consisting of a stylized chess knight (horse) facing left, positioned to the left of the word 'Springer' in a serif font.

*Editors*  
SAE-China  
Beijing  
People's Republic of China

FISITA  
London  
UK

ISSN 1876-1100  
ISBN 978-3-642-33740-6  
DOI 10.1007/978-3-642-33741-3  
Springer Heidelberg New York Dordrecht London

ISSN 1876-1119 (electronic)  
ISBN 978-3-642-33741-3 (eBook)

Library of Congress Control Number: 2012948289

© Springer-Verlag Berlin Heidelberg 2013

This work is subject to copyright. All rights are reserved by the Publisher, whether the whole or part of the material is concerned, specifically the rights of translation, reprinting, reuse of illustrations, recitation, broadcasting, reproduction on microfilms or in any other physical way, and transmission or information storage and retrieval, electronic adaptation, computer software, or by similar or dissimilar methodology now known or hereafter developed. Exempted from this legal reservation are brief excerpts in connection with reviews or scholarly analysis or material supplied specifically for the purpose of being entered and executed on a computer system, for exclusive use by the purchaser of the work. Duplication of this publication or parts thereof is permitted only under the provisions of the Copyright Law of the Publisher's location, in its current version, and permission for use must always be obtained from Springer. Permissions for use may be obtained through RightsLink at the Copyright Clearance Center. Violations are liable to prosecution under the respective Copyright Law.

The use of general descriptive names, registered names, trademarks, service marks, etc. in this publication does not imply, even in the absence of a specific statement, that such names are exempt from the relevant protective laws and regulations and therefore free for general use.

While the advice and information in this book are believed to be true and accurate at the date of publication, neither the authors nor the editors nor the publisher can accept any legal responsibility for any errors or omissions that may be made. The publisher makes no warranty, express or implied, with respect to the material contained herein.

Printed on acid-free paper

Springer is part of Springer Science+Business Media ([www.springer.com](http://www.springer.com))

# Contents

## Part I Alternative Fuel and New Engine

<b>Experimentation Investigate of Gasoline Engine Emergency Alternative Fuel</b> . . . . .	3
F2012-B01-003 Lianling Ren, Changfa Liu, Xingwang Wang and Rui Ge	
<b>Analytical Assessment of C2–C8 Alcohols as Spark-Ignition Engine Fuels</b> . . . . .	15
F2012-B01-004 Thomas Wallner, Andrew Ickes and Kristina Lawyer	
<b>Improvement of the Automotive Spark Ignition Engine Performance by Supercharging and the Bioethanol Use</b> . . . . .	27
F2012-B01-007 Constantin Pana, Niculae Negurescu and Alexandru Cernat	
<b>Theoretical and Experimental Investigations on the LPG Fuelled Diesel Engine</b> . . . . .	37
F2012-B01-009 Niculae Negurescu, Constantin Pana and Alexandru Cernat	
<b>The Research Development in Direct Injection Spark-Ignition Natural Gas Engine.</b> . . . . .	51
F2012-B01-010 Jianjun Zheng, Xiaodong Chen, Tiegang Hu and Zhangsong Zhan	

<b>Experimental Results Using Ammonia Plus Hydrogen in a S.I. Engine . . . . .</b>	<b>65</b>
F2012-B01-015 Stefano Frigo, Roberto Gentili, Giacomo Ricci, Giuseppe Pozzana and Massimiliano Comotti	
<b>Dual Fuel H2-Diesel Heavy Duty Truck Engines with Optimum Speed Power Turbine . . . . .</b>	<b>77</b>
F2012-B01-018 Alberto Boretti	
<b>Well-to-Wheel Analyses for Energy Consumption and Greenhouse Gas Emissions of Electric Vehicles Using Various Thermal Power Generation Technologies in China . . . . .</b>	<b>101</b>
F2012-B01-022 Wei Shen and Weijian Han	
<b>Effects of Fuel Thermo-Physical Properties on Spray Characteristics of Biodiesel Fuels . . . . .</b>	<b>117</b>
F2012-B01-023 Xinwei Cheng, Harun M. Ismail, Kiat Hoon Ng, Suyin Gan and Tommaso Lucchini	
<b>System Design for a Direct-Boost Turbocharged SI Engine Using a Camshaft Driven Valve . . . . .</b>	<b>127</b>
F2012-B01-024 Christoph Voser, Christopher Onder and Lino Guzzella	
<b>Exploring the Potential of Dual Fuel Diesel-CNG Combustion for Passenger Car Engine . . . . .</b>	<b>139</b>
F2012-B01-025 David Serrano and Lecointe Bertrand	
<b>Sustainable Mobility: Lithium, Rare Earth Elements, and Electric Vehicles . . . . .</b>	<b>155</b>
F2012-B01-026 Timothy J. Wallington, Elisa Alonso, Mark P. Everson, Frank R. Field, Paul G. Gruber, Gregory A. Keoleian, Stephen E. Kesler, Randolph E. Kirchain, Pablo A. Medina, Emily K. Kolinski Morris, Rich Roth and Andrew M. Sherman	

**Controller Design and Emission Improvement for Lean-Burn CNG Engine Based on UEGO Controller** . . . . . 167  
 F2012-B01-031  
 Xiaojian Mao, Junhua Song, Du Wang, Junxi Wang, Hangbo Tang and Bin Zhuo

**Biogas as a Fuel for City Buses** . . . . . 179  
 F2012-B01-037  
 Jerzy Merkisz and Wojciech Gis

**High-Concentration Ethanol Fuels for Cold Driving Conditions** . . . . . 193  
 F2012-B01-040  
 Juhani Laurikko, Nils-Olof Nylund, Jari Suominen and Mika P. A. Anttonen

**The Effects of Intake Valve Closing Timing on Engine Performance and Emissions in a DME Compression Ignition Engine at Low Load Cold Start Condition** . . . . . 211  
 F2012-B01-044  
 Jaeheun Kim and Choongsik Bae

**Environmental Performance of Diesel Fuels Containing Oxygenated Additive Packages** . . . . . 227  
 F2012-B01-045  
 Miłosław Kozak, Jerzy Merkisz, Piotr Bielaczyc and Andrzej Szczotka

**A Study of Dual-Diluted Control Strategy for NG Engine** . . . . . 239  
 F2012-B01-049  
 Yanchun Chen, Chao Wang, Dongxu Hua and Changbo Fu

**Research and Development of Heavy-Duty NG Engine and its Key Technologies of Combustion** . . . . . 251  
 F2012-B01-050  
 Huili Dou, Jun Li, Zhongshu Wang, Xiaocao Yu, Zhongchang Liu and Jingxue Li

**Part II Advanced Hybrid Electric Vehicle**

**Development of CHS Hybrid System for City Bus** . . . . . 265  
 F2012-B02-006  
 Guangkui Shi, Renguang Wang, Hongtao Chen and Zhiguo Kong

**Optimization of an Extended-Range Electric Vehicle . . . . . 275**  
 F2012-B02-009  
 Haitao Min, Dongjin Ye and Yuanbin Yu

**Driving Intention Identification Method for Hybrid Vehicles  
 Based on Fuzzy Logic Inference. . . . . 287**  
 F2012-B02-015  
 Qingnian Wang, Xianzhi Tang and Lei Sun

**The Control Technologies of PMSM for FAW-TMH System. . . . . 299**  
 F2012-B02-016  
 Cheng Chang, Huichao Zhao, Xiuhui Dong and Yandong Wen

**Modeling and Simulation of Power Train System  
 for Extended-Range Electric Vehicle Using Bond Graphs . . . . . 313**  
 F2012- B02-017  
 Ke Song and Tong Zhang

**Optimization of Hybrid Strategies with Heuristic Algorithms  
 to Minimize Exhaust Emissions and Fuel Consumption . . . . . 323**  
 F2012-B02-023  
 Michael Planer, Thorsten Krenek, Thomas Lauer, Zahradnik Felix,  
 Bernhard Geringer and Michael Back

**Development for Control Strategy of ISG Hybrid Electric Vehicle  
 Based on Model . . . . . 333**  
 F2012-B02-025  
 Hongtao Peng, Zheng Li, Bin Chen, Jieyu Wu, Zhenglan Zhao,  
 Yuehong Shu and Junjun Lei

**Development of New Hybrid Transaxle for Front-Wheel  
 Drive (FWD) 2.5-Liter Class Vehicles . . . . . 343**  
 F2012-B02-026  
 Kunihiro Kobayashi, Takahisa Yashiro, Hiroshi Takekawa  
 and Kazuhiro Fujita

**Key Items for Future Hybrid Applications: Energy Storage  
 and Power Electronics for Micro Hybrids up  
 to Full Hybrids and EVs . . . . . 355**  
 F2012-B02-027  
 Peter Willemsen, Feng Ji and Marc Nalbach



**Direct-Computation-Based Traction Motor Control for Dynamic Performance Improvement in Electric Vehicles . . . . . 365**  
 F2012-B02-033  
 Xi Zhang and Chengliang Yin

**Energy Optimization for the Mild Hybrid Electric Vehicle with CVT Under Driving Conditions . . . . . 375**  
 F2012-B02-036  
 Yongxia Zheng, Feng Zhao, Yugong Luo and Keqiang Li

**Development of Plug-in Hybrid System for Midsize Car . . . . . 387**  
 F2012-B02-037  
 Shinichi Matsumoto, Hiroaki Takeuchi and Kenji Itagaki

**Study on System Efficiency and Power Flow Optimization for Dual-Mode Hybrid Electric Vehicle . . . . . 401**  
 F2012-B02-038  
 Lijin Han, Changle Xiang, Weijing Yan, Yun-long Qi and Ran Liu

**Development of Commercial Hybrid Vehicle Automatic Transmission System . . . . . 417**  
 F2012-B02-040  
 Chiaki Umemura, Kazumi Ogawa, Toshinori Murahashi and Yasutoshi Yamada

**A Dynamic Coordinated Control Strategy for Mode-Switch of Hybrid Electric Vehicle Based on the Effect Control . . . . . 427**  
 F2012-B02-043  
 Na Zhang, Feng Zhao and Yugong Luo

**‘Commercial Vehicle Electrification’ Challenges in Dimensioning and Integration in the Entire Vehicle . . . . . 439**  
 F2012-B02-054  
 Winter Martin

**Plug-In Hybrid Vehicle with a Lithium Iron Phosphate Battery Traction Type . . . . . 449**  
 F2012-B02-062  
 Danut Gabriel Marinescu, Ion Tabacu, Florin Serban, Viorel Nicolae, Stefan Tabacu and Ionel Vieru

<b>Design and Simulation of Air Cooled Battery Thermal Management System Using Thermoelectric for a Hybrid Electric Bus . . . . .</b>	463
F2012-B02-065	
Vahid Esfahanian, Saber Ahmadi Renani, Hassan Nehzati, Nima Mirkhani, Mohsen Esfahanian, Omid Yaghoobi and Ali Safaei	
<b>Analysis of Rotor’s Magnetic Bridge and Yoke Design to EM’s Performance Influence . . . . .</b>	475
F2012-B02-069	
Ming Han, Wenxiang Huang and Pingliang Luo	
<b>HyBoost: An Intelligently Electrified Optimised Downsized Gasoline Engine Concept . . . . .</b>	483
F2012-B02-070	
Jason King, Matthew Heaney, James Saward, Andrew Fraser, Mark Criddle, Thierry Cheng, Guy Morris and Paul Bloore	
<b>Development of B70HEV and B50PHEV Based on Faw-TMH Powertrain . . . . .</b>	497
F2012-B02-073	
Jun Li, Minghui Liu, Dongqin Liu, Ziliang Zhao and Xingwang Yang	
<b>The Research of Electromagnetic Fields During Testing of a Hybrid Powerplant and a Hybrid Car Prototype . . . . .</b>	509
F2012-B02-074	
Elena Teriaeva	
<b>Research on the Efficiency of the Dual-Mode Hybrid Vehicle . . . . .</b>	519
F2012-B02-075	
Weijing Yan, Changle Xiang, Lijin Han and Donghao Zhang	
<b>Power Transmission Properties of Dry Hybrid V-Belt with Protuberant Tension Member on Contact Surfaces of Blocks: It’s Effect with Respect to Speed Ratio . . . . .</b>	531
F2012-B02-076	
Hirotoishi Kawakami, Kazuya Okubo, Toru Fujii, Hiroyuki Sakanaka and Ryuichi Kido	
<b>A Comparative Analysis of Optimization Strategies for a Power-Split Powertrain Hybrid Electric Vehicle . . . . .</b>	541
F2012-B02-077	
Jackeline Rios and Pierluigi Pisu	

**Part III Plug-in Electric Vehicle**

**Development of a Compact-Class Range Extended Electric Vehicle Demonstrator . . . . .** 553  
 F2012-B03-004  
 Michael Bassett, Jonathan Hall, John Powell, Simon Reader, Marco Warth and Bernd Mahr

**Modeling of the Lithium Battery Cell for Plug-In Hybrid Electric Vehicle Using Electrochemical Impedance Spectroscopy. . . . .** 563  
 F2012-B03-005  
 Hyun-sik Song, Tae-Hoon Kim, Jin-Beom Jeong, Dong-Hyun Shin, Baek-Haeng Lee, Byoung-Hoon Kim and Hoon Heo

**On-Board Powerplant Numerical Optimization of Internal Combustion Engines in Series Hybrid-Powertrains. . . . .** 573  
 F2012-B03-007  
 Thorsten Krennek, Thomas Lauer, Bernhard Geringer and Bacher Christopher

**Torque-Vectoring Driveline for Electric Vehicles . . . . .** 585  
 F2012-B03-009  
 Bernd-Robert Hoehn, Karsten Stahl, Philipp Gwinner and Ferdinand Wiesbeck

**Plug-In Hybrid Vehicle Powertrain Design Optimization: Energy Consumption and Cost . . . . .** 595  
 F2012-B03-012  
 João P. Ribau, João M. C. Sousa and Carla M. Silva

**Simulation-Based Energy Flow Study of Purely Electric-Drive Vehicles . . . . .** 615  
 F2012-B03-014  
 Bin Wang, Mian Li, Min Xu and Jianhua Zhou

**Design of Auxiliary Electric Driving System in Rear Wheels of Vehicles . . . . .** 631  
 F2012-B03-015  
 Hongzan Xu, Quan Sun, Xufeng Wu, Qiqian Jin, Yi You and Fuquan Zhao

**Study on the Relationship Between EV Cost and Performance . . . . .** 639  
 F2012-B03-018  
 Pupeng Wan, Zhiqiang Du, Qiqian Jin, Yi You and Fuquan Zhao

**Hil Validation of Extended-Range Electric Vehicle Control Unit Based on Orthogonal Test . . . . . 647**  
 F2012-B03-022  
 Haibo He, Qiqian Jin, Tingting Dong and Fuquan Zhao

**Development of a Control System of Hybrid Power System Based on the XPC Target for Electric Vehicles . . . . . 655**  
 F2012-B03-024  
 Yaming Zhang and Rui Xiong

**A Study on Effective Thermal-Shock Test Improvement of Battery Packs for PHEVs . . . . . 667**  
 F2012-B03-025  
 Byoung-Hoon Kim, Hong-Jong Lee, Jin-Beom Jeong, Baek-Haeng Lee, Dong-Hyun Shin, Hyun-Sik Song, Tae-Hoon Kim and Ji-Yoon Yoo

**Challenges in NVH for Electric Vehicles . . . . . 675**  
 F2012-B03-029  
 Benjamin Meek, Herman Van der Auwear and Koen De Langhe

**Study on New Concept Powertrain for Range-Extended Electric Vehicles . . . . . 687**  
 F2012-B03-032  
 Minghui Liu, Ziliang Zhao, Xingwang Yang, Chuan Li and Guopeng Luo

**Parameters Optimization of PHEV Based on Cost-Effectiveness from Life Cycle View in China . . . . . 697**  
 F2012-B03-037  
 Jiuyu Du, Hewu Wang and Minggao Ouyang

**Approach of Gasoline Hybrid Technology for “95G CO2/KM” Emissions Regulation. . . . . 705**  
 F2012-B03-038  
 Jun Li, Ziliang Zhao, Yihong Zheng, Minghui Liu and Heqi Liang

**Part IV Advanced Battery Technology**

**Study on Drive Battery High Voltage Safety System for Hybrid Electric Vehicle . . . . . 721**  
 F2012-B04-002  
 Xingfeng Fu, Sijia Zhou, Yingjun Zheng and Chengjiao Tu

**Automaker Energy Storage Needs for Electric Vehicles** . . . . . 729  
 F2012-B04-005  
 Alvaro Masias, Kent Snyder and Ted Miller

**Design of the Experimental Procedures for Analysis of Thermal and Electrical Properties of a Prismatic LiFeYPO<sub>4</sub> Battery in a Modified Electric Car** . . . . . 743  
 F2012-B04-007  
 Chayangkun Sanguanwatana, Chadchai Srisurangkul, Monsak Pimsarn and Shoji Tsushima

**Intelligent BMS Solution Using AI and Prognostic SPA** . . . . . 755  
 F2012-B04-008  
 Subrahmanyam Sista and Avinash Sista

**Thermal Modeling and Effects of Electrode Configuration on Thermal Behaviour of a LifePO<sub>4</sub> Battery** . . . . . 765  
 F2012-B04-013  
 Cheng Ruan, Kun Diao, Huajie Chen, Yan Zhou and Lijun Zhang

**Thermal Behavior and Modeling of Lithium-Ion Cuboid Battery** . . . . . 779  
 F2012-B04-020  
 Hongjie Wu and Shifei Yuan

**Application of Battery-Ultracapacitor Hybrid System in the Hybrid Electric Vehicles** . . . . . 785  
 F2012-B04-021  
 Huanli Sun, Xiaojuan Pei, Lichao Xu, Hemin Wang, Yi Sheng and Yuanbin Yu

**A Lithium-Ion Battery Fractional Order State Space Model and its Time Domain System Identification** . . . . . 795  
 F2012-B04-023  
 Hongjie Wu, Shifei Yuan and Chengliang Yin

**Optimizing BMS Operating Strategy Based on Precise SOH Determination of Lithium Ion Battery Cells.** . . . . . 807  
 F2012-B04-024  
 Karsten Mueller, Daniel Tittel, Lars Graube, Zecheng Sun and Feng Luo

**Part V Hydrogen Fuel Cell Vehicle**

**Novel Concept of Long-Haul Trucks Powered by Hydrogen Fuel Cells . . . . . 823**

F2012-B05-002

Bahman Shabani, John Andrews, Aleksandar Subic and Biddyut Paul

**Practical Research on Hydrogen Safety of Fuel Cell Vehicles . . . . . 835**

F2012-B05-004

Yong He, Bing Wu, Honghu Wang, Pengcheng Zhao and Yachao Li

**Modeling and Analysis of a Fuel Cell Hybrid Vehicle . . . . . 847**

F2012-B05-005

Mircea Nicolae Glazer, Ioan Mircea Oprean and Marius Valentin Băţăuş

**Optimal Battery Discharging Strategy for a Range Extended Fuel Cell City Bus . . . . . 859**

F2012-B05-008

Liangfei Xu, Minggao Ouyang, Jianqiu Li, Fuyuan Yang and Languang Lu

**Part VI Charging Infrastructure and Smart Grid Technology**

**EV Charging Through Wireless Power Transfer: Analysis of Efficiency Optimization and Technology Trends . . . . . 871**

F2012-B06-001

Heri Rakouth, John Absmeier, Andrew Brown Jr., In-Soo Suh, Miller John M., Randy Sumner and Richard Henderson

**Part VII Demonstration of Electric Vehicles in Cities**

**Development and Performance Evaluation of an Electric Mini Bus Equipped with an Inductive Charging System . . . . . 887**

F2012-B07-002

Thomas Pontefract, Kimiyoshi Kobayashi, Yuto Miyasaka, Kento Tanaka, Yushi Kamiya, Yasuhiro Daisho and Shunsuke Takahashi

**The Study of Re-construction Method of EV Business Model Based on Value Chain Analysis . . . . . 899**

F2012-B07-003

Qiang Ye and Hewu Wang

**Part VIII Other**

**Research on Parameter Matching and Fuzzy Logic Control Strategies of EMT Hybrid Energy Storage System . . . . .** 911  
 F2012-B08-008  
 Changle Xiang, Yanzi Wang, Weida Wang, Lijin Han and Donghao Zhang

**Cost-Effectiveness Analysis of CO<sub>2</sub> Reduction with Future Automobile Technologies in the Japanese Automotive Sector . . . . .** 923  
 F2012-B08-009  
 Shuichi Kanari

**The Small-Signal Model Stability Analysis of Full-Bridge Buck Converter with Compensation Network . . . . .** 937  
 F2012-B08-014  
 Lin Zhang, Dengmeng Fu and Haoxing Liu

**The HV Safety Management Design of Battery System in Electric Vehicle . . . . .** 951  
 F2012-B08-016  
 Tao Yan, Qi qian Jin and Fuquan Zhao

**The Free Piston Stirling Principle as Prime Mover for Alternant Hydraulic Propulsion Systems. . . . .** 957  
 F2012-B08-020  
 Horia Abaitancei, Cristi Irimia, Gabriel Carciumaru, Ionut Tudor Soare and Sebastian Radu

**Design and Analysis of a Dual Power Supply with Super-Capacitor for EV . . . . .** 969  
 F2012-B08-021  
 Ye Lu, Fen Liu, Xiaoyu Jia and Xiao Liang

**An Electrically Driven Chassis System Concept for Sub-Compact Vehicles with Integrated Close-to-Wheel Motors . . . . .** 979  
 F2012-B08-022  
 Shih-Jen Yeh, Ingo Albers and Stephan Pollmeyer

**Future Commercial Vehicle Powertrains: Contributions to Sustainable Transportation . . . . .** 987  
 F2012-B08-024  
 Heimo Schreier and Lukas Walter

**Part IV**  
**Advanced Battery Technology**



# Study on Drive Battery High Voltage Safety System for Hybrid Electric Vehicle

Xingfeng Fu, Sijia Zhou, Yingjun Zheng and Chengjiao Tu

**Abstract** The main characteristics of the vehicle Electric Power HV safety System are briefly analyzed, and then through analysis of key technology problem of this system currently, to research to this system key parameter and flow state based on CAN network technology. The simulation and test result was testified that HV safety systems are steady and robust.

**Keywords** Electric vehicle · HV safety · Power up/down

## 1 Introduction

Electric and hybrid vehicle are clearly becoming a growing part of the automotive scene. Although electric and hybrid vehicle supply low or no emissions and conceivably low cost of fuel from the power grid, they will continue to deliver safely from here to there. Drive battery and drive motor are the key parts of electric and hybrid vehicle. The operational voltage of drive battery and drive motor always over 100 V, then High Voltage (HV) risk is the focus research scope of electric and hybrid vehicle safety.

Electric and hybrid vehicle are bringing new challenges to the automotive industry as the hardware and software content of the vehicle grow. The main

---

F2012-B04-002

---

X. Fu · Y. Zheng · C. Tu  
Guangzhou Automobile Group Co.,Ltd, Automotive Engineering Institute,  
Guangzhou, China  
e-mail: fuxingfeng@gaei.cn

S. Zhou (✉)  
College of Mechanical and Electronic Engineering, Wenzhou University, Wenzhou, China

research scopes of HEV HV (high voltage) safety system are monitor and manage drive battery. The defend method of HEV HV safety system is mainly used in battery pack. The battery is used as the rechargeable electrical storage system in hybrid vehicle. Controlled release of the battery's energy provides useful electrical power in the form of current and voltage. Uncontrolled release of this energy can result in dangerous situations such as smoke, fire, high pressure events or any combination thereof.

In this paper, the basics of hybrid vehicle battery pack HV safety system designs and some of tests that should be discussed.

According to relative Chinese nation standard [1–6], HEV drive battery HV safety system should be designed specially. Firstly, all the battery cell and HV component should be build in seal pack. The insulation section prevents to connect between battery cell and HV junction box. The cooling air or cooling water flow setting is designed in battery pack. Secondly, Manual Service Disconnect (MSD) and High Voltage Interlock (HVIL) are used to protect maintenance man human safety when battery is repaired. MSD is built in the battery cell in order to prevent personal get an electric shock and protect maintenance man. Next, crash switch or crash sensor in battery system can cause BMS cut off immediately HV bus in vehicle collision. Thus prevent potential safety risk such battery smoke, fire, burning, liquid leak, explosion or any combination escape. Finally, the especially effective battery HV safety management system monitors and diagnose real time all linked point among battery pack interior and outer HV component. Usually, drive battery HV management system is developed and designed in BMS.

## **2 Battery HV Safety System Function**

The key scope of BMS is HV safety diagnoses and control. BMS is not only monitors the dynamic change of whole HV bus, but also detect and diagnose the work state of HV bus. The message of work state should be send to HCU and execute corresponding request timely. Battery HV safety system need to ensure all HV components steady work and prevent any potential permanent damage. Furthermore, battery HV safety system should prevent any potential HV power connect with vehicle LV control unite which caused dangerous hazard.

### ***2.1 Battery HV Safety System Basic Function***

- (1) Insulation and short circuit detection. BMS should detect insulation resistance and leak current change parameter timely;
- (2) GND detection. BMS should detect all HV components ground state, relay state and HVIL circuit open or close.
- (3) On-site diagnostic function. BMS should monitor HV bus work state timely;

- (4) HV bus can be manually, crash signal and HCU requirement cut off;
- (5) BMS has self learning and adaptive capability;
- (6) Rational and effective power up/down flow;
- (7) Low power waste and short response time.

In BMS battery HV safety system function, it is very important to diagnose and monitor power up/down procession, insulation and short circuit detection. Therefore, those functions will be discussed in next section.

## ***2.2 Pre-Charge Process Diagnoses and Control***

Logical HV power up flow is detect supply power, HV current load and main relay safety process. For many capacitance load are in HV bus, there are much current impact in HV electric circle when relay are closed immediately. Battery pack designs include alternate current paths for pre-charging the drive system through a pre-charge resistor or for powering auxiliary busses which will also have their own associated control relays. For obvious safety reasons these relays are all normally open.

When key on, BMS will be enabled immediately. After complete initialization and test itself, battery will enter standby state and wait for HCU messages. BMS initialization include BMS self test, program down load(boot), insulation test in battery pack, initialize I/O, peripherals, initialize CAN and start sending messages, and so on.

BMS will start advance diagnostic procedure after receive close main relay requirement from HCU. If battery SOC is enough, battery state is normal and no insulation and short-circuit fault, then pre-charge relay will be closed and pre-charge procedure will be started at the same time. When pre-charge procedure can be completed in scheduled time, then main relay will be closed and HV bus can be connected. However, if pre-charge procedure can't be completed in scheduled time, then BMS will send pre-charge fault signal to HCU and forbid main relay to be closed.

As is show in Fig. 1, BMS will close pre-charge relay 1 and negative relay 3 immediately and start pre-charge procedure after power up requirement from HCU. If HV bus voltage  $V_a$  can over 90 % of battery whole voltage  $V_b$  scheduled time, then pre-charge procedure can be completed. Otherwise, BMS will send pre-charge fault signal to HCU and forbid main relay to be closed.

## ***2.3 Power Down Process Diagnoses and Control.***

BMS will start power down process after received open relay request from HCU. BMS will diagnose battery state before main relay is opened. If battery state is normal, then HCU will start all HV components power down process in scheduled time and then BMS open relay. If battery temperature is high in BMS power down

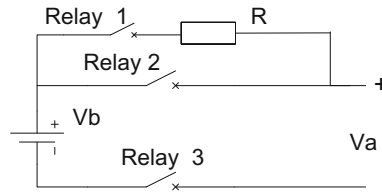


Fig. 1 Pre-charge circuit

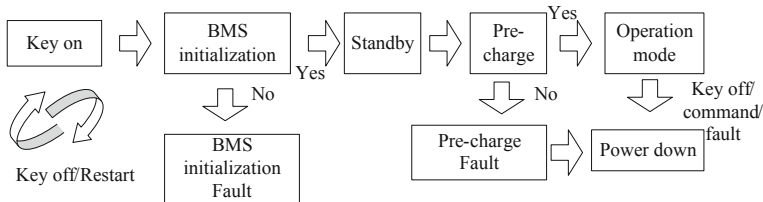


Fig. 2 BMS power up/down process

process, battery cooling fan must run to reduce battery temperature to normal value. The main relay can't be opened before battery temperature reduces to rational operational range. HCU can open main relay by emergency line under urgent condition.

The Fig. 2 is BMS power up/down process. When key on, BMS will be enabled, initialize and test itself. If can complete initialization process, then BMS will enter standby state, otherwise BMS will send initialization fault message to HCU for reminding driver key off or restart. If receive close main relay requirement from HCU, BMS will enter pre-charge process. When pre-charge procedure can be completed in scheduled time, then main relay will be closed and battery enters into operation mode. BMS will start power down process in case received open relay require from HCU, key off or fault message.

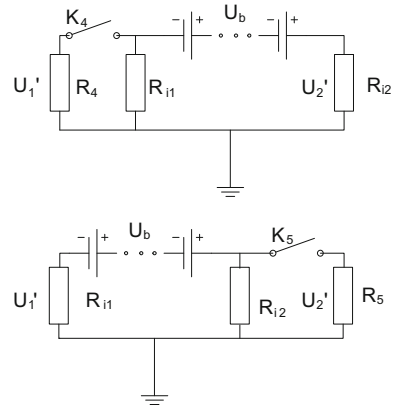
### 2.4 HV Insulation Test

The insulation resistance value between HV electric circle and chassis is change variably when vehicle is running for liberation, impact, battery liquid leak or dangerous gas gives out, and so on. The variable value of insulation resistance is relational with electric component state in HV bus. Therefore, it is key content to monitor dynamically insulation state of HV bus for HV safety dynastic system.

According to Chinese Nation criterion GB/T 18384.1-2001, the insulation resistance is key parameter which indicates EV and HEV safety performance. The ratio of insulation resistance and rated voltage should over 100 Ω/V.

As is shown in Fig. 3, the corresponding resistance to max leak current is virtual battery insulation resistance if the point between battery and ground is short circuit.

**Fig. 3** Schematic diagram of on-line insulation resistance detection



The resistance detectable value is limited under BMS operation normally. The resistance between positive and ground is  $R_{i1}$ , while the resistance between negative and ground is  $R_{i2}$ , then battery insulation resistance is the smaller one between  $R_{i1}$  and  $R_{i2}$ . For current can pass the electric circuit which connects with the smaller resistance and ground.  $U_b$  is battery voltage,  $R_b$  is battery resistance,  $U_1$  is voltage between battery negative and ground, while  $U_2$  is voltage between battery positive and ground. Compared with  $R_{i1}$  and  $R_{i2}$ ,  $R_b$  is too little and can be neglected.

The equation can be gained from the upper part of Fig. 3 [7, 8].

$$U_1 + U_2 = U_b \tag{1}$$

$$U_1/R_{i1} = U_2/R_{i2} \tag{2}$$

If  $U_1 \geq U_2$ , then battery insulation resistance is  $R_{i2}$ . The resistance  $R_0$  been added into battery negative and ground. The insulation electric circuit equation can be gained.

$U'_1$  is  $R_0$  voltage while  $U''_2$  is  $R_{i2}$  voltage, the equation can be gained from the lower part of Fig. 3.

$$U'_1 + U'_2 = U_b \tag{3}$$

$$U'_1/[R_0R_{i1}/(R_0 + R_{i1})] = U'_2/R_{i2} \tag{4}$$

From Eq. 1 to 4, the Eq. 5 of battery positive insulation resistance can be gained.

$$R_{i2} = R_0(1 + U_2/U_1)[(U_1 - U'_1)/U'_1] \tag{5}$$

If  $U_1 < U_2$ , then battery insulation resistance is  $R_{i1}$ . According to same calculation method, the Eq. 6 of battery negative insulation resistance can be gained.

$$R_{i1} = R_0(1 + U_1/U_2)[(U_2 - U'_2)/U'_2] \tag{6}$$

**Table 1** Battery insulation resistance test result

Expected resistance (k $\Omega$ )	Chassis to battery+	Chassis to battery–
1,000	1000.0	1000.0
500	502.5	502.5
100	97.5	100
90	90.0	90.0
80	80.0	80.0
70	67.5	70.0
60	60.0	60.0
50	50.0	50.0
40	40.0	40.0
30	30.0	30.0
20	20.0	20.0
10	10.0	10.0
0	0.0	0.0

When BMS detect insulation fault, the diagnostic procedure will start up immediately. BMS will execute different procedure according to different fault class and send message to HCU.

### 3 Testing Result and Analysis

#### 3.1 Testing for Insulation Resistance Test Model

In order to test drive battery insulation resistance calculation model validity, many test should be done. It's difficult to test directly battery insulation resistance and inverter equivalent capacitance. Therefore, a known resistance can be connected in the insulation test circuit, and then the insulation resistance calculation model validity can be testified compared with calculation value and testing value. In this testing, drive battery voltage is 300 V and inverter equivalent capacitance is 1,100  $\mu$ F, the decade box is connected to chassis and battery pack positive for the first half, then chassis to battery negative for second half.

The Table 1 is the testing result of drive battery insulation resistance. It is shown in Table 1, the max relative test error is 2.5 %, the insulation resistance calculation model validity is proved.

#### 3.2 Testing for Pre-Charge Process

The Fig. 4 is testing result of battery pack on vehicle. When key on, BMS will start initialize and check itself. If all initialization and check result are ok, BMS will start

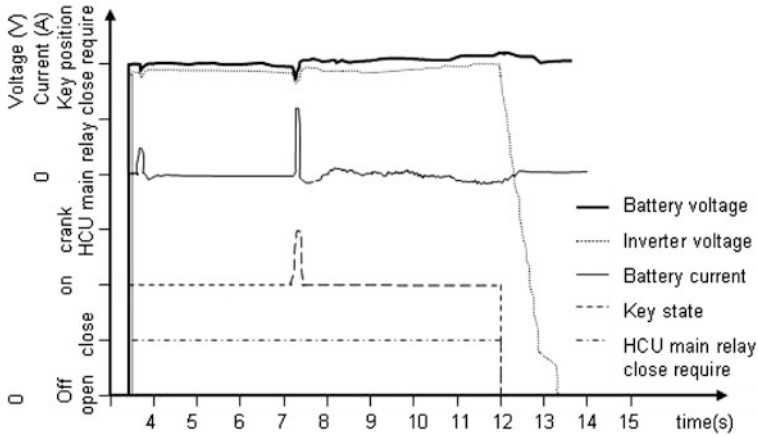


**Fig. 4** Testing result of battery pre-charge and power down process

pre-charge process in short time. Battery system enters standby state and wait for message from HCU after complete pre-charge process. The result is shown in Fig. 4.

When key crank and engine is ignited, drive battery will give bigger discharge current and voltage of battery and inverter drop heavy.

If pre-charge process can't complete in scheduled time (<300 ms), then main relay can't closed and BMS send pre-charge fault message to HCU. The result of test is testified the design requirement.

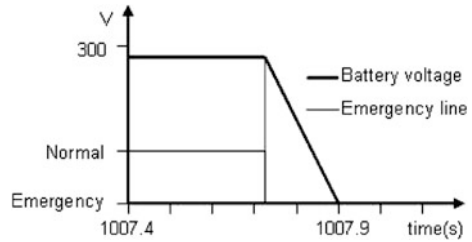
### 3.3 Testing for Power Down Process

As is shown in Fig. 4, BMS will open main relay in scheduled time (<3 s) after received open main relay requirement from HCU. HV power will be wasted by inverter inner circuit. The voltage reduce process time of inverter is less 4 s and satisfy design requirement. Repeating test of pre-charge and power down process testify that designed battery system is good robust.

### 3.4 Testing for hard shutdown

During vehicle are running, HCU and BMS monitor dynamic HV circuit connection state by HVIL loop. If HVIL loop is opened, insulation test fault or other serious mistake, HCU will open directly main relay and shutdown HV bus by emergency line. The hard shutdown process time is usually less 200 ms, and HV components maybe damaged in this process. The time of hard shutdown response is 0.1887 s in test. It is shown in Fig. 5.

**Fig. 5** The test of HV hard shut down



Reduplicate test result is satisfied the robust performance of HV safety management system.

## 4 Conclusion

According to hybrid electric vehicle HV drive system structure, the reasonable HV safety system is designed. The DTC table be collected and the fault management measure of HV management system be analyzed. The HV management system was testified to satisfy the design requirement by EV HV drive system power up/down test. This paper have provide useful reference for EV HV safety system study and development. With development of EV HV safety technology developed rapidly, EV HV safety system will become more and more perfect and. Finally, EV industrialization will be quickened up for the comprehensively HV safety technology.

**Acknowledgments** The authors acknowledge the financial support from the Zhe Jiang province public welfare project (No.2010C31094; No.2011C21068) and Wenzhou University project (No.11jg58B).

## References

1. GB/T 18384.1-2001 Electric vehicles-safety specification Part 1 :on-board energy storage
2. GB/T 18384.2-2001 Electric vehicles-safety specification Part 2: functional safety means and protection against failures
3. GB/T 18384.3-2001. Electric vehicle-safety specification Part 3: protection of persons against electric hazards
4. GB/T 19751-2005 Hybrid electric vehicles safety specification
5. ISO 6469-1-2009. Electrically propelled road vehicles—safety specifications —Part 1: On-board rechargeable energy storage system (RESS)
6. QC/T 743-2006. Lithium-ion batteries for electric vehicles
7. Liu B (2005) A study on the test system for high voltage safety in electric vehicle. *Automotive engineering* vol 27, pp 274–277
8. Song B-Y (2010) Research on high voltage fault diagnostics and safety management strategy of pure electric vehicle. *J Chongqing Jiaotong Univ (Nat Sci)* 29:804–807



# Automaker Energy Storage Needs for Electric Vehicles

Alvaro Masias, Kent Snyder and Ted Miller

**Abstract** The success of electric vehicles (EVs) is strongly tied to their performance and ability to meet customer expectations. A comparison of EV battery performance against the requisite targets created by the international community is presented. The performance attributes of greatest interest are energy, power and life. It is shown that only power has achieved the level of performance required by the automotive community for mass commercialization.

**Keywords** Electric vehicle · EV · BEV · Lithium ion battery · LIB

## 1 Research Objective

The success of global long term vehicle electrification efforts will depend heavily on the performance of their requisite batteries. The current revival of Electric Vehicles (EVs) is being enabled by recent improvements in Lithium Ion Batteries (LIB). Recently, a large number of automakers have made electrified vehicle product announcements and the US Government has targeted 1 million such vehicles to be on the road by 2015 [1]. Despite these recent announcements and targets, all current EVs require customers to make sacrifices when compared to similar gasoline powered vehicles. Our research objective is to quantify the gap between conventional gasoline powered vehicles and the battery technology of EVs in terms of energy, power and life. The current performance gap between EVs

---

F2012-B04-005

---

A. Masias (✉) · K. Snyder · T. Miller  
Ford Motor Company, Dearborn, USA  
e-mail: amasias@ford.com

and gasoline powered vehicles is large and is attributable to the performance limits of LIBs. These limits stem from material and design constraints of the current technology and will require extensive R&D to resolve over the long term. It is projected that over the next 10 years, significant reductions in the performance gap are likely, although the two systems will still not achieve parity.

## 2 Methodology

Our methodology is to quantify the current performance gap between internal combustion engine (ICE) and battery driven vehicles, with a focus on the performance features of energy, power and life. Due to its inherent performance advantages and nascent technical maturity, we will focus exclusively on lithium ion based battery chemistries. Performance specifications and targets for batteries are commonly described at various hardware levels (cell, module or pack) and for ease of comparison we will express all figures of merit in terms of actual or estimated pack level performance. EV research has been pursued in the recent past by various global organizations and as such our research will consider the performance and targets from a variety of international sources over the past 15 years. These performance specifications and targets will be considered for automotive relevant applications, rather than for consumer electronics applications which have historically been the technology driving industry for batteries. In the case of energy and power, these figures of merit will be examined as beginning of life (BOL) values. The study of life is most relevantly considered in terms of end of life conditions (EOL), and as such, given its greater complexity we will look at a variety of influencing factors.

The modern gasoline powered ICE vehicle has been in mass production since Henry Ford released the Model T in 1908 [2]. Since that time ICE vehicles have been tailored to meet ever evolving consumer expectations. Due to this optimization of features and capabilities, modern ICE vehicles also serve as the most useful benchmark for determining the features that EVs require to achieve mass market acceptance. Much as an engine determines many of the performance characteristics of an ICE vehicle, so too does the battery drive the capabilities of an EV. The most prominent technical performance features of an EV are its energy, power and life, and therefore these features will be the focus of our analysis.

Lithium is a very attractive material to base batteries on owing to its very low electrochemical potential which gives it the promise of a high cell voltage. As a result, lithium based batteries have been in development for over 40 years since the first intercalation/deintercalation was demonstrated in the 1970s [3]. Twenty plus years of research culminated in the first commercial production of a lithium ion battery by Sony Energy Device Corporation in 1991 [4]. Sony was able to create a product suitable for the consumer electronics market whose form factor (18,650 cylindrical cell or 18 mm  $\varnothing$  and 65 mm height) has since become an industry mainstay and is today produced in the billions annually. Due to its ubiquity and

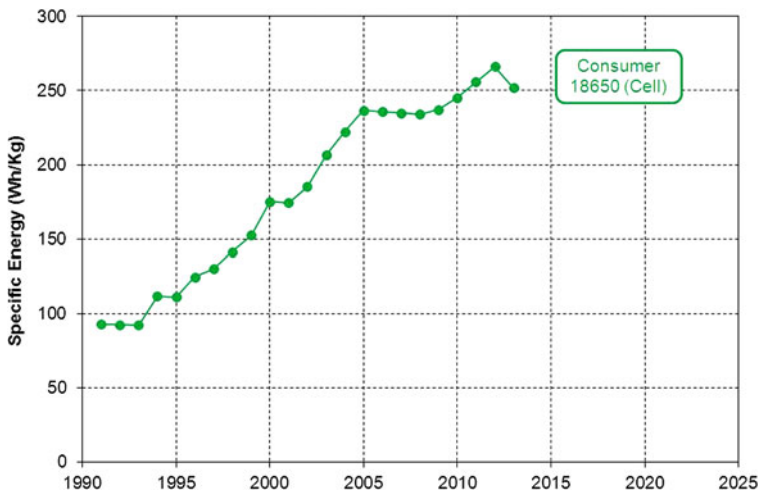
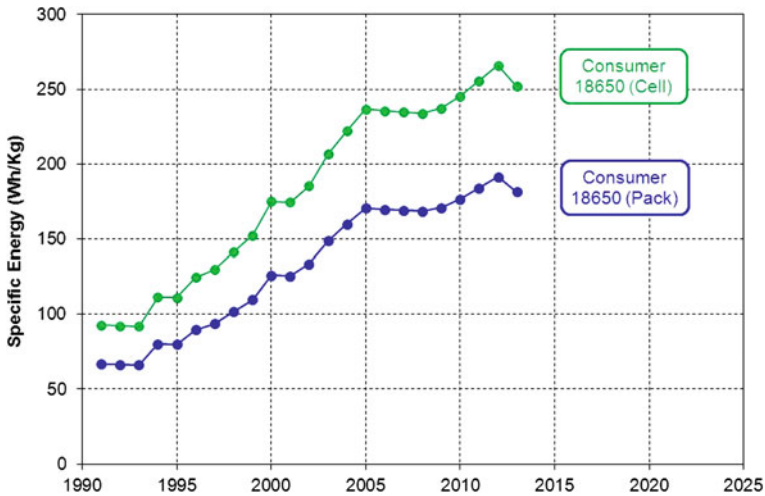


Fig. 1 Consumer 18,650 cell specific energy (Wh/kg) over time [5]

massive production volumes, the 18,650 cell is a useful benchmark for the development of lithium ion battery technology as a whole. The significant rate of progress of one figure of merit, specific energy (Wh/kg), is shown below in Fig. 1.

Despite the continuous improvements in commercial lithium ion technology over the last 20 years, it has been only in the last couple of years that the technology has been suitable for some automotive applications. In automotive applications we need to consider not only cell level figures of merit, but also at the module (a mechanical assembly of cells, often containing electrical/thermal sensing and interfaces) and battery pack level (a mechanical assembly of modules, often containing electrical and thermal control hardware and software). The assembly of cells into modules and subsequently packs is what makes the hardware relevant to an automotive designer and user. Although module and pack designs can vary substantially, they all add additional weight and volume which effectively de-rates the cell level performance values. In the case of weight, estimates of a 20 loss at the module level and a further 10 % loss at the pack level are often made by industry groups [6]. These estimates would yield a battery pack weight efficiency of 72, which falls at the high end of practical designs which yield values ranging from 50 to 75 %. The impact of these de-rated engineering estimates is shown in Fig. 2 below.

Vehicle electrification is a global phenomenon and the research of its development must be cast with a similarly wide viewpoint. Each of the three most mature automotive manufacturing regions (United States, Europe and Japan) has published EV battery targets. In the US, the United States Advanced Battery Consortium (USABC) is composed of Chrysler, Ford and General Motors in partnership with the US Department of Energy [7]. The European Council for Automotive Research and Development (EUCAR) is an analogous organization in



**Fig. 2** Consumer 18,650 pack specific energy (Wh/kg) over time

Europe [8]. In Japan, the Ministry of Economy, Trade and Industry (METI) established an agency to promote the development of new energy technologies in the form of the New Energy and Industrial Technology Development Organization (NEDO) [9]. Each of these respective organizations, USCAR, EUCAR and NEDO has created EV battery targets to guide industry's technology development in 1996, 2009 and 2008, respectively. Our research approach is strengthened by considering EV battery targets from a variety of regions in the world, published over a span of many years.

One of the principle differences between consumer electronics and automotive applications is the duration of use in terms of both calendar and cycle life. Typically, consumer electronics require 500 cycles and 1–2 years of useful life. In automotive applications, the battery is part of a traction system which is expected to last the life of the vehicle, requiring thousands (and in the case of hybrid electric vehicles, millions) of cycles over 10–15 years [10]. Due to this long duty cycle requirement for automotive applications, designers must specify BOL and EOL performance requirements, as the battery will inevitably degrade during use.

For our study we have identified power, energy and life to be of primary interest. Given that the majority of public battery performance specifications provided by battery makers and targets published by industry groups are BOL values, we will focus on this timing when considering energy and power. Due to the inherent requirement to consider life as an EOL condition and the large variety of calendar ageing and cycle life conditions, its study is more complicated. As such our approach is to look at a variety of factors which influence life performance including energy use, temperature and testing requirements.

**Table 1** BOL EV targets [6, 11–12]

Hardware level	USABC (1996)		EUCAR (2009)		NEDO (2008)					
	Pack		Pack		Module					
Target timing	Minimum	Long Term	2010	2015	2008	2015	2020	2030		
Energy (Wh/kg)	230	300	90–100	130–150	100	150	250	500		
Power (W/kg)	150	200	400–750	500–950	1,000	1,200	1,500	1,000		
Calendar life (Y)	10	10	8–10	10	5–8	8–10	10–15	10–15		
Cost (€/Wh)	\$0.15	\$0.10	\$0.40–0.50	\$0.30	100–200€	30€	20€	10€		

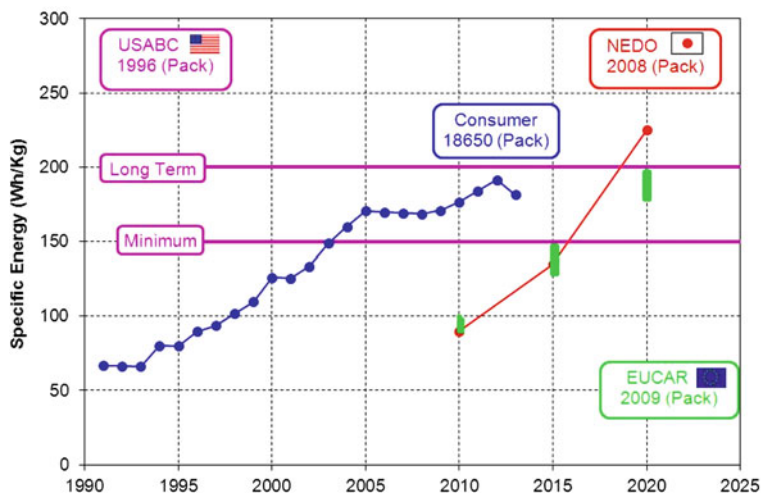


Fig. 3 Pack specific energy (Wh/kg) targets & 18,650 estimates

### 3 Results

Our research compared the performance of existing batteries to those of an international community of EV battery targets. These targets were developed in the United States, Europe and Japan over a period of many years. The most relevant targets for a variety of time periods are shown below in Table 1. The USABC goals have no timing attached, but rather represent a minimum level of performance and one required for true long term commercialization. The EUCAR and NEDO targets span 5 year intervals up to 2,030.

A comparison of Table 1 across organizations and time reveals a few consistent trends. A combined appraisal of specific energy implies that a value of  $\sim 200$  Wh/kg is required for a competitive EV and is predicted in the early 2020s. The EUCAR and NEDO targets for power are noticeably more aggressive than the USABC values. This is likely due to the pace of development of battery technology between 1996 and 2009/2008, which is the timing of the USABC and EUCAR/NEDO goals respectively. The energy of a battery is an intrinsic property determined by the choice of materials and their electrochemical properties of voltage and capacity. Power on the other hand is an extrinsic property, influenced by the material behaviour, but also substantially controlled by improved designs achieved through engineering refinements. Given the large industry which has evolved around lithium ion batteries in the last 20 years, it is not surprising that the fast pace of engineering improvements has exceeded that of new material discoveries. An appraisal of the life targets shows alignment on a life of the vehicle expectation of 10–15 years, as outlined above.

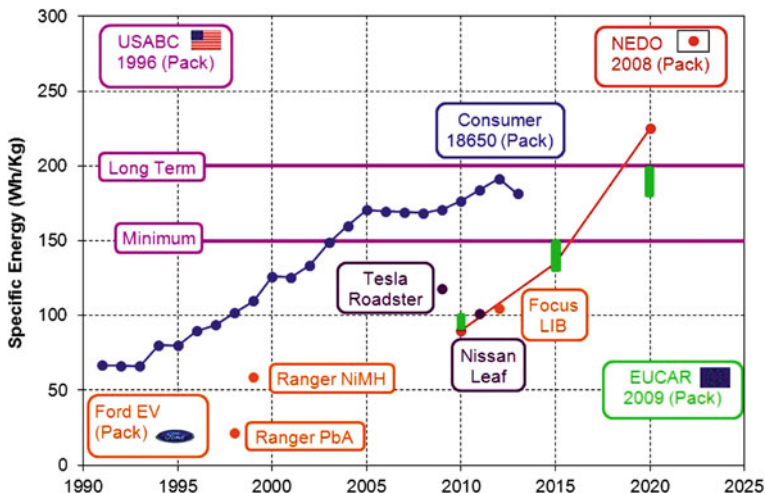


Fig. 4 Pack specific energy (Wh/kg) targets & performance

### 3.1 Energy

As outlined in our methodology, 18,650 cylindrical cells are the lithium ion battery format produced in the highest volume commercially to serve the consumer electronics industry. While posing many challenges for automotive applications, the usage of those cells in automotive applications was first proposed and demonstrated by AC Propulsion. The suitability of 18,650 s for automotive aside, this cell format and size is at the forefront of specific energy developments and so considering its rate of improvement can prove instructive relative to the broader class of lithium ion technology. In Fig. 3 below, it is shown that even when considering highly engineered and mass produced 18650 cells, the specific energy of current 18,650 technology is below the goals outlined by USABC for long term automotive production.

Although considering the capabilities of 18,650's in abstract designs is a useful calibrating investigation, it is also beneficial to examine existing vehicle designs. In Fig. 4, a variety of EV battery specific energies are plotted. Three EVs from Ford are shown, the 1998 Lead Acid Battery Ranger EV, the 1999 Nickel-Metal Hydride Ranger EV and the 2012 Lithium Ion Battery Focus EV. For comparison, the Nissan Leaf EV is also shown and overlays almost exactly over the Focus EV. Additionally, the Tesla Roadster using 18650 cells is shown and it should be noted that the specific energy achieved is far below the value estimated for the 18,650 cell-based pack specific energy capability available in that year. The specific energy achieved in an actual automotive application (Tesla Roadster) is approximately that

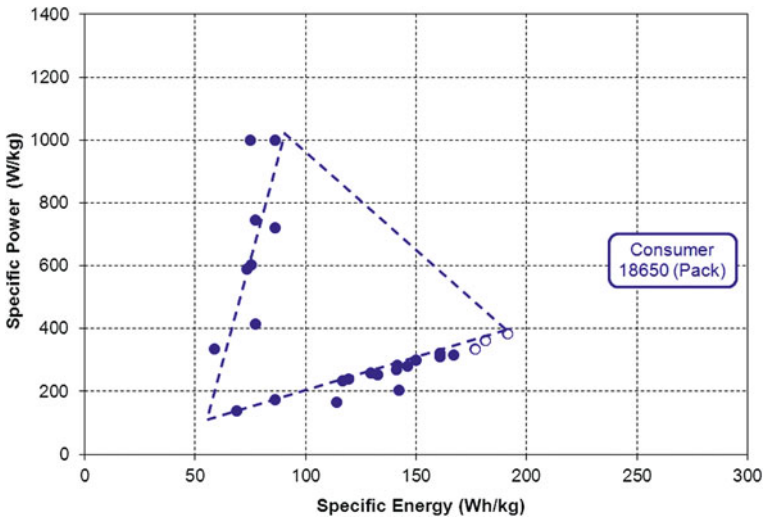


Fig. 5 Specific power (W/kg) of various 18,650 [13–15]

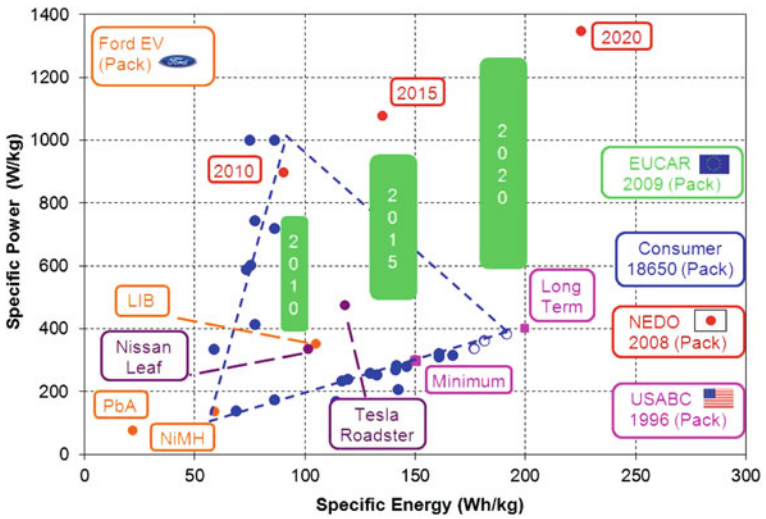


Fig. 6 Specific power (W/kg) targets & performance

which was predicted to be possible with an 18,650-cell-based pack about 8–9 years earlier. This can be attributed to several factors specific to battery designs for automotive applications, but in general communicates the challenges in using cells designed for consumer electronics in an automotive application.



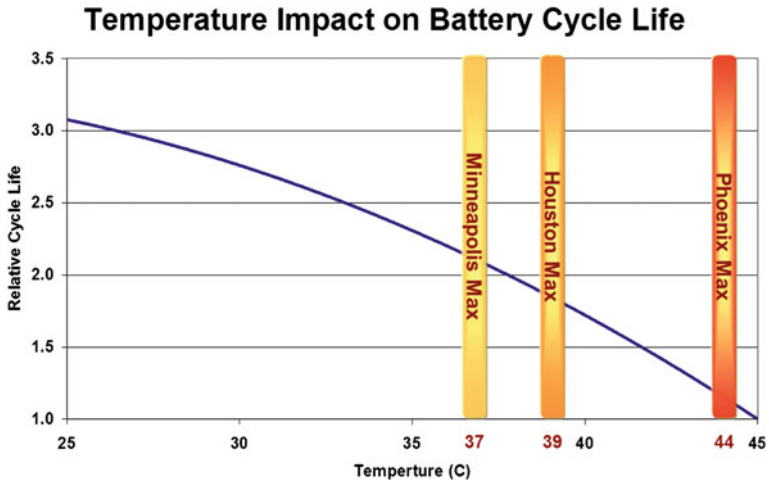


Fig. 7 Temperature impact on battery cycle life [16]

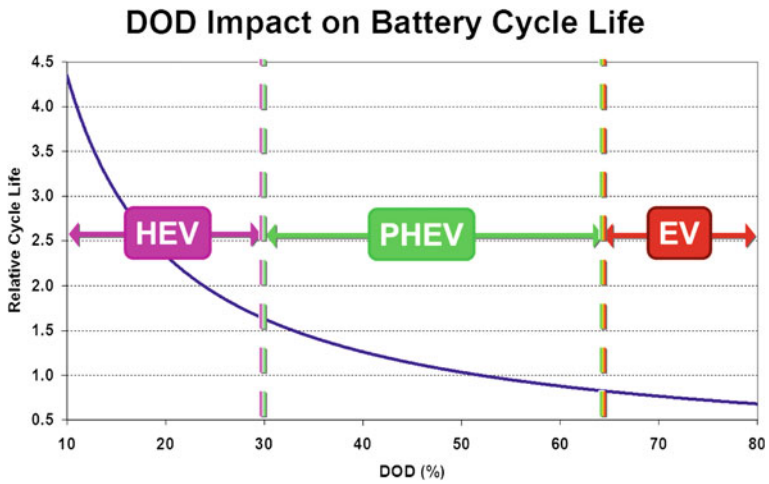


Fig. 8 DOD impact on battery cycle life [17]

### 3.2 Power

Our analysis of the power capability of existing lithium ion battery technology also begins by considering that achieved in the 18650 format. A general principle of battery design is that power and energy can be optimized, but rarely at the same

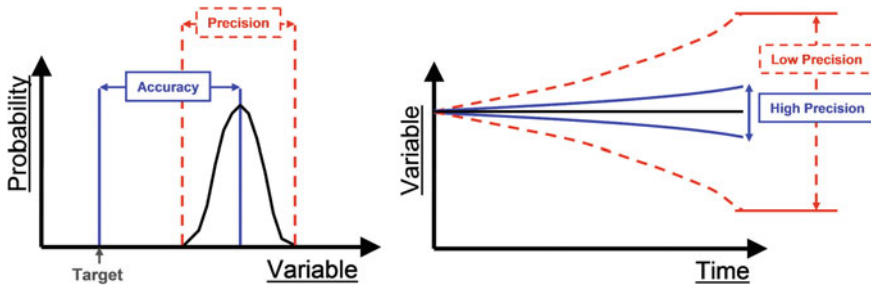


Fig. 9 Precision versus accuracy

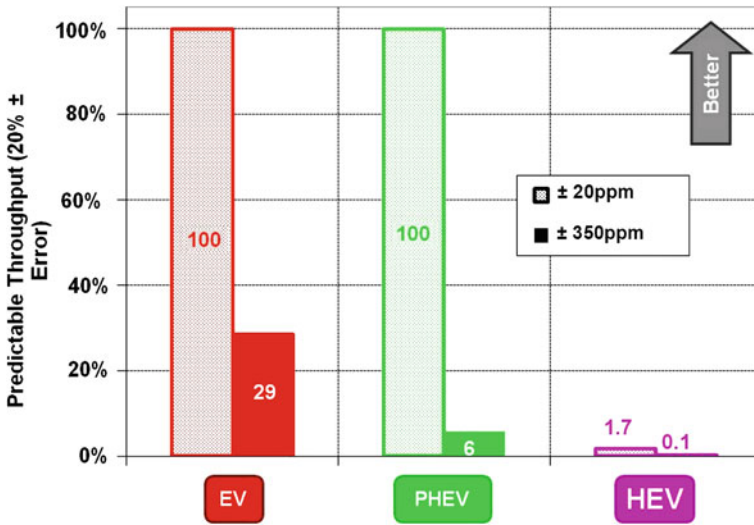


Fig. 10 Impact of precision on USABC test patterns ( $\pm 350 \rightarrow \pm 20$  ppm)

time, and this is shown below in Fig. 5 summary of existing state of the art 18,650-cell-based pack specific power versus energy. These cells are designed for either high energy or high power applications and the estimated performance envelope of the technology takes the shape of a triangle.

As in the case of energy, it is useful to consider the EV battery targets of the USABC, EUCAR and NEDO, as well as the performance of existing vehicles, and those results are plotted in Fig. 6. It is apparent that the performance of the Ford Focus, Nissan Leaf and Tesla Roadster all fit comfortably inside the 18,650 performance triangle. Additionally, the higher power performance targets of EUCAR and NEDO introduced in the methodology are highlighted here when compared to USABC targets.

### 3.3 Life

As outlined in the methodology, the research of life factors in this study is more complicated than that of energy and power, owing to the necessity to consider EOL versus BOL conditions, respectively. To address this EV battery need, we will examine three important factors affecting life requirements: temperature, energy usage and testing.

The relationship of the impact of temperature on battery cycle life is shown in Fig. 7. The relative cycle life decreases noticeably as the temperature increases, reflecting the impact on lithium ion battery materials and the related electrochemistry. For reference, the maximum annual temperatures of three US cities are shown, Minneapolis, Houston and Phoenix.

The depth of discharge (DOD) is the percentage of a battery's energy which has been used during a cycle. 100 % DOD cycle swings are not possible in automotive applications for a number of reasons; including their impact on life, as shown in Fig. 8. The DOD swing of various applications (Hybrids (HEV), Plug-In Hybrids and EVs) can vary from vehicle to vehicle, but the US Department of Energy-estimated DOD ranges are shown in Fig. 8 [17].

An often overlooked complexity of the life requirement is the need for high precision that the large cycle number and long calendar requirements introduce in terms of battery life data collection, life estimation and validation. In Fig. 9, we describe the distinction between precision and accuracy (L), as well as highlight the impact of a low precision system (R). Due to the high testing burden, the validation of automotive batteries benefits strongly from the ability to predict end of test performance based on an initial data set. Figure 9(R) shows the dangers of using data from a low precision system to perform such calculations. The compounding nature of precision and predictions can lead to a dramatic magnification of the impact as shown in Fig. 9(R).

The current state of the art in battery testers is estimated to achieve a precision of 350 ppm [18]. Based on extensive discussion with an industry expert and manufacturer, Arbin Instruments, a precision of 20 ppm may be achievable using existing technology concepts. During use, many performance variables will degrade and approximately 20 % degradation is often considered end of life. In Fig. 10, we calculate the impact of 350 and  $\pm 20$  ppm precision on the accumulated error involved in energy throughput (MWh) prediction using the USABC test patterns. It is shown that with a  $\pm 20$  ppm tester, it would be possible to predict 100 of an EV and PHEV battery's life with  $<20$  % error at the test's onset. Such a prediction would not be possible with a  $\pm 350$  ppm tester due to its high error.

## 4 Conclusions

In the three key battery performance categories (energy, power and life), only power has been achieved at levels sufficient to promote widespread electrification. Energy improvements have proven more elusive as they are based on fundamental material principles, whereas power is more generally a product of engineering effort. The quantification of life is more difficult and requires an understanding of the specific vehicle design and use conditions, as well as the impact of temperature, energy use, and testing as highlighted.

While the wholesale replacement of gasoline powertrains by EV powertrains will continue to be limited by LIB costs for the foreseeable future, continued incremental LIB cost reductions are expected. Although EVs will not reach performance and cost parity with gasoline systems over the timeline of this study (~ 10 years), it is projected that the scale of the gap will continue to decrease.

## References

1. "One Million Electric Vehicles by 2015: February 2011 Status Report." US DOE. [http://energy.gov/sites/prod/files/edg/news/documents/1\\_Million\\_Electric\\_Vehicle\\_Report\\_Final.pdf](http://energy.gov/sites/prod/files/edg/news/documents/1_Million_Electric_Vehicle_Report_Final.pdf). Accessed 10 July 2012
2. Ford H (1988) "Today and tomorrow". Productivity Press, Cambridge
3. Whittingham MS (1976) Electrical energy storage and intercalation chemistry. *Science* 192(4244):1126–1127
4. Reddy T (ed.) (2011) "Linden's handbook of batteries, 4th edn." McGraw-Hill, New York
5. "Battery Association of Japan Website" (2012) <http://www.baj.or.jp/>, Accessed 12 July 2012
6. "NEDO Technology Development Roadmap Secondary Battery (Battery RM 2010)." (2012) New energy and industrial technology development organization (NEDO). <http://www.nedo.go.jp/content/100153876.pdf>. Accessed 10 July 2012
7. "USABC Website"(2012) <http://www.uscar.org/guest/teams/12/U-S-Advanced-Battery-Consortium>. Accessed 12 July 2012
8. "EUCAR Website" (2012) <http://www.eucar.be/>. Accessed 12 July 2012
9. "NEDO Website" (2012) <http://www.nedo.go.jp/>. Accessed 12 July 2012
10. "USABC Manuals" [http://www.uscar.org/guest/article\\_view.php?articles\\_id=86](http://www.uscar.org/guest/article_view.php?articles_id=86), Accessed 13 July 2012
11. Teysstot A (2009) "HELIOS European project and EUCAR/VDA research roadmaps". EVS24, Stavanger, Norway, 13–16 May 2009
12. "USABC Goals for Advanced Batteries for EVs" (2012) United States advanced battery consortium (USABC). [http://www.uscar.org/commands/files\\_download.php?files\\_id=27](http://www.uscar.org/commands/files_download.php?files_id=27). Accessed 10 July 2012
13. "Panasonic 18650" (2012) Panasonic. <http://industrial.panasonic.com/www-cgi/jvcr21pz.cgi?E+BA+3+ACA4001+4++WW>. Accessed 14 July 2012
14. "LG Chem 18650" (2012) LG chemical. <http://www.lgchem.com>. Accessed 14 July 2012
15. "Samsung 18650" (2012) Samsung SDI. <http://www.samsungsdi.com/battery/cylindrical-rechargeable-battery.jsp>. Accessed 14 July 2012
16. Pesaran A, Smith K, Markel T (2009) "Impact of the 3Cs of batteries on PHEV value proposition: cost, calendar life, and cycle life." advanced automotive battery and EC capacitor conference, Long Beach, 8–12 June 2009

17. Duong T (2010) "Direction for energy storage R&D in the vehicle technologies program." Scalable energy storage beyond Li-Ion, Oak Ridge, 7 Oct 2010
18. Smith AJ, Burns JC, Trussler S, Dahn J (2010) "Precision measurements of the coulombic efficiency of lithium-ion batteries and of electrode materials for lithium-ion batteries." J Electr Soc 157(2):A196–A202

# Design of the Experimental Procedures for Analysis of Thermal and Electrical Properties of a Prismatic LiFeYPO<sub>4</sub> Battery in a Modified Electric Car

Chayangkun Sanguanwatana, Chadchai Srisurangkul,  
Monsak Pimsarn and Shoji Tsushima

**Abstract** As being the most important part in the energy supply system, the battery must be carefully monitored in order to optimize the performance and to prolong its life. The most affected parameter to the battery is the operating temperature as the higher operating temperature increase the performance but shorten the life and with lower operating temperature can ensure longer life but reduce the performance. With this, the battery thermal management system is created in order to keep the operating temperature at the suitable range. In order to achieve this, thermal behaviour in loaded condition must be analysed beforehand. A series of experimental procedures is designed for the selected lithium iron phosphate battery to determine the thermal properties such as heat capacity, heat generation, and cell temperature according to the electrical load applied. Derived thermal model of lithium ion battery was utilized for this purpose as it shows the relationship between the thermal, electrical properties and other parameters such as voltage, current and cell temperature. When the battery is applied with electrical load, the data of voltage, current, and surface cell temperature can be used to determine the thermal properties and at the same time, electrical properties such as open circuit voltage, state of charge and internal resistance are also obtained for the performance evaluation.

---

F2012-B04-007

---

C. Sanguanwatana (✉) · C. Srisurangkul  
Automotive Laboratory, National Metal and Materials Technology Center,  
Bangkok, Thailand  
e-mail: aura\_win@hotmail.com

M. Pimsarn  
King Mongkut's Institute of Technology Ladkrabang, Bangkok, Thailand

S. Tsushima  
Research Center for Carbon Recycling and Energy, Tokyo Institute of Technology,  
Tokyo, Japan

**Keywords** Lithium ion battery · Electric vehicle · Lithium ion battery thermal characterization · Battery thermal management system · Battery thermal model

## 1 Introduction

Electric vehicle has become one of the alternatives for replacing the fossil-fuel vehicle due to the rapid decrease in the energy source and increase in the automobile utilization. Also, with the zero pipe-tail emission, the replacement of electric vehicle can decrease a great deal of the amount of green house gas released into the earth's atmosphere. National Metal and Materials Technology Center, Thailand (MTEC) joined with Electricity Generating Authority of Thailand (EGAT) in order to form the electric car project modified from the conventional gasoline powered car. This has the conventional components replaced with the electrical ones such as motor and batteries. The benefits from this includes the reduced cost of purchasing a brand new electric car and this can demonstrate that in the future, used gasoline cars can be modified into electric cars which is a merit in terms of materials recycling.

Many tests are required in order to maximize the performance of the vehicle. In this paper, the main focus is put on the battery which is the most important component in the power supply system. With the proper design of battery management system, the performance of the battery can be maximized. Also, it is known that the greatest enemy of the battery is heat because heat is the main factor which impacts the battery's performance directly.

The sudden change in temperature can change the form of active chemicals in the battery. This result in many serious consequences depends on the temperature level. Extremely low operating temperature can cause lithium plating while charging the battery. On the other hand extremely high operating temperature can build up the pressure due to gassing inside the cell, cathode material breakdown and possibly thermal runaway. To keep the suitable operating temperature, battery thermal management system or in short BTMS can be a great help. BTMS is the system which monitors the battery temperature, provide the battery with the proper cooling system in order to prolong battery's life and maximize its performance. However, before the design of BTMS, it is best to understand the thermal behavior of the selected battery or to perform thermal characterization of the battery. This includes the determination of thermal properties of the battery which includes heat capacity and heat generation while the battery is loaded. As different amount of load is applied to the battery, it is expected to see the different results of thermal properties with different electrical load. With the data of thermal properties of the battery, thermal characterization can be performed to see the change in cell temperature and then BTMS can be designed based on those results.

**Table 1** Characteristics of several types of lithium ion batteries [1]

Cathode material	Typical voltage (V)	Energy density		Thermal stability
		Gravimetric (Wh/Kg)	Volumetric (Wh/L)	
Cobalt oxide	3.7	195	560	Poor
Nickel cobalt aluminum oxide (NCA)	3.6	220	600	Fair
Nickel cobalt manganese oxide (NCM)	3.6	205	580	Fair
Manganese oxide (Spinel)	3.9	150	420	Good
Iron phosphate (LFP)	3.2	90–130	333	Very Good

## 2 Lithium Iron Phosphate Battery

As known that lithium ion battery contains many attributes which has a lot of advantages over the other types of battery such as higher working voltage comparing to aqueous batteries, less self-discharge rate, higher energy density and contains no memory effect. With this, it was selected to be used for the modified electric car. The cell chemistry of the battery is “lithium iron yttrium phosphate” which has additional advantages comparing to the other types of lithium ion batteries. This includes the long life span, great thermal stability and less impact to the environment comparing to the cobalt cells. With great thermal stability, it becomes the safest lithium ion battery type because under the situation where the battery is misused such as in a very hot environment, lithium iron phosphate battery will not decompose at high temperature.

From Table 1, it can be seen that even though the operating voltage of lithium iron phosphate battery is the lowest among the others, the (thermal) stability is the best. As invented by John Goodenough’s research group at the University of Texas in 1996 [2], it gradually became popular and is utilized many applications such as One Laptop per Child Program in China, Solar Powered Path Lights and many electrical-converted vehicle projects.

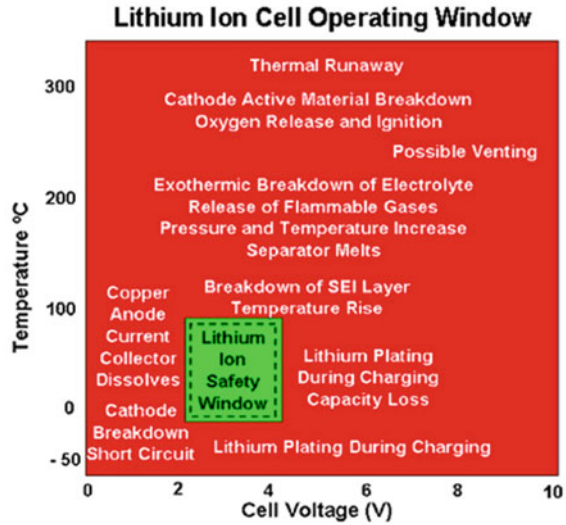
## 3 Battery Thermal Safety Issues and Thermal Management System

Abusive or uncontrolled use of a battery can lead to serious consequences. Cell voltage and operating temperature are the most affected parameters towards the failure of lithium batteries. It is needed to be controlled at some range. Figure 1 shows the safe area for using lithium ion cell.

From Fig. 1, it shows that many consequences from several abusive situation (dealing with voltage and temperature). This means that the user have to maintain the suitable range of operating voltage and temperature at the same time. For example, if the battery is used at room temperature but the battery was



**Fig. 1** Lithium ion cell operating window [3]



overcharged (overvoltage), it may result in lithium plating which permanently reduce the capacity. Or if the voltage is at 3.3 V but the operating temperature is well over 100 °C, it will surely melts the separator inside the cell and short circuit the whole system. Thermal runaway is the most severe consequences which could ever happen because it can lead to the explosion of the battery.

At this point, the consequences of using the battery outside the temperature range can be more severe than using it outside the voltage range as it will not only damage the battery but also damage the user. Therefore, it is important that the operating temperature is kept at the optimized range.

Battery Thermal Management System (BTMS) is therefore designed for this purpose. It can be used to observe and regulate the temperature not to exceed the limit. This can help prolonging the life of the battery, maximize the performance and also ensure the highest degree of safety of the user. However, some procedures are needed before the construction of BTMS. According to NREL, following issues are to be discussed: cell characteristics, module cooling strategy, operating conditions and battery thermal responses.

In this case, the battery thermal response is the main focus. Various tools can be used in the development of the battery thermal management system. This includes thermal analysis (CAD), fluid and heat transfer experiments and simulations (CFD), thermal characterization and vehicle testing [4] (Fig. 2).

An amount of work has been done in order to see how heat is transferred from the battery in the designed cooling method [5]. However, thermal properties of the battery used for this simulation is simply averaged from the data of chemistry structure of the cell in the manual from the manufacturer. To improve the accuracy of the results, thermal properties should be obtained by using thermal model of the battery.

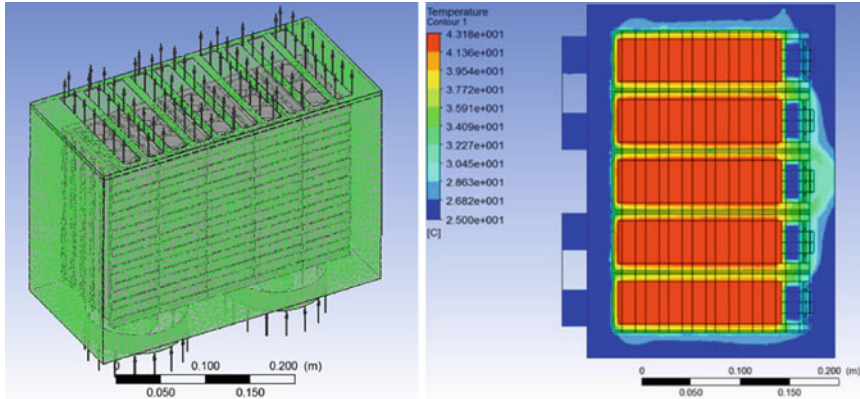


Fig. 2 Simulation of fluid and heat transfer with thermal analysis of the battery [5]

### 4 Battery Thermal Model

From the work of Newman et al. [6], it was found that many researchers[7, 8, 9] used the thermal model for a single cell in order to capture thermal behavior of the battery while being loaded. Few assumptions are needed for applying this model such as the uniform temperature distribution throughout the cell and stable chemical reactions. It is summarized as followed:

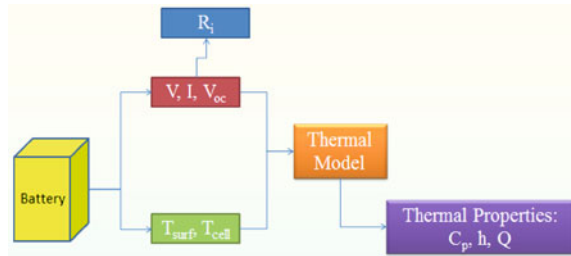
$$I(V_{oc} - V) + IT_{cell} \frac{\partial V_{oc}}{\partial T_{cell}} = h(T_{surf} - T_{amb}) + C_p \frac{dT}{dt} \tag{1}$$

$I$  = Current (A),  $V_{oc}$  = Open Circuit Voltage (V),  $V$  = Cell Voltage (V)  
 $T_{cell}$  = Internal Temperature ( $^{\circ}C$ ),  $T_{amb}$  = Ambient Temperature ( $^{\circ}C$ ),  
 $T_{surf}$  = Surface Temperature ( $^{\circ}C$ ),  $C_p$  = Heat Capacity (J/  $^{\circ}C$ ),  $h$  = Surrounding heat coefficient (W/  $^{\circ}C$ )

This equation is a result of a heat balance which considering the battery as a control volume. It can be seen that there are two terms on the left hand side. The first term is the overpotential resistance term which results from the electrical power applied, it is always positive. The second terms deal with the chemical reaction in the cell, the charge and discharge reaction can result in endothermic and exothermic condition for the battery respectively in which it can be related to the enthalpy change and Gibb’s free energy. This second term on the left hand side is usually called the reversible entropic term and it can either positive or negative.

As for the right hand side, the first term represents the heat transfer from the battery to the surroundings, it can also be considered in terms of the difference between the cell surface and the ambient temperature. Surrounding heat transfer coefficient,  $h$  will also be one of the properties to be investigated before the calculations of heat capacity  $C_p$ . In the second term on the right hand side, heat capacity represents the amount of heat required for changing the temperature of the battery. It is the main focus for this research work.

**Fig. 3** Block diagram shows overall picture of this research work



## 5 Design of the Experimental Procedures

The main objective of this work is to determine thermal properties of the selected Li-ion battery at different loads and thermal environments. To simplify the procedures, the block diagram below shows the overall picture of this work. The main objective of this work is to determine thermal properties of the selected Li-ion battery at different loads and thermal environments. To simplify the procedures, the block diagram below shows the overall picture of this work.

As illustrated in Fig. 3, to serve the main purpose of this work, it is needed to design the procedures in order to obtain the voltage and current load data while the battery is loaded and at the same time surface and cell temperature are also monitored. This is based on the thermal model shown in the previous section which requires those data in order to determine thermal properties of the battery. Furthermore,  $R_i$  or internal resistance is included for evaluating the battery's performance and is calculated from the data of voltage and current load.

From Fig. 4, a selected battery is connected to the electronic load/power supply with thermocouple probe attached to the surface and infrared temperature sensor attached at the top of the cell in order to measure the internal temperature. The electronic load and power supply are used for discharging and charging the battery respectively. The infrared thermal sensor for measuring the cell internal temperature. Thermocouple cannot be used for measuring internal temperature is because it is required to contact the core of the cell which can lead to short circuit. Therefore, using the non-contact measurement is more suitable. The small blue box represents the Data Acquisition tool where it is used for recording the temperature measured at the surface and the cell. A computer is used for storing the experimental data for the analysis. The transparent purple box is the thermal chamber where it will be used for regulating the environmental temperature around the battery, this deals with the temperature coefficient which will be explained in the next section.

The selected lithium ion battery is the Thunder Sky lithium iron phosphate battery with the capacity of 60 Ah. Specifications are shown below (Fig. 5) (Table 2):

The design of experimental procedures is based on the thermal model of the battery and also the specifications of the battery. The procedures are divided into two main parts:

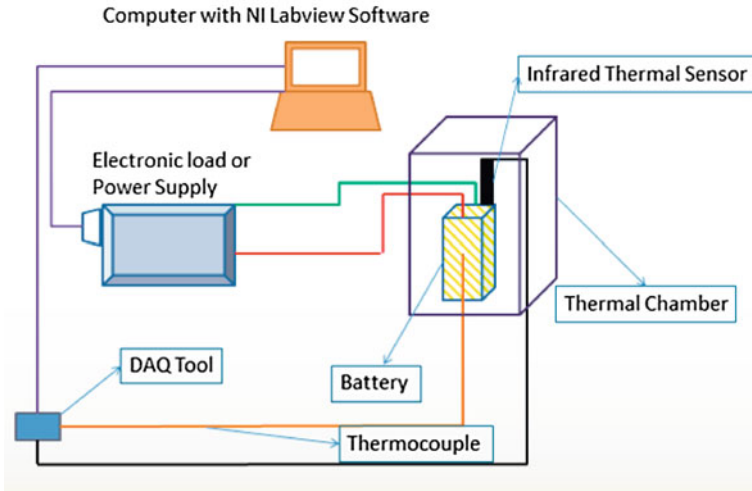


Fig. 4 Schematic diagram for the experimental setup

1. Determination of heat generated from the cell
2. Calculations of thermal properties of the cell

In the first part, the heat generated from the cell is the combination of all terms on the left hand side in Eq. 1. This can be obtained from recording the voltage, current and cell temperature while the battery is being charged or discharged. The main parameter here is the current load applied ( $I$ ), which can be 1 CA, 0.5 CA or 2 CA (Fig. 6).

However, in the second term,  $dV/dT$  or the temperature coefficient is present. This has to be determined in a separated experiment. See figure below for illustrations (Fig. 7):

The battery is put inside the adjustable temperature thermal chamber and while the environmental temperature is adjusted, the cell temperature and open circuit voltage will be observed and recorded. This will be used for the calculation of temperature coefficient.

In the second part, when the battery is charged or discharged and the voltage, current and temperature data are gathered, thermal properties can be determined. From Eq. 1 it can be seen that there are two variables to be determine. They are heat capacity ( $C_p$ ) and surrounding heat transfer coefficient ( $h$ ).

With the steady state condition, where the cell temperature stay constant with time ( $\partial T_{cell}/\partial t = 0$ ), the term with heat capacity will be eliminated and thus, surrounding heat transfer coefficient ( $h$ ) can be determined and while this depends on the current load applied to the battery,  $I$  (and also the heat generated,  $Q$ ). Therefore, when surrounding heat coefficient is determined, it can be applied in the transient condition ( $\partial T_{cell}/\partial t \neq 0$ ) to find the heat capacity of the battery.

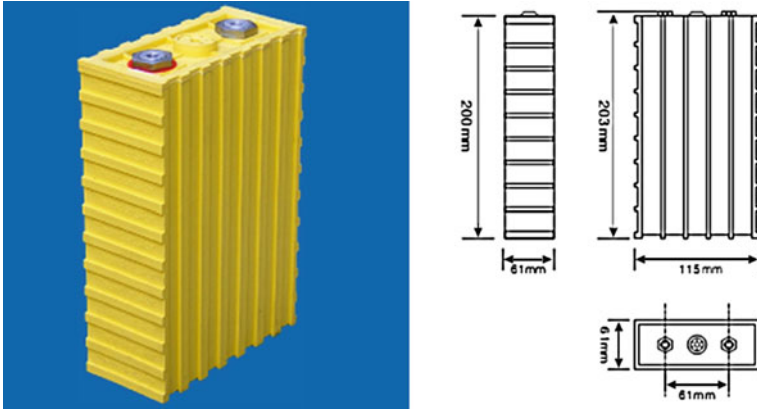


Fig. 5 The selected battery for the experiment [10]

Table 2 Specifications of the selected battery for the experiment [10]

Model	TS-LFP60AHA
Nominal capacity	60 Ah
Operation voltage	Charge: 4.0 V, Discharge: 2.8 V
Maximum charge current	Less or equal to 3 CA
Maximum discharge current	3 CA or less for constant current 20 CA or less for impulse current
Standard charge/discharge current	0.5 CA
Cycle life	(80DOD %) ≥ 3,000 times (70DOD %) ≥ 5,000 times
Temperature durability of case	≤200 °C
Operating temperature	-45 to 85 °C for both charge and discharge
Self-discharge rate	≤3 % (Monthly)
Weight	2.3 kg ± 50 g

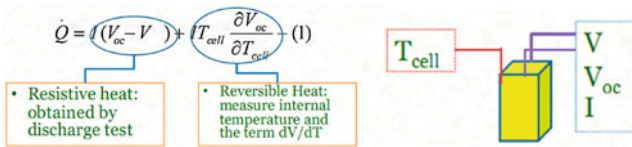
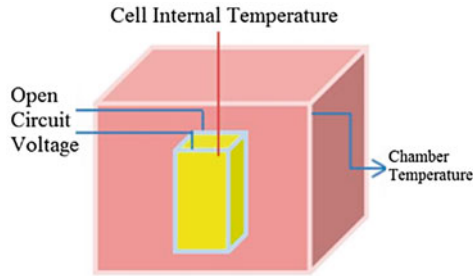


Fig. 6 Determination of heat generated from the cell

The initial condition has the 100 % charged battery stored in the room temperature. As the battery is put through the discharge test, the value of  $V-V_{oc}$  will be changed as the depth of discharge increases. Also, the cell temperature here will also be increased, then, the value of  $Q$  will be different in the different state of charges. This will also apply on surrounding heat transfer coefficient and heat



**Fig. 7** Experiment for the temperature coefficient

capacity and explained in the previous paragraph. This will also include the other experiment with different amount of current load applied to see the change in the focused thermal properties.

## 6 Preliminary Study and Results

At this stage, performance characteristics of the battery were studied. These include the charge and discharge profile (constant and pulsed current). The surface and terminal temperature were also recorded (Fig. 8).

From the figure, the voltage response from the constant current discharge shows that it tends to be flat from 10 to 80 % depth of discharge. This is suitable for the electric vehicle application due to its voltage stability. Furthermore, the chemistry of lithium iron phosphate gives the advantage in terms of thermal stability as it is unlikely to reach the stage of thermal runaway unless is extremely abused.

From Figs. 9 and 10, the temperature response from the pulse test shows that terminal temperature is more sensitive than surface temperature because when the load is put to zero, surface temperature dropped until the load is turned back on again.

The advantages of conducting pulse current test are that more data can be obtained and the dynamic of temperature change can also be captured. In this test, open circuit voltage can be observed as used for calculating heat generation as noted in thermal model. Furthermore, the data obtained from the pulsed discharge curve can be used to calculate the internal resistance which can also estimate battery's life as shown in Fig. 11.

Note that in this test, surface temperature is only measured at two points in front of and on the side of the battery. Also, it is observed that the positive terminal gives out heat more than that of negative terminal. This concludes that positive terminal is the point of heat concentration.

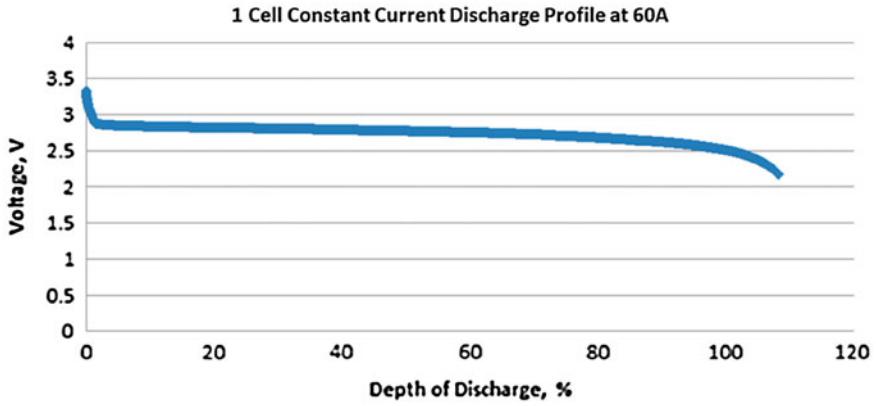


Fig. 8 Constant current discharge profile

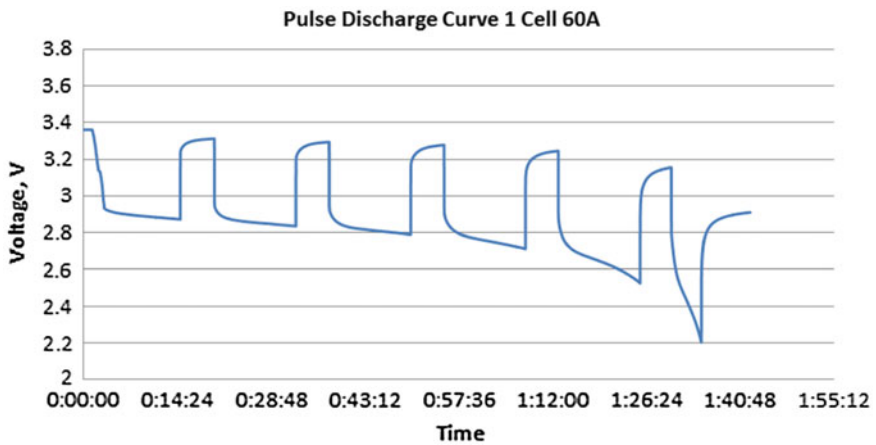


Fig. 9 Pulse discharge curve profile

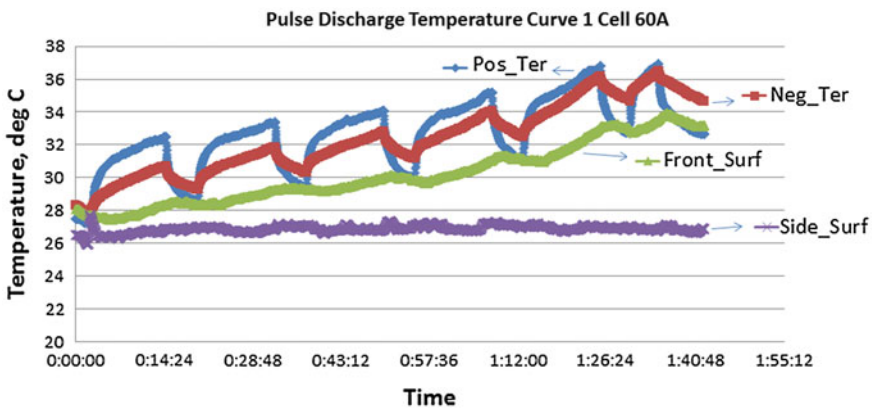


Fig. 10 Battery surface and terminal temperature response from pulse discharge test

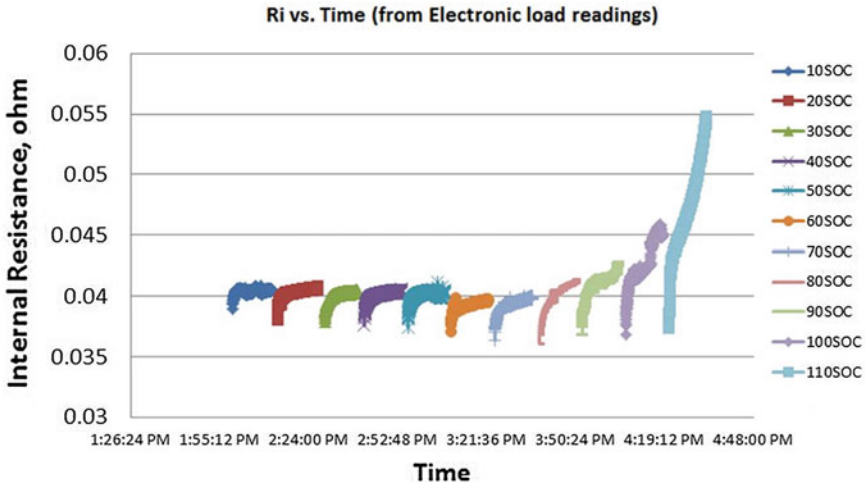


Fig. 11 Internal resistance calculated from the pulse test result (60 A)

## 7 Conclusions

Experimental procedures have been designed for the determination of thermal properties of the selected battery for the modified electric vehicle. Currently, the charge and discharge characteristics of the battery are obtained and in the same time surface and terminal temperature are monitored. In the next step, infrared temperature sensor will be installed at the top of the battery for internal temperature measurement. This is the main key towards the goal of this research work because the data of internal temperature of the battery can be used to calculate for thermal properties of the battery. Finally, when the data of thermal properties are obtained, it will be hand over to the design team of BTMS of the modified electric car and the cooling system of the battery.

## References

1. Woodbank Communication (2005) Rechargeable lithium batteries. Electropaedia: battery and energy technology <http://www.mpoweruk.com/lithiumS.htm>
2. Padhi AK, Nanjundaswamy KS, Goodenough JB (1996) LiFePO<sub>4</sub>: a novel cathode material for rechargeable batteries. Electrochem Soc Meet Abstr 96-1:73
3. Woodbank Communication (2005) Lithium battery failures. Electropaedia: battery and energy technology [http://www.mpoweruk.com/lithium\\_failures.htm](http://www.mpoweruk.com/lithium_failures.htm)
4. Pesaran A (2002) Battery thermal management, battery modeling and validation, ultracapacitor modeling and hybridization. Natl Renew Energy Lab
5. Vuthiwongvarakorn V, Taychavinijudom N (2010) Design of a battery thermal management system for electric vehicle



6. Thomas KE, Newman J (2003) Thermal modeling of porous insertion electrodes. *J Electrochem Soc* 150(2):176–192
7. Forgez C (2009) Thermal modeling of a cylindrical LiFePO<sub>4</sub>/graphite lithium-ion battery. *J Power Sources* 195:2961–2968
8. Onda K (2006) Thermal behavior of small lithium-ion battery during rapid charge and discharge cycles. *J Power Sources* 158:535–542
9. Sato N (2001) Thermal behavior analysis of lithium-ion batteries for electric and hybrid vehicles. *J Power Sources* 99:70–77
10. ThunderSky Lithium Battery. Thunder sky LiFeYPO<sub>4</sub> power battery specifications. ThunderSky

# Intelligent BMS Solution Using AI and Prognostic SPA

Subrahmanyam Sista and Avinash Sista

**Abstract** This paper presents a Novel, Low cost and Efficient Intelligent Battery Management Solution (iBMS) for Electric Vehicles (EV) and Hybrid Electric Vehicles (HEV). The solution provides a comprehensive topology for identifying the State of Charge (SOC), State of Health (SOH), charging and discharging including isolation of defective identified battery cell from healthy ones. The highly modular and scalable solution uses Bi-directional, 4 quadrant DC–DC converter; a non-isolated four switch topology design for the charging/discharging and cell cut off (infected cell), an Artificial Intelligence (AI) module using Fuzzy Logic (FL) and Signature Pattern Analysis (SPA) for envisaging the Battery stack health. The proposed design offers an affordable On-Board monitoring & diagnostics module leveraging the above intelligent modules and Impedance Analysis. This circumvents the need of further diagnostic tools; makes the system highly portable, Scalable for any chemical composition of battery cell and considerably extend the life cycle of EV/HEV battery stacks. In this paper, we will review some of the issues and associated solutions for battery thermal management and what information is needed for proper design of battery management systems. We will discuss about the issues related to impedance management which affects the battery life.

**Keywords** Artificial intelligence · Electric vehicles · Fuzzy logic · Hybrid electric vehicle · Impedance analysis · State of charging · State of health ·

---

F2012-B04-008

---

S. Sista (✉) · A. Sista  
Mahindra Satyam, Satyam Technology Center, Hyderabad, AP, INDIA  
e-mail: Sista\_Subrahmanyam@mahindrasatyam.com

A. Sista  
e-mail: Avinash\_Sista@mahindrasatyam.com

Bi-directional • 4 quadrant DC–DC convertor • UIS and CIP (use in series and charge in parallel)

## 1 Introduction

From portable Electronics to Electric vehicles (EVs), batteries are widely used as a main energy source in many applications. Battery management involves implementing functions that ensure optimum use of the battery in a system. Examples of such functions are proper charge handling and protecting the battery from misuse. The basic task of a BMS is to ensure that optimum use is made of the energy inside the battery powering the portable product and that the risk of damage inflicted upon the battery is minimized. This is achieved by monitoring and controlling the battery's charging and discharging process.

The purpose of the BMS is to guarantee safe and reliable battery operation. To maintain the safety and reliability of the battery, state monitoring and evaluation, charge control, and cell balancing are functionalities that have been implemented in BMS. Similar to the engine management system in a gasoline car, a gauge meter should be provided by the BMS in EVs and HEVs. BMS indicators should show the state of the safety, usage, performance, and longevity of the battery. Due to volatility, flammability and entropy changes, a lithium-ion battery could ignite if misused. This is a serious problem because an explosion could cause a fatal accident. Moreover, over-discharge causes reduced cell capacity due to irreversible chemical reactions. Therefore, a BMS needs to monitor and control the battery based on the safety circuitry incorporated within the battery packs. Whenever any abnormal conditions, such as over-voltage or overheating, are detected, the BMS should notify the user and execute the preset correction procedure. In addition to these functions, the BMS also monitors the system temperature to provide a better power consumption scheme, and communicates with individual components and operators [1].

Safety functions must be implemented and work correctly to ensure that no one gets hurt and that the BMU and battery cells are not damaged. If a battery cell has too low a cell voltage, it may result in voltage reversal. The consequences of reversal can be venting or rupturing depending on battery type. Under voltage can be prevented by measuring the voltage. In some cases, if there are weak battery cells in the battery pack, individual voltage measurements may be needed to detect low voltage. The cells should be monitored and not allowed to drop below the lower voltage threshold, thus minimizing the risk of voltage reversal. Cell Balancing/connect-disconnect circuit is a critical function for high-powered battery packs because a long series of individual cells is only as reliable as the weakest cell. Sometimes it may become necessary to rest a particular cell especially in case of an over temperature, therefore it needs to be disconnected and re-connected again.

The use of individual cell voltage measurements leads to a better precision in SOC and balancing, increasing the battery lifetime and capacity. It is important to follow the manufacturer's suggested cell voltage thresholds to avoid degradation of performance and improve safety.

## 2 The Current State of Electric Car Battery Technology

The value chain of electric car battery consists of seven steps: component production (including raw materials), cell production, module production, assembly of modules into the battery pack (including an electronic control unit and a cooling system) integration of battery pack into the vehicle and reuse and recycling. Automobile manufacturers have identified three types of rechargeable battery as suitable for electric car use. Those types are lead-acid batteries, nickel metal hydride (NiMH) batteries, and lithium-ion (Li-ion) batteries. Lithium-ion batteries comprise a family of battery chemistries that employ various combinations of anode and cathode materials. Each combination of anode and cathode has distinct advantages and disadvantages in terms of safety, performance, cost and other parameters. The most prominent technologies for automotive applications are lithium-nickel-cobalt-aluminium (NCA), lithium-nickel-manganese-cobalt (NMC), lithium-manganese spinel (LMO), lithium titanate (LTO) and lithium-iron phosphate (LFP) [2].

## 3 Proposed BMS Architecture

Our solution consists of batteries connected in series. Battery Management Solution is divided into the following three categories (Fig. 1):

- State of charge
- State of health
- Thermal Management

SOC and SOH are considered to be the methodologies for battery evaluation.

### 3.1 State of Charge

State of charge (SOC) is critical, but it is not measurable given the current onboard sensing technologies. The ratio of the currently available capacity to the maximum capacity can be expressed as SOC.

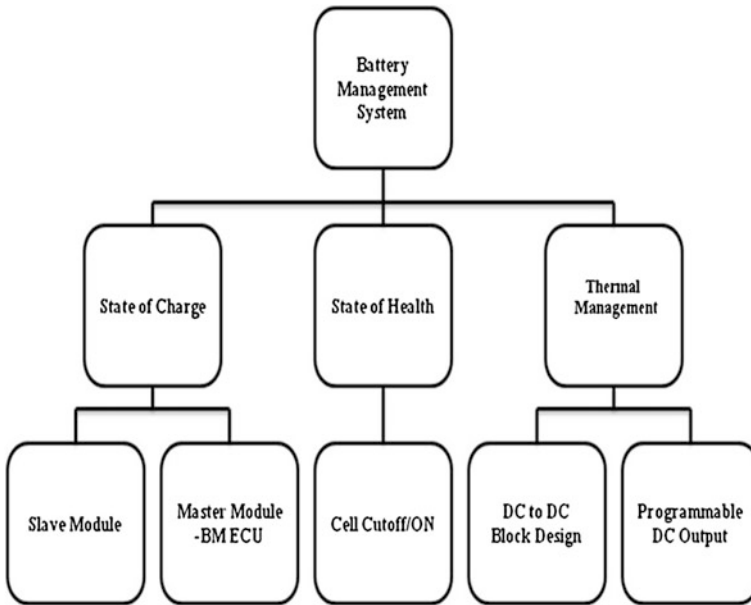


**Fig. 1** Battery management system

### ***3.2 State of Health***

State of health (SOH) describes the physical condition of a battery, ranging from internal behavior, such as loss of rated capacity, to external behavior, such as severe conditions. Unlike SOC, there is no clear-cut definition of SOH. A general definition of SOH is that it reflects the health condition of a battery and its ability to deliver specified performance compared to a fresh battery.

Figure 2 gives us an idea of how our solution architecture looks like.

In our solution we use two voltage sensors, two current sensors, 4 temperature sensors and an impedance sensor to measure and control the life of the battery [1].

#### **3.2.1 Thermal Management System**

The goal of a thermal management system is to deliver a battery pack at an optimum average temperature. LM35 is the temperature sensor used to sense the temperature in our solution. The LM35 series are precision integrated-circuit temperature sensors, whose output voltage is linearly proportional to the Celsius (Centigrade) temperature. The LM35 thus has an advantage over linear temperature sensors calibrated in ° Kelvin, as the user is not required to subtract a large constant voltage from its output to obtain convenient Centigrade scaling. The

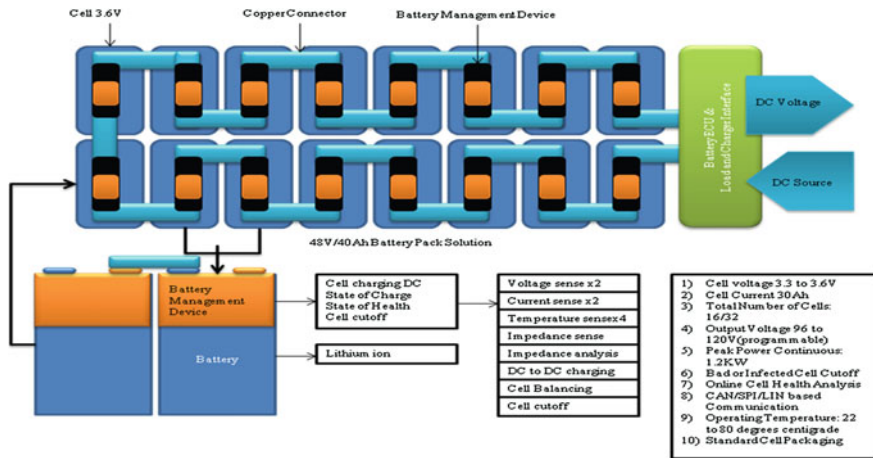


Fig. 2 Architecture

LM35 does not require any external calibration or trimming to provide typical accuracies of  $\pm 1/4$  °C at room temperature and  $\pm 3/4$  °C over a full  $-55$  to  $+150$  °C temperature range.

### 3.2.2 Impedance Measurement

Impedance is nothing but the Ohm’s Law for AC circuits. Voltage and current are sensed and are divided to give the impedance value. AD5934 is the impedance sensor used to sense the impedance. The AD5934 is a high precision impedance converter system solution that combines an on-board frequency generator with a 12-bit, 250 kSPS, analog-to-digital converter (ADC). The frequency generator allows an external complex impedance to be excited with a known frequency. The response signal from the impedance is sampled by the on-board ADC and a discrete Fourier transform (DFT) is processed by an on-board DSP engine. The DFT algorithm returns a real (R) and imaginary (I) data-word at each output frequency. Once calibrated, the magnitude of the impedance and relative phase of the impedance at each frequency point along the sweep is easily calculated using the following two equations:

$$\text{Magnitude} = 22 \text{ IR}+$$

$$\text{Phase} = \tan^{-1} (I/R) \text{ [3]}$$

### 3.2.3 Artificial Intelligence Approach to Estimate SOC

The battery pack charge and discharge processes are so complex that it is essential to consider many factors such as cell voltage, current, internal impedance and

temperature gradients. The battery pack connected in series presents a more complex problem. Careful monitoring and control is necessary to avoid any single cell within a Li-ion battery pack from undergoing over-voltage or under-voltage. In a Li-ion battery module-management system, the individual batteries SOC must be monitored because of overcharge and over-discharge issues. Therefore, it is essential to have methods capable of estimating the battery SOC.

Kalman Filter (KF) is a powerful tool for the state estimation of systems.

To achieve the accurate estimation of SOC, Artificial Neural Networks (ANN) and Fuzzy Logic systems have been treated as the universal approximates. Many techniques have been developed to approximate the nonlinear functions for practical applications. The BMF constructed in possesses the property of local control and has been successfully applied to Fuzzy Neural Control. Also, the hybridization of fuzzy logic with ANN has been used to improve the efficiency of function estimation.

The adaptive Neural Fuzzy method was proposed to estimate battery residual capacity. Although the estimation of battery residual is accurate, the algorithm utilizes the least-square method to identify the optimal values and hence, learning rate is computationally expensive; much time is wasted in training an ANN. A more practical approach, called merged-FNN for SOC estimation is proposed. In merged-FNN, the FNN strategy is combined with Reduced-form Genetic Algorithm (RGA) which performs effectively on SOC estimation in a series-connected Li-ion battery string. The merged-FNN achieved a faster learning rate and lower estimation error than the traditional ANN with a back-propagation method.

Due to the above-mentioned facts, it is not hard to see that AI is a promising approach for fast, precise and reliable SOC estimation [4].

### 3.2.4 Charge Estimation Algorithms

Several different techniques such as Fuzzy Logic, Kalman Filtering, Neural Networks and recursive, self-learning methods have been employed to improve the accuracy of the SOC estimation as well as the estimation of state of health (SOH).

(1) *FUZZY LOGIC* Fuzzy Logic is simple way to draw definite conclusions from vague, ambiguous or imprecise information. It resembles human decision making with its ability to work from approximate data to find precise solutions.

Unlike classical logic which requires a deep understanding of a system, exact equations, and precise numeric values, Fuzzy logic allows complex systems to be modeled using a higher level of abstraction originating from our knowledge and experience. It allows expressing this knowledge with subjective concepts such as big, small, very hot, bright red, a long time, fast or slow. This qualitative, linguistic representation of the expert knowledge presents a natural rather than a numerical description of a system and allows relatively easy algorithm development compared to numerical systems. The outputs can then be mapped into exact numeric ranges to provide a characterization of the system. Fuzzy logic is used extensively in automatic control systems.

Using this technique we can use all the information available to us about the performance of a battery to derive a more accurate estimation of its state of charge or the state of health.

(2) *KALMAN FILTER* The battery SOC is affected by many simultaneous factors and is continually changing due to the user driving pattern. The Kalman filter is designed to strip unwanted noise out of a stream of data. It operates by predicting the new state and its uncertainty, then correcting this with a new measurement. It is suitable for systems subject to multiple inputs and is used extensively in predictive control loops in navigation and targeting systems. With the Kalman Filter the accuracy of the battery SOC prediction model can be improved and accuracies of better than 1 % are claimed for such systems.

(3) *NEURAL NETWORKS* A Neural Network is a computer architecture modeled upon the human brain's interconnected system of neurons which mimics its information processing, memory and learning processes. It imitates the brain's ability to sort out patterns and learn from trial and error, discerning and extracting the relationships that underlie the data with which it is presented.

Each neuron in the network has one or more inputs and produces an output; each input has a weighting factor, which modifies the value entering the neuron. The neuron mathematically manipulates the inputs, and outputs the result. The neural network is simply neurons joined together, with the output from one neuron becoming input to others until the final output is reached. The network learns when examples (with known results) are presented to it; the weighting factors are adjusted on the basis of data - either through human intervention or by a programmed algorithm-to bring the final output closer to the known result. In other words, neural networks "learn" from examples and exhibit some capability for generalization beyond the training data.

Neural networks thus resemble the human brain in the following two ways:

1. A neural network acquires knowledge through learning.
2. A neural network's knowledge is stored within inter-neuron connection strengths known as synaptic weights.

The true power and advantage of neural networks lies in their ability to represent both linear and non-linear relationships and in their ability to learn these relationships directly from the data being modeled. Among the many applications are predictive modelings and control systems.

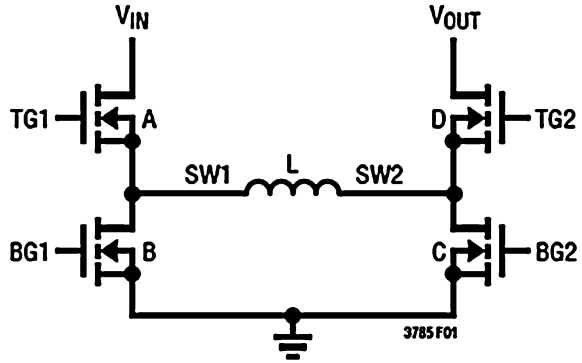
Neural Network techniques are useful in estimating battery performance which depends on quantifying the effect of numerous parameters most of which cannot be defined with mathematical precision. Algorithms are refined with the aid of experience gained from the performance of similar batteries [4].

### 3.2.5 DC-DC Converter Operation

A DC-DC converter allows DC voltages to be raised or lowered similar to how a transformer does with AC voltages. DC-DC conversion became very popular with



**Fig. 3** Representative output switch configuration



the advent of power transistors, and since then many circuits have been invented. There are countless types of DC–DC converter circuits but they all operate on the same basic principles. The simplest types of converter are the non-isolated buck and boost converters. Other types include the Cuk converter and the Buck-Boost converter, as well as isolated designs such as the forward converter and flyback converter.

(1) *POWER SWITCH CONTROL*: Figure 3 shows a simplified diagram of how the four power switches are connected to the inductor,  $V_{IN}$ ,  $V_{OUT}$  and GND.

Figure 4 shows the regions of operation as a function of duty cycle  $D$ . The power switches are properly controlled so that the transfer between modes is continuous.

(2) *BUCK REGION ( $V_{IN} > V_{OUT}$ )*: Switch D is always on and switch C is always off during buck mode. When the error amp output voltage,  $V_C$ , is approximately above 0.1 V, output A begins to switch.

During the off time of switch A, synchronous switch B turns on for the remainder of the switching period. Switches A and B will alternate similar to a typical synchronous buck regulator.

As the control voltage increases, the duty cycle of switch A increases until the max duty cycle of the converter in buck mode reaches  $D_{MAX\_BUCK}$ , given by:

$$D_{MAX\_BUCK} = 100 - D4 (SW) \%$$

Where  $D4 (SW)$  = duty cycle % of the four switch range.

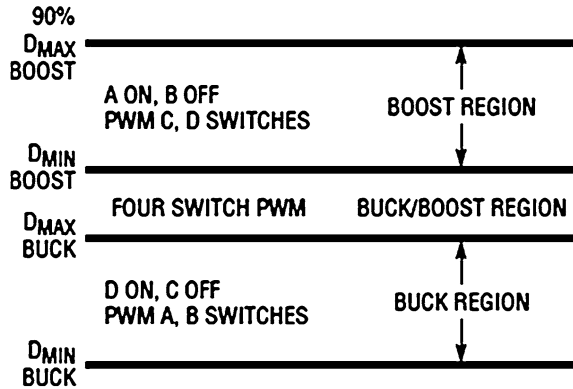
$$D4 (SW) = (300 \text{ ns} \cdot f) \cdot 100 \%$$

Where  $f$  = operating frequency, Hz.

Beyond this point the four switch or buck-boost region is reached.

(3) *BUCK-BOOST OR FOUR SWITCH ( $V_{IN} \sim V_{OUT}$ )*: When the error amp output voltage,  $V_C$ , is above approximately 0.65 V, switch pair AD remain on for duty cycle  $D_{MAX\_BUCK}$ , and the switch pair AC begin to phase in. As switch pair AC phases in, switch pair BD phases out accordingly. When the  $V_C$  voltage reaches the edge of the buck-boost range, approximately 0.7 V, the AC switch pair completely phase out the BD pair, and the boost phase begins at duty cycle,  $D4 (SW)$ .

**Fig. 4** Operation mode versus *V<sub>ic</sub>* voltage



The input voltage, *V<sub>IN</sub>*, where the four switch region begins is given by:

$$V_{IN} = \frac{V_{OUT}}{1 - (300ns \cdot f)} V$$

The point at which the four switch region ends is given by:

$$V_{IN} = V_{OUT} (1 - D) = V_{OUT} (1 - 300 \text{ ns} \cdot f) V$$

(4) **BOOST REGION** (*V<sub>IN</sub>* < *V<sub>OUT</sub>*) Switch A is always on and switch B is always off during boost mode. When the error amp output voltage, *V<sub>C</sub>*, is approximately above 0.7 V, switch pair C and D will alternately switch to provide a boosted output voltage. This operation is typical to a synchronous boost regulator. The maximum duty cycle of the converter is limited to 90 % typical [5].

### 3.2.6 Cell Connecting and Disconnecting

Cell balancing is a critical function for high-powered battery packs because a long series of individual cells is only as reliable as the weakest cell. It is critical that the charge level of all cells does not stray outside the recommended SOC range. To ensure that the batteries cannot be over-discharged during inactivity, the BMS idle power must be significantly less than the self-discharge of the battery cells.

More importantly, the idle current along the battery string must be well matched to ensure that batteries do not become unbalanced during storage. Once placed into operation, the batteries will experience high charge and discharge currents. In this situation, the charge level of each cell must be actively balanced to derive maximum pack energy and lifetime.

In our solution in case if a battery in the series is not functioning properly, all the other batteries in the series compensate the lost voltage and maintains a constant output voltage through the 4 Quadrant DC to DC converter. The battery is isolated from the flow circuit.

## 4 Conclusion

As batteries are the core energy sources in EVs and HEVs, their performance greatly impacts the salability of EVs. Therefore, manufacturers are seeking for breakthroughs in both battery technology and BMSs. Chemical reactions in the battery are subject to operating conditions, and hence, the degradation of a battery may vary in different environments. Developing a comprehensive and mature BMS is critical for manufacturers who would like to increase the market share of their products. The major concerns of BMSs were discussed in this paper. They include battery state evaluation, modeling, and cell balancing, wherein the evaluation methodologies of battery status were viewed as the crucial issue. A BMS framework was proposed to deal with the deficiencies of current BMSs in both research and commercial products. Based on previous work, specific challenges facing BMSs and their possible solutions were presented as a solid foundation for future research. Due to varying situations in real-world applications, a standard solution was not wanted. Based on the specific situation, different strategies should be applied to improve and optimize the performance of BMSs in future EVs and HEVs.

## References

1. Xing Y, Ma EWM, Tsui KL, Pecht M (2011) Battery management systems in electric and hybrid vehicles
2. Batteries for Electric Cars; Challenges, Opportunities, and the Outlook to 2020 The Boston Consulting Group Inc.: Boston, MA, USA, 2010; Available online: <http://www.bcg.com/documents/file36615.pdf>. Accessed on 20 July 2011
3. [http://www.analog.com/static/importedfiles/data\\_sheets/AD5934.pdf](http://www.analog.com/static/importedfiles/data_sheets/AD5934.pdf)
4. <http://www.mpoweruk.com/soc.htm>
5. <http://cds.linear.com/docs/Datasheet/3785fc.pdf>

# Thermal Modeling and Effects of Electrode Configuration on Thermal Behaviour of a LiFePO<sub>4</sub> Battery

Cheng Ruan, Kun Diao, Huajie Chen, Yan Zhou and Lijun Zhang

**Abstract** The temperature distribution of a LiFePO<sub>4</sub> battery was studied by using the finite difference method in this study. The heat generation considers both Bernardi expression and current heat generation in current collectors. A temperature measurement experiment at the geometry center inside battery at 2C discharge was done to validate the model temperature prediction results. The effects of electrode configuration such as placing and center distance of current collecting tabs on battery temperature distribution were analysed. The results showed that the placing and center distance of current collecting tabs have significant effects on temperature rising and uniformity. The results could contribute to the battery design.

**Keywords** Li-ion battery · Thermal model · Current heat generation · Electrode configuration · Temperature distribution

## 1 Introduction

Li-ion battery has great application prospects on electric vehicles for its advantage of high voltage, high power density, high energy density, long service life and no memory effect etc. For the performance of Li-ion battery is closely related to its

---

F2012-B04-013

This work was supported by National Basic Research Program of China (No.2011CB711200)

---

C. Ruan (✉) · K. Diao · H. Chen · Y. Zhou · L. Zhang  
School of Automotive Studies, Clean Energy Automotive Engineering Center, Tongji University, Shanghai, China  
e-mail: ruanc06@gmail.com

operating temperature, the battery thermal management technique is considered to be one of the key techniques in EVs.

There have been many previous researches on thermal modeling of lithium based battery. Bernardi et al. [1] derived a general heat generation expression for battery by using thermodynamic energy balance analysis on the cell control volume (not including current collectors). Chen and Evans [2–4] developed two and three dimensional models to study the thermal behaviour of LPBs and LIBs. Chen et al. [3] developed a three-dimensional model of LIBs which considered convection and radiation boundaries to analyze the effects of different facts on thermal behaviour. The heat generation in these studies was assumed uniform. As the volume of power battery becomes larger and larger, the heat generation of current in current collectors which make the temperature field distribution nonuniform (with higher temperature near the tabs) can not be neglected. Keyser et al. [6] studied the thermal behaviour of three generations of CPI Lithium battery at discharge by using infrared imager. The results showed there was obvious heat concentration near the positive current collecting tab which was in agreement with the current distribution. The uniformity of temperature could be improved by improving electrode design. Kwon et al. [7] established a model to study current distribution in electrode. Kim et al. [8] developed a two dimensional thermal model which considers electrochemistry heat generation and current heat generation to study the effects of electrode configuration on thermal behaviour.

In this study, a thermal model of a 40 Ah LiFePO<sub>4</sub> battery was developed by using finite difference method. The heat generation considers both Bernardi expression and current heat generation. A temperature measurement experiment of the geometry center inside battery at 2C discharge was done to validate the model temperature prediction results. Then the effects of electrode configuration such as placing and center distance of current collecting tabs on battery temperature distribution were analysed.

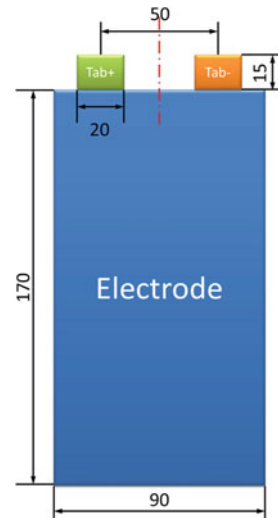
## 2 Modeling

A finite difference heat transfer method is used to establish the thermal model of a 40 Ah LiFePO<sub>4</sub> battery. The battery is composed of 77 positive electrode integrations, 78 negative electrode integrations, and the separators between them. Each electrode integration is composed of the metal (Al or Cu) current collector in the middle and the active electrode material on both side of collector. So a single cell consists of half positive electrode integration, half negative electrode integration, and the separators between them. The thickness of each layer in a cell is shown in Table 1. The geometry of a cell is shown in Fig. 1.

The conductive heat transfer is the main mechanism inside a battery. Simplify the battery into a two-dimensional model. The transient two-dimensional conductive heat transfer equation is as follows [8]:

**Table 1** Thickness of each layer in a cell

Number	Layer	Thickness/ $\mu\text{m}$
1	Positive current collector	11.5
2	Positive electrode	70.5
3	Separator	37
4	Negative electrode	56.5
5	Negative current collector	4

**Fig. 1** Geometry of a cell

$$\rho C_p \frac{\partial T}{\partial t} = \frac{\partial}{\partial x} \left( k_x \frac{\partial T}{\partial x} \right) + \frac{\partial}{\partial y} \left( k_y \frac{\partial T}{\partial y} \right) + \dot{q} - \dot{q}_{conv} \quad (1)$$

Where  $\rho C_p$  is the average volume specific heat capacity of the battery ( $J/(m^3 \cdot K)$ ),  $k_x, k_y$  are the effective thermal conductivities along the x and y directions ( $W/(m \cdot K)$ ),  $\dot{q}$  is the heat generation rate ( $W/m^3$ ), and  $\dot{q}_{conv}$  is the heat dissipation rate caused by convection at the x-y surfaces ( $W/m^3$ ).

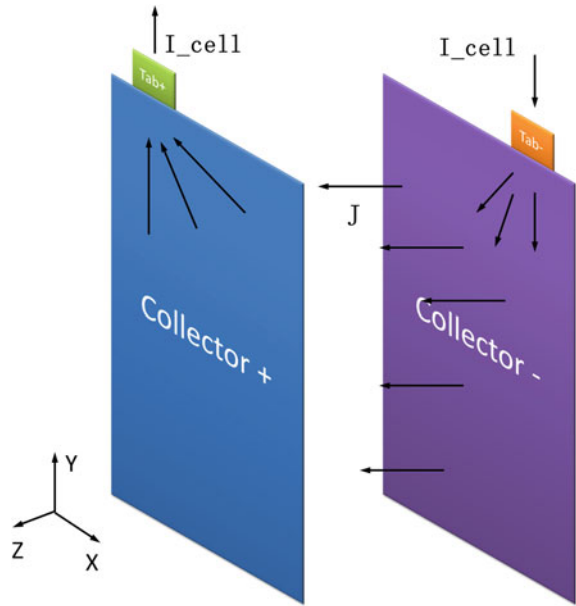
The effective thermal conductivities  $k_x$  and  $k_y$  can be considered as parallel thermal resistances of each component in the cell

$$k_x = k_y = \frac{\sum_i \delta_i \cdot k_i}{\sum_i \delta_i} \quad (2)$$

The average volume specific heat capacity  $\rho C_p$  is the average volume specific heat capacity of each component in the cell

$$\rho C_p = \frac{\sum_i \rho_i C_{p,i} V_i}{\sum_i V_i} \quad (3)$$

**Fig. 2** Current flow in parallel electrodes of a cell



The heat generation rate  $\dot{q}$  is composed of Bernardi heat in the active material in electrodes and current Ohmic heat in current collectors. The expression of  $\dot{q}$  is given as follows

$$\dot{q} = \frac{I}{V_{total}} \left( E_{oc} - E - T \frac{dE_{oc}}{dT} \right) + i_p^2 r_p + i_n^2 r_n \tag{4}$$

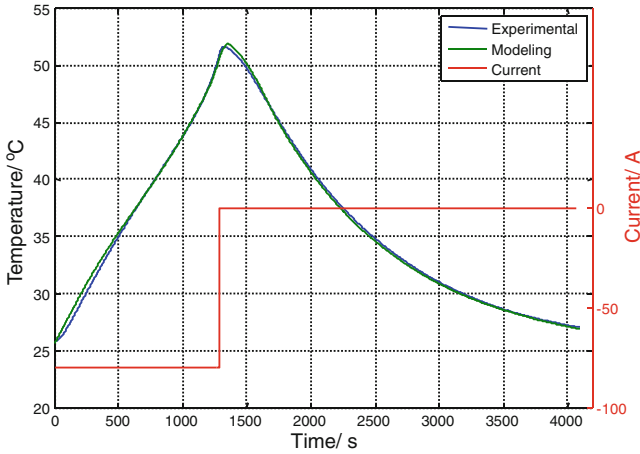
Where  $E_{oc}$  is the open-circuit potential of the cell (V),  $E$  is the cell voltage (V),  $dE_{oc}/dT$  is the entropy coefficient of the cell (mV/k),  $i_p, i_n$  are the current density in positive and negative current collectors ( $A/m^2$ ),  $r_p, r_n$  are the electrical resistivity of positive and negative current collectors ( $\Omega \cdot m$ ).

Figure 2 shows the simplified current flow in parallel electrodes of a cell. The current  $I_{cell}$  flows in through the Tab-, conducts in the collector - and flows to the collector + as current  $J$ . The current flow in collector + is opposite to that in collector-. And then the current  $I_{cell}$  flows out from the Tab +. Here we assume that the current  $J$  is homogeneous. Then we acquire the current distribution in collector + and collector-.

Two-dimension current conductivity differential equation

$$\nabla \left( \frac{1}{r_p} \nabla V_p \right) + J = 0 \quad \text{in collector +} \tag{5}$$

$$\nabla \left( \frac{1}{r_n} \nabla V_n \right) - J = 0 \quad \text{in collector -} \tag{6}$$



**Fig. 3** Comparison between experimental and modeling temperature curves at discharge rate of 2C

The boundary conditions for  $V_p, V_n$  are

$$\frac{1}{r_p} \frac{\partial V_p}{\partial n} = -\frac{I_{cell}}{a_{tab} * \delta_{pc}} \quad \text{at tab +} \tag{7}$$

$$\frac{1}{r_n} \frac{\partial V_n}{\partial n} = \frac{I_{cell}}{a_{tab} * \delta_{nc}} \quad \text{at tab -} \tag{8}$$

$$\frac{1}{r_p} \frac{\partial V_p}{\partial n} = 0 \quad \text{at other boundary} \tag{9}$$

$$\frac{1}{r_n} \frac{\partial V_n}{\partial n} = 0 \quad \text{at other boundary} \tag{10}$$

Where  $V_p, V_n$  is the voltage in positive and negative current collectors (V),  $a_{tab}$  is the width of the tab (m),  $\delta_{pc}, \delta_{nc}$  is the thickness of current collectors (m).

Then the  $i_p, i_n$  can be acquired by

$$i_p = -\frac{1}{r_p} \nabla V_p \tag{11}$$

$$i_n = -\frac{1}{r_n} \nabla V_n \tag{12}$$

The heat dissipation rate,  $\dot{q}_{conv}$ , is derived as

$$\dot{q}_{conv} = 2h(T - T_{ambient})/\delta_{all} \tag{13}$$



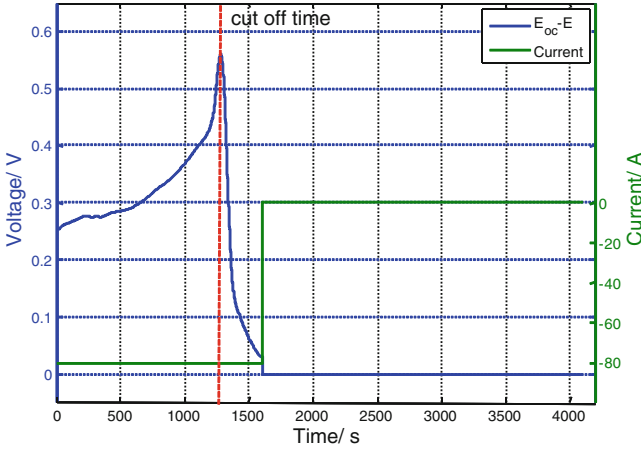


Fig. 4 ( $E_{oc}-E$ ) curve at discharge rate of 2C

Where  $h$  is the convection heat transfer coefficient ( $W/(m^2 \cdot K)$ ),  $\delta_{all}$  is the total thickness of the battery ( $m$ ),  $T_{ambient}$  is the ambient temperature ( $K$ ). The other convective boundary condition of the electrode is written as

$$-k \frac{\partial T}{\partial n} = h(T - T_{ambient}) \tag{14}$$

### 3 Experiment Verification

In order to acquire the temperature inside the battery, we put a sealed and isolated thermocouple in the geometry center of the battery before the electrolyte was filled in. Then a constant current discharge experiment was proceeded on this special battery. The fully charged battery was put in the thermotank at constant temperature of 25 °C. Keep standing until the temperature difference between the geometry center inside the battery and the ambient is less than 1 °C. Then discharge the battery at 2C rate until the voltage reached the discharge cut-off voltage. Cut off the circuit and keep still until the battery was cooled down. Record the temperature, voltage and current. Figure 3 shows the result of experiment and simulation.

The experimental temperature curve didn't drop down directly after the cut off time. It remained a gentle slope for about 200 s then dropped down quickly. The reason of this phenomenon is mainly that the curve reflected the temperature variation inside the battery. After the circuit was cut down, the temperature dissipation needed time to conduct from the surface to the center. In order to reflect the gentle slope in the simulation, a small voltage difference (shown in Fig. 4) was added after the circuit cut off, and the current remained relevantly. Then the simulation reaches high agreement with the experimental result.

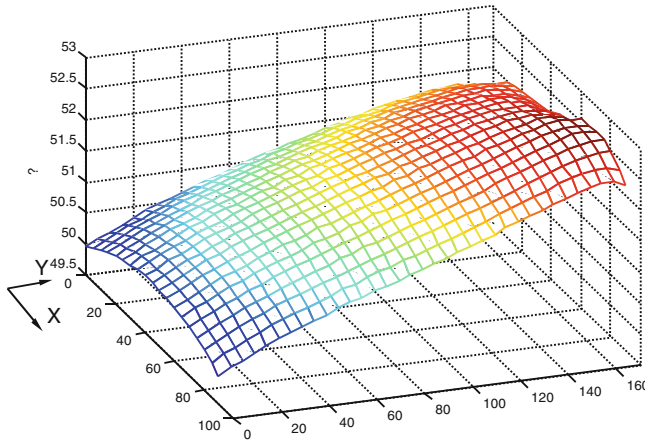


**Fig. 5** Temperature distribution at the end of discharge

Figure 5 shows the temperature distribution at the end of discharge. The area near the tabs has higher temperature. The highest temperature appears near the negative tab for the negative current collector is much thinner. Based on the model, the effect of electrode configuration on thermal behaviour could be analysed.

## 4 Discussion and Result

To analyse the effect of different electrode configuration on thermal behaviour, we assumed three types of tab placing configuration: Type (a) both tabs on the short side, Type (b) opposite tabs on short side, Type (c) both tabs on the long side. As shown in Fig. 6, the areas of active electrode material in three types are the same, so the three types of battery have the same capacity. The temperature distribution was analysed by changing the center distance of tabs,  $L$ . The battery was discharged at a constant current of 2C rate. The center temperature, maximum temperature, minimum temperature, mean temperature and the temperature standard deviation were chosen to describe temperature field at the end of 2C discharge. The simulation results are shown in Tables 2, 3, 4.

For the Type (a) and Type (c), which have the tabs on the same side, the minimum of center distance,  $L$ , starts at 20 mm. Because the manufacturing processing makes the positive and negative current collectors assemble alternately. If  $L < 20$  mm, the tabs overlap and the short circuit will occur.

As shown in Fig. 7, the center temperatures of Type (a) and Type (c) decrease first and then increase with the growth of center distance,  $L$ , while that of Type (b) monotonic increases. The maximums of center temperature of Type (a) and Type (b) are acquired at maximum of  $L$  and that of Type (c) is acquired at minimum of  $L$ . The

**Fig. 6** Three types of electrode configuration Type (a), Type (b), Type (c)

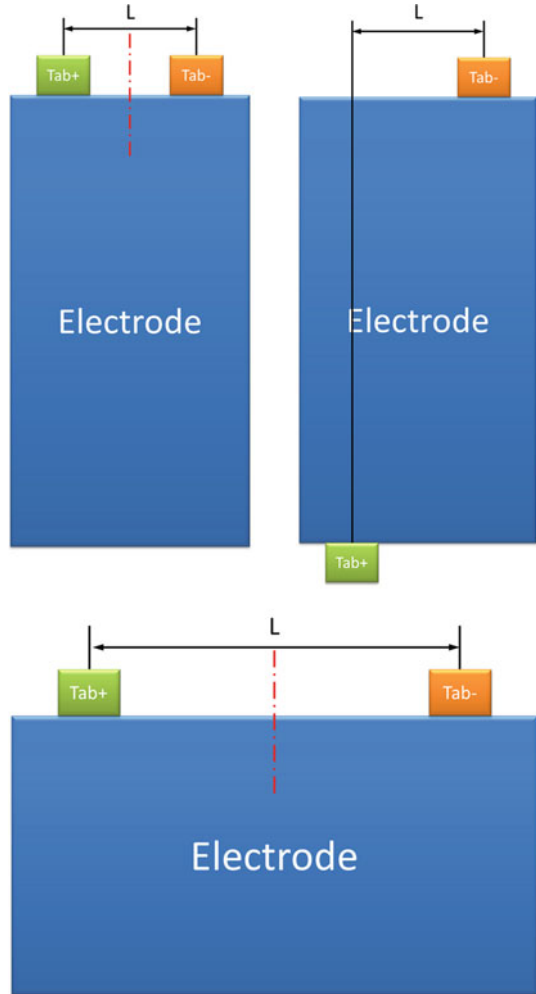


**Table 2** Result of type (a)

Center distance /mm	Center temperature / °C	Max. temperature / °C	Min. temperature / °C	Mean temperature / °C	Temperature standard deviation / °C
20	51.7234	52.8268	49.9548	51.4962	0.6852
30	51.6678	52.5653	49.9309	51.4224	0.6374
40	51.6821	52.5590	49.9376	51.4397	0.6432
50	51.7056	52.6001	49.9486	51.4683	0.6557
60	51.7403	52.7126	49.9646	51.5108	0.6768

**Table 3** Result of type (b)

Center distance /mm	Center temperature / °C	Max. temperature / °C	Min. temperature / °C	Mean temperature / °C	Temperature standard deviation / °C
0	51.6418	51.9626	50.4259	51.3886	0.2924
10	51.6443	51.9688	50.3855	51.3916	0.2938
20	51.6506	51.9863	50.3558	51.3993	0.2976
30	51.6651	52.0262	50.3402	51.4171	0.3046
40	51.6839	52.0854	50.3331	51.4401	0.3144
50	51.7115	52.1806	50.3387	51.4739	0.3277
60	51.7525	52.3379	50.3601	51.5244	0.3455

**Table 4** Result of type (c)

Center distance /mm	Center temperature / °C	Max. temperature / °C	Min. temperature / °C	Mean temperature / °C	Temperature standard deviation / °C
20	51.8642	52.4095	50.3106	51.3081	0.4878
40	51.7598	52.1337	50.1808	51.2500	0.4440
60	51.7286	52.0488	50.1244	51.2701	0.4152
80	51.7009	52.0060	50.1317	51.2986	0.3860
100	51.6972	52.0256	50.1504	51.3496	0.3643
120	51.7128	52.1088	50.1886	51.4151	0.3552
140	51.7652	52.3438	50.2388	51.5125	0.3671

**Fig. 7** Center temperature results

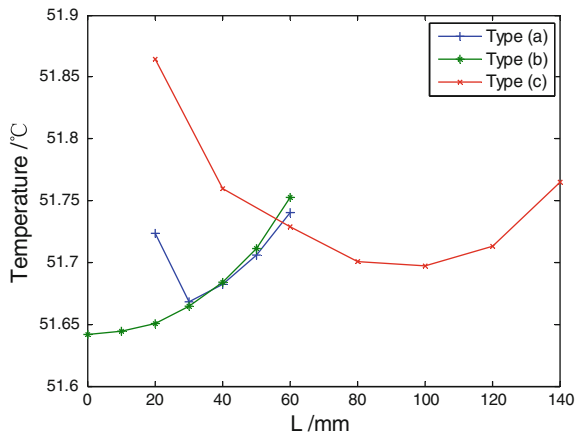
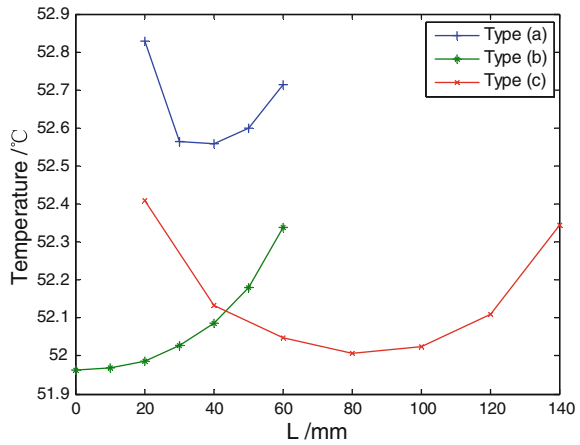


**Fig. 8** Maximum temperature results



minimums of center temperature of three types are at the point where  $L = 0, 0, 100$  mm. The center temperature sequence of three types of battery is that Type (c) > Type (a) > Type (b).

The variation tendency of the maximum temperature of each type of battery is similar to that of center temperature (Fig. 8). The battery of Type (a) and Type (c) gets its highest maximum temperature at  $L = 20$  mm while Type (b) at  $L = 0$  mm. The Type (a) battery has the maximum temperature obviously much higher than Type (b) and Type (c).

Figure 9 shows the variation of minimum temperature. The effects of center distance variation on minimum temperature is less than  $0.1$  °C for battery of Type (a) and Type (b). The variation range of minimum temperature of Type (c) is a little larger, about  $0.2$  °C. The minimum temperature sequence of three types of battery is that Type (a) > Type (c) > Type (b).

The variations of mean temperature of three types of battery are described in Fig. 10. The variation tendencies of the mean temperature are similar to those of center temperature and maximum temperature of the same battery. The maximums mean temperature of three types of battery are approximately the same, while battery Type (c) gets its minimum temperature at  $L = 40$ , which is much lower than that of Type (a) and Type (b).

The temperature standard deviation is used to describe the uniformity of battery temperature field. The battery has a more uniform temperature with smaller standard deviation. The three types of battery get the lowest temperature standard deviation at  $L = 0, 30, 120$  mm respectively (Fig. 11). The sequence of battery temperature standard deviations is that Type (b) < Type (c) < Type (a). That means the Type (b) has the best uniformity, Type (c) takes the second place, Type (a) takes the worst.

The effect of tabs center distance on battery temperature distribution is caused by the current heat generation in current collectors which is more concentrated near the tab. If the tabs get closer, there will be a larger superposition of current

**Fig. 9** Minimum temperature results

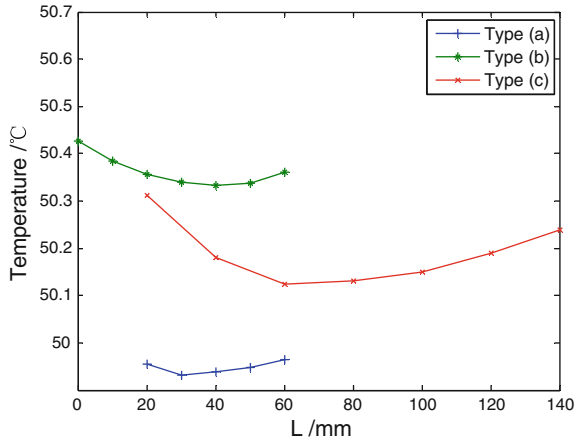


**Fig. 10** Mean temperature results

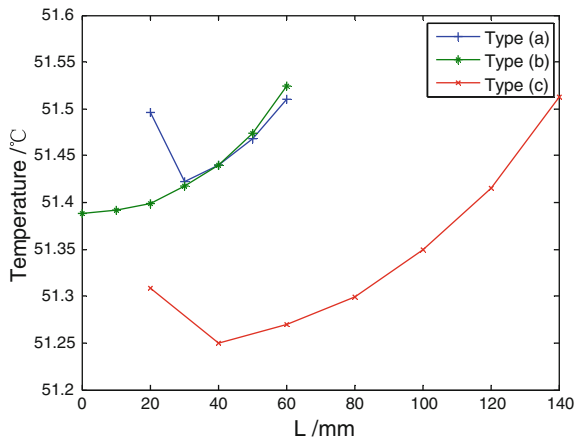


**Fig. 11** Temperature standard deviation results

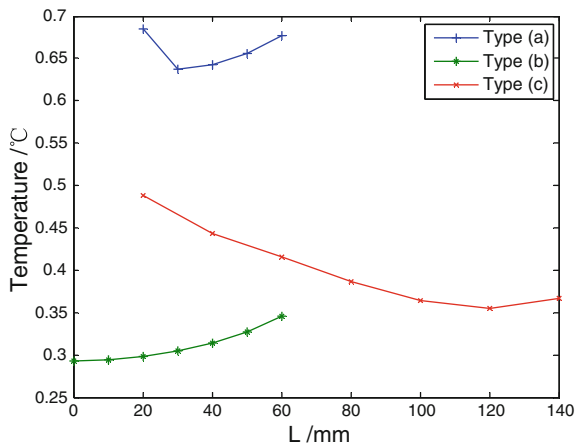
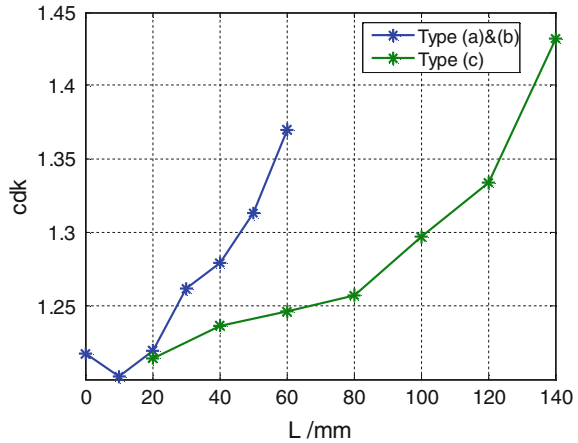


**Fig. 12** cdk varies with center distance L



heat generation. Thus for Type (a) and Type (c) which have tabs on the same side, the total heat generation near the tab gets the largest value when the center distance gets its minimum. However, with the growth of center distance, the concentration of current near the tab is more obvious. The cdk, which is defined as the ratio of the maximum of current density in the current collector and the average current density in the tab, is introduced to describe the extent of concentration of current density in current collectors. Figure 12 shows the variation of cdk with the center distance. The cdk increases with the center distance. That means the concentration of current is more obvious when L gets larger. This explains the variation of battery temperature distribution with the change of center distance. For the types which have tabs on the same side (Type (a), Type(c)), there is an optimum L for the temperature distribution.

For the battery used in the paper, the highest temperature appears near the negative tab because the copper foil negative current collector is too thin ( $4\ \mu\text{m}$ , while the aluminium foil positive current collector is  $11.5\ \mu\text{m}$ ). The current heat generation will be reduced by enlarging the thickness of copper foil appropriately. But it will cause additional cost.

In order to get a higher electric performance, the best electrode configuration on thermal behaviour is that which has the lowest charge/discharge temperature rise and the most uniform temperature distribution. That means the opposite tabs configuration (Type (b)) is the best choice. However, the battery design considers not only thermal behaviour but also electric performance, safety, assembling, cost and so on. This paper could provide the guidance on temperature in battery design.

## 5 Conclusion

A two dimensional thermal model of LiFePO<sub>4</sub> battery is developed by the finite difference method in this paper. The heat generation considers both Bernardi expression and current heat generation in current collectors. By comparing the experimental geometry center temperature curve with the model result at 2C discharge, the model temperature prediction was validated. Then, based on the result of the model temperature distribution, the effects of electrode configuration on thermal behaviour at 2C discharge were analysed. The result shows that the electrode configuration of opposite tab has the best thermal performance and there is an optimum center distance for the electrode configuration of same side tab. The electrode configuration results may contribute to the battery design.

## References

1. Bernardi D, Pawlikowski E, Newman J (1985) A general energy balance for battery systems. *J Electrochem Soc* 132:1
2. Chen Y, Evans JW (1993) Heat transfer phenomena in lithium/polymer-electrolyte batteries for electric vehicle application. *J Electrochem Soc* 140:1833
3. Chen Y, Evans JW (1994) Three-dimensional thermal modeling of lithium-polymer batteries under galvanostatic discharge and dynamic power profile. *J Electrochem Soc* 141:2947
4. Chen Y, Evans JW (1996) Thermal analysis of lithium-ion batteries. *J Electrochem Soc* 143:2708
5. Chen SC, Wan CC, Wang YY (2005) Thermal analysis of lithium-ion batteries. *J Power Sources* 140(1):111–124
6. Keyser MA, Pesaran A, Mihalic M (2003) Thermal characterization of advanced lithium-ion polymer cells. [2003-06-01]. <http://www.nrel.gov/vehiclesandfuels/energystorage>
7. Kwon KH et al (2006) A two-dimensional modeling of a lithium-polymer battery. *J Power Sources* 163(1):151–157
8. Kim US, Shin CB, Kim C (2008) Effect of electrode configuration on the thermal behavior of a lithium-polymer battery. *J Power Sources* 180(2):909–916



# Thermal Behavior and Modeling of Lithium-Ion Cuboid Battery

Hongjie Wu and Shifei Yuan

**Abstract** Thermal behaviour and model are important items should be considered when designing a battery pack cooling system. Lithium-ion battery thermal behaviour and modelling method are investigated in this paper. The temperature of the battery is measured when charging and discharging experiments in various styles including constant current charge, constant current discharge, pulse current charge, pulse current discharge, and simulation styles in EV and HEV. The lithium-ion battery temperature in various charge/discharge style are presented as a function of time. The thermal modeling is studied and compared with experiments. The results show that the battery thermal behavior is relevant with battery internal resistance, current, time and initial temperature.

**Keywords** Lithium-ion battery · Electric vehicle (EV) · Hybrid electric vehicle (HEV) · Thermal behavior · Thermal modeling

## 1 Introduction

Batteries are the most common electrical energy storage devices in Electric Vehicles (EV). The performance of a battery when it is connected to a load or a source is based on the chemical reactions inside the battery. The heat will be

---

F2012-B04-020

---

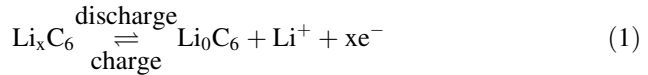
H. Wu (✉) · S. Yuan  
National Engineering Lab of Automotive Electronics Control Technology, Shanghai Jiao  
Tong University, Shanghai, China  
e-mail: wuhongjie@sjtu.edu.cn

generated in the process of charge and discharge, thus the thermal in the battery increase to higher. If the thermal of battery can not be controlled under a threshold according to the specification of manufacture, Batteries maybe destroyed in over temperature. Thus the thermal behaviour and thermal model inner battery and maximum thermal estimating method are important for properly use of battery.

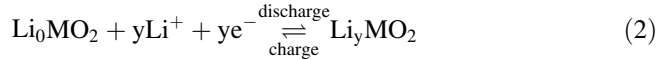
## 2 Battery Modeling

Reactions in Li-ion battery consist of mass transfer process, electro-chemical reaction, heat generating reaction and thermal diffusion process.

Li-ion battery consists of three domains: the negative composite electrode, separator, and positive composite electrode. During discharge, Li-ion diffuse to the surface of  $\text{Li}_x\text{C}_6$  active material particles (solid phase) in the negative electrode where they undergo electrochemical reaction



And transfer into a liquid or gelled electrolyte solution. The positively charged ions travel through the electrolyte solution via diffusion and ionic conduction to the positive electrode, where they react



And diffuse towards the inner regions of metal oxide active material particles (solid phase). The porous separator serves as an electronic insulator, forcing electrons to follow an opposite path through an external circuit or load.

End of charge or discharge, accompanied by sudden voltage rise, occurs when solid phase Li concentrations at their electrode surface become saturated or depleted, or electrolyte phase Li concentrations become depleted in their electrode.

### 1-D electrochemical model

Composite electrodes are modelled using porous electrode theory, meaning that the solid and electrolyte phases are treated as superimposed continua without regard to microstructure. The conservation of Li in a single spherical active material particle is described by Fick's law of diffusion,

$$\frac{\partial c_s}{\partial t} = \frac{D_s}{r^2} \frac{\partial}{\partial r} \left( r^2 \frac{\partial c_s}{\partial r} \right) \quad (3)$$

With boundary conditions

$$\left. \frac{\partial c_s}{\partial r} \right|_{r=0} = 0 \quad (4)$$

$$D_s \frac{\partial c_s}{\partial r} \Big|_{r=R_s} = \frac{-j^{Li}}{a_s F} \tag{5}$$

Where  $c$  represents Li concentration and the subscripts  $s$  denotes the solid phase.  $D_s$  is the solid phase diffusion coefficient,  $j^{Li}$  the volumetric rate of electrochemical reaction at the particle surface (with  $j^{Li} > 0$  indicate discharge),  $a_s$  the interfacial surface area, and  $F$  is the Faraday’s constant (96,487 C/mol). For spherical active material particles of radius  $R_s$  occupying electrode volume fraction  $\varepsilon_s$ , the interfacial surface area is  $a_s = 3\varepsilon_s/R_s$ . Equation are applied on a continuum basis across each electrode giving solid phase concentration a 2D spatial dependency, i.e.  $c_s(x, r, t)$  where  $x$  is the particle position,  $r$  is the radial position within a particle, and  $t$  is time. The electrochemical model depends only upon concentration at the particle surface, where the subscript  $s, e$  denotes the solid/electrolyte interface.

Another battery thermal behaviour model is described in paper [1]:

$$\nabla \cdot \vec{i}_p - J = 0 \text{ in } \Omega_p \tag{6}$$

$$\nabla \cdot \vec{i}_n + J = 0 \text{ in } \Omega_n \tag{7}$$

Where  $\vec{i}_p$  and  $\vec{i}_n$  are the linear current density vectors (current per unit length A cm<sup>-1</sup>).

To be simple, The battery heat generating power function is as the following:

$$\Phi = I[(E_0 - E) - T \frac{dE_0}{dT}] \tag{8}$$

where,  $\Phi$  is heat generating power (W),  $I$  is current (A), positive in charge and negative in discharge,  $E$  is the terminal voltage (V),  $E_0$  is open circuit voltage (V),  $T$  is the temperature (K).

In a thermal insulation condition

$$\Phi = mc_p \frac{dT}{dt} \tag{9}$$

where,  $m$  is the mass of battery (kg),  $c_p$  is the specific heat capacity of the battery ( $J/(kg \cdot K)$ ),  $t$  is time (s).

And

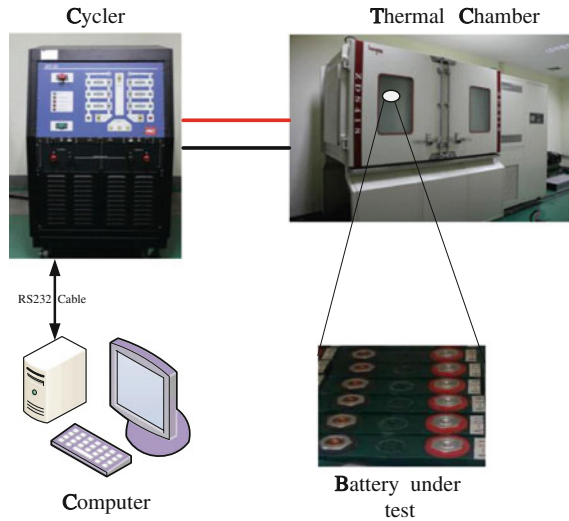
$$E_0 - E = IR_z \tag{10}$$

where,  $R_z$  is internal resistance in Ohm ( $\Omega$ ).

According to Eqs. (8) (9) (10),

$$\frac{1}{I} \frac{dT}{dt} = \frac{R_z}{mc_p} I - \frac{T}{mc_p} \frac{dE_0}{dT} \tag{11}$$

**Fig. 1** Configuration of the battery test bench



In Eq. (11),  $T \frac{dE_0}{dt}$  is a function of electro-chemical reaction, and treated as a constant in this paper. To constant current,  $I = \text{const}$ , when the time is short enough, the  $\frac{dT}{dt}$  can be treated as constant, thus heat generating power be a function of current. The character of battery can be test in different currents.

### 3 Simulation

Simulation work is done in Matlab-Simulink software. The lithium-ion battery temperature in various charge/discharge style are presented as a function of time. The thermal modeling is studied and compared with experiments.

### 4 Testing Methodology

The test bench setup is shown in Fig. 1. It consists of four parts: the battery cycler, the thermal chamber for environment control, the computer for human-machine interface and test data storage and the battery cells under test. The power cables of the cycler are connected to the battery, which are placed in the thermal chamber for the temperature maintaining. Table 1, shows the parameters of the battery.

The tests are conducted by putting a lithium-ion battery (LiFePO<sub>4</sub>) cell into an adiabatic box. Charge and discharge the battery with equipment in various styles including constant current charge/discharge, pulse current charge/discharge, drive cycle simulation style in EV or HEV. Temperatures of the battery surface and electrode are measured.

**Table 1** Main specification of the test cells

Type	Normal capacity (Ah)	Normal voltage (V)	Upper cut-off voltage (V)	Lower cut-off voltage (V)
Li FePO4	60	3.2	3.8	2.5

**Fig. 2** Pulse current profile data

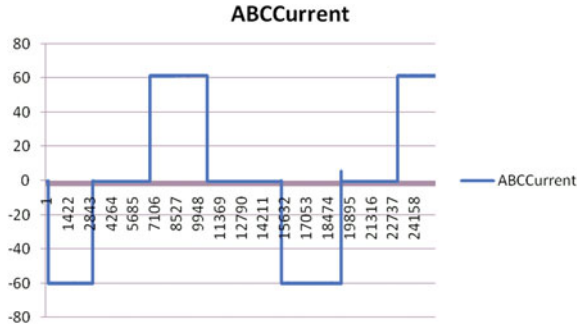


**Fig. 3** Temperature at positive electrode of a cell

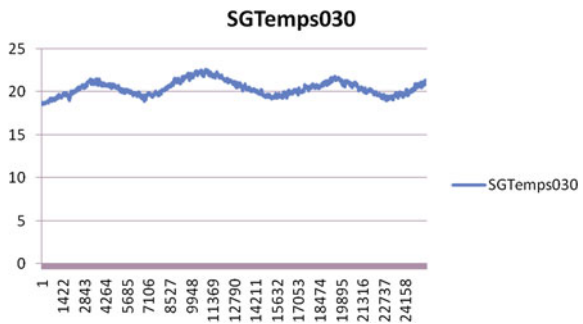


Figure 2 shows the current profile of the Pulse current test. And Fig. 3 is the electrode temperature of the cell.

## 5 Conclusion

Thermal behavior and model of a Lithium-ion cuboid battery is studied in this paper. Proper cooling system should be designed to main battery in a good temperature. The thermal behavior and model could be used in designing of battery pack and cooling system.

## Reference

1. Kwon KH et al (2006) A two-dimensional modeling of a lithium-polymer battery. J Power Sources 163:151–157

# Application of Battery-Ultracapacitor Hybrid System in the Hybrid Electric Vehicles

Huanli Sun, Xiaojuan Pei, Lichao Xu, Hemin Wang, Yi Sheng and Yuanbin Yu

**Abstract** The main factors which include low charge/discharge efficiency of high current, low power density and poor low-temperature performance lead to the unsatisfactory situation for hybrid electric vehicles (HEVs), which involves the inadequate braking-energy recovery and short battery lifetime and limitation of working environment. To make up the performance of single battery, a battery and ultracapacitor (UC) hybrid system is used to give full play to the energy of the battery and power of the UC. This paper aims to put forward the design method of a battery-UC hybrid system from the perspective of the vehicle requirements and parameter matching. The experiment indicates that the hybrid power system has improved the efficiency of braking-energy recovery and has decreased the demanding power of battery markedly, thus prolonged the battery lifetime. Meanwhile, the UC's high low-temperature performance has improved the low-temperature performance of integrated power system.

**Keywords** Hybrid electric vehicles · Battery · Ultracapacitor · Bidirectional DC/DC convector · Braking energy recovery

---

F2012-B04-021

---

H. Sun (✉) · X. Pei · L. Xu · H. Wang · Y. Sheng  
China FAW Co., Ltd R&D Centre, , China  
e-mail: sunhuanli@rdc.faw.com.cn

Y. Yu  
Jilin University, Jilin, China

## 1 Introduction

The electric load profile of HEVs consists of high peaks and steep valleys due to repetitive acceleration and deceleration. The power battery is mainly providing the auxiliary power for start/stop, acceleration and climbing, while it enhances the fuel economy as storage to recover the braking-energy. Nowadays, the dominant battery type of HEV is NI-MH. Because of low power density, low charge–discharge efficiency of high current, short lifetime and poor low-temperature performance of the battery, the efficiency of braking energy recovery is low and the working environment is limited [1, 2]. However, UCs offer superior efficiency, longevity and are less temperature dependent as compared to batteries. By the synergic use of power battery and UC, the power battery is only supposed to provide the average power of the electric system, and the UC would compensate the exceeding power required [3]. In the other words, the UC will assist the battery during vehicle acceleration and hill climbing, and capture the regenerative braking energy. The characteristic parameters of NI-MH battery and UC are list in Table 1.

## 2 Configuration of the Hybrid Power System

### 2.1 *Passive Parallel Hybrid Power System*

The configuration of passive parallel connection is shown in Fig. 1. The advantages are that the structure is simple and the cost is low. The disadvantages are that firstly the terminal voltages of the two power sources are forced to be equal, the utilization ratio of UC is reduced because of the markedly different charge/discharge characteristics between UC and battery; secondly, it is lack of flexibility because the actual output power of battery and UC is only decided by the own characteristics of the two power sources [4].

### 2.2 *Active Controlled Hybrid Power System*

The configuration of active controlled hybrid power system is shown in Fig. 2. The UC is connected with the power battery in parallel by the DC/DC convertor. And the power battery should provide the average power of the workload while the UC providing the instantaneous high power to compensate the lack of battery power during working. This structure has a marked superiority because of the existing of DC/DC: firstly, it is possible to be different between the terminal voltages of the two power sources, which make the design more flexible. Secondly, output current

**Table 1** Ni/MH battery and ultracapacitor performance parameters

Type	Operating temperature range	Power density	Specific energy
Ni/MH	-20 to 55 °C	600 w/kg	24 wh/kg
Ultracapacitor	-40 to 65 °C	12,000 w/kg	4 wh/kg

**Fig. 1** Direct parallel hybrid configuration diagram

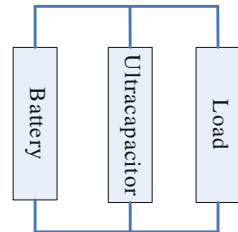
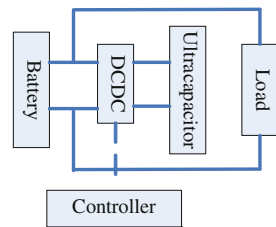


**Fig. 2** Active control-hybrid configuration diagram



of power battery would be smoothed and the discharge procedure would be optimized by the DC/DC [5]. The disadvantages include complicated structure and high cost. By contrasting the two schemes above, the active controlled system is applied to HEVs in this paper.

### 3 Hevs Requirements of the Power Source

The vehicle requirement is analyzed in this paper based on a hybrid electric car of FAW, which is equipped with an engine with 75 kW peak power, a main drive motor with 30 kW peak power, a BSG motor with 10 kW peak power and a Ni/MH battery pack with 288 V/6Ah. The service life of complete vehicle is 10 years/250,000 km. And the service life of power system is comparable with the complete vehicle's, whose working environment temperature range is -30 to 65 °C (Fig. 3).

The complete vehicle is supposed to drive 11.2 km and the maximum speed is 120 km/h in a NEDC drive cycle. The available demanding energy of the power system derived from simulation is 0.3 kWh, which is shown by Fig. 4 and Table 2. It is visible that the peak power demanding is far greater than the average power demanding.



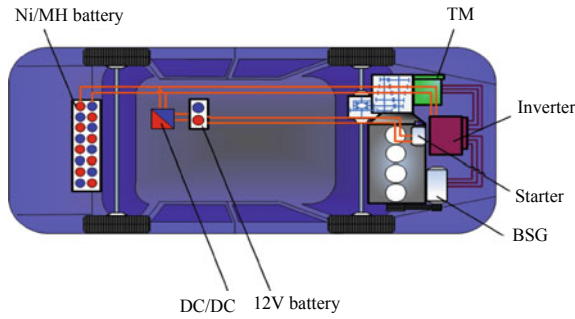


**Fig. 3** Hybrid-electric vehicle system configuration diagram

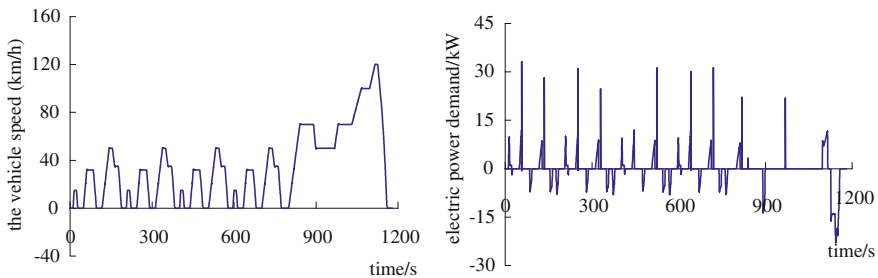


**Fig. 4** NEDC drive cycle and the electric power demand

**Table 2** The electric power demand statistic

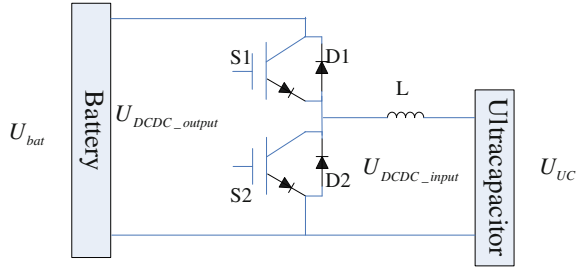
Max driving power	Max braking power	Average driving power	Average braking time
33 kW	23 kW	2 kW	2 kW

## 4 Parameter Matching of Hybrid Power System

### 4.1 Scheme Description

The basic control strategy of active controlled scheme is to control the conversion ratio of DC/DC in order to reasonable allocate the output power of battery and UC according to the power demanding [6]. The bidirectional Buck/Boost DC/DC with constant current control is applied in the scheme whose topological structure has been shown in Fig. 5. The voltage of UC is always lower than the battery's in the system. Both of the power battery and electric load are connected to the high-voltage end of DC/DC, while the UC is connected to the low-voltage end. When the DC/DC doesn't work, the power battery releases energy to the motor or stores energy passively. During regenerative braking, the current is fed back to UC as the

**Fig. 5** Hybrid power system configuration diagram with Boost/Buck DC/DC convertor



DC/DC is in Buck mode. And the UC is supposed to discharge as the DC/DC is in Boost mode.

### 4.2 Parameter Matching Principles

The active controlled scheme is to allocate the power supplied by battery and UC according to the power demanding of the whole vehicle. The desired effect is to provide and absorb condition demanding power by UC as much as possible, which could minimize the charge/discharge power of battery. And then, match the battery economically with the premise of meeting the required work condition. Here are the matching conditions below:

- $P_{bat} \geq$  the average electric power demanding,  $P_{bat}$  is the power of battery.
- $P_{UC} \geq$  the peak power demanding-average power demanding,  $P_{UC}$  is the power of UC.
- $E_{bat} \geq$  the energy demanding of NEDC drive cycle,  $E_{bat}$  is the available energy of battery.
- $E_{UC} \geq$  the energy demanding by twice hundred kilometre acceleration,  $E_{UC}$  is the energy of UC.
- $U_{bat-rate} = 288V$ ,  $U_{bat-rate}$  is the nominal voltage of battery package.
- $U_{UC-rate} = 250V$ ,  $U_{UC-rate}$  is the nominal voltage of UC.
- $P_{DCDC\_max} \geq P_{UC}$ ,  $P_{DCDC\_max}$  is the maximum power of DC/DC.
- $U_{DCDC\_input} \geq U_{UC}$ ,  $U_{DCDC\_input}$  is the input terminal voltage of DC/DC.
- $U_{DCDC\_output} \geq U_{bat}$ ,  $U_{DCDC\_output}$  is the output terminal voltage range of DC/DC.
- $W_{bat} + W_{uc} \leq W_{veh\_req}$ ,  $W_{bat}$  is the actual weight of power battery,  $W_{uc}$  is the actual weight of UC,  $W_{veh\_req}$  is the weight of power system required by complete vehicle.
- $B_{bat} + B_{uc} \leq B_{veh\_req}$ ,  $B_{bat}$  is the actual volume of power battery,  $B_{uc}$  is the actual volume of UC,  $B_{veh\_req}$  is the volume of power system required by complete vehicle.

**Table 3** The braking energy recovery of two schemes

Project	Single battery	Hybrid system
Total braking energy	279 Wh	279 Wh
The actual braking energy recovery	203 Wh	234 Wh
Percentage of braking energy recovery	73 %	84 %

The matching results: high voltage NI-MH battery pack with 288 V/3Ah; the UC pack with 250 V/12F; high power DC/DC convertor with the rated output power of 15 kW and the peak output power of 30 kW. The input voltage range of DC/DC is 250–250 V, and the output voltage range is 250–360 V.

## 5 Results

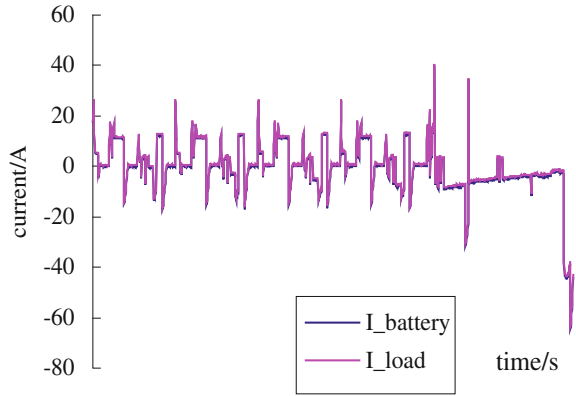
The analysis data of braking-energy recovery between two power systems is shown in Table 3 under the NEDC driving cycle. The efficiency of braking energy recovery is defined as energy saved in power system/gross energy during electric braking. It shows that the braking energy recovery rate of hybrid power system is 11 % higher than that of the only battery system. The main reason is that the UC has ability to charge very quickly.

Figure 6 shows the current curve of single battery scheme under the NEDC driving cycle. It is obvious that the battery could meet the power demanding of the driving cycle independently, however, the charge/discharge is quite frequent, and the current is quite big.

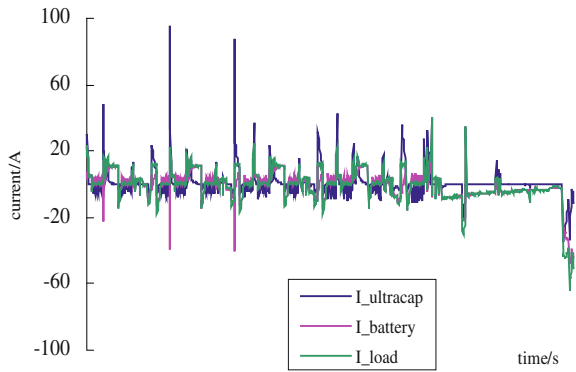
The load current, battery current and capacitor current of active controlled scheme is shown in Fig. 7 under the NEDC cycle. It figures that the hybrid power system could decrease the output current of power battery markedly, especially during the initial seconds of load current change. The UC delivers the most significant portion of the load current, and the battery bank current is a relatively smooth in vehicle running. Figure 8 shows the partial enlargement of the current curves with the hybrid system. It shows that firstly battery current increases, then UC current is much bigger than the load current after load current change rapidly. The appearance is caused by DCDC overshoot and lag problems. After about 1 s, UC current reduces gradually, and battery current increases gradually.

The cycle lifetime of UC can be a number of millions, which is able to meet the requirement of HEVs. Thus, this paper will only discuss the lifetime of battery. Ma Liping and some others have researched the cycle lifetime of MI-MH battery under the 1C and 10C discharging. The result shows that discharging by 10C has lead the cycle lifetime decreases from about 400 by 1C to only 76 because the internal resistance has been increased under high rate discharging which makes the temperature higher and ultimately breaks the internal structure of the battery [7]. Wang Xuefei and some others have also researched the cycle lifetime of Li-ion battery under different discharge rate [8]. The result shows in Table 4. It's obvious

**Fig. 6** The current with only battery



**Fig. 7** The current with the hybrid system



that the cycle lifetime is being decreased as the discharging rate increases. So the battery lifetime can be prolonged by decreasing the output current of the battery.

The working temperature range of power battery is commonly from  $-20$  to  $55$  °C. However, the working temperature range of UC is from  $-40$  to  $65$  °C, which could compensate the low-temperature performance of the power battery and enhance adaptability to environment of hybrid power system.

## 6 Conclusions and Prospects

### 6.1 Conclusions

The three conclusions are proposed by the research above:

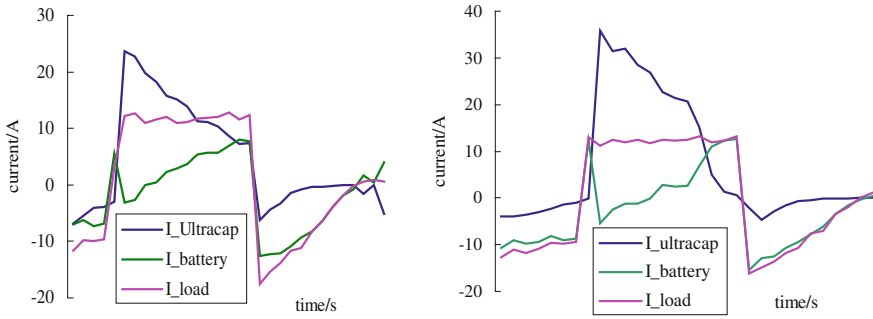


**Fig. 8** The partial enlargement of the current with the hybrid system

**Table 4** Statistics of cycle life

Test cycle	Cycle life
20 °C–100 % DOD-1C	1,278
20 °C–100 % DOD-2C	1,250
20 °C–100 % DOD-3C	1,236
20 °C–100 % DOD-4C	1,172
20 °C–100 % DOD-5C	1,084

- (i) The braking energy recovery efficiency of hybrid power system is higher than that of single battery.
- (ii) The output power of battery is obviously decreased, which prolongs indirectly the battery life.
- (iii) The working temperature range of UC is bigger to compensate the battery’s lacking of power under low temperature.

### 6.2 Prospects

There are overshoot and lag problems in the application of DC/DC. And during the high current charge/discharge, the battery will discharge current at a high rate instantaneously. These problems will be solved successfully by the mature technique of DC/DC in the future.

In order to avoid the response time long and efficiency of DC/DC, a new hybrid power system is proposed. By exchanging the power battery and the UC position based on the existing hybrid power system, the passive connecting between UC and the load could improve the efficiency of braking energy recovery further. We think using the hybrid scheme in a hybrid electric bus will deserve a more satisfactory effect on the considering of the vehicle requirements including power performance, cost, weight and arrangement space.

## References

1. Pay S (2000) Hybrid electric vehicle regenerative braking using ultracapacitors. M.S. Thesis, University of Nevada, Las Vegas, Dec
2. Pay S, Baghzouz Y (2003) Effectiveness of battery UC combination in electric vehicles. In: IEEE Bologna Power Tech Conference, June 23th–26th
3. Shin D, Kim Y, Seo J, Chang N, Wang Y, Pedram M (2011) Battery-supercapacitor hybrid system for high-rate pulsed load applications. IEEE Conference, 14–18 March, pp 1–4
4. Xiaojin Y, Yan P, Wu N, Yongzhen C (2006) Design and analysis of the structure of ultracapacitor/battery hybrid system. *Power Electronic* 44(5):75–77
5. Xiaojin Y, Yan P, Qi J (2009) Design of bidirectional DC/DC converter for compound power supply. *Electrical engineering* 11:52–54
6. Ye M (2006) Study on the estimation for SOC of battery in synergic electric power supply system on HEV. Jilin University
7. Ma L, Li X, Luo Y, Xia B (2005) Degradation model of cycle life for Ni/MH battery at 10 C rate discharge. *J Functional Mat Dev* 11(1):103–108
8. Wang X (2011) Research of life for lithium power battery based on simulation of condition. Harbin University of Science and Technology

# A Lithium-Ion Battery Fractional Order State Space Model and its Time Domain System Identification

Hongjie Wu, Shifei Yuan and Chengliang Yin

**Abstract** This paper deals with a fractional order state space model for the lithium-ion battery and its time domain system identification method. Currently the equivalent circuit models are the most popular model which was frequently used to simulate the performance of the battery. But as we know, the equivalent circuit model is based on the integer differential equations, and the accuracy is limited. And the real processes are usually of fractional order as opposed to the ideal integral order models. So here we propose a lithium-ion battery fractional order state space model, and compare it with the equivalent circuit models, to see which model fit with the experiment results best. Then the hybrid pulse power characterization (HPPC) test has been implemented in the lithium-ion battery during varied state-of-charge (SOC). Based on the Levenberg–Marquardt algorithm, the parameters for each model have been obtained using the time-domain test data. Experimental results show that the proposed lithium-ion fractional order state space model has a better fitness than the classical equivalent circuit models. Meanwhile, five other cycles are adopt here to validate the prediction error of the two models, and final results indicate that the fractional model has better generalization ability.

**Keywords** Fractional order state space model · Equivalent circuit model · Time domain system identification · HPPC test · Lithium-ion modelling

---

F2012-B04-023

---

H. Wu (✉) · S. Yuan · C. Yin  
National Engineering Laboratory for Automotive Electronic Control Technology,  
Shanghai Jiao Tong University, Shanghai, China  
e-mail: wuhongjie@sjtu.edu.cn

## 1 Introduction

The lithium-ion battery is a promising energy sources used in the hybrid or pure electric vehicles for its high energy and power density. During the battery real application, the battery model plays the key role for the battery safety and efficiency. About the modeling methods, there are two main approaches, one is physical based model, the other is data-driven model.

- Physical-based model: this kind of model is built according to the battery internal physical principle and chemical reaction. It provides more information about the battery on the real working condition, and is also the basic for the battery material design. Many scholars have done scientific research on this topics, such as [1–3]. Due to its complexity and nonlinear effects, this approach has not gained most usage in the real cars.
- Data-driven model: it's another important kind of modeling method. This method is just based on the input data/output data. It doesn't take more consideration on the battery system itself. Meanwhile, it's also a universal way for system modeling. Many battery models belong to this part, such as the artificial neural network [4, 5], fuzzy logic model [6–8], equivalent circuit model [9–13], and the fractional model [14–17], to be shown here laterly.

This paper is organized as follows: Section 2 describes an integer order model with first order and then fractional order model; Section 3 shows the experiment design and the parameter identification method for each model, and the final result is shown here; Then in section 4, we will conduct a comparison and validation for each model; The conclusion and future work will be presented finally.

## 2 Model Construct

### 2.1 Integer Model Construct

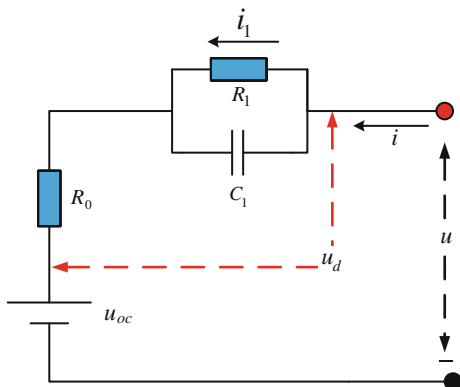
There are many battery modeling methods as mentioned in the introduction before. And a model which covers the complex nonlinear behaviour of a battery, and describes all facts of the battery performance over the entire life cycle, are difficult (or impossible) to obtain from the available test data. As proven by Hu' work, the equivalent circuit model with first order is quite suitable for the lithium-ion battery. Therefore the equivalent circuit (shown in Fig. 1) has been used here. For its simpleness and intuitiveness, this model provides sufficient and accurate information that meets the need of realtime battery management system application.

The parameters of this model are defined as follows:

- $u_{oc}$  = battery open circuit voltage ,
- $u_d$  = battery dynamic characteristics voltage,



**Fig. 1** Equivalent circuit model of the first-order (ECM-1)



- $u$  = battery terminal voltage,
- $R_0$  = battery internal ohmic resistance,
- $R_1$  = battery internal polarization resistance,
- $C_1$  = shunt capacitance,
- $i$  = load current (positive for charge and negative for discharge),
- $i_1$  = polarization current

Based on the basic principal of the electronic circuit, we could deduct the mathematical relationship between the flow current  $i$  and battery terminal voltage  $u$ , just as follows [1–2].

$$\left\{ C_1 \cdot \frac{d(i_1 \cdot R_1)}{dt} + i_1 = i \right. \tag{1}$$

$$\{ i_1 \cdot R_1 + R_0 \cdot i = u - u_{oc} = u_d \tag{2}$$

Execute the Laplace transformation, we can infer the transfer function:

$$\begin{aligned} G(s) &= \frac{U_d(s)}{I(s)} = \frac{U(s) - U_{oc}(s)}{I(s)} = \left( \frac{R_1}{s \cdot C_1 \cdot R_1 + 1} + R_0 \right) \\ &= \frac{s \cdot R_0 R_1 C_1 + R_0 + R_1}{s \cdot C_1 R_1 + 1} \end{aligned} \tag{3}$$

Assuming the time sample frequency is 1 Hz, formulation of the ECM-1 can be represented in state-space form as follows:

$$x_1 = i_1(t); \quad x_2 = u_{oc};$$

$$\begin{bmatrix} \dot{x}_1 \\ \dot{x}_2 \end{bmatrix} = \begin{bmatrix} -\frac{1}{R_1 C_1} & 0 \\ 0 & 0 \end{bmatrix} \begin{bmatrix} x_1 \\ x_2 \end{bmatrix} + \begin{bmatrix} \frac{1}{R_1 C_1} \\ 0 \end{bmatrix} i(k) \tag{4}$$

$$u = [R_1 \quad 1] \begin{bmatrix} x_1 \\ x_2 \end{bmatrix} + [R_0] i(k) \tag{5}$$

## 2.2 Fractional Model Construct

Based on the above analysis of the lithium-ion battery model and its transfer function, we can see that: as for the equivalent circuit model of the first order (ECM-1), the transfer function is like Eq. (3), which can be summarized as the form of:

$$G(s, \theta) = \frac{a_1 s + a_0}{1 + b_1 s} \quad \theta = [a_0, a_1, b_1] \quad (6)$$

And for any integer order system, the transfer function can be summarized as the form of:

$$G(s, \theta) = \frac{\sum_{k=0}^n a_k s^k}{1 + \sum_{k=1}^m b_k s^k} \quad \theta = [a_0, a_1, \dots, a_n, b_1, \dots, b_m] \quad (7)$$

In order to improve the accuracy, we shall give a simple fractional order system to simulate the character of the battery, just as the constant phase element (CPE). The transfer function structure of the fractional model is as follows:

$$\begin{aligned} G(s, \theta) &= \frac{U_d(s)}{I(s)} = \frac{U(s) - U_{oc}(s)}{I(s)} \\ &= \frac{\sum_{k=0}^n a_k s^{k\alpha}}{1 + \sum_{k=1}^m b_k s^{k\alpha}} \quad \theta = [a_0, a_1, \dots, a_n, b_0, b_1, \dots, b_m] \end{aligned} \quad (8)$$

The difference between the Eqs. (7) and (8) is the coefficient  $\alpha$  of the  $s^{k\alpha}$  term. When the  $\alpha = 1$ , the Eq. (8) identify with the (7). So in a way, the integer model is the special form of the fractional model.

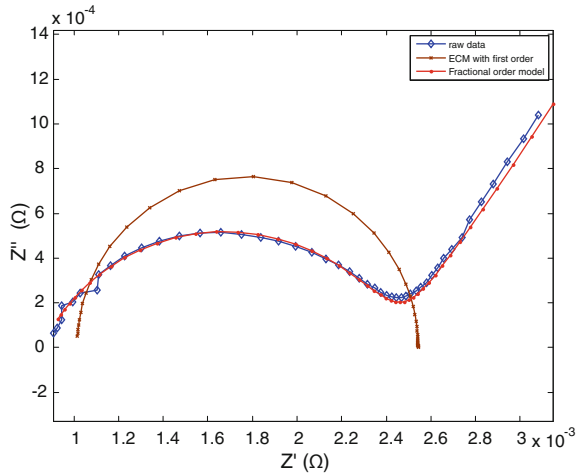
As known, the electrochemical impedance spectroscopy is a useful and non-destructive method for the battery cell measurement, and has gained a common usage in the battery modeling and fault analysis. Intuitively, we conduct a comparison of nyquist diagram about the integer model and fractional model, as shown in Fig. 2:

After the comparison between the integer model and the fractional model, this paper adopt one fractional model of the highest order as first order (short for FM-1). The equation is as follows:

$$\text{FM - 1: } G(s, \theta) = \frac{a_2 s^1 + a_1 s^{0.5} + a_0}{1 + b_2 s^1 + b_1 s^{0.5}} \quad \theta = [a_0, a_1, a_2, b_1, b_2] \quad (9)$$

The fractional state space representation is given by:

**Fig. 2** Comparison of nyquist diagram for three models



$$D^v x(t) = Ax(t) + Bu(t) \tag{10}$$

$$y(t) = Cx(t) + Du(t) \tag{11}$$

Conversion from fractional transfer function to fractional state space representation is easily achieved using either the commensurate fractional transfer function by way of control toolbox script *tf2ss*.

### 3 Experiment Design

#### 3.1 Open Circuit Voltage Test

The Open Circuit Voltage is a function of the state of charge, just like the Fig. 3. Technically, the OCV can have small variation with respect to the temperature. However, in this work the experiment is conducted at a temperature of 25 °C. Explicitly, the OCV can be modeled by a regression equation as:

$$u_{oc} = -0.80128 * soc^4 + 2.1533 * soc^3 - 2.0239 * soc^2 + 0.87432 * soc + 3.1553, soc \in [0, 1] \tag{12}$$

So for a specific state of charge, we'll get the  $u_{oc}$  by the calculation of polynomial (12).

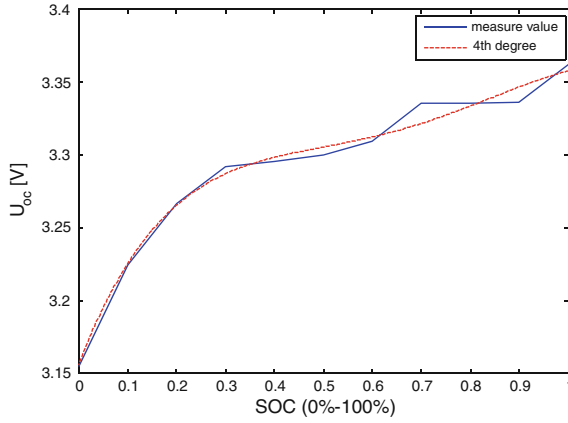


Fig. 3 Open-circuit voltage versus state of charge (SOC)

### 3.2 HPPC Test

The characterization testing can be performed on a cell at different SOC to establish the performance parameters for the lumped parameter model, including capacity, resistance, and so on.

The load current  $i$  and terminal voltage  $u$  for one pulse of HPPC test (shown in Fig. 4) are inputs to the system identification Procedure.

### 3.3 Parameter Identification Method

The parameters identification of fractional & integer order system is based on an output error approach summarized by the diagram in Fig. 5:

The fractional order model could be defined as follows:

$$G(s, \theta) = \frac{\sum_{k=0}^n a_k s^{k\alpha}}{1 + \sum_{k=1}^m b_k s^{k\alpha}} = \frac{U_d(s)}{I(s)} \tag{8}$$

And above equation can be rewritten in the time domain as :

$$u_d(kh) + b_1 D^\alpha u_d(kh) + \dots + b_m D^{m\alpha} u_d(kh) = a_0 i(kh) + a_1 D^\alpha i(kh) + \dots + a_n D^{n\alpha} i(kh) \tag{13}$$

which  $u_d = u - u_{oc}$ .h denotes the sampling period.

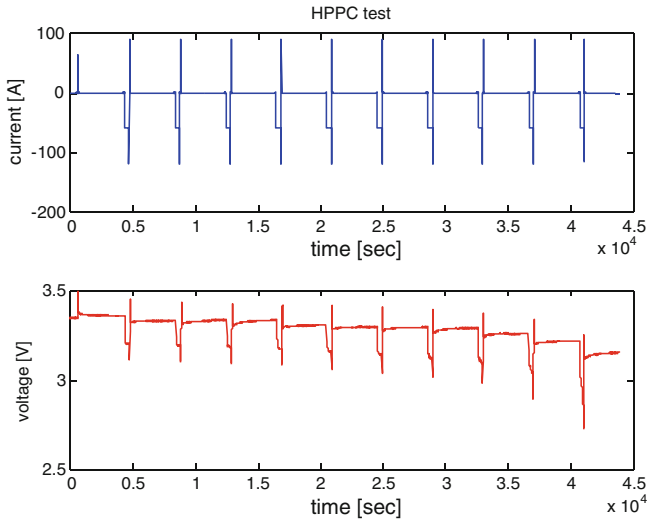


Fig. 4 Load current and terminal voltage for one-pulse of HPPC data

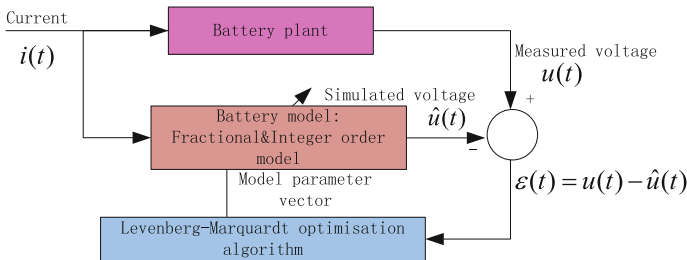


Fig. 5 Parameter estimation diagram of fractional & integer model by output error approach

The parameter vector  $\theta$  of the fractional model is as follows:

$$\theta = [-b_1 \dots b_m a_0 a_1 \dots a_n]^T$$

The regression vector is given by

$$\phi^*(kh) = [D^\alpha u_d(kh) \dots D^{m\alpha} u_d(kh) i(kh) D^\alpha i(kh) \dots D^{n\alpha} i(kh)]^T$$

The system output can be expressed as the following regression form:

$$\hat{u}_d(kh) = \phi^*(kh) * \theta \tag{14}$$

The identification is performed in time domain, using an output error method. Given a set of input–output series  $\{i(kh) u(kh)\}$ , the parameters can be solved using the Levenberg–Marquardt algorithm.

Vector  $\hat{\theta}$  being an estimation of  $\theta$ , output prediction error is given by

$$\varepsilon(kh, \hat{\theta}) = u_d(kh) - \hat{u}_d(kh, \hat{\theta}) \tag{15}$$

The optimal value of  $\hat{\theta}_{opt}$  is obtained by minimization of the quadratic criterion

$$SSE = J(\hat{\theta}) = \sum_{k=0}^{K-1} \varepsilon^2(kh, \hat{\theta}) \tag{16}$$

Since the output prediction  $\hat{u}_d(kh, \hat{\theta})$  is nonlinear in  $\hat{\theta}$ , the non-linear Levenberg–Marquardt algorithm is used to estimate  $\hat{\theta}$  iteratively

$$\theta_{i+1} = \theta_i - \{[J''_{\theta\theta} + \zeta I]^{-1} J'_\theta\}_{\hat{\theta}=\theta_i}, \tag{17}$$

{

with

{

$J'_\theta = -2 \sum_{k=0}^{K-1} \varepsilon(kh) S(kh, \hat{\theta})$  : gradient

$J''_{\theta\theta} \approx 2 \sum_{k=0}^{K-1} S(kh, \hat{\theta}) S^T(kh, \hat{\theta})$  : hessian

$S(kh, \hat{\theta}) = \frac{\partial \hat{u}_d(kh, \hat{\theta})}{\partial \theta}$  : output sensitivity

function

$\zeta$  : monitoring parameter

To conclude, the general steps for the parameter identification is as follows:

- (a) Choose a desired integer/fractional model structure. The integer/fractional model adopt here (ECM-1 & FM-1) is just as Eqs. (3 and 9).
- (b) Design and collect test datasets of the battery. Here two kind of datasets are used, the first one is pulse current test, for model identification; the second one is DST profile, for model validation. The datasets can be taken as  $\{i(kh) u(kh)\}$
- (c) Using the OCV versus SOC function (12), to eliminate the effect of the OCV by  $u_d = u - u_{oc}$ , we will get  $\{i(kh) u_d(kh)\}$ .
- (d) Perform a global optimization over all the datasets use the Levenberg–Marquardt algorithm, as Eqs. (13–17), we’ll get the optimal value of  $\hat{\theta}_{opt}$ .
- (e) Algorithm end.

### 3.4 Parameter Identification Results

Parameters for the integer order model (Figs. 6, 7)

**Fig. 6** Identification results of integer order model

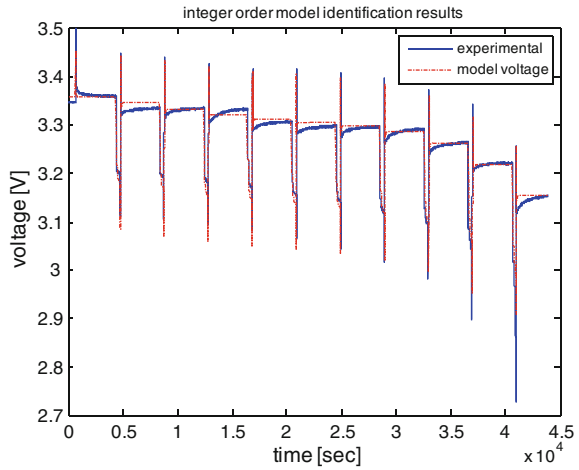
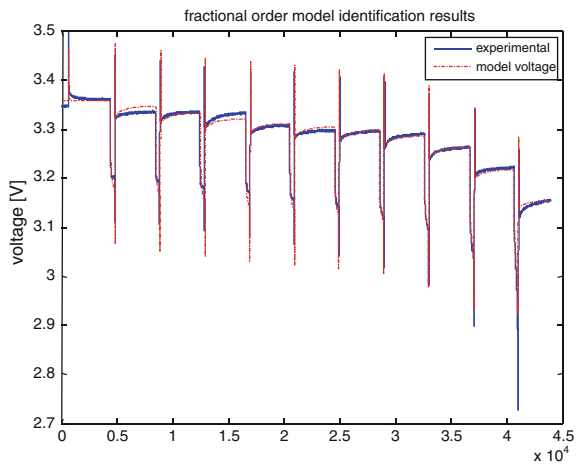


**Fig. 7** Identification results of fractional order model



## 4 Model Comparison and Validation

### 4.1 Model Error Comparison

From the above Tables 1, 2 we can find that the integer order model average error is just about 12.2 mV, and the fractional order model has better fitness as low as just 8.6 mV. The simulation result shows that the fractional model has higher accuracy than the equivalent circuit model of first order. The reason lays on that the fractional model contains more information about the battery system, and can be a better description of the battery dynamics performance.

**Table 1** Parameters for the ECM-1

Item	R0(ohms)	R1(ohms)	C1(F)	SSE	RMS (mV)
Value	0.0014	0.0015	41887	6.5077	12.2

**Table 2** Parameters for the fractional order model FM-1

Item	a0	a1	a2	b1	b2	SSE	RMS (mV)
FM-1	0.005832	0.0446	-0.01865	23.86	-0.7526	4.6030	8.6

**Table 3** Final validation results comparison of two models

Validation sequence	Model error comparison: RMS (mV)	
	Integer model	Fractional model
DST cycle	14.23	6.01
FUDS cycle	7.9	6.11
0.5C full charge	11.47	5.79
1C full charge	12.03	6.42
2C full charge	12.87	6.37

## 4.2 Model Validation Analysis

To validate the generalization of the fractional model, here we adopt five common working cycles, such as dynamic stress test (DST), federal urban driving sequence (FUDS), 0.5/1/2C full charge cycles. The final validation results are shown in the following Table 3.

## 5 Conclusion

A novel fractional order battery model is put forward in this paper and its state space equation and parameters identification method is shown. One classical equivalent circuit model with first order is adopted here as the reference to show the difference between the integer order model and the fractional order model. The pulse current profiles and the five other profiles are used to identify and validate the two proposed models. Experiments and simulation results indicate that the proposed fractional order model has good dynamic performance and gives more accurate terminal voltage estimation.

The future work will be focused on the order reduction of the fractional order model, which will reduce the computation complexity and make the fractional model more suitable for the real-time application. In addition the state of charge estimation based on the fractional order model could be developed, and then implement the fractional model and its related algorithm in the real time application, such as the EVs.



**Acknowledgments** This research work is supported by CERC-CVC: U.S. - China Clean Energy Research Center Clean Vehicles Consortium (2010DFA72760-305). The Sinopoly Battery Ltd, a sponsor of the battery cells for experimental test, is also gratefully acknowledged. And many thanks are also given to the authors whose papers were referred here.

## References

1. Dees DW et al (2002) "Electrochemical modeling of lithium polymer batteries," pp 310–320
2. Song L, Evans JW (2000) Electrochemical-thermal model of lithium polymer batteries. *J Electrochem Soc* 147:2086–2095
3. Hellwig C et al (2011) "A multi-scale electrochemical and thermal model of a LiFePO battery"
4. Fang K et al (2012) A prediction model based on artificial neural network for surface temperature simulation of nickel-metal hydride battery during charging. *J Power Sources* 208:378–382
5. Chan CC et al (2000) Available capacity computation model based on artificial neural network for lead-acid batteries in electric vehicles. *J Power Sources* 87:201–204
6. Erdinc O et al (2009) A wavelet-fuzzy logic based energy management strategy for a fuel cell/battery/ultra-capacitor hybrid vehicular power system. *J Power Sources* 194:369–380
7. Salkind AJ et al (1999) Determination of state-of-charge and state-of-health of batteries by fuzzy logic methodology. *J Power Sources* 80:293–300
8. Singh P et al (2006) Design and implementation of a fuzzy logic-based state-of-charge meter for Li-ion batteries used in portable defibrillators. *J Power Sources* 162:829–836
9. "Equivalent circuit models"(2006) *Motion Syst Des* 48:42
10. Gomez J et al (2011) Equivalent circuit model parameters of a high-power Li-ion battery: thermal and state of charge effects. *J Power Sources* 196:4826–4831
11. He H et al (2011) Evaluation of lithium-ion battery equivalent circuit models for state of charge estimation by an experimental approach. *Energies* 4:582–598
12. Hu X et al (2011) "A comparative study of equivalent circuit models for Li-ion batteries." *J Power Sources* 198(2012):359–367
13. Norian KH (2011) Equivalent circuit components of nickel-cadmium battery at different states of charge. *J Power Sources* 196:5205–5208
14. Cugnet M et al (2009) "Fractional order model validation for the lead-acid battery resistance estimation: application to cranking capability." In 7th IFAC international symposium on fault detection, supervision and safety of technical systems, SAFEPROCESS'09, 30 June 2009, 3 July 2009, Barcelona, Spain, pp 558–563
15. Podlubny I (1999) *Fractional differential equations*. Academic Press, New York
16. Sabatier J et al (2006) Fractional system identification for lead acid battery state of charge estimation. *Signal Proc* 86:2645–2657
17. Sabatier J et al (2010) A fractional order model for lead-acid battery crankability estimation. *Commun Nonlinear Sci Numer Simul* 15:1308–1317

# Optimizing BMS Operating Strategy Based on Precise SOH Determination of Lithium Ion Battery Cells

Karsten Mueller, Daniel Tittel, Lars Graube, Zecheng Sun and Feng Luo

**Abstract** Safety and lifetime issues are the dominant properties of a battery management system (BMS) in automotive applications. To ensure this at first a methodology for an exact determination of the current battery health state represented by the State of Health (SOH) value will be introduced by using electro-impedance spectroscopy (EIS) for determining of the battery model parameters. In the second step an accurate measurement of the relevant measures for the current dynamic operating mode of the battery (voltage, current, temperature...) the mid-(10 s) and intermediate-time (30 s) must be performed. The operating strategy can then be optimised for the lifetime requirements of the battery by using the measured and calculated values. Due to EIS measurements cannot be performed in dynamic operation an estimation of the relevant parameters must be performed by applying the Kalman-filtering. The paperwork shows the first results of this approach.

---

F2012-B04-024

---

K. Mueller (✉)

IAV GmbH, E-traction systems, Gifhorn, Germany  
e-mail: karsten.mueller@iav.de

D. Tittel · L. Graube

IAV GmbH, E-traction systems, Chemnitz, Germany  
e-mail: daniel.tittel@iav.de

L. Graube

e-mail: lars.graube@iav.de

Z. Sun · F. Luo

Tongji University, Clean Energy Automotive Engineering Center, Shanghai,  
People's Republic of China  
e-mail: sunzechang@fcv-sh.com

F. Luo

e-mail: luo\_feng@tongji.edu.cn

**Keywords** Lithium ion batteries • SOH determination • Battery management system

## 1 Introduction

Lithium ion batteries are still very popular and the most promising technology for the energy storage of the individual mobility of the near future. The main advantage of this storage technology is the relatively high energy density in conjunction with the high number of series applications in the field of consumer electronics. But there are a lot of open issues for the appliance in the automotive industry. In example the operating strategy must be different to guaranty the longer lifetime up to 10–12 years. It is known, that influences like cycle aging, calendrical aging, differences in the cells and so on will affect the battery life time. As durability is crucial related to lifetime-costs of traction batteries, this aspect concerns more and more car manufacturers. This paperwork will show an approach how to get offline (on test benches) and online (installed inside the car) information regarding the current healthy and state inside the cell and to use these information in combination with dynamically measured values (temperature voltage, current) for the performance prediction of the battery in the mid-(10 s) and intermediate-time (30 s). Goal of this approach is to decrease the performance restrictions as long as no effects on the lifetime of the battery.

## 2 General Processing Procedure

The idea to find the optimized operating and charging strategy must be split into two phases: At first the characteristics of the cell chemistry and battery behavior must be analysed on a test bench and in the second step test bench results and online measurement of the actual values must be used for the SOH determination. The overall procedure is shown in Fig. 1.

In general a suitable model for the battery must be found and verified at first on the test bench. The model parameters (Cap,  $R_i$ , C, Z etc.) at begin of life (BOL) of the controlled cell must then be extracted from the measured values and transferred to the model observer used in the battery management system (BMS) by a basic parameter calibration. During operation the State of Health (SOH) value will be calculated by using impedance measurement online—which is only applicable in stationary phases—or by parameter estimation using extended Kalman filter or similar algorithm. The calculated value must be compared with the target value coming from the life strategy. In this strategy all the influences to the target lifetime of the battery will be included, like

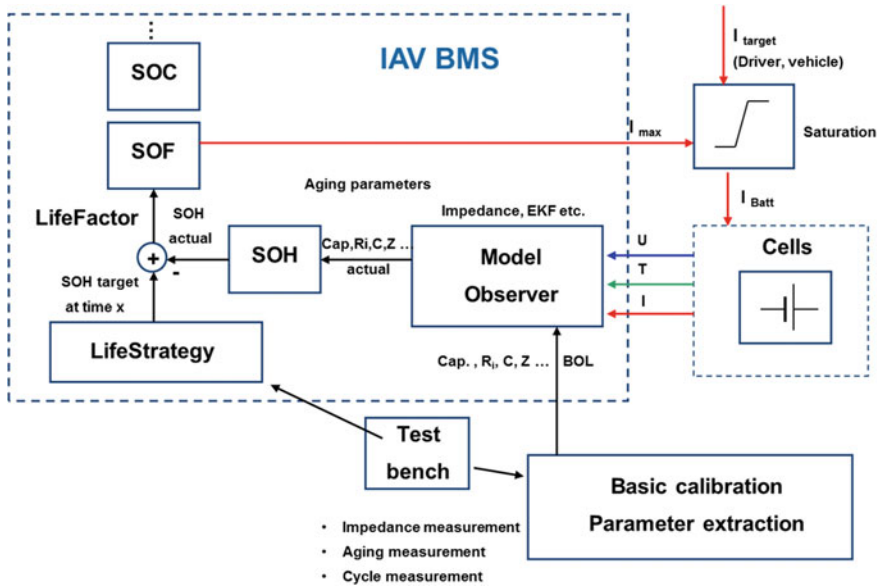


Fig. 1 General processing procedure

- Mission profiles (region, temperature, performance...)
- Target life time
- Target performance
- Driving cycles mix representing the overall lifetime (city, urban, racing, transport) etc.

Based on the comparison between target and actual value of the SOH the current thresholds to protect the battery can be widened or shortened in the performance prediction in the mid-(10 s) and (30 s) prediction.

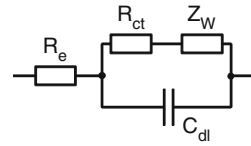
### 3 Battery Modeling

For the diagnosis of batteries different models are used. Empirical models describe the behavior of the cell voltage for a given current in the time domain. A good overview is given in [1]. These models can be found in different diagnosis algorithms often in conjunction with SOC dependent coefficients and a Kalman filter as a state estimator.

Models using electro-impedance spectroscopy (EIS) for parameter determination can be divided into two groups.

- abstract models consisting of equivalent circuits [2, 3] and
- electrochemical-physical based models [4, 5] which are often complex differential equation systems.

**Fig. 2** Randles equivalent circuit



Due to abstract models being the most common for the modeling impedance spectra of batteries, this approach will be used for further investigations. The Randles model describes the electrochemical process of charge transfer for one electrode in a liquid electrolyte.

Figure 2 shows the Randles circuit with the electrolyte resistance  $R_e$ , the charge transfer resistance  $R_{ct}$ , in parallel with the double layer capacitance  $C_{dl}$  and the Warburg impedance  $Z_W$  (characterized by  $\sigma_w$ ). The Impedance is calculated according to:

$$Z(j\omega) = 1 + \frac{1}{j\omega C_{dl} + \frac{1}{R_{ct} + \frac{\sigma_w(1-j)}{\sqrt{\omega}}}} \quad (1)$$

To model the impedance behavior of a battery cell two Randles circuits in series must be used which will lead to ambiguities in the parameter extraction process [6]. Another problem is the assumption of a flat electrode surface which is not the case for modern porous electrodes. Based on the work of DeLevie and others, models for porous electrodes were developed using different approaches like transmission line theory or fractional electrodes, [7]. These models can describe the high frequency behavior of the impedance which often employs a flat slope towards higher frequencies as seen in Fig. 3.

Based on a transmission line model DeLevie derived the impedance for an electrode with cylindrical pores:

$$Z(j\omega) = \sqrt{R'Z'} \coth \left( l \sqrt{\frac{R'}{Z'}} \right) \quad (2)$$

Here  $R'$  is the electrolyte resistance per pore length and  $Z'$  is the surface impedance per pore length. All these models describe the information that's in the impedance spectra or in the time behavior of a cell by a limited number of parameters and are therefore highly suitable for defining more complex measures of the battery like SOC or SOH. One of the main problems is therefore the extraction of these parameters from the measurements.

## 4 Parameter Extraction

As an approach to get information regarding the current healthy and state inside the cell on test benches modeling of physical effects by the help of EIS will be described. If the impedance spectra should be described with a linear model (i.e.

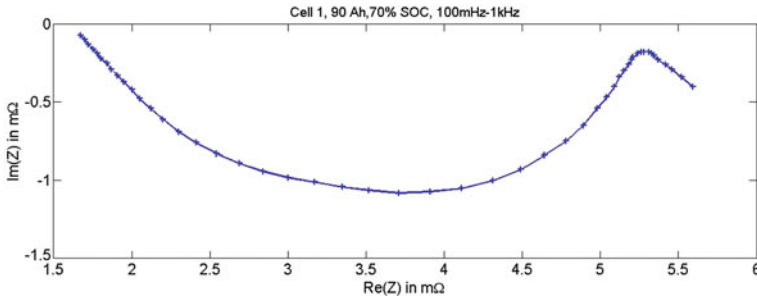


**Fig. 3** Impedance data obtained from a high capacity cell at 70 % SOC showing porous electrode behavior

by using a Voigt circuit) the problem reduces to a linear optimization problem [8], in other cases the parameter extraction becomes more difficult. In all approaches the solution is based on the minimization of a cost-function describing the error between the model and the measurement. The choice of this cost function is determined by the assumption of the underlying noise distributions in the process, [9]. The most common method used in impedance spectroscopy is the nonlinear least square fitting with a deterministic method like the Levenberg–Marquardt algorithm [10, 11]. Deterministic methods often have problems with non-smooth cost functions which is often the case for noisy data and they also suffer from the high risk of being trapped into local minima of the cost function. As a possible solution to these problems stochastic methods are used. The first use of stochastic methods to the authors knowledge is presented in [12] where a genetic algorithm is used to fit impedance data. Other stochastically based algorithms are i.e. the simulated annealing is presented in [13] or particle swarm optimization (PSO) [14]. Investigations showed promising results with hybrid algorithms, which delivers better parameter estimation results [15]. PSO algorithm in its basic structure consists of two equations:

(1) Determination of the new velocity

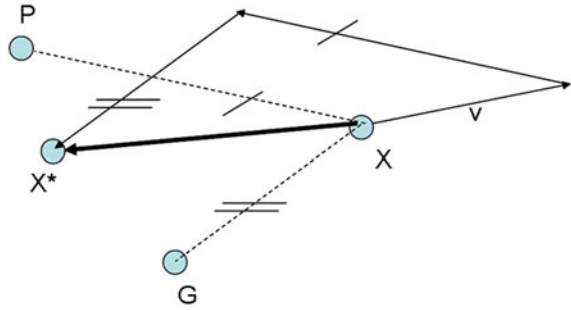
$$v^* = w \cdot v + c_1 r_1 [P - X] + c_2 r_2 [G - X] \tag{3}$$

- P = best personal parameter fit of a particle in the past
- G = best global parameter fit of all particles in the past
- X = current parameter fit of a particle
- $r_{1,2}$  = Equal distributed random numbers
- w,  $c_1$ ,  $c_2$  = weighting values

(2) Update of the position

$$X^* = v^* + X \tag{4}$$

**Fig. 4** Visualisation of the particle swarm optimisation approach



The visualization of the two equations is shown in Fig. 4:

The hybrid PSO according to [15] works as follows. Derived from the parent generation a child generation will be created. In parallel a second child generation is generated by using Cauchy mutation. This should ensure that the algorithm can escape from a local minimum. Out of the child generations an offspring is determined, in which the better fitness value of a particle is taken as criterion. Finally the parent and the offspring will compete with random selected other particle sets regarding their fitness as used in the natural selection. The particle sets, which won the most comparisons, are selected as the new parent generation.

This hybrid algorithm was successfully tested on cell and on battery level. In general the results are as good as the used measurement values. For reliable results the battery state parameters (i.e. SOC, temperature) must not be changing high dynamically. Else the super positioning of the effects influences the results too much (Fig. 5).

Figure 6 shows first results on the model with fitted parameters extracted from the hybrid algorithm. Also non-significant changes on the input or output of the cell can be used for verification of the algorithms. If there for example only driving profiles available for verification of the parameter estimation, the comparison between calculated and measured values shows very good accordance, if the parameter estimation is calculated by the mentioned algorithm as seen in Fig. 7.

## 5 In-Vehicle Parameter Estimation

The biggest challenge in the determination of the aging behavior is to find suitable parameters that truly reflect the batteries state. As aging is directly linked to physics inside the cells, a method of identifying related parameters would lead to more in depth information. It is difficult to put the aging state (often found as SOH in the literature) of an electro-chemical system into a numerical value, even it has a significant influence to all other parameters and thresholds.

The SOH represents the synthesized health state of the traction battery. The range of this purely synthetic parameter “SOH” is determined by 0–100 %. At Begin of life (BOL) the SOH is 100 %, at End of life (EOL) the SOH is 0 %, at

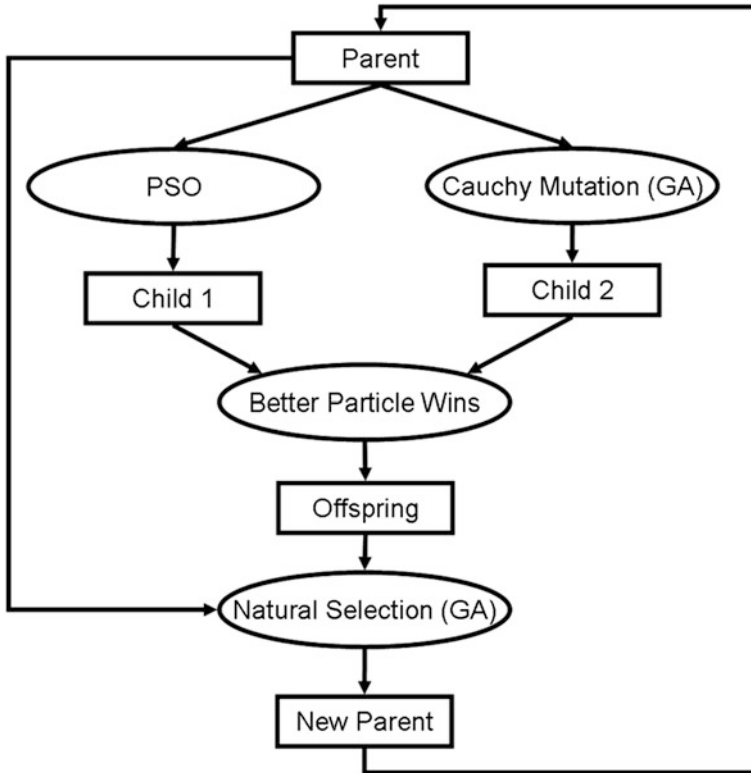


Fig. 5 Visualisation of the hybrid algorithm

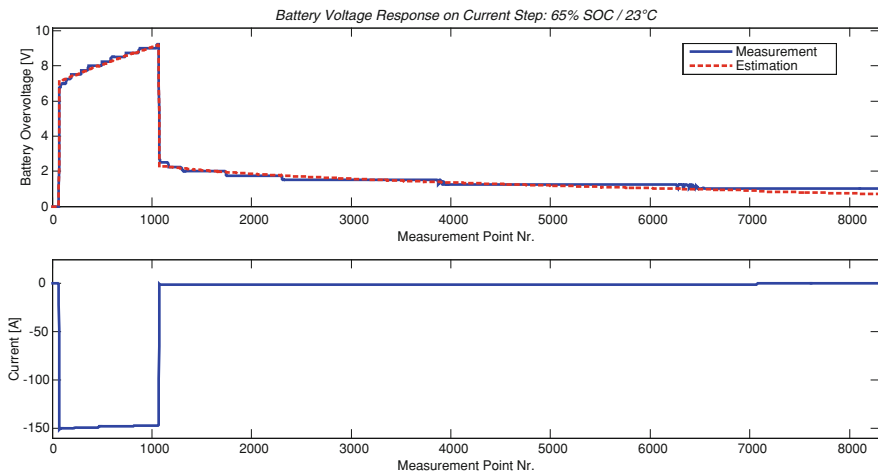
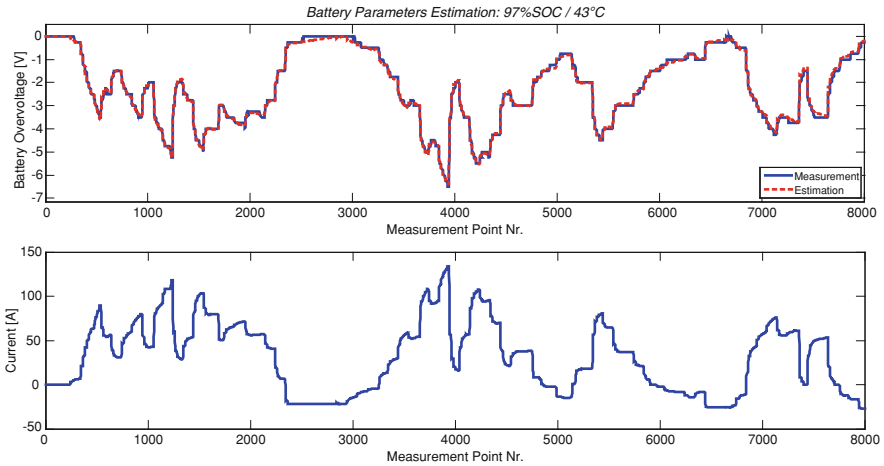


Fig. 6 Comparison of a current drop response measured on test bench and estimated based on the parameters extracted by the hybrid algorithm





**Fig. 7** Comparison of a driving cycle measured on test bench and estimated based on the parameters extracted by the hybrid algorithm

which means the battery can no longer be used for the application specified in the vehicle requirements specification. The authors define that the battery reaches its EOL state if battery-capacity decreases to 80 % of its initial value, or the internal resistance doubles, or the required maximum power of a cell can no longer be provided. Therefore, the main measures for the SOH value are capacity and internal resistance of the lowest performing cell. Depending on the type of vehicle, the relevance of the particular parameter is different. The achievable electrical range, defined by the battery capacity is more important for an electric vehicle. On the other side the maximum available power is important for hybrid electric vehicles (HEV), a constantly small internal resistance is preferable. Summarized, there are different requirements the SOH in EV and HEV/PHEV applications. This can be considered with weighting factors:

$$SOH = f(C_{act}, R_{i,act}) = \alpha \cdot \left( \frac{C_{EOL} - C_{act}}{C_{EOL} - C_N} \right) + \beta \cdot \left( \frac{R_{i,EOL} - R_{i,act}}{R_{i,EOL} - R_{i,N}} \right) \quad (7)$$

with

- $C_{act}$  actual capacity
- $C_N$  nominal capacity
- $C_{EOL}$  capacity at end of life
- $R_{i,act}$  actual internal resistance
- $R_{i,N}$  nominal internal resistance
- $R_{i,EOL}$  internal resistance at end of life
- $\alpha$  weighting factor capacity
- $\beta$  weighting factor internal resistance

There are two options to estimate the SOH parameters inside the vehicle. One possibility is an approach that uses the electro-impedance spectroscopy as described for the test bench activities. For a simple extraction of the impedance, some limitations are to set:

- (1) Causality
- (2) Time Invariance
- (3) Stationarity
- (4) Linearity

If all these conditions are fulfilled the non-linear impedance approximated by a Taylor series can be abandoned after the linear term. Thus, the following expression for the impedance becomes valid:

$$Z(j\omega) = \frac{U(j\omega)}{I(j\omega)} \quad (8)$$

For the application of EIS on board of a car a low cost and low space consuming solution is required. The challenges of an automotive application are the high number of cells inside of a battery which have to be checked and the strong EMC disturbances generated by high currents inside and outside the battery enclosure. Beside of this there are further restrictions due to processing and memory limitations. So i.e. the maximum sampling frequency of the used BMS hardware was only 10 Hz, which leads to an EIS frequency range of 40 mHz–5 Hz. For this reasons EIS is normally not suitable for in-vehicle use. But the measurements inside the vehicle looks promising for further investigations as shown in Fig. 8.

The measurements shows that criteria linearity and time invariance must be fulfilled and improved for further improvements and the BMS hardware is the limiting factors due to processing time and measurement accuracy restrictions. This concludes that true onboard application of EIS might not be the next step. However, the reverse application of solved battery models and improved parameter estimator algorithms are a promising opportunity. So the use of Kalman filters for the estimation of the SOH parameters capacity and internal resistance is a second possibility for SOH estimation might be a suitable approach for the first step. The equivalent circuit diagram of the battery model is transferred into a state space model and the state matrices and vectors have to be identified. The filters are designed and adjusted for the targeted state space [16]. The schematic of the Kalman filter is shown in Fig. 9. The algorithm consists of a set of equations and works in two steps. In the first step called “Time update” the Kalman filter predicts the state of the system given the past state estimation and the system input. It also computes the uncertainty of the prediction.

In a second step called “Measurement update” the algorithm compares the predicted values with the measured values. Based on the prediction error, the state estimation is updated. In reference to the prediction error the uncertainty is also updated.

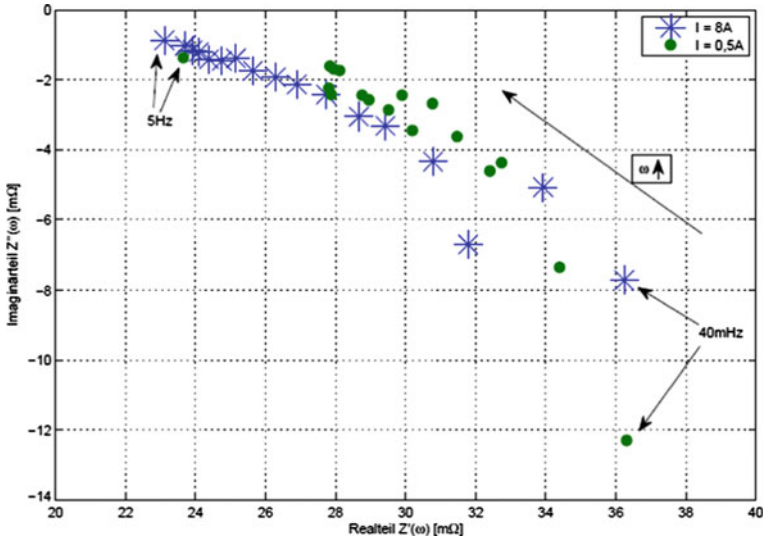


Fig. 8 Impedance spectrum  $Z(j\omega)$  in dependency of current rate

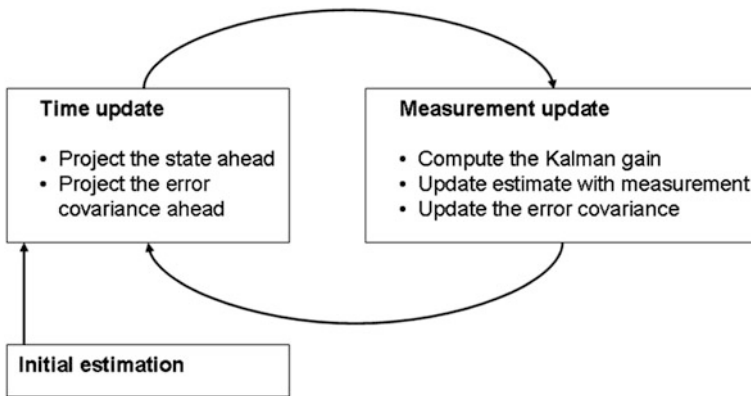


Fig. 9 Schematic of Kalman filter

It should be made clear, the calibration of robust Kalman filter arrangements require very extensive measurement work. Current benchmarking shows, these Kalman filter algorithms sometimes cannot deliver true values; if cells fade to internal defects the algorithm cannot differentiate the cause. Therefore, a clear analysis for robustness is required to prevent misleading functionality.

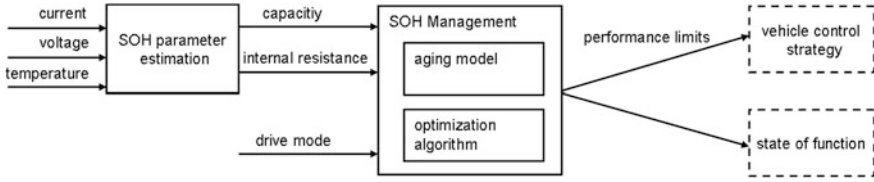


Fig. 10 Schematic of SOH-Management and processing for different EE-Architectures

## 6 Optimizing BMS Operating Strategy

To find optimal operating strategies, the problem needs to be defined generally. An always valid optimization function and constraints need to be defined. The general optimization problem is defined by

$$F(x_1, x_2, \dots, x_n) \rightarrow \text{Min} \tag{9}$$

and the constraints

$$G_i(x_1, x_2, \dots, x_n) \leq d_i \tag{10}$$

There are several optimization strategies with different characteristics and implementations. A common classification is noted below:

- (a) Global optimization
- (b) Local optimization
- (c) Heuristic optimization

Global optimization methods can be numerical or analytical. Information about the constraints is given at each time step. In Local optimization the global problem is separated in a set of local problems. In this case information about past and present conditions is necessary. Heuristic approaches have no explicit optimization.

Derived from energy management of hybrid electric vehicles, that is also supposed to find the optimal solution to use a combustion engine in combination with an electric motor, the SOH Management needs to solve the problem to find the optimal performance limits against the drive mode and the estimated parameters of the SOH, shown in Fig. 10. The input values for the SOH estimation are the actual current, voltage and temperature. A special configuration of Kalman-filters was used to estimate the SOH parameters capacity and internal resistance. The driving mode can accept the values “sport” and “range”. In the sports-mode the major aim is the allocation of the maximum power, the electrical range would be disregarded. On the other side the range-mode stands for preserve driving. The developed SOH-Management consists of an aging model and an optimization block.

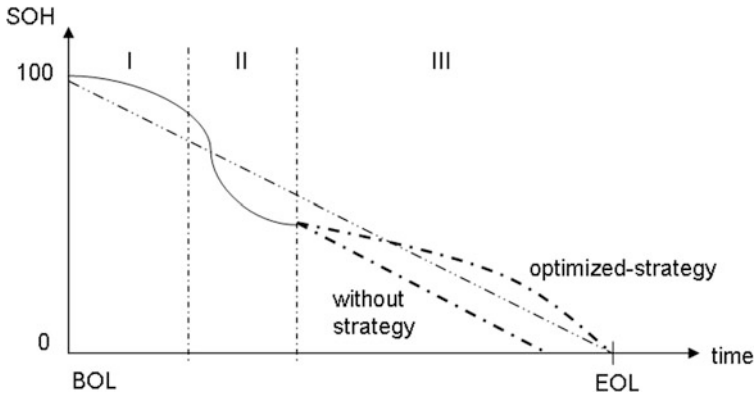


**Fig. 11** SOH-Management with optimized and without optimized strategy

With the information about the current estimated SOH parameters, the aging model for SOH-prediction and the optimization block finds the optimal values for the performance limits to achieve the specified driving mode.

The performance values are the state of charge limits, the maximum current, the time limits for the maximum current, and the temperature limits. Finally, these values are processed differently in different EE-architectures. Some architectures process performance prediction decentralized, others integrate drive control strategies on vehicle-control-unit level.

For demonstration purpose, Fig. 11 shows an exemplary history of the synthetic SOH parameter for a traction battery in use for some years. Section I describes a moderate driver. The estimated SOH is higher than the Reference-SOH-line (broken line). Section II shows the SOH in a critical area below specification. The SOH falls under the reference line due to an aggressive driving style. Without an optimizing strategy it cannot be assured, that the battery will reach the predefined EOL target, shown in area III. By using the proposed optimization strategy the performance values will be limited to assure the lifetime goal.

This method also can be helpful if the vehicle changes its place of application. Different ambient storage and operation temperatures have a major influence of the SOH even if the car has been never driven in this period. So the adaption of the performance values guarantees the achievement of the predefined EOL targets in different sales regions. It also helps to keep the vehicles economic value predictable for a long time period which in many sales regions is important to attract customers.

## 7 Conclusion

As the traction battery still is a very expensive maintenance component, the reliability of the health states over long-term becomes extremely relevant. It also needs to be mentioned, the life-time expectations differ much from customer

specific driving cycles. The prediction method for SOH management decreases the engineering and validation efforts to assure EOL specifications for all occurring cycles. The validation efforts can be focused on standard aging models as long as they are reliable. Interactive calibration and adaptation of the performance values help to control the highly varying aging behavior of battery cells. The presented approach seems to be an improvement of the aging determination inside the vehicle with regards to the accuracy and reliability; even some efforts are to do with regards to the measurement and calculation requirements inside the vehicle, where the resources are more limited due to cost issues.

## References

1. Plett G (2004) Extended Kalman filtering for battery management systems of LiPB-based HEV battery packs Part 2. Modeling and identification. *J Power Sources* 134:262–276
2. Randles JEB (1947) Kinetics of rapid electrode reactions. *Discussion Faraday Soc* 1:11–19
3. De Levie R (1967) Electrochemical response of porous and rough electrodes. *Adv Electrochem Electrochem Eng* 6:329–397
4. Botte GG et al (2000) Mathematical modeling of secondary lithium batteries. *Electrochim Acta* 45:2595–2609
5. Gomadam PM et al (2002) Mathematical modeling of lithium-ion and nickel battery systems. *J Power Sources* 110:267–284
6. Kanoun O et al (2006) Benefits of evolutionary strategy in modeling of impedance spectra. *Electrochim Acta* 51:1453–1461
7. Lasia A (2009) Modeling of impedance of porous electrodes in modern aspects of electrochemistry, Springer, New York, pp 67–137
8. Tröltzsch U (2005), Modellbasierte Zustandsdiagnose von Gerätebatterien, PhD thesis, Universität der Bundeswehr, pp 59 ff
9. Smola AJ et al (1998) A tutorial on support vector regression. *NeuroColt2- TR 1998-030 report*
10. MacDonald JR (1982) Applicability and power of complex nonlinear least squares for the analysis of impedance and admittance data, *J Electroanal Chem* 131:77–95
11. Boukamp BA (1986) A nonlinear least squares fit procedure for analysis of immittance data of electrochemical systems. *Solid State Ionics* 20:31–44
12. Vandernoot TJ et al (1998) The use of genetic algorithms in the nonlinear regression of immittance data. *J Electroanal Chem* 448:17–23
13. Bello A et al (1999) Distribution of relaxation times from dielectric spectroscopy using Monte Carlo simulated annealing: application to  $\alpha$ -PVDF. *Physical Review B* 60:12764–12774
14. Shi YH, Eberhart RC (1998) Parameter Selection in Particle Swarm Optimization. San Diego, CA
15. Li C, Liu Y, Zhou A et al A fast particle swarm optimization algorithm with cauchy mutation and natural selection strategy. Online Resource. *Lect Notes Comput Sc* 4683/2007:334–343
16. de Silva R (2010) Online-Ermittlung des state-of-health von Lithium-Ion-Akkumulatoren. Diplomarbeit, TU Braunschweig

**Part V**  
**Hydrogen Fuel Cell Vehicle**

# Novel Concept of Long-Haul Trucks Powered by Hydrogen Fuel Cells

**Bahman Shabani, John Andrews, Aleksandar Subic and Bidyut Paul**

**Abstract** A scale-model hydrogen fuel-cell truck has been designed and its performance tested to gain an improved understanding of the technical challenges of full-scale trucks employing on-board storage and hydrogen fuel-cell systems. A 1/14th scale battery-based replica of a Scania R470 Highline truck was equipped with two 30-W PEM fuel cell stacks and their control units, four metal-hydride hydrogen bottles storing in total 6 g hydrogen. A bank of super-capacitors was employed to smooth out the load placed on the fuel cells and meet the maximum demand of the truck. The hydrogen fuel cell system with the super-capacitor buffer was able to maintain stable operation and continuously supply the dynamic load of the truck over a full range of driving conditions, including during purging periods of the fuel cells. The fuel cell system was found to be more responsive to the changing load than the original batteries. The gravimetric energy density of the fuel cell system was measured to be about 30 % better than the original batteries of the truck.

**Keywords** Hydrogen fuel cell · Zero-emission · Road freight · Sustainable transport

---

F2012-B05-002

---

B. Shabani (✉) · J. Andrews · A. Subic · B. Paul  
School of Aerospace, Mechanical, and Manufacturing Engineering,  
RMIT University, Melbourne, Australia  
e-mail: bahman.shabani@rmit.edu.au



## 1 Introduction

Over 85 % of the global energy demand is met through the consumption of fossil fuels, primarily through combustion processes [1]. Currently the main fossil fuel that global transportation relies upon is oil. For example, the dependency of the European Union's transport sector on oil is around 98 % [2]. On average, more than 90 % of the global transport sector relies on oil [3], whereby transportation alone consumes around 49 % of oil production and is the most rapidly growing consumer of the world's energy [4]. According to projections by IEA [5], world transport energy demand will grow by about 40 % by 2035 compared to 2008. The combined impact of increasing global energy demand and eventual depletion of resources (i.e. fossil fuels) pose serious long-term challenges to maintaining security of energy supply at an economically affordable level [6] and this threat will be most serious for all oil-importing countries [7].

Greenhouse gas (GHG) emissions are another major concern associated with increasing use of fossil fuels in the transport sector [8]. According to IEA [9], the transport sector is the second-largest source of GHG emissions at the global level, accounting for about 6,500 Mt CO<sub>2</sub>-e/y into the atmosphere, that is, 23 % of global CO<sub>2</sub> emissions in 2009, with road transport as the largest contributor (about 5,900 Mt CO<sub>2</sub>). Subic and Koopmans [10] and Subic, Wellnitz et al. [11] provided a detailed overview of the implications of reduced fossil-fuel supplies and greenhouse gas (GHG) emissions reduction on road transport and associated vehicle technologies.

Many research studies have concluded that hydrogen will have an important role to play as a future alternative transport fuel [2, 12–15]. Subic [16] and Subic and Koopmans [10] presented some technology options for sustainable vehicle design based on alternative propulsion technologies. Contrary to Internal Combustion Engines (ICEs), power generation using fuel cells running on high-purity hydrogen, generated using renewable energy sources such as solar or wind as well (i.e. zero-emission generation), can supply electrical power and heat with no emissions [17–19]. The zero-emission hydrogen fuel cell option for road freight transport is discussed in this paper. This discussion is supported by some findings from an RMIT University pilot project that involves the design, construction and testing of a scale-model hydrogen fuel cell truck. In this research we identify the hurdles confronting the development of hydrogen fuel cell technology for transport, and trucking in particular, and provide some practical strategies for future development.

## 2 Zero-Emission Technologies for Road Transport

Currently the principal zero-emission solutions for transport being considered by automotive industries and governments around the globe are biofuel-based ICEs,

Battery Electric Vehicles (BEVs) charged from the main electricity grid supplied by zero-emission sources, and hydrogen-based ICEs and hydrogen fuel cell vehicles (HFCVs) with hydrogen produced from renewables. The biofuel options are able to be used in existing ICEs, have low net carbon emissions, are biodegradable [20], and emit no sulphates and sulphuric acid into the atmosphere as they are mainly vegetable oils with no sulphur content. However, diesel engines running on biofuels can arguably produce more  $\text{NO}_x$  than engines running on petroleum diesel. Moreover, the global contribution of biofuels will be severely limited by ruling out crops and land needed to supply food to a growing world population, and by the constraints on available land, water and fertilisers [12, 21, 22]. Battery electric technology offers advantages such as the possibility of using regenerative braking, wide availability of recharging stations (can be charged through any electric outlets connected to the main grid), and zero-in-operation emissions. However, factors such as long recharging time, restrictions relating to depth of discharge, the weight penalty associated with batteries, and relatively low energy storage capacity (compared to conventional fossil-fuel-based ICEs) are regarded as the key disadvantages [23, 24]. It is also noteworthy here that security of supply and the current and future costs of materials such as neodymium, dysprosium and lithium that are commonly used for battery production are of major concern [24].

Hydrogen has proven to be a feasible fuel solution for spark ignition (SI) ICEs [25] but not for compression ICEs (e.g. diesel engines) used in trucks [26, 27]. This is notable that using hydrogen in ICEs may not offer an absolutely zero-emission solution due to  $\text{NO}_x$  and possible  $\text{N}_2\text{O}$  production even at a higher level than for conventional ICEs running on petrol or diesel [28]. Hydrogen fuel cell technology is another option for generating zero-emission propulsion power from hydrogen. The silent electrochemical reaction of recombining hydrogen and oxygen in a fuel cell results in generating power at potentially up to twice as efficiently as an ICE in converting hydrogen energy to mechanical power [29, 30]. Refuelling HFCVs takes considerably less time than recharging BEVs [31]. Fuel cell systems including hydrogen storage can weigh less and occupy less space compared to batteries and these advantages become more dominant in the case of longer driving ranges (e.g. over 500 km) [31], such as required by long-haul trucks. Most major automotive companies, such as Toyota and Honda [32], BMW [33, 34], GM [35], Ford [34]; Daimler-Chrysler [36], Kia and Hyundai (REFS) have shown their interest in hydrogen cars (either fuel cell or hydrogen internal combustion engine) by developing demonstration models of their popular products running on hydrogen.

Unlike buses, there have not been many demonstrations to date of using hydrogen fuel cell technology in heavy-duty trucks. One of the most notable trials currently in progress, however, has been of a Class 8 short-haul truck developed by Vision Motor Corporation (called Tyrano) for use in ports in California [37]. A primary motivation for this project is to reduce smog caused by conventional diesel trucks. The Tyrano can cover 320 km over an eight hour shift by carrying up to 40 kg of gaseous hydrogen on board [38], while its hydrogen tanks can be

refilled in 4–7 min. Although the initial cost of this demonstration vehicle is nearly 2.5 times that of a standard diesel truck of the same size, its operating cost is 30–40 % less.

### 3 Scale Model Hydrogen Fuel Cell Truck

#### 3.1 Fuel Cell System Sizing

A pilot study has conducted at RMIT University to determine the feasibility of using hydrogen fuel cell technology in long-haul trucks. For this purpose a small-scale (1/14th) exact replica of a Scania R470 Highline truck [39] has been converted to hydrogen power. The model semi-trailer truck uses a RS0-540 DC motor [40] that originally ran on a 7.2 V, 2400 mAh Tamiya racing Li-ion battery pack. The critical performance characteristics of the truck such as maximum required power ( $\sim 55$ – $60$  W) current ( $\sim 7.5$  A) and voltage (8 V) were measured in order to size a fuel cell system to replace entirely the battery system. In designing the fuel cell system for the truck, it was decided to choose the fuel cell(s) such that their output voltage could meet the requirements of the RS-540 DC motor directly without stepping down or increasing the output voltage of the fuel cell(s). Accordingly, to fulfil the power requirement of the truck, two self-humidified 30-W fuel cell stacks (H-30 model) with 7–12 V voltage output [41] have been chosen (Fig. 1). The stacks are operated at 55 °C, use 0.3–0.4 bar hydrogen pressure (gauge) as input, and consume a maximum of 421 standard litre (sl) per minute (slpm) per stack of hydrogen at rated power. Measurements on the 30-W fuel cells used in the model truck at RMIT Renewable Energy Laboratory (REL) found that the operating voltage of the fuel cell varied between 7 and 12 V, while the range of variation for the current was 0–5 A. These characteristics indicated that the fuel cells should be arranged in parallel in order to meet the requirements of the RS-540 DC.

#### 3.2 Hydrogen Storage Solution

For on-board hydrogen storage, metal hydride was selected as the desired solution for this application (Fig. 1). Small metal hydride bottles (8-bar discharge pressure), using an AB2 alloy, were purchased from Horizon Fuel Cell Technologies. Four 16-sl metal hydride (MH-16) aluminium canisters ( $25.4 \times 105$  mm), storing  $\sim 1.5$  g hydrogen each (equivalent to about 30 Wh<sub>c</sub> at a 50 % fuel cell efficiency), were used for the hydrogen storage in the model. The total mass of each hydrogen bottle and a regulator to regulate the pressure down to about 0.5 bar (gauge) was measured to be 165 g. Although metal hydride bottles need heat to release

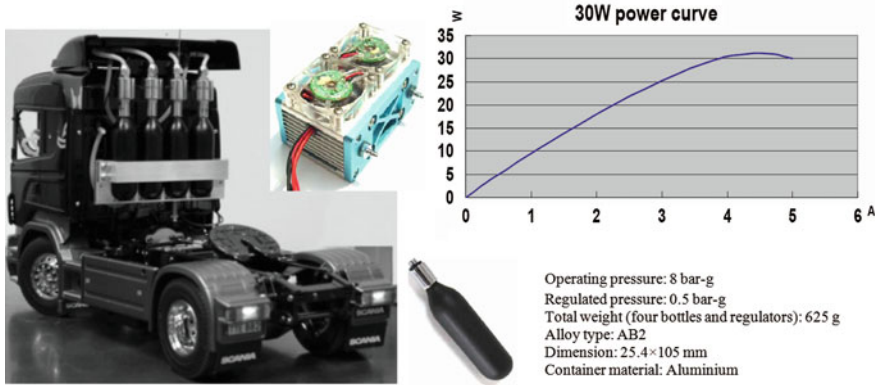


**Fig. 1** Fuel cell and hydrogen storage system; Four 16 sl metal hydride bottles (620 g) used for storing six hydrogen on board the truck. The bottle’s photo has been taken from the Horizon Fuel Cell Technologies; Two 30-W PEM fuel cell stacks used to propel the truck

hydrogen, the maximum 0.84 slpm hydrogen consumption rate by the two 30-W fuel cells was able to be supplied by these four bottles using just the heat they absorb from atmosphere without the need for supplementary heating.

### 3.3 Buffer System

An initial performance test on the truck using the fuel cell system with no buffer showed periodic interruption in the power supply to the motors, mainly during the hydrogen purging time, and in particular when the two fuel cells happened to undergo purging at the same time. Consequently an electrical energy buffer was needed in order to stabilise the operation of the truck. Previous experience with fuel cell technology for transport suggested two options for the buffer: batteries (i.e. Li-ion), and super-capacitors. For example, the Tyrano class 8 short-haul hydrogen truck discussed earlier used a Li-ion battery as both buffer and energy storage system [38]. The hydrogen buses used in Perth Australia and 10 European cities [42] employed ultra-capacitors to buffer the output power of the fuel cells. The initial versions of Honda FCX clarity used ultra-capacitors to buffer the fuel cell output power, but more recently Li-ion batteries have been employed.

Lifetimes of ultra-capacitors (e.g. one million duty cycles) are far longer than batteries, and their round-trip energy efficiency (~95 %) is slightly better than that for batteries (~80–90 %). Unlike batteries, ultra-capacitors can be deep discharged without affecting their lifetime. Ultra-capacitors also show better gravimetric power densities than batteries, although their gravimetric energy densities are considerably lower than that achieved for Li-ion batteries, and they self-discharge quicker than batteries. Ultra-capacitors are an excellent solution for meeting very sharp demands over a short period of time.

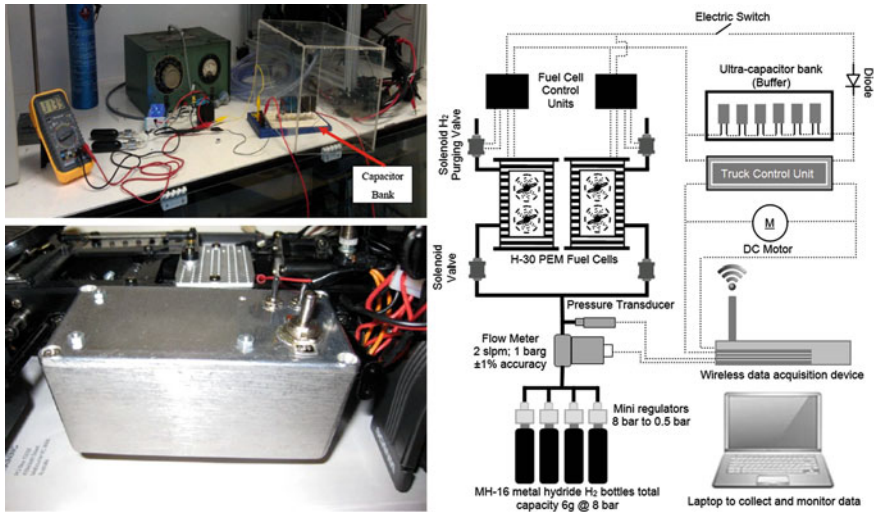


**Fig. 2** Buffer setup based on six 50 *F* capacitors connected in series forming a capacity bank of *C* = 8.3 *F*

To design such a buffer system, the voltage, current and total stored energy required were taken as the key parameters. A 10 s duration of standalone operation was assumed to size the super-capacitor bank. Six 50 *F* capacitors forming a capacity bank of *C* = 8.3 *F* with maximum voltage of 13.8 *V* (2.3 *V* each) were selected (Fig. 2). Based on the experimental observations, the two fuel cells connected in parallel could supply at maximum ~ 11 *V*; hence, the capacitor bank could take the maximum voltage provided by the fuel cells. At this charge voltage, the fully charged capacitor bank can provide about 0.14 *Wh<sub>e</sub>* energy storage capacity ( $W = 0.5 CV^2$ , *C* = 8.3 *F*, and *V* = 11 *V*), able to meet this maximum demand (55–60 *W*) in the absence of fuel cells for about 10 s. The fuel cells were found to be able to charge the capacitors in less than 15 s, consistent with the following estimation:

$$I \cdot dt = CdV \tag{1}$$

where *I* is current, *t* is time, *C* is the capacitance, and *V* is voltage. Hence charging up a capacitor bank of 8.3 *F* from 0 to about 11 *V* while the current varies from 0 to maximum 7 *A* would take about 13 s.

The capacitors used in the buffer system have low resistance of 0.02 Ω each to avoid considerable energy loss. High losses are not acceptable from an energy efficiency perspective and can also be a potential safety hazard as the capacitors become overheated.

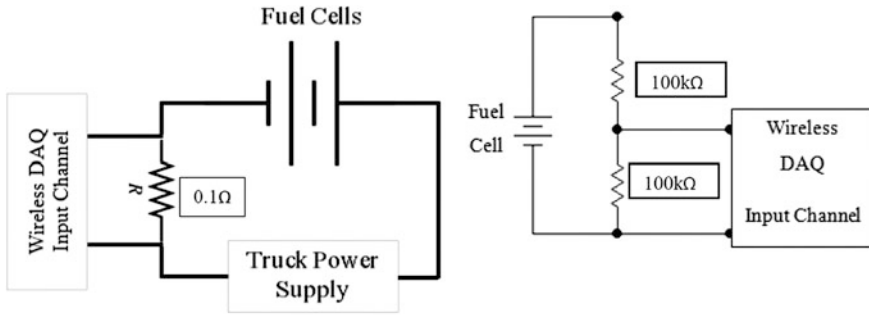


**Fig. 3** Circuit diagram to use the NI WLS-9205 IEEE 802.11 g (National Instrument) for remote monitoring of fuel cell performance

### 3.4 Data Acquisition System

The system was equipped with sensors to monitor the inputs to the DC motor and to measure the rate of hydrogen consumption during the performance test. A 32 channel wireless data acquisition system obtained from National Instrument (NI WLS-9205 IEEE 802.11 g) with LabView interface was used to transfer the real time data collected by the sensors to a nearby monitoring laptop (Fig. 3). The maximum voltage the system could handle was 10 v; hence, a resistor circuit was made to divide the voltage in half. For instance if the actual voltage is 12 v, the data acquisition system will be showing 6 v. A power resistor of very low resistance (e.g. 0.1 ohm) was used to measure the voltage drop across it and read the current using Ohm’s law ( $V = IR$ ).

The performance of the truck was monitored with and without the buffer system by using this data acquisition system and testing the truck on a 38-m driving track (Fig. 4). The track was designed to simulate the driving conditions for a typical truck including high and low speed zones and gradient.

## 4 Summary of Results and Observations

The fuel cell system was found to be more responsive to the changing load than the original batteries. The gravimetric energy density of the fuel cell system was measured to be about 30 % better than the original batteries of the truck. As the direct result of this, the 6 g hydrogen stored on board the model gave 18 km driving range in about 2.6 h, whereas the original battery pack was able to run the truck under the same driving conditions for 1.6 km for about 14 min only.

The power output of the fuel cell was monitored and recorded for certain period of time (e.g. for over 5 min). As shown in Fig. 5, the power output showed sharp maximums and minimums lasting for a fraction of a second only, which were

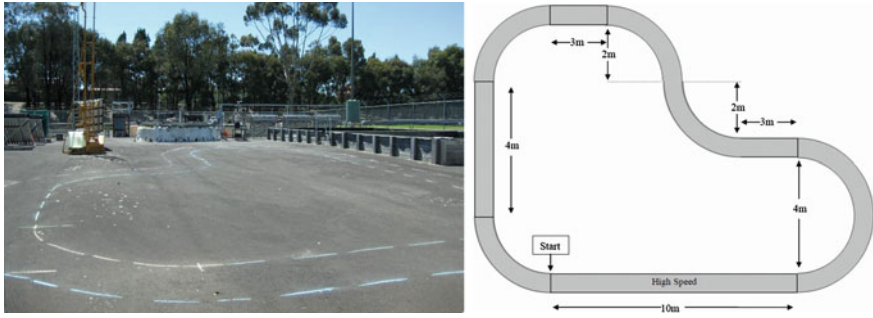


**Fig. 4** 38-m driving track used to study the performance of the truck and comparing it with its performance when using the original battery pack [43]

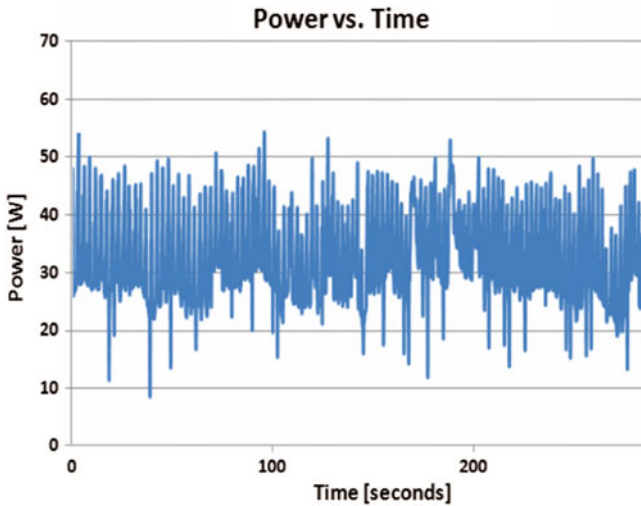


**Fig. 5** A sample of monitoring power supplied by the fuel cell in about 5 min of continuous operation [43]

obviously different to those normal peaks that could happen due to changing the demand along the testing track. Further investigation revealed that these sharp minimums and maximums are related to the operation solenoid vale (Fig. 6). Voltage overshooting and undershooting related to activation and ohmic overpotentials relating to the sudden variation of the fuel cell load, particularly when the operation of the solenoid valve operates, can well explain this behaviour [44, 45].

To demonstrate further how the buffer system can smooth out the power supplied to the DC motor, the fuel cell system was tested off the truck with and without the buffer system by increasing the power output of the system (adding load). The procedure was like that used to obtain the polarisation curve of the fuel cell; however, data were recorded immediately after changing the load rather than

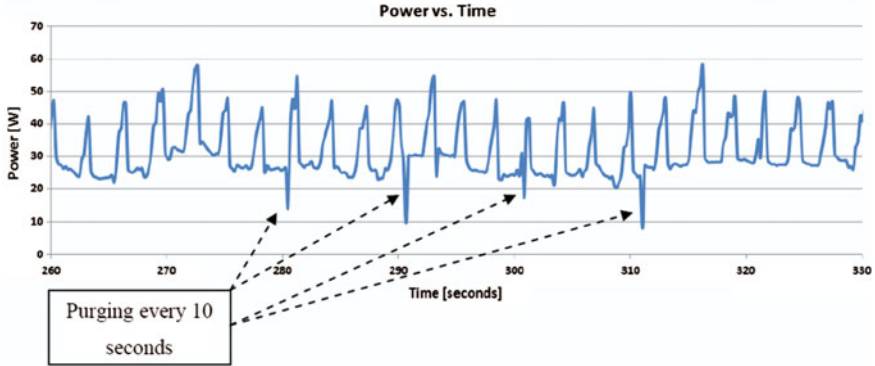


Fig. 6 Purging pattern of the fuel cell system [43]

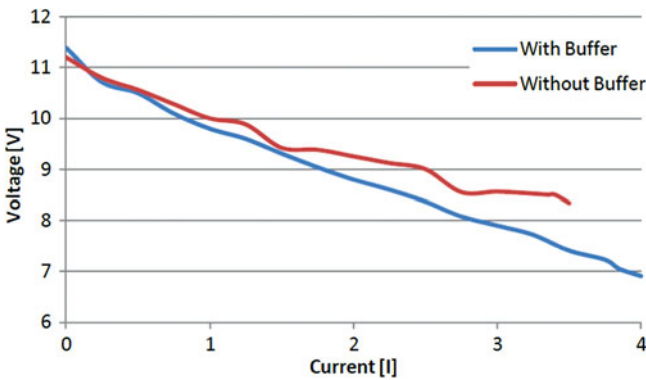


Fig. 7 The performance of the 30 W fuel cell system in supplying a variable load with and without using super-capacitors to buffer the output power [43]

waiting for a few seconds for the fuel cell to provide a stable output. As illustrated in Fig. 7, the output of the fuel cell is very smooth with the buffer in place as expected from an ideal polarisation curve, while its output oscillates significantly when no buffer is used. This is worth mentioning that adding the buffer caused a small drop (an average of about 7 % and maximum 15 %) in the net power output delivered by fuel cells as expected, because of the energy dissipated as heat in the super-capacitors due to their inherent internal resistance, particularly at higher currents.

Figure 6 suggests that the control unit in the fuel cell used have been set up to provide a constant purging period interval (every 10 s). However, this interval will be variable in larger fuel cells used in full scale fuel cell vehicles (shorter at higher power output and longer at lower power outputs). Clearly in our case it is preferable to avoid the two fuel cells purging hydrogen together at exactly the same time. Staggering the purging ensured the effectiveness of the buffering system in



handling the variable output of the fuel cell system. The procedure employed was thus to turn on the first fuel cell and then bring the second one into operation after a few seconds of delay.

## 5 Conclusions

Hydrogen fuel cell technology supported by renewables for hydrogen production is a promising sustainable solution for long-haul trucks, and for passenger vehicles with a driving range comparable to today's diesel-based trucks. Hydrogen fuel cell (HFC) road trucks are capable of having zero GHG emissions, near silent operation, and low operational costs. In this paper, we have reported on the results obtained from a 1/14th scale model HFC truck development that employs solid state storage of hydrogen in four metal hydride canisters, storing in total 6 g hydrogen to run a 60 W fuel cell system, propelling the truck. The scale-model hydrogen fuel-cell truck has been designed and its performance tested aimed at gaining an improved understanding of the technical challenges and requirements of full scale trucks employing hydrogen fuel-cell and on-board hydrogen storage systems. The gravimetric energy density of the fuel cell system was measured to be about 30 % better than the original batteries of the truck, which confirmed the potential suitability of this option to be used in road freight transport, where the driving range matters as an important factor. Clearly, the main limitation of this model is its size, which is far smaller than a full size truck. However, this initial exploratory phase has greatly assisted in establishing some key attributes of the hydrogen fuel cell system, including the need for a properly-sized power buffering system. The initial test on the truck showed that the fuel cells were not able to smoothly operate the truck and this result highlighted the fact that the fuel cell system had to be supported by a buffer system. As the result of this finding a suitably-sized super-capacitor bank was added to the system to buffer the output power of the truck. The hydrogen fuel cell system with the super-capacitor buffer was able to maintain stable operation and continuously supply the dynamic load of the truck over a full range of driving conditions, including during purging periods of the fuel cells. The added buffer was found to increase the responsiveness of the system to the dynamic load of the truck, in particular to meet sharp short-term demands, as well as eliminate the supply interruptions that occurred due to purging of the fuel cells.

## References

1. Jacob B (2010) On the role of fuel cells and hydrogen in a more sustainable and renewable energy future. *Curr Appl Phys* 10(2, Supplement):S9–S17

2. Ramesohl S, Merten F (2006) Energy system aspects of hydrogen as an alternative fuel in transport. *Energy Policy* 34(11):1251–1259
3. van Vliet O, Brouwer AS, Kuramochi T et al (2011) Energy use, cost and CO<sub>2</sub> emissions of electric cars. *J Power Sources* 196(4):2298–2310
4. Amjad S, Neelakrishnan S, Rudramoorthy R (2010) Review of design considerations and technological challenges for successful development and deployment of plug-in hybrid electric vehicles. *Renew Sustain Energy Rev* 14(3):1104–1110
5. IEA (2008) Key World Energy Statistics. International Energy Agency, Paris
6. Hal T (2006) Sustainable global automobile transport in the twenty-first century: an integrated scenario analysis. *Technol Forecast Soc Chang* 73(6):607–629
7. Kim J, Moon I (2008) The role of hydrogen in the road transportation sector for a sustainable energy system: a case study of Korea. *Int J Hydrogen Energy* 33(24):7326–7337
8. Cuda P, Dincer I, Naterer GF (2011) Hydrogen utilization in various transportation modes with emissions comparisons for Ontario, Canada. *Int J Hydrogen Energy* 2011(InPress, Corrected Proof)
9. IEA (2011a) IEA Statistics, CO<sub>2</sub> emissions from fuel combustion highlights. International Energy Agency
10. Subic A, Koopmans L (2010) Global green car learning clusters. *Int J Veh Des* 53(3/4):36–52
11. Subic A, Wellnitz J, Leary M et al (2012) Sustainable automotive technologies III. Springer, Berlin
12. Andrews J, Shabani B (2012) Re-envisioning the role of hydrogen in a sustainable energy economy. *Int J Hydrogen Energy* 37(2):1184–1203
13. Zhao J, Melaina MW (2006) Transition to hydrogen-based transportation in China: lessons learned from alternative fuel vehicle programs in the United States and China. *Energy Policy* 34(11):1299–1309
14. Offer GJ, Howey D, Contestabile M et al (2010) Comparative analysis of battery electric, hydrogen fuel cell and hybrid vehicles in a future sustainable road transport system. *Energy Policy* 38(1):24–29
15. Andrews J (2011) Designing a sustainable hydrogen economy. *Int J of sustainable design* 1
16. Subic A (2008) Sustainable mobility, vehicle design and development. *Int J Veh Des* 46(2):139–142
17. Shabani B, Andrews J (2010) Fuel cell heat recovery, electrical load management, and the economics of solar-hydrogen systems. *Int J Power Energy Syst* 3(4):256–263
18. Shabani B, Andrews J (2011) An experimental investigation of a PEM fuel cell to supply both heat and power in a solar-hydrogen RAPS system. *Int J Hydrogen Energy* 36(9):5442–5452
19. Andrews J, Shabani B (2012) Dimensionless analysis of the global techno-economic feasibility of solar-hydrogen systems for constant year-round power supply. *Int J Hydrogen Energy* 37(1):144–155
20. Yusuf NNAN, Kamarudin SK, Yaakub Z (2011) Overview on the current trends in biodiesel production. *Energy Convers Manage* 52(7):2741–2751
21. Stoeglehner G, Narodoslowsky M (2009) How sustainable are biofuels? Answers and further questions arising from an ecological footprint perspective. *Bioresour Technol* 100(16):3825–3830
22. Havlík P, Schneider UA, Schmid E et al (2011) Global land-use implications of first and second generation biofuel targets. *Energy Policy* 39(10):5690–5702
23. Shabani B, Andrews J, Watkins S (2010) Energy and cost analysis of a solar-hydrogen combined heat and power system for remote power supply using a computer simulation. *Int Solar Energy J* 84(1):144–155
24. RET (2011b) Strategic framework for alternative transport fuels. Department of resources, energy and Tourism, Australian Government
25. BMW (2011) BMW Hydrogen 7. Accessed on Dec, Available from. [http://www.bmw.com/com/en/insights/technology/efficient\\_dynamics/phase\\_2/clean\\_energy/bmw\\_hydrogen\\_7.html](http://www.bmw.com/com/en/insights/technology/efficient_dynamics/phase_2/clean_energy/bmw_hydrogen_7.html)

26. Miyamoto T, Hasegawa H, Mikami M et al (2011) Effect of hydrogen addition to intake gas on combustion and exhaust emission characteristics of a diesel engine. *Int J Hydrogen Energy* 36(20):13138–13149
27. Szwaja S, Grab-Rogalinski K (2009) Hydrogen combustion in a compression ignition diesel engine. *Int J Hydrogen Energy* 34(10):4413–4421
28. Berckmuller M, Rottengruber H, Eder A et al (2003) Potentials of a charged SI-Hydrogen engine. *SAE Int* 2003-01-3210
29. Hoffmann P (2001) *Tomorrow's energy: hydrogen, fuel cells, and the prospects for a cleaner planet*. The MIT Press, Cambridge
30. Mock P, Schmid SA (2009) Fuel cells for automotive powertrains—a techno-economic assessment. *J Power Sources* 190(1):133–140
31. CE T (2009) Fuel cell and battery electric vehicles compared. *Int J Hydrogen Energy* 34(15):6005–6020
32. *Fuel Cells Bulletin* (2003) Honda, Toyota expand California FCV fleets. *Fuel Cells Bulletin* 2003(11):3–4
33. Brunner T, Kircher O (2008) Progress on cryogenic hydrogen vehicle storage. In: *World hydrogen energy conference*. Brisbane, Australia
34. Verhelst S, Wallner T (2009) Hydrogen-fueled internal combustion engines. *Prog Energy Combust Sci* 35(6):490–527
35. Ahluwalia RK, Wang X, Rousseau A et al (2004) Fuel economy of hydrogen fuel cell vehicles. *J Power Sources* 130(1–2):192–201
36. *Fuel Cells Bulletin* (2008) GM, Chrysler unveil luxury concept FCVs. *Fuel Cells Bulletin*. 2008(3):2–2
37. HFCN (2011) Vision Tyrano truck. Accessed on June; Available from. <http://www.hydrogencarsnow.com/vision-tyrano.htm>
38. Vision (2011). Vision Tyrano. Accessed on July, Available from. <http://www.visionmotorcorp.com/maxvision.htm>
39. Tamiya Scania (2011) R470 Highline. Accessed on Jan, Available from. <http://www.tamiya.com/english/products/56317scania/index.htm>
40. BaneBots (2011) RS-540 motor-12 V specifications. Accessed on Jan, Available from. <http://banebots.com/pc/MOTOR-BRUSH/M2-RS540-120>
41. Horizonfuelcell (2010) Accessed on Dec., Available from. <http://www.horizonfuelcell.com/>
42. DSEWPC (2009). Hydrogen fuel cell bus trial. Department of Sustainability, Environment, Water, Population and Communities 2009 Accessed on June, Available from. <http://www.environment.gov.au/atmosphere/fuelquality/emerging/alternative/hydrogen.html>
43. Aizad S (2011) Hydrogen fuel cell trucks. School of Aerospace, Mechanical, and Manufacturing Engineering, RMIT University
44. Cho J, Ha T, Park J et al (2011) Analysis of transient response of a unit proton-exchange membrane fuel cell with a degraded gas diffusion layer. *Int J Hydrogen Energy* 36(10):6090–6098
45. Tang Y, Yuan W, Pan M et al (2010) Experimental investigation of dynamic performance and transient responses of a kW-class PEM fuel cell stack under various load changes. *Appl Energy* 87(4):1410–1417

# Practical Research on Hydrogen Safety of Fuel Cell Vehicles

Yong He, Bing Wu, Honghu Wang, Pengcheng Zhao and Yachao Li

**Abstract** With the development of technology and economy, people's demand for energy has been increasing. But the environmental pollution caused by the use of traditional energy sources has threatened to the people's lives. In order to avoid reducing the welfare of human's future, we must find new, clean, sustainable energy systems, and apply them to human beings' real life. Fuel cell vehicles are hydrogen's specific applications in transportation field. The power of this new energy vehicle is provided by the electricity produced by hydrogen and oxygen through fuel cells, and its emission is only water which has no pollution to the environment. However, if a new energy system wants to get the promotion and application, its safety should be firstly concerned comparing to conventional cars. Hydrogen has its own characteristics, such as the phenomena of leakage, dispersion, flammability, detonation and embrittlement, which make the board hydrogen system have certain security risks. In order to further develop and promote fuel cell vehicles, it is necessary to do hydrogen safety research. This study is based on the theory at home and abroad. Firstly, the article introduces the basic principles of fuel cell vehicles and basic characteristics of hydrogen. Secondly, we discuss the special safety problems of hydrogen, such as the safety of hydrogen supply system, car-inside, components and pipe and hydrogen fuel cells engines. Lastly, facing these hydrogen safety issues, we put forward corresponding improvement measures and control strategies through testing and analysis to help the development and promotion of fuel cell vehicles.

---

F2012-B05-004

---

Y. He (✉) · B. Wu · H. Wang · P. Zhao · Y. Li  
SAIC Motor Corporation Limited, Shanghai, China  
e-mail: heyong01@saicmotor.com

**Keywords** Fuel cell vehicles · Hydrogen energy · Hydrogen safety · Practical research

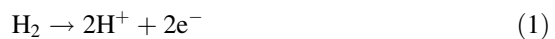
## 1 Introduction

With the development of science and technology, people's demand for energy is increasing and the damage to the environment is much more serious. We have to seize the opportunity to develop green energy; only by this way can we fundamentally solve the increasingly prominent contradiction between human needs with energy and environmental protection, and do not be constrained by the shortage of traditional energy sources. In this context, green energy systems with hydrogen as an intermediary—the hydrogen energy system gradually aroused widespread concern [1]. The fuel cell vehicle is the specific application of clean energy hydrogen in the transport field. The power of this new energy vehicle is provided by electricity that fuel cells produce from hydrogen and oxygen. In the process, the emission is only water [2], which has no pollution to the environment.

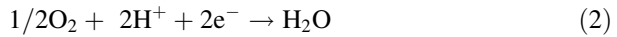
However, due to the hydrogen's characteristics, fuel cell vehicle hydrogen systems have certain security risks. Based on the study at home and abroad on the theory, firstly, this paper introduced the basic characteristics of hydrogen and the basic principles of fuel cell vehicle. Secondly, we discuss the special safety problems of hydrogen, such as the safety of hydrogen supply system, car-inside and so on. Lastly, in the operation of the Expo demonstration, we distributed sensors in all parts of the test vehicle in order to find out the hydrogen exceeded parts, and compared the difference, analyzed the causes and proposed improvement measures and control strategies to help the fuel of the future promotion and development of cell vehicles.

## 2 Relevant Principles

This paper uses Proton Exchange Membrane Fuel Cell (PEMFC) in the practical research. PEMFC uses perfluorinated sulfonic acid solid polymer solid polymer as electrolyte, Pt/C as electro-catalyst, hydrogen as fuel, air as the oxidant, the graphite with gas flow channels or metal plates with surface modification as the bipolar plate [3]. The electrode reaction in PEMFC is similar to other acidic electrolyte fuel cell. In the anodic, hydrogen is oxidized to hydrogen ions and emits electrons.



Hydrogen ions transfer to the cathode through the proton exchange membrane, and the electrons transfer to the cathode through the external circuit. Oxygen, hydrogen ions and electrons react in the cathode generating water, which will not dilute the electrolyte, but be discharged with the reaction exhaust gas through the electrode.



The PEM supply hydrogen ion channel as the electrolyte, meanwhile, it plays the role of diaphragm isolating bipolar reaction gas.

### 3 Fuel Cell Hydrogen Safety

Hydrogen as one of the fuel cell reaction gases determines that the fuel cell has different hazardous characteristics from conventional energy systems. The following describe the characteristics of hydrogen and hydrogen safety design strategies in fuel cell vehicle.

#### 3.1 Hydrogen Characteristics

Hydrogen mainly has the following physical characteristics.

(1) Leakage:

Hydrogen is the lightest element, and its molecular diameter is very small, so it more easily leaks from the hole than liquid fuels and other gases. Once the leakage occurs, hydrogen will be rapidly spread. Moreover, the hydrogen flame is almost invisible in the air [4]. People close to the hydrogen flame may not know the existence of the flame, thus increasing the risk.

(2) Dispersion [5]:

Compared with gasoline, propane and natural gas, hydrogen has a greater buoyancy (rapid rising) and stronger diffusion (lateral movement).

(3) Flammability

Hydrogen has a good performance of burning and a wide range of combustible when mixed with air. What's more, it is burning very fast.

(4) Detonation:

Explosion limit of Hydrogen is 4–75VOL %, while the explosion limit of methane is 5–15VOL %. In other words, in order to stay safe, the hydrogen

concentration should remain below the lower flammability limit of 4 %, and install the detector alarm and exhaust fans working together to control the hydrogen concentration.

(5) Embrittlement:

Hydrogen embrittlement means that the mechanical performance of metal is severely degrading and the occurrence of the phenomenon of brittle fracture, which due to the hydrogen absorption or hydrogen permeation in the process of smelting, processing, heat treatment, pickling and plating, or in a long-term use with a hydrogen medium.

## ***3.2 Hydrogen Safety Design Strategies***

### **3.2.1 Safety of Hydrogen Supply System**

For the safety of hydrogen supply system, the practice research in this paper took the following measures.

- (1) Isolation arrangement, separate the hydrogen space and other space;
- (2) Conduct the collision analysis optimization, simulation and crash test [6];
- (3) Control the crash; Install the collision sensors so that the hydrogen supply can automatically turn off when the collision occurs;
- (4) Use safety value and relief value for the over-temperature, overpressure and over-current protection;
- (5) Reliability; Conduct vibration tests.

### **3.2.2 Car-Inside Hydrogen Safety**

The practice research in this paper monitored the hydrogen concentration of fuel cell car space, including the space of hydrogen supply system, hydrogen device space, pipe laying parts and the crew cabin space. When the detected hydrogen concentration reaches the limit, the hydrogen supply will automatically turn off. Vehicle monitoring to identify hydrogen leak and alarming were used in the research, while performing control functions if necessary.

When the concentration of hydrogen is between 3,000 and 6,000 ppm, the system alarms; when the hydrogen concentration is between 6,000 and 12,000 ppm, the system alarms, and stop and check the vehicle at the same time; when the hydrogen concentration is greater than 12,000 ppm, the system will automatically cut off the source of hydrogen.

### 3.2.3 Components and Pipe Hydrogen Safety

Components and pipe also have the existence of hydrogen safety issues. Hydrogen embrittlement, this practice research use the materials without hydrogen embrittlement, such as 316 stainless steel, aluminum, etc.; hydrogen barrier; antistatic gathered; leak test problem, this paper uses a gas-tight test.

### 3.2.4 Hydrogen Safety of Fuel Cell System

Leak testing, reliability testing, anti-static accumulation and over-temperature overpressure protection for fuel cell system hydrogen safety were conducted in this research.

## 4 Practice Test

### 4.1 Practice Test Design

The practice conducted in Expo had more than 140 vehicles to be tested, including 100 sightseeing cars, 42 cars and 6 buses. To ensure the safety and success of the testing work, we design the work flow, show in Fig. 1.

### 4.2 Statistical Analysis of Practice Results

In this paper we took certain types of cars and buses as examples, test results, such as shown in Table 1, showed that cars and buses were respectively detected 3,468 and 1,119 times, in which cars were exceeded 62 times and buses were exceeded 16 times. The hydrogen excessive rate of cars and buses were respectively 1.79 and 1.43 %.

The position distribution of car hydrogen excessive times is shown in Table 2. In the table, the letters ABCDEFGH respectively represent the various locations of car. A: car surrounding, B: wheel cover, C: the edge of the first turbine cover, D: trunk, E: crew compartment, F: manual vent, G: vent, H: filler.

In order to directly get the test result of both dispatch and storage and the relationship between the car hydrogen excessive times of different positions, see Figs. 2 and 3. In the figures, the thicker the digital frame, the more the hydrogen excessive times. The thickest frame is the filler (H), which on the both side of the fuel cell car with the hydrogen excessive times of 26. With the frame becoming thinner, followed by are the wheel cover (B) and the edge of the first turbine cover (C).



**Fig. 1** Flow chart of the practice test work

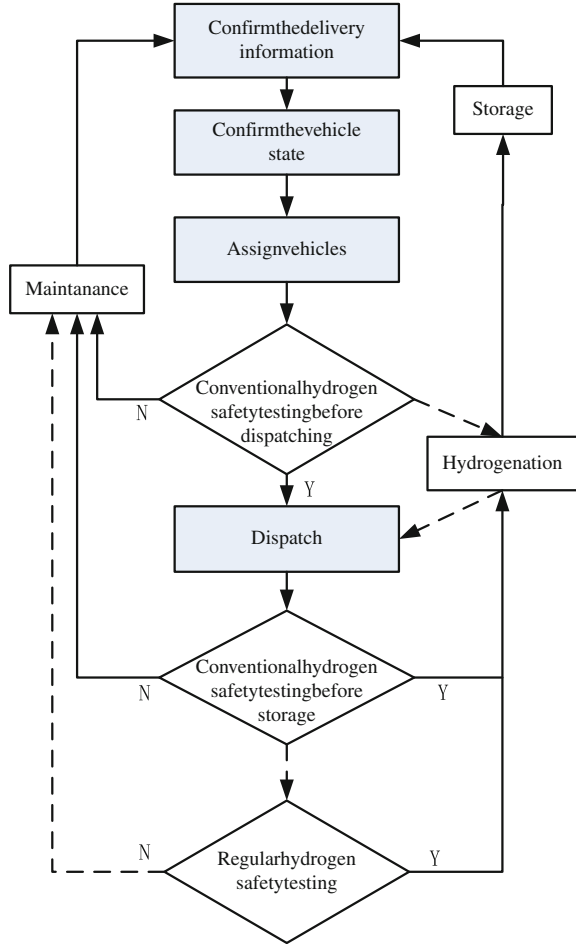


**Table 1** Statistics of test data

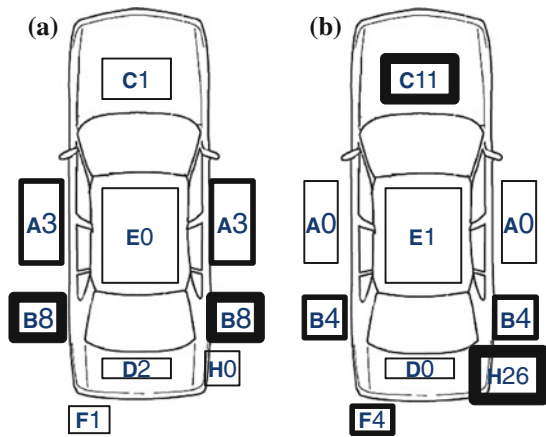
	Car	Bus
Number	30	6
Total test times	3468	1119
Total excessive times	62	16
Hydrogen excessive rate (%)	1.79	1.43

The position distribution of bus hydrogen excessive times is shown in Table 3. In the table, the letters IJKL respectively represent of the various locations of bus. I: car surrounding, J: the rear of crew compartment, K: the cell cabin, and L: the filler. The number statistics of each position of bus hydrogen exceeded is shown in Fig. 4, and the main exceeded positions are the rear of crew compartment, the cell

**Table 2** Position distribution of car hydrogen exceeded

State	Position distribution									Hydrogen excessive rate (%)
	A	B	C	D	E	F	G	H	Sub-total	
Total	3	12	12	2	1	5	1	26	62	1.79
Dispatch	3	8	1	2	0	1	0	0	15	0.43
Storage	0	4	11	0	1	4	1	26	47	1.36

**Fig. 2** Position distribution of car hydrogen exceeded.  
**a** Dispatch **b** Storage



cabin, and the filler. Meanwhile, in the figure, we can get that the number of exceeded times in storage is far more than in dispatching.

From the above chart, storage exceeded more often than dispatching. Following are the possible reasons.

- (1) Environment: when storage, there are many vehicles around, and their emissions of hydrogen affect the storage test results, while in dispatching, there is no other vehicle around.
- (2) Characteristics of filler: when storage, the filler just finish filling hydrogen, with its own structural design, resulting in the gathering of a small amount of hydrogen within a short time. But it is normal and will not affect the vehicle safety.
- (3) Hydrogen excessive of the outside edge of cockpit: when in storage tests, a number of hydrogen excessive happen in the outside edge of cockpit, in which there has amount of hydrogen released by 12 V lead-acid batteries. However, it won't have safety problem to the whole vehicle.

In addition, this practice conduct periodic testing every month to check all of the hydrogen pipe line interface, and in the Expo detection, there is no hydrogen leak in pipeline interface.

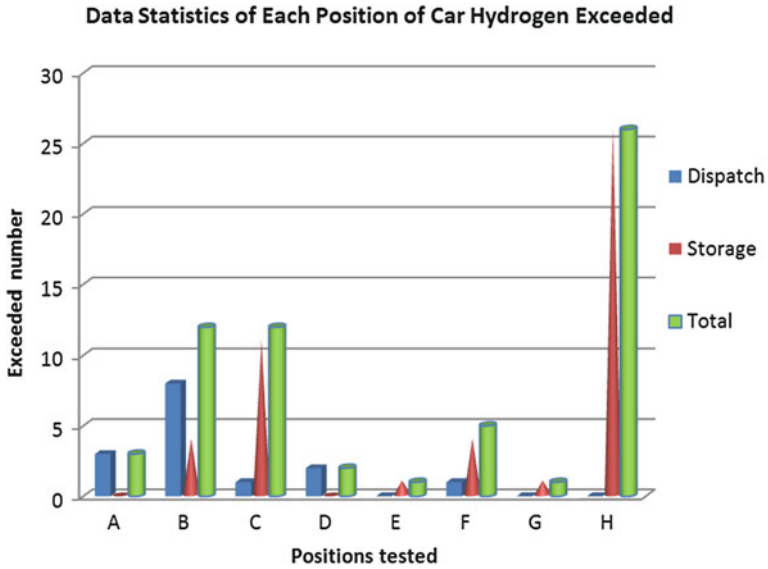


Fig. 3 Data statistics of each position of car hydrogen exceeded

Table 3 Position distribution of bus hydrogen exceeded

State	Position distribution					Hydrogen excessive rate (%)
	I	J	K	L	Sub-total	
Total	1	4	5	6	16	1.43
Dispatch	0	0	2	0	2	0.18
Storage	1	4	3	6	14	1.25

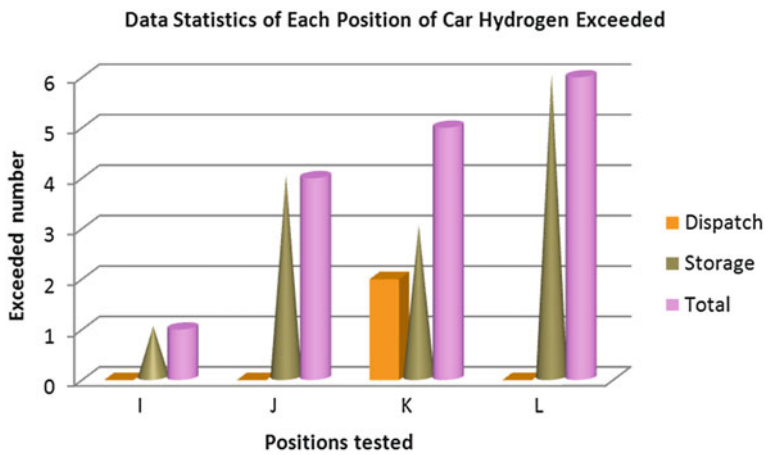


Fig. 4 Data statistics of each position of bus hydrogen exceeded

**Table 4** Test point streamlining

Serial number	Position	Test object	After optimization	Reason
1	Crew compartment	The whole car's hydrogen safety	√	Ensure safety
2	Trunk	The whole car's hydrogen safety	×	Hydrogen excessive frequency is extremely low
3	Car surrounding-left	The fuel cell	×	No hydrogen in electric piles cannot achieve the goal
4	Car surrounding-right	The fuel cell	×	
5	Wheel cover-left back	Hydrogen supply system of high pressure	√	Data prove good effect
6	Wheel cover-right back	Hydrogen supply system of high pressure	√	Data prove good effect
7	Automatic vent	PRD, pressure relief valve	√	Data prove good effect
8	Manual vent	Emptying manual valve	×	No practical significance
9	Filler	Filler	×	No practical significance

### **4.3 Improvement Solutions**

Through the practice tests and statistics above, we propose two aspects of the optimization improvements, streamlining the test points and test frequency to reduce the operating costs to simplify the practice procedure on the basis of the practice research, which also provide reliable data support for the further practice.

#### **4.3.1 Test Point Streamlining**

At present there are nine test points on the car and after optimization there are only four points, namely the four places marked by yes. The object tested on each position and the reasons why we retain or omit every point after optimization are shown in Table 4.

#### **4.3.2 Test Frequency Streamlining**

The conventional test frequency in the practice is twice a day (before dispatching and after storage). According to the test results in the process of operation, we cancel tests after storage and only test the situation before dispatching. The results following turn out well.

According to the statistics, the test accuracy before dispatching is higher than 93 % (only one is misstatement in 15 hydrogen exceeded tests), and in contrast the accuracy after storage is lower than 5 % (only two are accurate in 46 hydrogen exceeded tests).

At the same time, we haven't found any hydrogen interface leakage in regular tests during the Expo period.

Take all into consideration and we can test only before dispatching and change regular test frequency from once a month to once every 2 months.

In conclusion, according to the test statistics and scheme put forward, we can reduce the operation cost for the fuel cell tests and provide reliable basis for the further fuel cell research and application.

## **5 Conclusion**

Hydrogen safety is of vital importance in the operation of the fuel cell system, but we find out there are not many researches on hydrogen safety of the fuel cell through the conclusion of the practical experience and the investigation of the related literature. We take the research and practice tests on the safety of hydrogen which is one of the fuel cell reaction gases according to the physical properties and security classifications of hydrogen from the principle of the fuel cell in this

article. Test results show that the practice tests are very strict and receive good effects. The statistics lays the foundation for the fuel cell car testing and operation in the future; at the same time, the improvement scheme put forward in this article will provide the direction for further practice, decrease operation cost and improve the testing efficiency. The corresponding improvement measures and control strategies proposed according to the practice tests are helpful to the promotion and development of the fuel cell vehicle.

## References

1. Wang X, Ma J, Wu M et al (2008) Hydrogen safety problems of fuel cell vehicles. Chinese scientific and technical papers online 5:365–369
2. Feng W, Wang S, Ni W et al (2003) Safety of hydrogen energy and hydrogen safety problems of fuel cell vehicles. *J Sol Energy* 5:103–114
3. Ma J et al (2008) Fuel cells overview. Tongji University Car Institute
4. Ford Motor Company (1997) Direct hydrogen fueled proton exchanged membrane fuel cell system for transportation application: hydrogen vehicle safety report. Department of Energy, US
5. Wang Q, Luo M, Luo Z et al (2011) Vehicle hydrogen safety study of fuel cell cars. *J Wuhan Univ·Ed Inf Manag Eng* 2:232–235
6. Wu B, Chen P, Leng H et al (2007) Vehicle hydrogen supply systems. Shanghai automobile 9

# Modeling and Analysis of a Fuel Cell Hybrid Vehicle

Mircea Nicolae Glazer, Ioan Mircea Oprean  
and Marius Valentin Băţăuş

**Abstract** This paper presents the results of a Fuel Cell Hybrid Electric Vehicle (FCHEV) modeling, in which the fuel cell system is integrated with an on-board rechargeable energy storage system (RESS) for electric energy supply to propulsion and auxiliary systems. The objectives of the model is to design a tool suitable for predicting hydrogen consumption, dynamic performances analysis and power management optimization. The global model is the integration of vehicle longitudinal dynamic equations, transmission model and validated models for power sources and power electronics. The model was developed using Matlab/Simulink programming environment with SimPowerSystems library. In order to adapt the steep voltage drop in respect to electrical current load of the fuel cell to a more constant voltage requirement, a DC/DC converter was implemented between the fuel cell and the high power Li-ion battery. The results indicate the suitability of the model in predicting vehicle range and dynamic performances.

**Keywords** Fuel cell · Electric drive system · Simulation · PEM · PMSM

---

F2012-B05-005

---

M. N. Glazer (✉) · I. M. Oprean · M. V. Băţăuş  
University Politehnica of Bucharest, Bucharest, Romania  
e-mail: glazer\_mircea@yahoo.com

## 1 Introduction

More stringent emissions regulations have imposed vehicle manufacturers to implement new solutions with the main purpose of increasing well to wheel energy conversion efficiency, while maintaining or even increasing dynamic performance and passenger comfort. These demands lead to the reduction of green house gas emissions quantified as  $\text{CO}_2$  g/km [1].

Battery electric vehicles achieve lowered energy consumption and gas emissions (especially in urban environment) than internal combustion engines powered vehicles. The main drawbacks concerning the use of electric energy as the main energy source are long recharge time and a lack of electric charging infrastructure, thus limiting the usage of the electric vehicles. An efficient solution to improve vehicle range and reduced refueling time is represented by the implementation of Fuel Cell Hybrid Vehicles. Due to the increased range supplied by hydrogen tanks the fueling infrastructure can be implemented more easily than battery charging as fewer stations are necessary.

Introducing the FCX model as early as 2002 in Japan and USA, Honda is one of pioneers in applying fuel cell technology to automobiles [2]. By 2004 the Japanese company had developed a new FCX version fitted with a fuel cell capable of cold start at  $-20$  °C. Increasing dynamic performances and capacity to work in a wide range of climate conditions made the fuel cell power train, developed on FCX models, competitive with the internal combustion engine in terms of performance, drivability, reliability and economy.

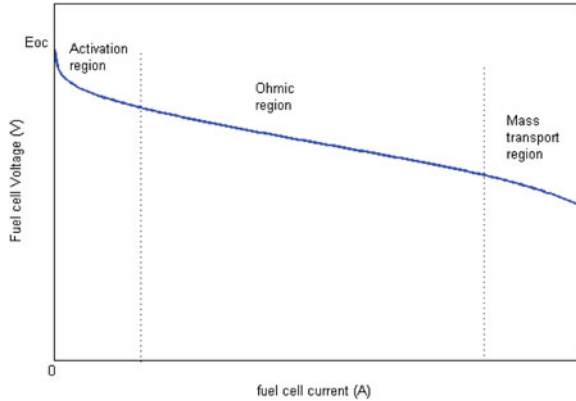
Dynamic modeling with a high degree of accuracy of the integrated vehicle-powertrain system is required for fuel cell power train systems synthesis and fast optimization of the necessary control and command system. In addition, if it is desired to follow a drive cycle it is necessary to create a control loop with a driver model.

## 2 Proton Exchange Membrane Fuel Cell (PEMFC)

PEM fuel cells operate at temperatures lower than 100 °C, considered low temperatures [3], which make them temperature-compatible with many of today's automotive systems. However, due to the low temperature gradient to the ambient temperature, it requires larger heat exchangers. A chemical reaction takes place in a fuel cell in order to convert hydrogen and oxygen into water, releasing electrons in the process. In other words, the hydrogen fuel is oxidized in a simple reaction that produces water and electrical current. The power densities of both PEM and Solid Oxide Fuel Cell (SOFC) are in the range of  $500 \text{ mW/cm}^2$  under typical operating conditions. Peak power densities, under ideal conditions, were rated at greater than  $1,000 \text{ mW/cm}^2$  [3].



**Fig. 1** Example of a fuel cell polarization curve



An example of the polarization curve for a PEM fuel cell is presented in Fig. 1 [4].

The voltage drop results from four major irreversibilities:

- Activation losses: in the transfer of electrons from or to the electrode a part of the energy is lost.
- Fuel crossover and internal currents: part of the fuel and of the electrons pass through the electrolyte, without giving useful energy.
- Ohmic losses: the electrodes and the interconnections have their own resistance to the passage of electrons. As a result a part of energy is lost in heat.
- Mass transport or concentration losses: the concentration of the reactants at the surface of the electrode decreases with the increasing of the output current [4].

The reversible open circuit voltage is the theoretical maximum voltage that a fuel cell can deliver. To calculate this parameter some chemical considerations have to be done: for every reaction the difference between the Gibbs free energy of the products and the reactants is a measure of the ‘external work’ which the reaction needs or delivers.

$$\Delta G_f = G_{fprod} - G_{freact} \tag{1}$$

Inside a fuel cell, this external work is used to move electrons in the circuit which connects anode and cathode;  $2 N$  electrons pass inside the circuit for each mole of hydrogen oxidized, where  $N$  is the Avogadro’s number:

$$-2Ne = -2F \tag{2}$$

where:

e: charge of one electron (C);

F: Faraday’s number (C).

If all the Gibbs free energy is used to move electrons, the reaction has no losses [5]:

$$\overline{\Delta g_f} = -2F \cdot E \rightarrow E = -\frac{\overline{\Delta g_f}}{2F} \quad (3)$$

where:

$\overline{\Delta g_f}$ : Gibbs free energy released by one mole of hydrogen (KJ/mol)

### 3 Sympowersystems Fuel Cell Model

This detailed model available in SymPowerSystems Library from Simulink represents a particular fuel cell stack when the parameters such as pressures, temperature, compositions and flow rates of fuel and air vary [6]. The variations of these parameters affect the open circuit voltage ( $E_{oc}$ ), the exchange current ( $i_0$ ) and the Tafel slope ( $A$ ). The rates of conversion (utilizations) of hydrogen ( $U_{fH_2}$ ) and oxygen ( $U_{fO_2}$ ) are determined in Block A as follows:

$$U_{fH_2} = \frac{60000 \cdot R \cdot T \cdot N \cdot i_{fc}}{z \cdot F \cdot P_{H_2} \cdot V_{l_{pm}(H_2)} \cdot x \%} \quad (4)$$

$$U_{fO_2} = \frac{60000 \cdot R \cdot T \cdot N \cdot i_{fc}}{2z \cdot F \cdot P_{aer} \cdot V_{l_{pm}(aer)} \cdot y \%} \quad (5)$$

where:

$N$ —number of cells;

$i_{fc}$ —generated electric current;

$P_{H_2}$ —absolute supply pressure of hydrogen;

$V_{l_{pm}(H_2)}$ —hydrogen flow rate;

$P_{air}$ —absolute supply pressure of air;

$V_{l_{pm}(air)}$ —air flow rate;

$x$  %—percentage of hydrogen in the fuel;

$y$  %—percentage of oxygen in the air.

Based on relations (4) and (5) it can be concluded that for the fuel cell stack to work at an optimum efficiency, close to nominal conversion values, a flow control system is necessary. For the purpose of solving this problem a control block was realized. It regulates the mass flow of hydrogen and air in function of the estimated electric current consumption of the drive system. Hydrogen mass flow is determined with the formula:

$$m = \frac{p \cdot M}{R \cdot T} \cdot V_{l_{pm}(H_2)} \cdot \frac{1}{60000} \left[ \frac{g}{s} \right] \quad (6)$$

where:

$p$ —hydrogen pressure;

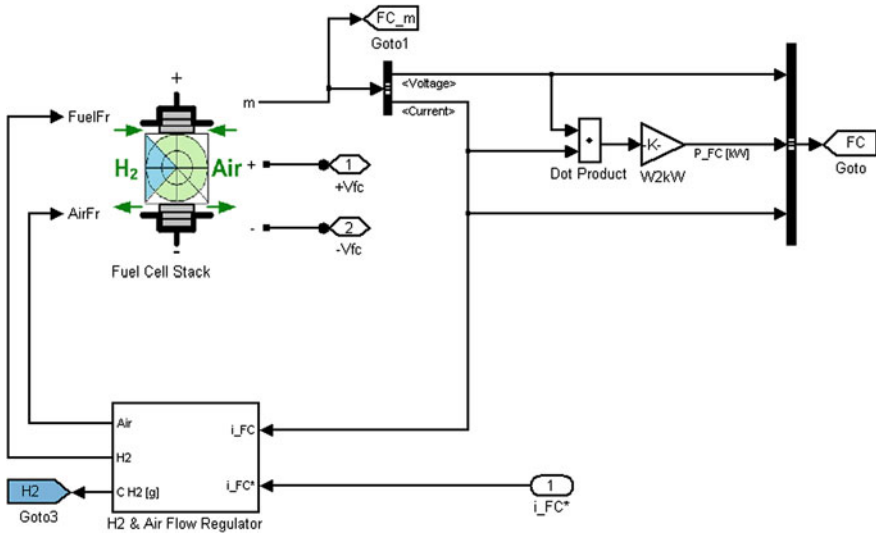


Fig. 2 Fuel cell stack with H<sub>2</sub> and air flow regulator

$M$ —hydrogen molar mass.

### 4 Fuel Cell Command and Control

For the Fuel Cell to work as efficiently as possible a H<sub>2</sub> and air flow regulator has been implemented. Fuel Cell Command and Control uses a mass flow regulator (H<sub>2</sub> and Air Flow Regulator) in order to manage the consumption of hydrogen and air according to estimated electrical current consumption. The system involves two closed loop configurations. One use a direct measurement of the Fuel Cell electrical current ( $i_{FC}$ ) and the other is based on the estimated current consumption which is calculated in the Power Estimator. The highest value from these two is always used to calculate the mass flow of the PEM Fuel Cell. The Fuel Cell block made in MATLAB/Simulink is presented in Fig. 2.

### 5 The Electric System

The Fuel Cell Stack and H<sub>2</sub> and Air Flow Regulator are fitted into the FC Stack Module, which is connected to a DC/DC converter in order to charge the Li-ion battery inside the Electrical System. The detailed diagram of the Electrical System is shown in Fig. 3.

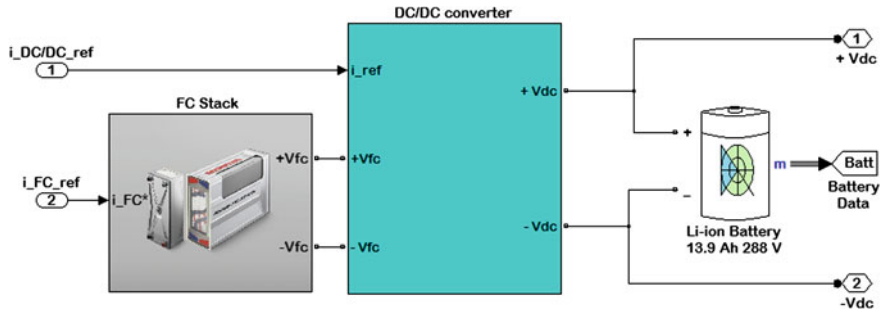


Fig. 3 The electrical system

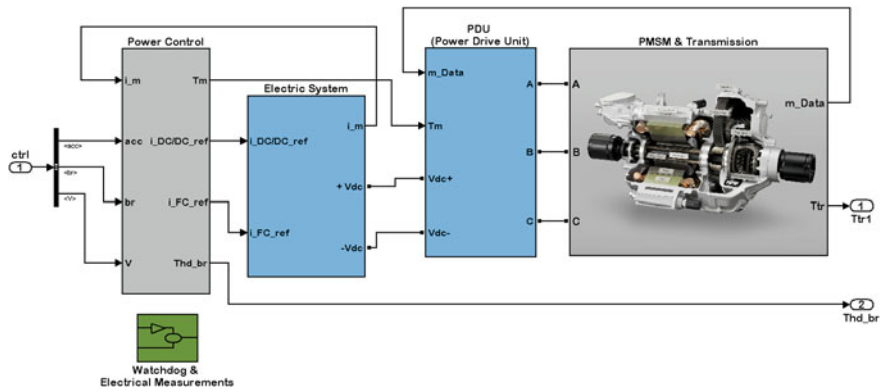


Fig. 4 The electric drive system

The DC/DC Converter contains a Bus Duty Cycle Controller block which controls the Insulated Gate Bipolar Transistor (IGBT) module in the Power Electronics block. The electrical diagram for Power Electronics block is based on a Buck DC/DC converter. In order to speed up the simulation process a mathematical average current model was used for the IGBT Module. The Li-ion battery implemented from SymPowerSystems Library is a generic dynamic model parameterized by a nominal voltage of 288 V and a rated capacity of 13.9 Ah.

The Electric System is integrated into the Electric Drive System which is described below.

## 6 The Electric Drive System

A representation of the Simulink model for the Electric Drive System is presented in Fig. 4.

The Electric Drive System is made up of four main blocks and a safety module:

1. Electric power management block (Power Control);
2. Electric system block (Electric System);
3. Electric motor controller block (PDU—Power Drive Unit);
4. Permanent magnet synchronous motor and Transmission block (PMSM and Transmission);
- 5 Safety and electrical measurements module (Watchdog and Electrical Measurements).

The PDU (Power Drive Unit) is based on modified average value inverter (AC6 block from SymPowerSystems Library). The inverter is comprised of one controlled current source on the DC side and of two controlled current sources and two controlled voltage sources on the AC side. The DC current source allows the representation of the average DC bus current behavior following the next equation:

$$I_{dc} = (P_{out} + P_{losses})/V_{in} \quad (12)$$

with  $P_{out}$  being the output power,  $P_{losses}$  the losses in the power electronic devices, and  $V_{in}$  the DC bus voltage.

On the AC side, the current sources represent the average phase currents fed to the motor. The regulation being fast, the current values are set equal to the current references sent by the current regulator. A small current is injected to compensate for the current drawn by the three-phase load (needed because of the inverter current sources in series with inductive motor).

The model is discrete. Good simulation results have been obtained with a 2  $\mu$ s time step. To simulate a digital controller device, the control system has two different sampling times:

- Speed controller sampling time;
- Vector controller sampling time.

The speed controller sampling time has to be a multiple of the vector controller sampling time. The latter sampling time has to be a multiple of the simulation time step. The average-value inverter allows the use of bigger simulation time steps since it does not generate small time constants (due to the RC snubbers) inherent to the detailed converter. Good simulation results have been obtained for a simulation time step of 75  $\mu$ s. The simulation time step can not be higher than the vector controller time step. Since the rotor flux is supplied by the permanent magnets the stator current direct component is set to zero inside the vector controller block.

The transmission subsystem, which is contained inside the electric motor block, contains a gear ratio of 9.44:1 and a constant efficiency of 96 %.

In order to control the electric motor torque, fuel cell current and DC/DC inverter current a power management was implemented inside a Power Control module.

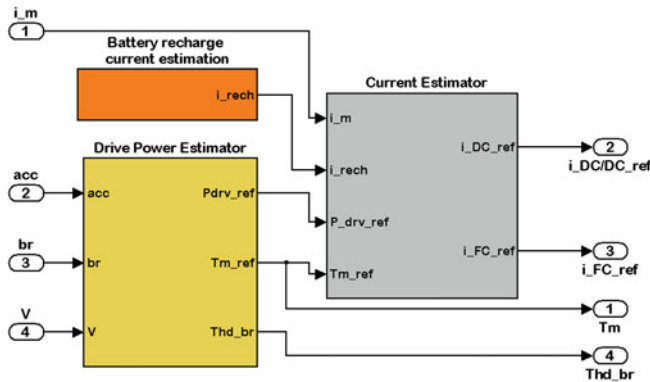


Fig. 5 The power control modules and rate transition blocks

## 7 Power Control Management

Inside the Power Control module are three blocks: Battery recharge current estimation, Drive Power Estimator and Current Estimator. The modules are presented in Fig. 5.

Based on signals from the accelerator pedal position ( $acc$ ), brake pedal position ( $br$ ) and vehicle speed ( $V$ ), the Drive Power Estimator module carries out the following functions:

- Estimates the reference power necessary for traction ( $P_{drv\_ref}$ );
- Estimates the reference motor torque ( $Tm$ );
- Calculates braking torque for the hydraulic braking system ( $Thd\_br$ ).

The Battery recharge current estimation determines the recharge current ( $i_{rech}$ ) according to SOC (battery state of charge). The battery is recharged at a constant current of 15 A when SOC is less than 80 % while the vehicle is stationary or cruising. When regenerative braking is applied the current will be proportional to braking torque, but no higher than 60 A. The estimated traction power is limited between  $-12.5$  and 100 kW, while the estimated motor torque has a lower limit of  $-256$  Nm and an upper limit of 256 Nm. The reference Fuel Cell current estimated is limited between a minimum of 2.7 A and a maximum of 347 A while the DC/DC converter current is saturated between 2.8 and 350 A. The Electric Current Estimator calculates the reference values for the following:

- Fuel Cell current ( $i_{FC\_ref}$ );
- DC/DC converter current ( $i_{DC/DC\_ref}$ ).

The Electric Drive System is part of the Global Model, which is a representation of the vehicle and driver.

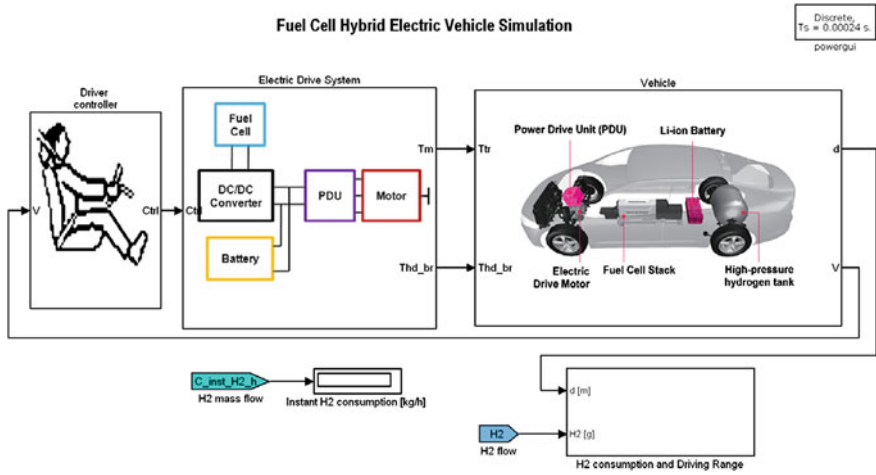


Fig. 6 The global model for the FCHEV

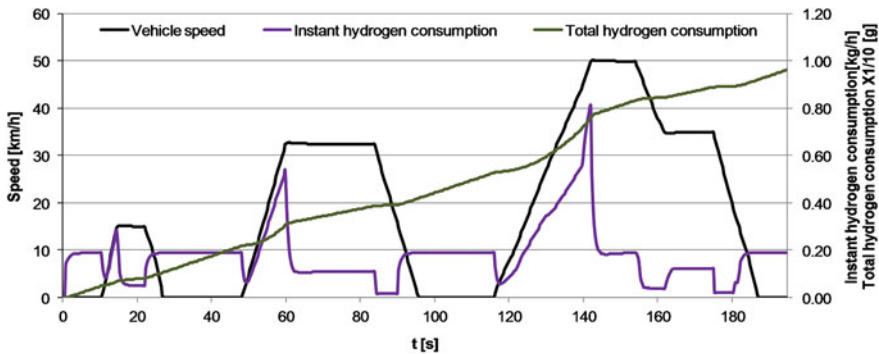


Fig. 7 Hydrogen consumption and vehicle speed during ECE15 cycle

## 8 Global Model

The global model is presented in Fig. 6 and contains the following subsystems:

1. The Driver is based on a PID controller and has the role of maintaining a small difference between real and reference speed;
2. The Electric Drive System is made up of the fuel cell, the Li-ion battery, the DC/DC converter, the inverter and the PMSM (permanent magnet synchronous motor);
3. The Vehicle is based on a longitudinal dynamic model of the automobile;
4. The H<sub>2</sub> consumption and Driving Range estimates the instant hydrogen consumption in relation to distance and the overall range of the vehicle.

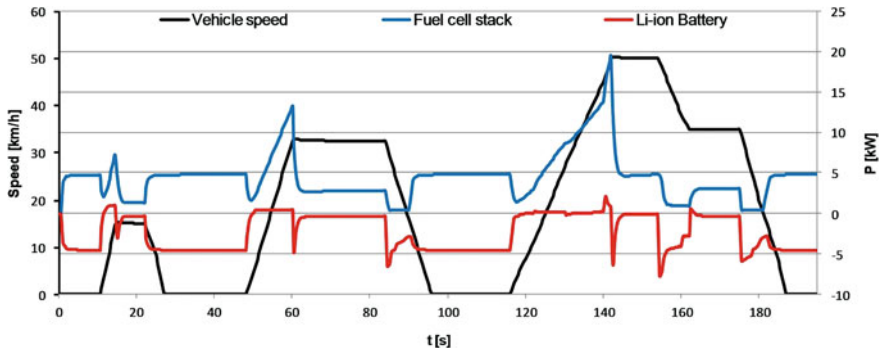


Fig. 8 Vehicle speed and electrical power for fuel cell stack and battery during ECE15 cycle

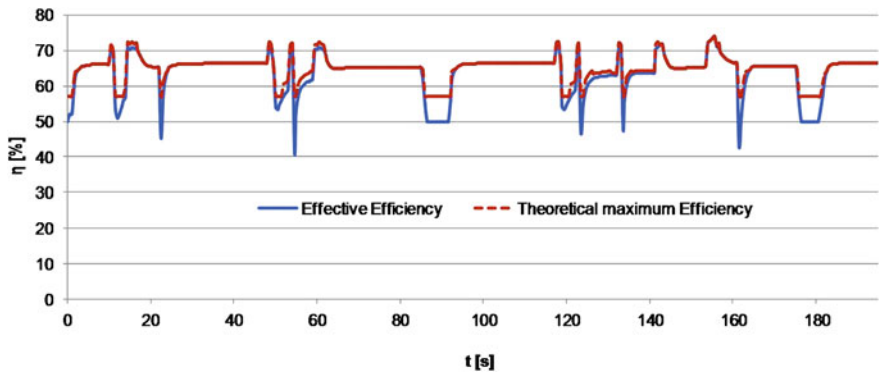


Fig. 9 Fuel cell stack efficiency during ECE15 simulation

The Global Model was used especially for calculating hydrogen consumption in relation to vehicle velocity, measuring electrical power consumption and estimating Fuel Cell efficiency.

## 9 Results

The instantaneous hydrogen consumption, as it can be observed in Fig. 7, rises to a maximum of 0.8 kg/h when accelerating and it drops to a minimum value of 0.05 kg/h while regenerative braking is in use.

The high fuel cell response time is caused by the “charge double layer” phenomenon due to the buildup of charges at electrode/electrolyte interface and the dynamics of external equipments, like regulators, compressor and loads [7].

The surplus of electrical energy goes into the battery, thus maintaining the system in balance. This phenomenon can be observed in Fig. 8, as a high negative



**Table 1** Comparison between simulation and real vehicle performance

Performance	Honda FCX clarity	Simulation	Error [%]
0–65 km/h	4.7 s	5.02 s	6.81
0–80 km/h	6.7 s	6.65 s	–0.75
0–100 km/h	9.3 s	9.45 s	1.61
0–110 km/h	11.5 s	11.16 s	–2.96
0–130 km/h	16.8 s	15.32 s	–8.81
400 m	17.1 s	16.97 s	–0.76
Max speed	160 km/h	159.1 km/h	–0.56
Vehicle range (NEDC)	460 km	446 km	–3.04

current at the battery terminals, while going from positive acceleration to steady speed.

A comparison between effective and maximum theoretical efficiency of the fuel cell, during ECE15 cycle, shows that the fuel cell management could be slightly improved by introducing a gradually current reduction while regenerative braking is applied, so as to avoid sharp current changes. The fuel cell efficiency results can be observed in Fig. 9.

The simulated model shows similar results compared to Honda FCX Clarity data [8], in terms of acceleration, maximum vehicle speed and range, as it is represented in Table 1.

## 10 Conclusions

The mean value obtained for effective efficiency of the fuel cell stack was 63.88 %. This result is very close to the mean maximum theoretical value which could be obtained in case of an ideal control (64.95 %). Therefore, the efficiency of the algorithm implemented for the control of hydrogen and air mass flow was demonstrated. The error concerning the vehicle speed compared with NEDC reference speed, by using the block for acceleration and braking command (Driver- PID Controller), is very small (0.67 %).

For NDEC cycle, if 93 % of fuel tank is used, an estimated hydrogen consumption of 0.832 kg/100 km and a range of 441 km are obtained. However, according to [9], there is a limit for the allowable energy change in the rechargeable energy storage. Because this limit was exceeded a hydrogen consumption correction coefficient was calculated and applied. After this correction the fuel consumption is 0.823 g/100 km (equivalent with a gasoline consumption of 2.905 l/100 km) and the range is 446 km. An error of 3.04 % has resulted when compared to the range stated by Honda for NEDC (460 km) [2].

The calculated tank to wheel efficiency, during the NEDC test procedure, was 57.92 %, which is a reasonable high value for a modern vehicle, compared to ICE

powered vehicles with a tank to wheel efficiency of 20.6 % for a DI gasoline engine and 21.1 % for DI Diesel, as specified in Ref. [10].

## References

1. Froeschle P (2009) Electrification of the drivetrain—evolution or revolution?. In: 8th international CTI symposium & transmission expo
2. Nakajima T (2009) Fuel cells & hydrogen for sustainable transport, Industry Update Meeting, Copenhagen, 30 Nov 2009
3. Boccaletti C, Duni G, Fabbri G, Santini E (2006) Simulation models of fuel cell systems. 11 July 2006
4. Larminie J, Dicks A (2003) Fuel cell systems explained, 2nd edn. Wiley & Sons Ltd., Chichester. ISBN 0-470-84857-X
5. Brinkman N, Wang M, Weber Trudy, Darlington T (2005) Well-to-wheels analysis of advanced fuel/vehicle systems—a north american study of energy use, greenhouse gas emissions, and criteria pollutant emissions. May 2005
6. Mathworks help toolbox—SymPowerSystems
7. Honda Emergency Response Guide—Honda Fuel Cell Vehicle—FCX Clarity. American Honda Motor Co., Inc. Reorder Number Y0804 2008
8. <http://automobiles.honda.com/fcx-clarity/specifications.aspx>
9. ISO 23828:2008(E) (2008) Fuel cell road vehicles—energy consumption measurement—vehicles fuelled with compressed hydrogen
10. Matsunaga M, Fukushima T, Ojima K (2009) Powertrain system of honda FCX clarity fuel cell vehicle. World Electr Veh J 3—ISSN 2032-6653

# Optimal Battery Discharging Strategy for a Range Extended Fuel Cell City Bus

Liangfei Xu, Mingguo Ouyang, Jianqiu Li, Fuyuan Yang and Languang Lu

**Abstract** This paper proposes an optimal energy management strategy for a range extended fuel cell city bus, which is powered by a Proton Exchange Membrane (PEM) fuel cell system and a Li-ion battery system. Targeting at minimizing the daily operating cost, the strategy is deduced based on the dynamic programming (DP) algorithm for a global optimized problem. The strategy is compared with several other strategies in simulating model, e.g. Charge Depleting and Charge Sustaining (CDCS) and two-stage linear blended strategies. The operating cost with the linear blended strategy is the lower than other two-stage linear blended strategies. The operating cost with the CDCS strategy is 1.3 % less than that of the linear blended strategy. The operating cost with the DP strategy is 10 % less than that of the linear blended strategy. The hydrogen cost occupies more than 95 % of the entire operating cost. To minimize the hydrogen consumption is the key to reduce the operating cost. With the DP strategy, the efficiency of fuel cell system is 58.7 %, compared to an average level of 53 % with other strategies. The battery efficiency influent the daily operating cost slightly. In order to apply the optimal strategy into a vehicle, the optimal State of Charge (SOC) trajectory curve is fitted with a nonlinear exponential formula. An iterative algorithm based on this formula is deduced, and can be applied to an embedded digital control unit.

**Keywords** Range extended fuel cell electric vehicle · Battery · Energy management · Dynamic programing · Iterative algorithm

---

F2012-B05-008

---

L. Xu (✉) · M. Ouyang · J. Li · F. Yang · L. Lu  
State Key Lab of Automotive Safety and Energy, Tsinghua University,  
Beijing, 100084, People's Republic of China  
e-mail: wolkeman@gmail.com

## 1 Introduction

During the recent 5 years, great progresses were made in the fuel cell vehicle technologies. Several big international automobile manufactures, e.g. GM, Toyota, Volkswagen, Benz, announced that, the Proton Exchange Membrane (PEM) fuel cell vehicles may be available for the market after the year 2015. Fuel cell vehicles will be no more expensive and fragile, but strong and common in the very near future [1].

However, a PEM fuel cell system can never be as strong and robust as an internal combustion engine (ICE) in recent years. In order to extend the working life time and recover braking energy, a fuel cell system is always hybrid with an energy storage system (ESS), e.g. a Li-ion battery system, or a super capacitor system. Considering different configurations and components parameters, there comes out diverse fuel cell power-trains.

The fuel cell system can serve as the primary power source. It is very common for fuel cell passenger vehicles, where the secondary power source is a small battery system, or a super capacitor. In such a power-train system, the fuel cell provides the average power requirement, and part of the dynamic power requirement. The battery system can be charged from grid, or be kept charge sustaining by the fuel cell system.

The fuel cell system can also serve as a secondary power source. In such a system, a Li-ion battery system is always regarded as the primary power source. The fuel cell system is designed to offer the average power requirement, or part of the average power requirement. Sometimes, a super capacitor is also utilized to provide the very high frequent power source. Such a power-train structure is very common in city buses.

The first kind of fuel cell vehicle is regarded as a traditional fuel cell hybrid vehicle (FCHV), where the battery should be kept charging sustaining during operation. If the battery system of the hybrid power-train can be charged from the grid, it is called as a plug-in FCHV. The third one is always regarded as a range extended fuel cell electric vehicle (RE-FCEV), where the fuel cell system is not for keeping the battery in charge sustaining, and the battery can be charged from the grid.

For such a power-train with two power sources, how to split power between the two so as to minimizing the operating cost becomes a challenging problem. Generally speaking, there is no difference in the power-train structure for the FCHV and the RE-FCEV. However, the electric energy of the battery can be charged from the grid in the RE-FCEV and the plugin FCHV, resulting in a different optimal energy management problem from the serial hybrid system, as shown in Table 1.

For a traditional FCHV, the battery is kept charge sustaining during operation. It is therefore the optimal problem is always defined in one driving cycle. Because the battery can only be charged by the fuel cell system, a cost function based on an energy equivalent model is utilized. For a RE-FCEV or a plugin FCEV, the battery State of Charge (SOC) is always decreases from a high value (90 %) to an end value (10 %). It is therefore the optimal problem is always defined for several

**Table 1** Comparison of optimal energy management problems between RE-FCEV and FCHV

	Traditional FCHV	Plugin FCHV and RE-FCEV
Time horizon	One cycle	Several cycles for one charge
Battery SOC	Charge sustaining function	Decreases from a high value to an end value
Cost		Battery equivalent consumption based on energy
Battery	equivalent consumption based on price	

driving cycles per one charge. And because the battery can be charged from the grid, a cost function based on the price is utilized.

For the RE-FCEV or the plugin FCHV, the essential of the problem is how to control the battery SOC trajectory. Currently there are different control strategies, e.g. Charge Depleting and Charge Sustaining (CDCS) and blended strategies. Dynamic programming is a powerful tool to solve the optimal problem.

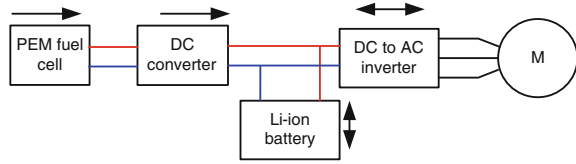
Recently researchers have done plenty of work on the energy management strategy for range extended vehicles. Comparison study among different strategies was carried out. Three energy management strategies were compared by Jeffrey [2]. The CDCS and DP strategy were compared by Rousseau [3]. Phillip B. Sharer studied the blended and CDCS strategies for a pre-known driving cycle. Results show that the blended strategy will lead to relative higher fuel efficiency than that of the CDCS strategy [4]. Researchers from the University of Michigan studied the Stochastic Dynamic Programming (SDP) strategy. Results show that the SDP algorithm can be more practical than DDP strategy [5]. Researchers in GM did some work on the real-time quasi-optimal strategy based on an interface facility [6].

This paper focuses on the optimal energy management strategy for a range extended PEM fuel cell city bus. Section 2 describes the system architecture. Section 3 introduces the optimal strategy based on the dynamic programming algorithm. Section 4 compares the operation costs with different strategies, and analysis the reason for cost reduction. Section 5 deduces the real-time control algorithm based on the DP strategy. Section 6 is the conclusions.

## 2 System Description

The power-train structure of the range extended fuel cell city bus is shown as in Fig. 1. The Li-ion battery serves as the primary power source, and the PEM fuel cell works as the secondary power source. A DC converter is installed to link the fuel cell system, the Li-ion battery and the AC inverter together. The length of the city bus is 12 m, and the unloaded mass is about 15 ton. According to the requirements of public traffic transportation, the maximal vehicle velocity is designed to 80 km h<sup>-1</sup>, and the accelerating from zero to 50 km h<sup>-1</sup> is less than 25 s. The driving distance is more than 250 km.

Fig. 1 Power-train structure



The rated power of the AC inverter for the electric motor is 100 kW, and the peak power can be as high as 180 kW. As the primary power source, a 175 Ah Li-ion battery is selected to fulfill the requirement of driving distance of being more than 200 km. The bus voltage varies between 260 and 395 V. With such a battery system, the peak current of the Li-ion battery is less than 3C, which is normally regarded as in the safe range. A PEM fuel cell system with a rated power of 50 kW is chosen to extend the driving range. An electric air condition is selected to adjust the inner-vehicle air quality.

### 3 Optimal Battery Discharging Strategy

The China Typical City Bus Cycle (CTCBC) is selected as the simulation standard of the testing cycle for the simulation. Its maximal velocity is about 60 km h<sup>-1</sup>. The cycle duration is 1,304 s and the driving distance in every cycle is 5.8 km. According to some statistic results, the daily driving distance of a city bus varies between 150 and 200 km, depending on cities and routes. The target of the optimal problem is to minimize the daily operating cost. It is defined in a time horizon of about 25 cycles, which lasts for 9.3 h and 150 km. It can be mathematically described as follows.

$$J = \text{Min} \Delta t \left( \sum_{k=0}^{N-1} C_{fc,k} + C_{bat,k} \right) \tag{1}$$

$$\text{subject to : } \begin{cases} \text{SOC}_L \leq \text{SOC} \leq \text{SOC}_H \\ V_{\text{Min}} \leq V_{\text{bat}} \leq V_{\text{Max}} \\ 0 \leq P_{\text{dc}} \leq P_{\text{dc,max}} \end{cases} \tag{2}$$

where  $J$  is the minimal operating cost,  $\Delta t$  is the control algorithm cycle,  $C_{fc}$  and  $C_{bat}$  are instantaneous PEM fuel cell and battery cost, respectively,  $V_{bat}$  is battery working voltage,  $V_{\text{min}}$  and  $V_{\text{max}}$  are the minimal and maximal battery voltages,  $P_{dc}$  is the output power of the DC converter. The two cost variables can be noted as follows.

$$\begin{cases} C_{fc} = M_{h2} b_e P_{fc} \\ C_{bat} = M_{ele} P_{bat} (\eta_{\text{dis\_avg}} \eta_{\text{chg\_avg}})^{-\text{sgn}(P_{bat})} \end{cases} \tag{3}$$

where  $M_{h_2}$  and  $M_{ele}$  are prices for hydrogen gas and electric energy in RMB  $\text{kg}^{-1}$  and RMB  $\text{kJ}^{-1}$ , respectively. The parameter  $b_e$  is the fuel cell hydrogen consumption rate in  $\text{kg kJ}^{-1}$ , and  $P_{fc}$  is the fuel cell output power in kW. The parameter  $P_{bat}$  is the battery power in kW, and  $\eta_{dis\_avg}$  and  $\eta_{chg\_avg}$  are average discharging and charging efficiencies, respectively.

The global optimized problem can be solved with dynamic programming (DP). DP is based on the Bellmann's principle of optimality and gives the optimal solution to the problem using an efficient enumeration technique. It is based on backward computation. It is useful as a study tool to understand the potential of an HEV architecture and generate rule-based strategies. However, it cannot be implemented in a real-time controller, because it needs a perfect prediction of future driving cycle. The iteration process of the dynamic programming can be found in [7]. An optimal battery discharging curve can be achieved with the DP algorithm.

## 4 Comparison Between Different Strategies

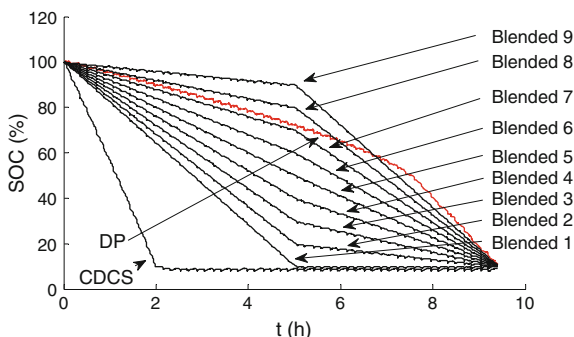
### 4.1 SOC Trajectories

In order to verify the effectiveness of the DP strategy, it is compared with other energy management strategies, e.g. Charge Depleting and Charge Sustaining (CDCS) and Blended strategies. In a CDCS strategy, the vehicle firstly operates in a pure battery driven mode, and then switches into a hybrid driven mode where the battery is kept charge sustaining. In a blended strategy, the vehicle operates in a hybrid driven mode from the very beginning, and the battery SOC decreases during the whole process. Generally speaking, the DP strategy can also be regarded as a blended strategy. However, in this paper, the blended strategy is defined as a two-stage linear SOC discharging strategy. Figure 2 shows the different SOC trajectories with varies energy manage strategies. The battery SOC starts at 100 % and ends at 10 %.

### 4.2 Operating Cost and Energy Flows

Figure 3 illustrates the general energy flow diagram for the PEM fuel cell power-train. The diagram is very effective in describing the efficiency of each component and energy flows among components.  $E_{h_2}$  is the hydrogen energy delivered by the hydrogen gas. It is calculated according to the low heat value (LHV) of hydrogen.  $E_{f_{cc}}$  is the net output energy of the fuel cell engine.  $E_{dc}$  is the output energy of the DC converter.  $E_{aux}$  is the energy consumed by the vehicle auxiliary components, e.g. the air condition and the electric steering system.  $E_{bat}$  is the output energy of the battery.  $E_{mb1}$  is the electric output energy of the electric motor during braking

**Fig. 2** SOC trajectories with different energy management strategies



regenerative process.  $E_{mb2}$  is the mechanical input energy of the electric motor during braking regenerative process.  $E_{md1}$  is the electric input energy of the electric motor during driving process.  $E_{md2}$  is the mechanical output energy of the electric motor during driving process. Parameters  $\eta_{fce}$ ,  $\eta_{dc}$ ,  $\eta_{bat}$ ,  $\eta_{mb}$ ,  $\eta_{md}$  and  $\eta_{recycle}$  are efficiencies for the fuel cell engine, the DC converter, the battery, the electric motor in braking regenerative process, the electric motor in driving process and the recycled efficiency. The recycled efficiency  $\eta_{recycle}$  is defined as the ratio of recycled mechanical energy in the mechanical driven energy for the electric motor.

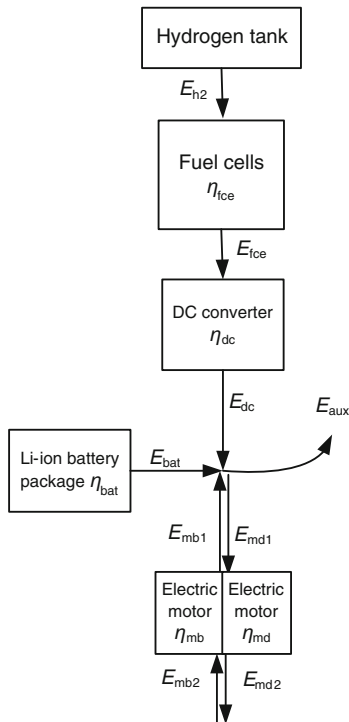
Table 2 shows the simulation results of different energy management strategies proposed in Fig. 3 for the RE-FCEV. The daily operating cost with the DP strategy is the lowest among all the strategies, 498.4 RMB. The two-stage linear blended strategy with lowest operating cost is blended 5, with which the battery SOC decreases linearly from the beginning to the end, also being called as linear blended strategy. The CDCS strategy is less in operating cost than the linear blended (blended 5) strategy, 546.5 RMB and 553.9 RMB, respectively. Compared to the blended 5 strategy (553.9 RMB), the operating cost can be lowered by 1.3 % and 10 % with the CDCS and the DP strategies, respectively.

The driving distance, driving durability, SOC decrement, auxiliary energy consumption, mechanical driving energy and recycled efficiency are almost the same. The vehicle drives for 150 km in 9.4 h. The battery SOC decreases from 100 to 10 %, corresponding to 60 kWh. From the mechanical output port of the electric motor, about 589 MJ energy is consumed, corresponding to 109 kWh/100 km. About 7.5 % of the driving energy is recycled. The vehicle auxiliary energy is about 320 MJ, corresponding to 9.46 kW in average.

The energy flows differ in efficiencies of the fuel cell engine, the DC converter and the battery system. Since the hydrogen energy is more expensive than the electric energy for equivalent energy, the daily operating cost is more sensitive for the fuel cell and DC efficiencies than the battery efficiency. In Table 2, with the DP strategy, the power-train system can operate with the highest fuel cell engine and DC converter efficiencies, 60.6 and 97.8 %, respectively. The battery efficiency with the DP strategy is the lowest among all strategies, 91.3 %.



**Fig. 3** General energy flow diagram of the hybrid power-train



### 5 Real-Time Application of the Optimal Strategy

With the DP strategy, a minimal operating cost can be achieved. However, the DP strategy can't be applied in real-time control unit directly. The optimal SOC trajectory contains key information for the optimized process. It is therefore it can be used as an equivalent optimized strategy. An approximate analytical formula is proposed as follows.

$$SOC(t) = SOC_0 - k_1 t - k_2 \left( e^{t/\tau} - 1 \right) \tag{4}$$

where  $SOC_0$  is the initial SOC value,  $k_1$ ,  $k_2$ ,  $\tau$  are coefficients that need to be determined. These coefficients can be calculated using least square error algorithm. Figure 4 shows the SOC trajectories with DP and approximate formula,  $k_1 = 4.55 \% h^{-1}$ ,  $k_2 = 0.24 \%$ ,  $\tau = 1.76 h$ . The absolutely error can be within 1 % when  $\tau = 1.76 h$ .

An iterative formula can be deduced basing it, shown as follows.

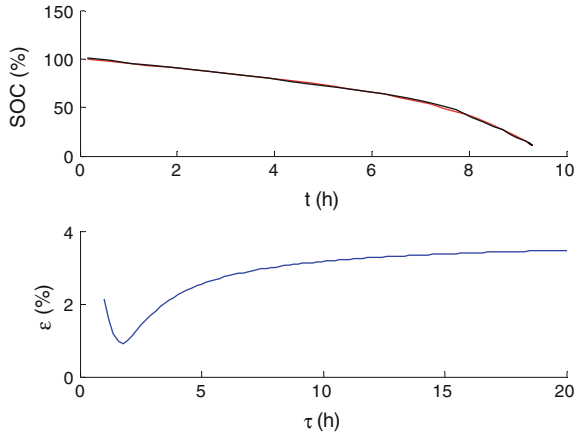
$$SOC = SOC/\tau + k_1 t/\tau - ((SOC_0 + k_2)/\tau + k_1) \tag{5}$$

Formula (5) can be discretized, and be applied into a digital embedded controller. A time clock is required to give the time signal. According to formula (5), a

**Table 2** Simulation results of different energy management strategies for RE-FCEV

Parameters	$\eta_{fice}$	$\eta_{dc}$	$\eta_{ibat}$	$\eta_{la}$	$\eta_{lb}$	$\eta_{recycle}$	$L$	$\Delta SOC$	$T$	$\Delta m_{h2}$	Cost (H2)	Cost (Ele)	Cost (total)
Units	%	%	%	%	%	%	km	%	h	kg	RMB	RMB	RMB
DP	58.69041	97.828	91.267	85.725	82.456	7.405222	149.9	-89.156	9.4	10.85939	483.2	15.2	498.4
CDCS1	53.26499	97.726	92.817	85.721	82.45	7.490648	149.89	-90.896	9.4	11.93797	529.1	17.4	546.5
Blended1	53.20608	94.528	96.125	85.721	82.45	7.483521	149.94	-90.135	9.4	12.28701	546.8	15.2	562
Blended2	53.15773	95.086	96.518	85.721	82.45	7.482632	149.94	-90.049	9.4	12.20099	542.9	15	557.9
Blended3	53.01845	95.73	96.752	85.721	82.45	7.482632	149.94	-89.961	9.4	12.13896	540.1	14.9	555
Blended4	52.76643	96.21	96.884	85.721	82.45	7.482632	149.94	-89.871	9.4	12.13317	539.9	14.8	554.7
Blended5	52.66684	96.528	96.959	85.721	82.45	7.482632	149.94	-89.78	9.4	12.1158	539.1	14.8	553.9
Blended6	52.65027	96.409	96.989	85.721	82.45	7.482632	149.94	-89.688	9.4	12.13565	540	14.7	554.7
Blended7	52.87617	96.024	96.977	85.721	82.45	7.482632	149.94	-89.593	9.4	12.13482	540	14.7	554.7
Blended8	53.073	95.42	96.924	85.721	82.45	7.482632	149.94	-89.483	9.4	12.17287	541.7	14.7	556.4
Blended9	53.15387	94.801	96.827	85.721	82.45	7.482632	149.94	-89.321	9.4	12.244	544.8	14.9	559.7
Parameters	$E_{dc}$	$E_{fce}$	$E_{fc}$	$E_{h2}$	$E_{bat}$	$E_{md1}$	$E_{mb1}$	$E_{md2}$	$E_{mb2}$	$E_{bat}$	$E_{aux}$		
Units	MJ	MJ	MJ	MJ	MJ	MJ	MJ	MJ	MJ	kWh	MJ	MJ	MJ
DP	753.8	770.54	795.02	1312.9	219.92	685.86	-35.9	587.95	-43.539	61.08889	323.76	323.76	323.76
CDCS1	751.27	768.75	789.23	1443.3	218.72	686.04	-36.32	588.08	-44.051	60.75556	320.27	320.27	320.27
Blended1	747.14	790.39	819.52	1485.5	216.16	686.69	-36.32	588.64	-44.051	60.04444	312.93	312.93	312.93
Blended2	745.6	784.13	812.81	1475.1	216.97	686.78	-36.32	588.71	-44.051	60.26944	312.11	312.11	312.11
Blended3	744.88	778.11	806.81	1467.6	217.19	686.78	-36.32	588.71	-44.051	60.33056	311.61	311.61	311.61
Blended4	744.68	774.02	803.41	1466.9	217.1	686.78	-36.32	588.71	-44.051	60.30556	311.32	311.32	311.32
Blended5	744.66	771.45	801.07	1464.8	216.95	686.78	-36.32	588.71	-44.051	60.26389	311.15	311.15	311.15
Blended6	744.74	772.48	802.04	1467.2	216.81	686.78	-36.32	588.71	-44.051	60.225	311.09	311.09	311.09
Blended7	744.92	775.76	804.88	1467.1	216.65	686.78	-36.32	588.71	-44.051	60.18056	311.11	311.11	311.11
Blended8	745.3	781.08	809.69	1471.7	216.38	686.78	-36.32	588.71	-44.051	60.10556	311.22	311.22	311.22
Blended9	745.91	786.82	815.85	1480.3	215.96	686.78	-36.32	588.71	-44.051	59.98889	311.41	311.41	311.41

**Fig. 4** SOC trajectories with DP and approximate formula



target SOC can be calculated. By designing a PI feedback control algorithm, the actual SOC will follow the target SOC, so as to realize a quasi-optimal energy management strategy.

## 6 Conclusions

An optimal battery discharging strategy is proposed based on DP algorithm for a range extended fuel cell city bus targeting at minimizing the daily operating cost. Simulation for the DP, the CDCS and the two-stage linear blended strategies are carried out.

- (1) The operating cost with the linear blended strategy is the lower than other two-stage linear blended strategies.
- (2) The operating cost with the CDCS strategy is 1.3 % less than that of the linear blended strategy.
- (3) The operating cost with the DP strategy is 10 % less than that of the linear blended strategy.
- (4) The hydrogen cost occupies more than 95 % of the entire operating cost. To minimize the hydrogen consumption is the key to reduce the operating cost. With the DP strategy, the efficiency of fuel cell system is 58.7 %, compared to around 53 % of being with other strategies.
- (5) The battery efficiency influent the daily operating cost slightly. This is because the average battery efficiency is very high, more than 95 %, and the price of the electric energy is relative cheap. There is not much potential to reduce entire operating cost by increasing the battery efficiency.
- (6) The DP strategy can be applied in an embedded digital controller by designing a feedback control algorithm and an iterative formula to calculate the target SOC value.

**Acknowledgment** Supported by the NSFC (National Natural Science Foundation) of China under the contract of No. 61004075, the MOST (Ministry of Science and Technology) of China under the contract of No. 2010DFA72760 and No. 2011AA11A269, and the Tsinghua University Initiative Scientific Research Program (Grand No. 2010THZ08) is greatly acknowledged.

## References

1. Baolian Y, Ming H (2011) Solutions for the durability of fuel cells in vehicle applications [J]. *J Automot Saf Energy (Chinese)* 2(2):91–100
2. Jeffrey G, Tony M (2007) Energy management strategies for plug-in hybrid electric vehicles [C]. SAE paper 2007-540-40970
3. Rousseau A, Pagerit S, Gao D (2007) Plug-in hybrid electric vehicle control strategy parameter optimization [C/CD]. U.S 23rd international electric vehicle symposium (EVS23)
4. Phil S, Aymeric R, Dominik K, Sylvain P (2008) Plug-in hybrid electric vehicle control strategy: comparison between EV and charge-depleting options [C]. SAE paper 2008-08PFL-554
5. Lin CC, Peng H, Grizzle JW (2004) A stochastic control strategy for hybrid electric vehicles [C]. American control conference, Boston, vol 5, pp 4710–4715
6. Cory D, Abboud E (2011) Comprehensive overview of human interface for an extended range electric vehicle [C]. SAE paper 2011-01-1023
7. Xu L, Yang F, Li J, Ouyang M, Hua J (2012) Real time optimal energy management strategy targeting at minimizing daily operation cost for a plug-in fuel cell city bus. *Int J Hydrogen Energy* (accepted)

**Part VI**  
**Charging Infrastructure and Smart Grid**  
**Technology**

# EV Charging Through Wireless Power Transfer: Analysis of Efficiency Optimization and Technology Trends

Heri Rakouth, John Absmeier, Andrew Brown Jr., In-Soo Suh,  
Miller John M., Randy Sumner and Richard Henderson

**Abstract** This paper presents the technology trends for wireless power transfer (WPT) for electric vehicles (EV), and analyzes the factors affecting its power transfer efficiency (PTE) and describes the techniques currently used for its optimization. The review of technology trends encompasses both stationary and moving vehicle charging systems. The study of the stationary vehicle charging technology is based on developments at WiTricity and Oak Ridge National Lab (ORNL). The moving vehicle charging technology is primarily described through the results achieved by the Korea Advanced Institute of Science and Technology (KAIST). The factors affecting the PTE are determined through the analysis of the equivalent circuit of magnetic resonant coupling. The air gap between both transmitting and receiving coils along with the magnetic field distribution and the relative impedance mismatch between the related circuits are the primary factors affecting WPT efficiency. Currently the industry is looking at an air gap of 20 cm or below. To control the magnetic field distribution, KAIST has recently developed the Shaped Magnetic Field In Resonance (SMFIR) technology that uses optimized shaped ferrite material to provide a low reluctance path or maximum exposure of the magnetic field to the resonant coils. The PTE can be further

---

F2012-B06-001

---

H. Rakouth (✉) · A. Brown Jr. · R. Sumner · R. Henderson  
Delphi Automotive Systems, Michigan, U.S.A  
e-mail: heri.rakouth@delphi.com

J. Absmeier  
Delphi Automotive Systems, Shanghai, China

I.-S. Suh  
Korea Advanced Institute of Science and Technology, Daejeon, Republic of Korea

M. John M.  
Oak Ridge National Lab, Oak Ridge, U.S.A

improved by means of impedance matching. As a result, Delphi's current implementation of WiTricity's technology exhibits WPT efficiency above 90 % for stationary charging with power capacity of 3.3 kW, while KAIST has demonstrated a maximum efficiency of 83 % for moving vehicle with its On-Line Vehicle (OLEV) project with the power capacity of 100 kW.

**Keywords** Resonant · Magnetic · Wireless charging · Impedance matching

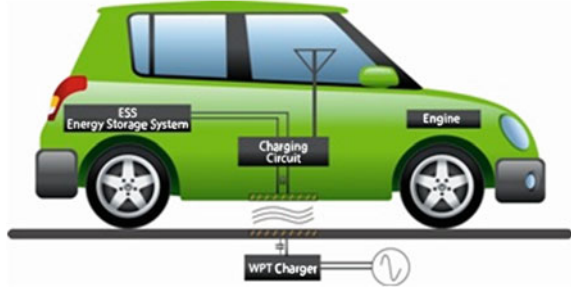
## 1 Introduction

The growth of vehicle electrification is fostering the development of efficient and operation-friendly charging systems. However, the battery cost and range (BCR) equation remains the primary impediment to mass adoption of EV. Currently all EV and Hybrid Electric Vehicles (HEV) are commercialized with on-board conductive charging systems. Though this charging technology clearly meets the efficiency requirements with power transfer ratio virtually equal to 100 %, the need for handling the charging cable and accessories makes it mildly operation-friendly, and has inherent safety concerns. Moreover, it fails to provide a viable solution to the BCR equation without requiring tremendous progress in battery technology.

Over the past decade, research institutions such as Massachusetts Institute of Technology (MIT) [1] and Oakridge National Lab (ORNL) [2, 3], have demonstrated the feasibility of wireless charging by means of magnetic resonant coupling through laboratory demonstrations and scientific publications. This novel technology is commonly known as wireless power transfer (WPT). WiTricity is working to commercialize a WPT-based deployment kit for EVs [4]. Delphi is working with several OEMs on pilot programs aimed at an automotive grade implementation of the WiTricity solution [5]. These activities support stationary vehicle charging (SVC), however, they are paving the way for a battery-independent solution to the BCR equation through dynamic vehicle charging (DVC). Since 2009, KAIST has worked to develop DVC technology [6], and introduced the concept of On-line Electric Vehicle (OLEV) in 2010, which has selected by Time magazine as one the 50 Best Inventions of 2010 under the name of "Road-Embedded Rechargers" [7].

With the appropriate infrastructure (e.g. charging coil buried in the roadbed) enabling much shorter but more repetitive charging, DCV-equipped EV will have today's range with a fraction of the battery capacity. This paper highlights key insights for understanding the technical and business challenges and opportunities pertaining to wireless charging.

**Fig. 1** Stationary vehicle charging: basic principle



## 2 Wireless Power Transfer

### 2.1 Basic Principle

Figure 1 displays a simplified representation of WPT-based stationary vehicle charging.

For simplification purposes, we focus on the equivalent circuit of the entire charging system as sketched in Fig. 2 that involves the equivalent circuit of a transformer.  $U_s$  is the voltage delivered by a power voltage source operating at the angular frequency  $\omega$ .  $C_1$  and  $L_{11}$  are the transmitter (or primary) coupling capacitor and inductance respectively, whereas  $C_2$  and  $L_{22}$  are the receiver (or secondary) parallel capacitor and inductance respectively. The primary resistive portion is the series combination of the WPT charger source resistance  $r_g$  and the overall ohm loss  $r_s$ . The secondary resistive circuit comprises the load  $R_L$  along with the overall ohm loss  $r_2$ .  $M$  is the mutual inductance of the charging system equivalent transformer.

### 2.2 Resonant Coupling

For further analysis, let's represent the series combination of  $C_1$  and  $L_{11}$  by the equivalent impedance  $Z_1$ , and the series combination of  $C_2$  and  $L_{22}$  by  $Z_2$ , as well as the mutual inductance by  $M$ . For additional simplification of the analytical process, we make the assumption that both primary and secondary impedances are identical, that is:  $C_1 = C_2 = C$  and  $L_{11} = L_{22} = L$ . Thus,

$$Z_1 = Z_2 = j \left( L\omega - \frac{1}{C\omega} \right) \tag{1}$$

As a result, both primary and secondary resonators have the same natural resonance angular frequency



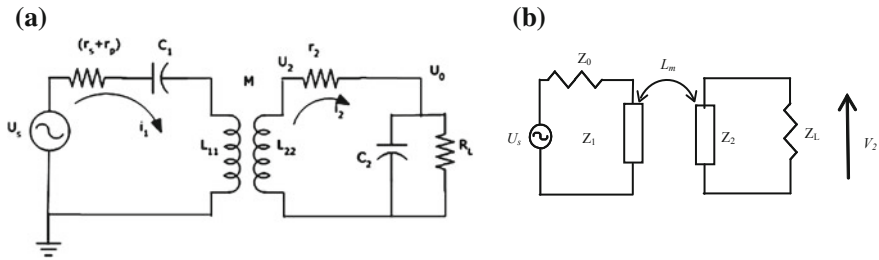


**Fig. 2** Charging system equivalent circuit: **(a)** with system components; **(b)** with equivalent impedances

$$\omega_0 = \frac{1}{\sqrt{LC}} \tag{2}$$

The application of Kirchhoff’s voltage law around the primary and secondary loops leads to the equation of the charging output voltage  $V_2$  that can be maximized at two resonant angular frequencies  $\omega_m$ (known as magnetic resonant frequency below) and  $\omega_e$ (known as electric resonant angular frequency above) respectively equated by:

$$\omega_m = \frac{1}{\sqrt{(L_m + L)C}} = \frac{\omega_0}{\sqrt{1 + k}} \tag{3}$$

$$\omega_e = \frac{1}{\sqrt{(L - L_m)C}} = \frac{\omega_0}{\sqrt{1 - k}} \tag{4}$$

Where,  $k$  is the magnetic coupling factor equated by

$$k = \frac{L_m}{L} = \frac{L_m}{\sqrt{L_{11}L_{22}}} \tag{5}$$

The terms below and above are explained by the double inequality

$$\omega_m < \omega_0 < \omega_e \tag{6}$$

### 2.3 System Efficiency

The determination of the system efficiency requires the identification of the value of the magnetic coupling factor  $k$  as well that of the coupling capacitor  $C$ , and the inductance  $L$  derived from the geometry of the transmitting and receiving coils in factoring the relative permeability of the linkage medium.



**Fig. 3** Delphi WPT charging system left: residential charging controller. *Middle*: floor-based source resonator. *Right*: source/capture resonator pair

### 3 Automotive and Transportation Applications

#### 3.1 Stationary Vehicle Charging Systems

##### 3.1.1 Delphi

Delphi has been collaborating with WiTricity since 2010. WiTricity commercializes the wireless power technology invented at MIT [1]. WiTricity has over 270 patents and patent applications worldwide that include highly resonant non-radiative magnetic field coupling (HRNRM) as well as energy transfer system improvements. Delphi has developed a HRNRM-based WPT stationary charging system that is capable of delivering 3.3 kW (Level 2) with up to 20 cm ground clearance that is highly efficient up to 90 % from AC main to the vehicle battery and is well tolerant to parking misalignment ( $\pm 20$  cm in vehicle side to side axis). Delphi is able to further reduce capture coil size to improve vehicle fitment, with a moderate diminution of lateral tolerance that can be managed with simple driver assistance mechanisms commonly used in the industry. Using a High-Q Magnetic Resonant system Delphi is able to optimize vehicle components size and mass reducing the secondary coil that is mounted on the vehicle to approximately 30 cm  $\times$  30 cm  $\times$  3 cm and weighs less than 5 kg (Fig. 3).

##### 3.1.2 Korea Advanced Institute of Science and Technology

KAIST developed an application model to apply WPT to stationary charging.

During the Phase 1 development period, 2010–2011, the static charging system achieved 80 % PTE with a power pick-up capacity of 30 kW, equipped on a micro bus as shown in Fig. 4. The system incorporates an electricity billing system through an interactive touch-screen.

The Phase 2 development of an SUV resulted in achievement of 93 % PTE with a ground height of 6 cm and a power capacity of 25 kW per pick-up unit.



**Fig. 4** KAIST stationary WPT charging system KAIST phase 1 phase 2

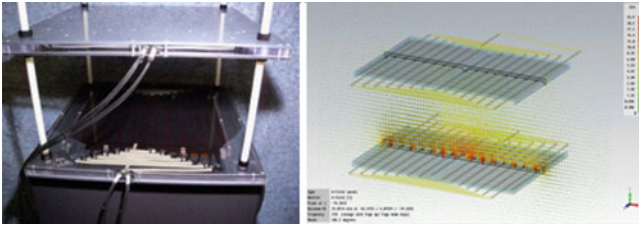


**Fig. 5** Distributed winding coupling coil set and FEA analysis

### 3.1.3 Oakridge National Lab

ORNL has developed stationary WPT charging of a PEV at SAE Level 2 power of 6.6 kW using coupling coils fabricated with five strands of 14 AWG Litz cable in parallel and a soft ferrite back plane design. Figure 5 shows the coupling coils in a laboratory test fixture having adjustable standoffs for the secondary coil. Magnetic finite element analysis was employed to analyse the coupling field, side and backplane emissions levels, and coupling coefficient,  $k$ .

Coupling coil efficiency is shown at the single damped resonant peak at approximately 23 kHz and efficiency of 96 % when S-P is tuned to approximately 22 kHz. In these tests the high frequency (HF) power inverter is operated at low rail voltage resulting in an additional reduction in DC-DC efficiency due to the low voltage operation ( $\sim 70$  V) of 600 V IGBTs.

## 3.2 Dynamic Vehicle Charging System

### 3.2.1 Korea Advanced Institute of Science and Technology

An OLEV system is comprised of the power supply system as a part of a paved road installation and the electric vehicle equipped with power pick-up modules. On a closed travel route, the powered road distance is limited to approximately 20 % of the total travel distance, and the battery supplies the driving energy to the motor of the electric vehicle across the non-powered or standard road surface. The

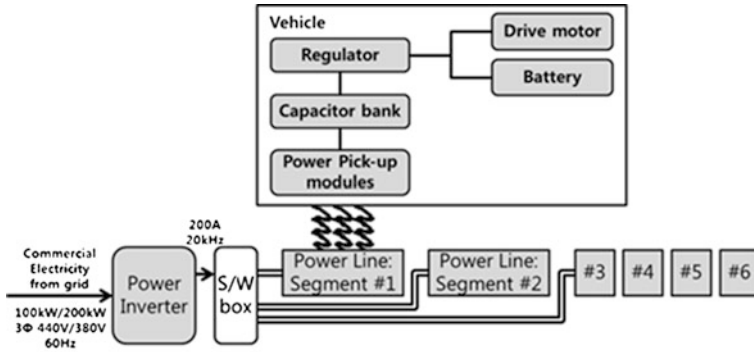


Fig. 6 Complete OLEV system architecture: vehicle and power supply system

battery’s energy storage capacity is reduced to 1/5th the size of a standard EV in most cases. As a result of this, the powered road length, battery size, and pick-up power capacity for a given motor size become design variables for optimization dependent on the application rather than design constraints as the case for a standard EV. The communication between the road installation and the power supply controller is performed through magnetic transmission. In addition, the powered track can be an add-onto an established road system, or included as part of a new road construction. The schematic architecture of an OLEV system is shown in Fig. 6.

OLEV power supply system or powered road is composed of a set of power tracks throughout the vehicle travel road. A powered track is composed of a set of segments, which can have different lengths, controlled by a set of power inverters through a switch box. An example of a powered track layout consisting of six segments is shown in Fig. 8. Between each segment, there can be enough distance to accommodate road crossings such as bridges or pedestrian crossings. In Seoul Grand Park, where the first prototype in public demonstration is installed, the first segment is 2.5 m long while the other five segments are 25 m each. The distance between each segment varies from 3 m to 100 m. In addition, the distance from the power track has no limitation in view of installations as long as the inverter is placed properly. In optimizing the design of the power supply and the pick-up system, the PTE has reached the maximum value of 83 % with an air gap of 20 cm a misalignment tolerance of ±20 cm leading to half of the transmitted power (Fig. 7).

### 3.2.2 Oakridge National Lab

ORNL successfully demonstrated dynamic WPT charging of an electric vehicle using embedded primary coils in June 2012. In this application, specially designed coils were developed to be embedded into existing roadway pads containing each a pair of coils. ORNL’s early in-motion work was based on large area rectangular geometry ( $a = 1 \text{ m} \times b = 0.8 \text{ m}$ ) copper tube coils. [8].

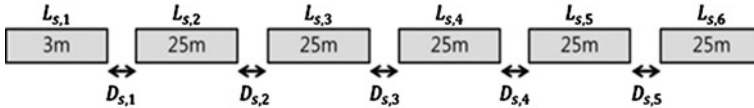


Fig. 7 Example of a powered track layout

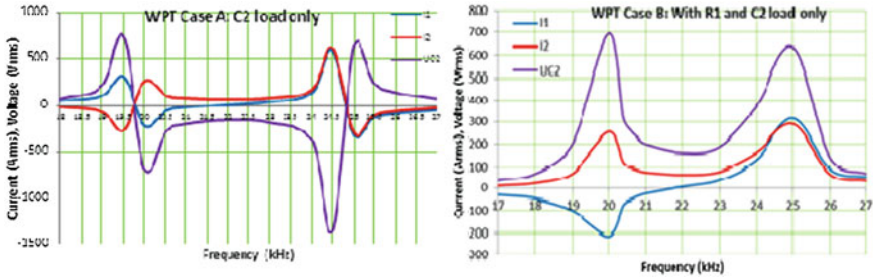


Fig. 8 Resonance behaviour vs. primary and secondary load when  $f_0 \sim 22$  kHz

### 4 Power Transfer Optimization

There is considerable literature on WPT that spans coupling coil design [9–11], inverter design including soft switching and very high frequency operation [12, 13], and system control and optimization [14–16]. As discussed in Sect. 2.2, the WPT charging system exhibits two resonances (see Fig. 9) whose responses are affected by the primary resistance  $R_I = r_s + r_g$  and the secondary load  $R_L$  (refer to Fig. 2a) whose value affects the primary and secondary quality factor  $Q_1$  and  $Q_2$ .

### 5 Alignment Tolerance

For non-optimized resonance control, alignment of the vehicle mounted secondary coil with a floor or roadway primary coil is critical to optimal PTE and minimization of emissions. For example, 50 % aligned coils will have high fringe fields and also much higher than desired fields in the secondary back plane. As a result, in non-controlled quality factors charging mode, the alignment tolerance can be as stringent  $\pm 25$  mm in both x-axis and y-axis, across the vehicles longitudinal and lateral axes respectively.

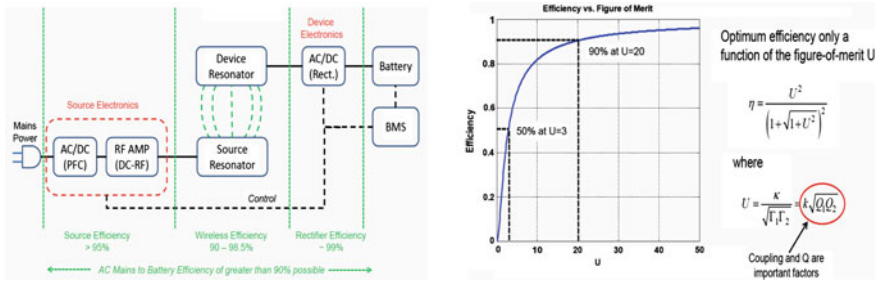


Fig. 9 Left: efficiency distribution. Right: wireless efficiency  $\eta$  and figure of merit  $U$

## 6 End to End Optimization

The left hand side of Fig. 9 provides the breakdown for the power transfer efficiency [17]. While the conducted linkages (i.e. source electronics and device electronics) offer a combined efficiency greater than 94 %, the total transfer efficiency is dictated by the performance of the wireless coupling. Under HRNRCM (see Sect. 3.1.1), the wireless efficiency  $\eta$  is a function of the figure of merit  $U$  [18] that can be controlled through impedance matching and power factor control. This leads to a much higher misalignment tolerance (i.e.  $\pm 20$  cm in vehicle side to side axis) and a wireless efficiency of 90 % or higher.

### 6.1 Shaped Magnetic Field in Resonance

#### 6.1.1 SMFIR<sup>®</sup> Technology and Wireless Charging System [19]

KAIST has developed SMFIR<sup>®</sup> technology enables to charge wirelessly at stationary and/or in driving motion efficiently. The pick-up device is a T-shaped iron core with turned coil sets in the middle. The induced electromagnetic field shape can be controlled by the layout of the ferrite core in the power supply and the pick-up sides, air gap, core-to-core distance and the tuned coils in the pick-up.

## 7 Industry Trends

### 7.1 Practical Challenges

Given potential liability issues and the relatively low penetration of EV/HEV cars, the development of the WPT charging technology is highly dependent upon OEMs and on-going standardization works. Each OEM is in a different phase of adoption

coping with issues such as location, form factor, operating frequency, and user's safety. The multiplicity of operating frequencies poses the problem of charging station interoperability.

The different agents of the WPT charging value chain (see [Sect. 5.3.3](#)) in various cooperation pools to resolve the above challenges.

## ***7.2 Operating Frequency Criteria***

The magnetic resonance technology is applicable across the kHz–MHz frequency range. The choice of frequency depends on factors such as device size, component performance, EMC/EMI concerns. The general trend is: the higher the frequency, the higher the quality factor, the higher the efficiency for a smaller device size. As discussed above, frequency-agnostic solution needs to be investigated for ensuring interoperability.

## ***7.3 Commercialization Readiness***

### **7.3.1 Standardization**

There are four critical areas where standardization is required: (1) Transmitter configuration and form factor; (2) Receiver location in the vehicle; (3) Communication protocol between on and off-board electronics; and, (4) Operating frequency. With these four interfaces standardized, any vehicle from any manufacturer in a given region will be able to wirelessly refuel their electrified vehicle's battery via stationary or dynamic charging installations.

The following standardization committees are working for addressing these areas: SAE J2954, IEC 61980-1 Electric vehicle inductive charging systems, ISO/IEC 15118 Communication Interface between the vehicle and the grid, IEC 61851 Communication protocol between off-board inductive charger and electric vehicle.

### **7.3.2 Regulation**

The American National Standards Institute, ANSI, is active into support WPT deployment, along with IEC, SAE, IEEE and UL and others. Relevant existing standards include SAE J1772 for alternating current charge coupler (being modified to include dc fast charging), and IEEE P2030.1 covering electric sourced transportation infrastructure.

Regulation is needed to address safety, EMF, EMC/EMI, and grid interfacing issues.

In the U.S. the National Institute for Science and Technology (NIST) has been charged with leading the coordination of smart grid standards activities. Underwriters laboratories (UL) has already standardized EVSE (UL2594, UL2251), protection systems (UL 2231-1, -2), smart meters (UL 2735) and charging equipment for wireless chargers (UL 2750).

WPT systems under commercialization globally are being designed to limit electromagnetic field exposure to below limits set by the International Commission on Non-ionizing Radiation Protection (ICNIRP-2010). The new guideline limits peak exposure to 27  $\mu\text{T}$  over the range 3 kHz to 100 kHz and special averaging to within a maximum of 6.25  $\mu\text{T}$ . A more comprehensive definition of EMF exposure must wait until standards setting organizations—now evaluating WPT—define the measurement points and special averaging technique.

### 7.3.3 Business models

Wireless charging technology is in its infancy stage. Multiple competitors across the world are positioning to capitalize on its growth with opportunities at varying levels of commercialization. There are prospects ranging from universities to start-up companies with little or no automotive experience to Tier-1 automotive suppliers who license the technology and commercialize it for the automotive environment. Delphi's business model is based on upstream and downstream partnership involving game changing technology providers along with forward thinking OEMs that understand that WPT is uniquely positioned for alleviating the concerns regarding the BCR equation through stationary charging in the medium run, and for effectively solving it in the long run through the ultimate adoption of the technology of dynamic vehicle charging. The following value chain (see Fig. 10) can be used to derive different business models that can be either OEM or aftermarket driven.

## 8 Conclusion

This paper is the result of a team effort led by engineers, researchers, and innovation leaders at Delphi, WiTricity, KAIST, and ORNL. Each of these organizations is pioneering wireless power transfer for passenger electrified vehicles and/or ground mass transportation in the context of stationary or dynamic vehicle systems. Their respective experience has been described through past and on-going projects such as Delphi and WiTricity cooperation for automotive applications, KAIST's OLEV implementation, and ORNL's fundamental research projects both in stationary and dynamic charging techniques.

A review of the related technology trends has highlighted key factors affecting the charging efficiency such as alignment tolerance, magnetic field coupling, impedance mismatch and operating frequency. The basic principles of two related



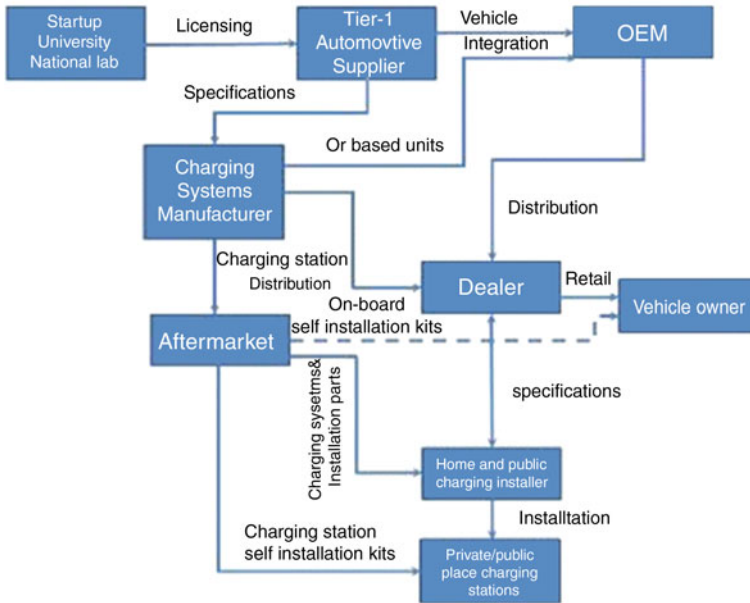


**Fig. 10** Wireless charging value chain

proprietary solutions were discussed. The end to end optimization is reliant on strongly-coupled resonance for mid-range wireless non-radiative energy transfer whereby misalignment and increased distance between transmitting and receiving coils can be compensated in controlling the figure-of-merit through impedance matching and the enhancement of both the source resonator and device resonator quality factors respectively at the resonance frequency. Another alternative is the shaped magnetic field in resonance that takes advantage of the magnetic field channelling by means of shaped low reluctance magnetic material conveniently placed at both the primary and secondary coils. Both of these solutions exhibit wireless efficiency 90 % or higher for stationary charging and 83 % or lower for moving vehicle charging with a 20 cm or less air-gap.

The above efficiency optimization techniques have proven very promising. However, the wireless charging market is yet to be developed because of many challenges such as interoperability limitation due to operating frequency selectivity, billing portability, and electromagnetic field emissions concerns. The technical challenges are being resolved through global standardization works such as SAE J2954, IEC 61980-1, ISO/IEC 15118, ICNIRP-2010, IEC 61851 that address transmitter configuration and form factor, receiver location in the vehicle, operating frequency, and communication interface between the vehicle and the grid, non-ionizing radiation protection, as well as communication protocol between off-board charger and vehicle.

While mass commercialization is dependent upon the customer adoption of electrified vehicles and the completion of the above standardization works and the ensuing regulations, various partnerships between research organizations (e.g. KAIST, ORNL), leading wireless power transfer technology providers (e.g. WiTricity), tier-one suppliers such as Delphi along leading automobile manufacturers are paving the way to a new industry. WPT is uniquely positioned for alleviating the concerns regarding the BCR equation through stationary charging in the medium run, and for effectively solving it in the long run through the ultimate adoption of the technology of dynamic vehicle charging.

## References

1. André Kurs et al (2007) Wireless power transfer via strongly coupled magnetic resonances. [www.scienceexpress.org/7June2007/Page2/10.1126/science.1143254](http://www.scienceexpress.org/7June2007/Page2/10.1126/science.1143254)
2. Miller JM (2011) Wireless Power Transmission In: ORNL power electronics industry symposium, ORNL conference center, 22 July 2011
3. Miller JM (2012) Wireless power charging fundamentals and challenges, SAE2012 hybrid vehicle technologies symposium. Town & Country Resort & Conference Center, San Diego, pp 21–22
4. WiT-3300 Development Kit. [http://www.witricity.com/pdfs/WiT-3300\\_data\\_sheet.pdf](http://www.witricity.com/pdfs/WiT-3300_data_sheet.pdf)
5. Delphi Press Release, November 1, 2010. <http://green.autoblog.com/2010/11/01/delphi-partners-with-witricity-on-automated-wireless-charging-sy/>
6. OLEV Brochure. <http://eews.kaist.ac.kr/test/MHOLEV/D.%20OLEV%20Brochure.pdf>
7. Time magazine (2010) The 50 best inventions of 2010, 22 Nov 2010. [http://www.time.com/time/specials/packages/article/0,28804,2029497\\_2030622\\_2029703,00.html](http://www.time.com/time/specials/packages/article/0,28804,2029497_2030622_2029703,00.html)
8. Miller JM, Omer Onar (2012) ORNL's in-motion WPT system. In: conference on electric roads and vehicles, CERV2012, Newport Resort and Hotel, Park City, 16–17 Feb 2012
9. Grant A. Covic, Michael L. G. Kissin, Dariusz Kacprzak, Niels Clausen, Hao Hao (2011) A bipolar primary pad topology for EV stationary charging and highway power by inductive coupling. In: IEEE energy conversion congress & exposition, ECCE2011, Hyatt Regency Hotel, Phoenix, 17–22 Sept 2011, pp 1832–1838
10. Mickel Budhia, Grant A. Covic, John T. Boys, Chang-Yu Huang (2011) Development and evaluation of a single sided flux couplers for contactless electric vehicle charging. In: IEEE energy conversion congress & exposition, ECCE2011, Hyatt Regency Hotel, Phoenix, 17–22 Sept 2011, pp 614–621
11. Budhia Mickel, Covic Grant A, Boys John T (2011) Design and optimization of circular magnetic structures for lumped inductive power transfer systems. IEEE Trans Power Electron 26(11):3096–3101
12. Seung-Hwan Lee, Robert D. Lorenz (2011) A design methodology for multi-kW, large airgap, MHz frequency, wireless power transfer systems. In: IEEE 3rd energy conversion congress & exposition ECCE2011, Hyatt-Regency Hotel, Phoenix, 17–20 Sept 2011
13. Pickelsimer Michael, Tolbert Leon, Ozpineci Burak, Miller JM (2012) Simulation of an electric vehicle class wireless power transfer system as viewed from the power grid. In: IEEE international electric vehicle conference, IEVC2012. CU-ICAR, Greenville, pp 4–8
14. Takehiro Imura, Hiroyuki Okabe, Yoichi Hori (2009) Basic experimental study on helical antennas of wireless power transfer for electric vehicles by using magnetic resonant couplings. In: IEEE vehicle power and propulsion conference, VPPC2009, Fairlane Conference Center, Dearborn, 7–10 Sept 2009, pp 936–940

15. Wu HH, Gilchrist A, Sealy K, Israelsen P, Muhs J (2011) A review on Inductive charging of electric vehicles. In: IEEE 2011 international electric machines and drives conference, IEMDC2011, Niagara Falls, NY, 15–18 May 2011, pp 866–871
16. Miller JM, Clifford P White, Omer C. Onar, Phillip M. Ryan (2012) Grid side regulation of wireless power charging of plug-in electric vehicles. In: IEEE energy conversion congress & exposition, ECCE2012, Raleigh Convention Center, Raleigh, NC, 15–20 Sept 2012 [submitted for publication]
17. Morris Kesler (2012) Wireless charging of electric vehicles using highly-coupled magnetic resonance. WiTricity Presentation at the Haus der Technik Technical Conference and Vehicle Exhibition, Electric & Electronic Systems in Hybrid and Electric Vehicles and Electrical Energy Management, Miesback near Munich, Germany, 23–24 April 2012
18. Aristeidis Karalis et al (2008) Efficient wireless non-radiative mid-range energy transfer. *Ann Phys* 323:34–48
19. Suh IS (2011) Application of shaped magnetic field in resonance (SMFIR) technology to future urban transportation, CIRP design conference

**Part VII**  
**Demonstration of Electric Vehicles in**  
**Cities**

# Development and Performance Evaluation of an Electric Mini Bus Equipped with an Inductive Charging System

Thomas Pontefract, Kimiyoshi Kobayashi, Yuto Miyasaka, Kento Tanaka, Yushi Kamiya, Yasuhiro Daisho and Shunsuke Takahashi

**Abstract** The limited range, high cost and long charging time of electric vehicles continue to stand in the way of their widespread adoption. In response to this, our research group has created the “Waseda Electric mini Bus (WEB)” series of vehicles based on a short range, frequent charging concept that minimises the weight and cost of batteries compared to other electric vehicles. This paper reports on the design, construction and performance evaluation of the new “Waseda advanced Electric mini Bus 3 (WEB-3)”, which is larger than previous vehicles and utilises an improved inductive power supply (IPS) for non-contact rapid charging. A diesel bus was converted to an EV, and the engine, flywheel and clutch were removed, reducing the vehicle’s rotating weight by 80 %. A new inductive charging system was designed and fabricated, allowing non-contact rapid charging from a transmission coil in the road surface over a longer air gap of 140 mm, at 92 % efficiency. The finished WEB-3 was tested on public roads in Honjo and Kumagaya cities, Saitama prefecture, Japan. An effective reduction in CO<sub>2</sub> emissions of 60 % over the original diesel bus was achieved.

---

F2012-B07-002

---

T. Pontefract (✉) · K. Kobayashi · Y. Miyasaka · K. Tanaka · Y. Kamiya · Y. Daisho  
Waseda University, Tokyo, Japan  
e-mail: tspontefract@asagi.waseda.jp

Y. Kamiya  
e-mail: kamiya@waseda.jp

S. Takahashi  
Showa Aircraft Industry Co. Ltd, Tokyo, Japan

**Keywords** Electric bus · Inductive charging system · Lithium-ion battery · Short-range · Rapid charging

## 1 Introduction

In recent years, the automobile industry has begun to take a more proactive approach to environmental issues, in particular addressing the problem of climate change by reducing CO<sub>2</sub> emissions. One way to achieve this is by a shift to electric vehicles, but unsatisfactory range, slow charging and high costs have thus far prevented their widespread adoption.

With this in mind, our research group has designed, built and trialled vehicles based on a short range, frequent charging concept with the aim of creating a community bus with exceptional environmental performance [1]. This paper presents the results of performance testing of the latest vehicle to come out of this research, the Waseda Electric Mini Bus 3 (WEB-3), which has a greater passenger capacity than earlier models (25, compared to 13 in the previous model).

## 2 The WEB-3 Vehicle

As with previous WEB vehicles, the WEB-3 features an inductive power supply system [2] to allow the rapid charging necessary for the short range, frequent charging model to be practical. By reducing the range of the vehicle, the battery load is significantly reduced and reductions in vehicle cost and weight are made possible. Although the shorter range makes more charging stops necessary, the use of a wireless rapid charging system aims to make charging faster, safer and more convenient than would be possible with a conventional plug-in system.

To minimise costs, the WEB series are converted from conventional ICE vehicles already on the market. The WEB-3 is based on the “Poncho” mini-bus from Hino Motors. Comparative specifications are shown in Table 1.

Some important improvements over the base diesel bus are as follows:

### 2.1 *Reduction of Rotating Weight*

The clutch and flywheel, rendered unnecessary by the electric conversion, were removed, realising an 80 % reduction in rotating weight. This results in improved performance, particularly under acceleration, and this effect is particularly pronounced in a large vehicle, whose unmodified rotating weight is much higher than a conventional passenger car.

**Table 1** Specifications of the Base Vehicle and WEB-3

		Base vehicle	WEB-3
Capacity		31 persons	25 persons
Weight	Net	5730 kg	6430 kg
	Gross	7415 kg	7805 kg
Power plant performance	Type	Diesel engine	PMSM motor
	Manufacturer	HinoMotors	UQM technologies
	Max. output	132 kW@2800 rpm	145 kW @2200–2800 rpm
	Max. torque	490 Nm	400Nm @0–2200 rpm
Battery	Type	–	Mn–Li-ion
	Manufacturer	–	GS-YUASA
	Max. output	–	241 kW
	Capacity	–	44 kWh
	Weight	–	756 kg
IPS	Weight/dimensions (vehicle side)	–	60 kg/120 × 120 mm
	Max. power transmission	–	30 kW
	Mechanical clearance	–	110 mm
	Coil to coil air-gap	–	140 mm

## 2.2 Long Air-Gap Inductive Power Supply

Earlier WEB models have utilised inductive power supplies, but the air gap between the transmitting and receiving coils was limited, meaning that the ground unit had to be raised from the road surface. This presented an obstacle to vehicles and was susceptible to accidental damage. The latest iteration, however, achieves power transfer at 92 % efficiency over an air gap of 140 mm. Combined with the Poncho's kneeling function, this allows the bus to charge efficiently even when the transmitting coil is fully embedded in the ground. Figure 1 shows the previous system, with the concrete housing for the transmission coil protruding significantly from the road. Figure 2 shows the new system, embedded in the ground.

## 3 Comparative Performance Testing of WEB-3 and Base Diesel Bus

To quantify the improvement in environmental performance due to the electric conversion, the WEB-3 was tested alongside the unmodified Poncho bus on public roads in Saitama prefecture, Japan.

**Fig. 1** Previous model (WEB-1A) and charger



**Fig. 2** WEB-3 and new charging system





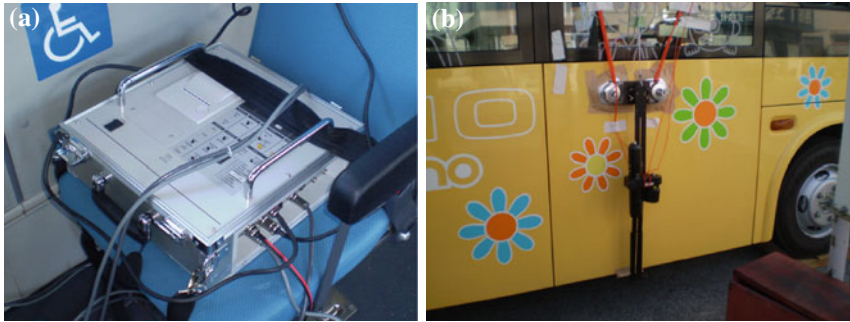


Fig. 3 Speed measuring equipment a LC-5200 data logger b LC1100 optical speedometer

Fig. 4 Honjo course



### 3.1 Testing Apparatus and Method

The WEB-3 is equipped with a data logger that automatically gathers data from the ECU, including battery and inverter current and voltage, motor speed and vehicle speed, which is used to calculate energy consumption and other performance data. The diesel bus does not have this capability, so instead an optical speedometer (Ono Sokki LC-1100) and data logger (Ono Sokki LC-5200), shown in Fig. 3, were used to monitor vehicle speed. Fuel consumption was measured by filling the fuel tank at the beginning of the test, and measuring the amount of fuel needed to restore the same level at the end of the test.

### 3.2 Test Conditions

Two separate tests were performed, one in the city of Kumagaya, and one in the city of Honjo, in which both buses were driven on identical routes at similar speeds, making the same stops. The Honjo test course, shown in Fig. 4, connects



Fig. 5 Kumagaya course

Table 2 Test Conditions

		Diesel bus	WEB-3
Occupants (incl. driver)		3	3
Weight	Net	5730 kg	6430 kg
	Gross	5895 kg	6595 kg
HVAC		OFF	OFF

Honjo railway station with the Waseda University Honjo campus, a return trip of 12.5 km. The Kumagaya course, shown in Fig. 5, is a 5.0 km loop around the centre of the city. To accurately reflect the effect of the increased weight of the electric version of the bus, the tests were carried out with the same number of people aboard. The conditions for both tests are shown in Table 2.

### 3.3 Results and Discussion

The vehicle speed pattern for the Honjo test is shown in Fig. 6, and for the Kumagaya test in Fig. 7. The average vehicle speeds were 17 km/h for the Honjo test, and 15 km/h for the Kumagaya test. HVAC systems were switched off throughout.

Fuel/electricity consumption for each vehicle was measured, and from this, effective CO<sub>2</sub> emissions rates were calculated using the following methods:

Diesel bus:

$$\epsilon = \frac{(e_{WTT} + e_{TTW})}{C}$$

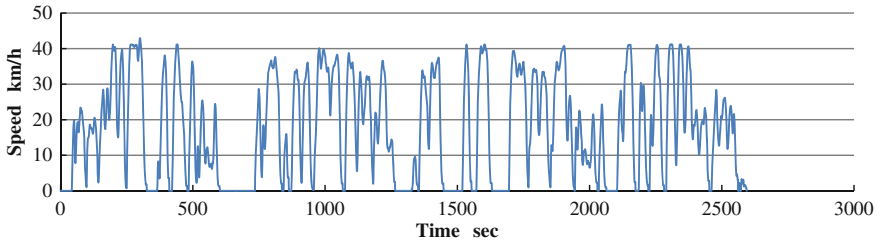


Fig. 6 Speed pattern for Honjo test

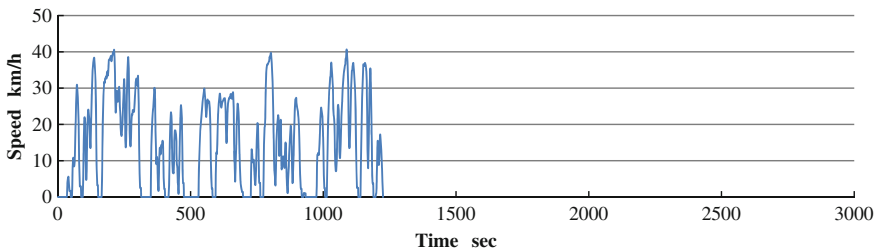


Fig. 7 Speed pattern for Kumagaya test

Table 3 Honjo test results

	Diesel	WEB-3	Improvement (%)
Energy consumption (kWh)	(26.7)	8.39	69
Fuel consumption (L)	2.65	(0.825)	
Mileage (km/kWh)	(0.464)	1.49	–
Mileage (km/L)	4.68	(15.15)	
CO <sub>2</sub> emissions (kg/km)	0.606	0.248	59

Where

$\epsilon$ : CO<sub>2</sub> emissions rate [kg/km]

$e_{WTT}$ : Well-to-tank CO<sub>2</sub> emissions factor [0.19 kg/L [3]]

$e_{TTW}$ : Tank-to-wheel CO<sub>2</sub> emissions factor [2.64 kg/L [4]]

$C$ : Fuel consumption [km/L]

Electric bus:

$$\epsilon = \frac{e_{gen}}{E \cdot \eta_{IPS} \cdot \eta_{batt}}$$

Where

$\epsilon$ : CO<sub>2</sub> emissions rate [kg/km]

$e_{gen}$ : Electrical generation CO<sub>2</sub> emissions factor [0.324 kg/kWh [5]]

$E$ : Energy consumption [km/kWh]

**Table 4** Kumagaya test results

	Diesel	WEB-3	Improvement (%)
Energy consumption (kWh)	(10.0)	3.76	62
Fuel consumption (L)	0.994	(0.372)	
Mileage (km/kWh)	(0.501)	1.34	–
Mileage (km/L)	5.05	(13.57)	
CO <sub>2</sub> emissions (kg/km)	0.562	0.272	52

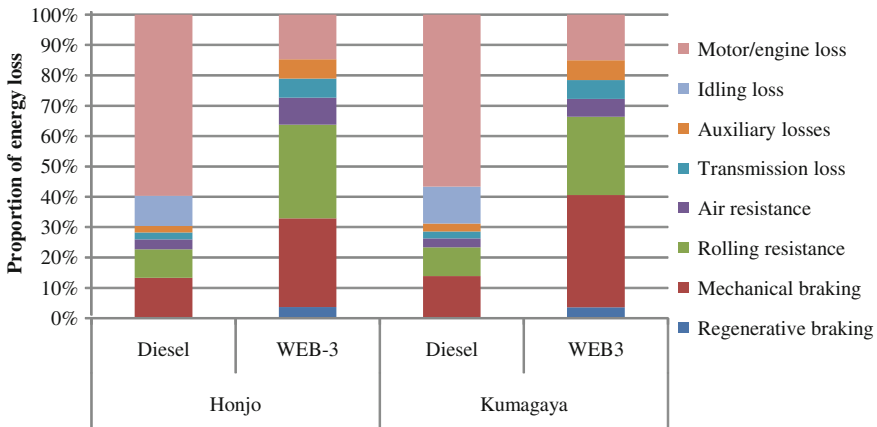


**Fig. 8** Breakdown of energy losses (proportional) from simulation

$\eta_{IPS}$ : IPS efficiency [92 %]

$\eta_{batt}$ : Battery charging efficiency [96.5 %]

The recorded energy and fuel consumption vales, and the CO<sub>2</sub> emissions rates calculated from them, are shown in Table 3 for the Honjo test and Table 4 for the Kumagaya test.

In both tests, improvements in tank-to-wheel energy consumption of over 60 % were attained. Due to well-to-tank losses, this translates to a smaller, but nonetheless significant improvement of over 50 % in effective CO<sub>2</sub> emissions.

To understand in more detail the reasons for this increase in efficiency, numerical simulations of the test runs were carried out using MATLAB/Simulink to calculate the breakdown of tank-to-wheel energy losses in the vehicles. The calculated energy losses for each test are shown as a percentage of total energy consumption in Fig. 8 and as absolute values in Fig. 9. In the case of the diesel bus, approximately 70 % of the energy released from the fuel is lost through the engine under power and idling. By contrast, only around 15 % of the WEB-3’s battery energy is lost through motor losses. As the WEB-3 shares its transmission, tyres and body with the original diesel bus, the transmission, rolling resistance and air resistance losses are unchanged.

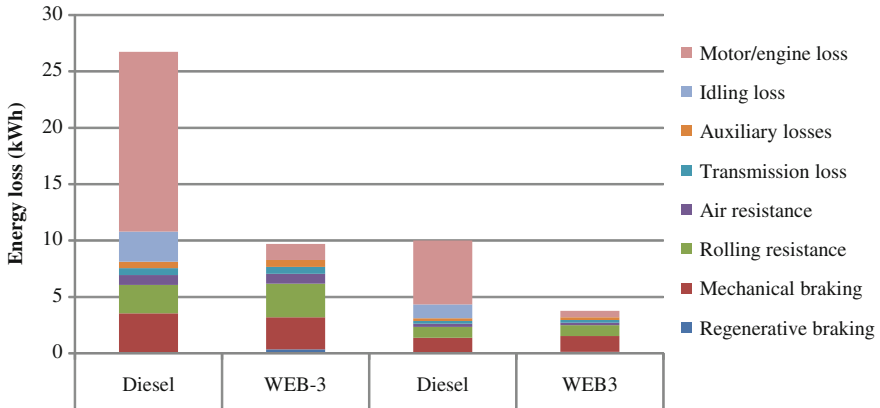


Fig. 9 Breakdown of energy losses (absolute) from simulation

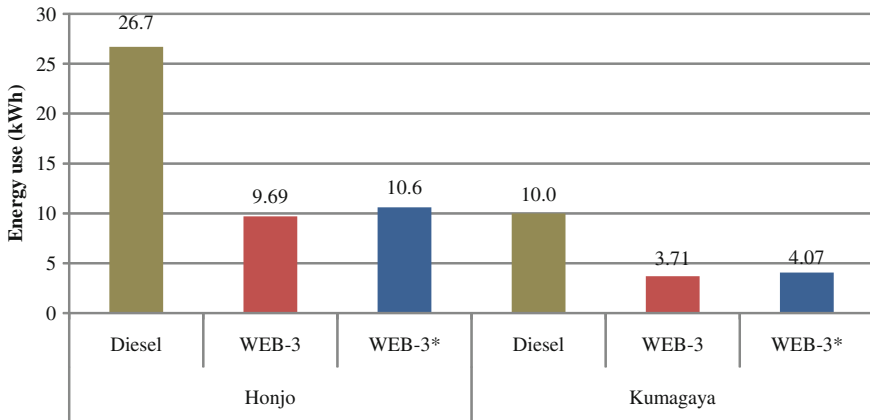


Fig. 10 Simulated tank-to-wheel energy use (absolute)

From this breakdown, we can see that the two largest energy sinks in the WEB-3 system are rolling resistance and mechanical braking. Rolling resistance can be reduced by reducing the weight of the vehicle, and although kinetic energy must be lost to braking whenever the vehicle slows, the proportion of energy which is recovered and returned to the batteries by regenerative braking can be increased. Realising improvements in these areas must be a priority for future development to improve efficiency further.

One major improvement that the WEB-3 makes over the diesel bus is the large reduction in rotating weight and the accompanying improvement in efficiency. To investigate the extent of this improvement, the simulation was run again, this time with a version of the WEB-3 that retained the original bus' larger rotating weight.

The results of this analysis, with the heavier WEB-3 setup shown as “WEB-3\*”, are shown in Fig. 10. An improvement in energy efficiency of nearly 10 % due to the rotating weight reduction was calculated, and a similar improvement in CO<sub>2</sub> emissions can be assumed.

## 4 Conclusions

The design, construction and testing of the new (WEB-3) have been examined, and the following conclusions can be drawn.

### 4.1 Design and Construction

The WEB-3 takes the short range, rapid charging concept of earlier WEB buses and applies it to a larger vehicle, with reduced rotating weight and improved inductive charging performance. By removing the base vehicle’s clutch and fly-wheel, rotating weight was cut by around 80 %, and by optimising IPS design, efficient power transfer over a 140 mm air gap was achieved and the charger’s transmitting coil could be fully embedded in the ground.

### 4.2 WEB-3 Performance Evaluation

In on-road performance testing in Saitama, Japan, WEB-3’s effective CO<sub>2</sub> emissions rate was more than 50 % lower than the diesel bus on which it was based. Additionally, the reduction in rotating weight alone was calculated to have reduced energy consumption by around 10 %.

## References

1. TakakiOgiro, Kimihiko Sato, Kimiyoshi Kobayashi et al (2010).Development and performance evaluation of an advanced electric micro-bus transportation system, 4<sup>th</sup> report— investigation of performance improvements due to introduction of Li-ion battery and inductive charging system. Soc Automot Eng Japan, Proceedings No. 52–10, 252:5–8 (Japanese)
2. Kimiyoshi Kobayashi, Yushi Kamiya (2009) Development and performance evaluation of an inductive charging system for electric vehicles. In: Proceedings of the JMAG conference 2009 transformer session, pp18/1–18/10 (Japanese)
3. Ministry of Economy Trade and Industry Manufacturing Industries Bureau. Heat generation and CO<sub>2</sub> emissions. <http://www.meti.go.jp/committee/materials/downloadfiles/g41116b12j.pdf> (Japanese)

4. Toyota Motor Corporation (2004), Mizuho Information and Research Institute, Well-to-wheel emissions values of transportation fuels (Japanese)
5. Tokyo Electric Power Company (2009). Environmental action report. <http://www.tepco.co.jp/eco/report/glb/02-j.html> (Japanese)

# The Study of Re-construction Method of EV Business Model Based on Value Chain Analysis

Qiang Ye and Hewu Wang

**Abstract** Due to the difference on powertrain configuration and energy supply, there must be new business models from that of CVs. Moreover, as the change of internal and external conditions, EV business models will also do some adjustment. In this paper, firstly, the traditional auto industry and business model of China is analysed to see what the value chain of CV is like. Secondly, as the technical and organizational innovation of electric mobility happens, what changes will happen to the EV industry is discussed. Thirdly, the concept of re-construction is introduced to illustrate the transformation of EV business model. There are two types of methodology used. One is the value chain analysis, which was developed and popularized in 1985 by Michael Potter, the professor of Harvard Business School. In this paper, the value chain analysis is extended to the EV industry chain to understand the generation of margin in business models. The other is re-construction method, which is put forward originally to illustrate the mechanism of transformation of EV business model from systematic angle. The results of this paper concentrate on the following areas, one is that the main internal reason of the transformation of EV business model is the change of industry value chain, the second is that the re-construction of EV business model is the outcome of the adjustment to technical and organizational innovation, and the third is that by re-construction the business models achieve the innovation, which plays the positive role in promoting EVs. Lack of effective quantitative tools, we only discuss the re-construction of value chain and business model by the systematic framework, so the comparison of margins between new business models and old business models

---

F2012-B07-003

---

Q. Ye (✉) · H. Wang

State Key Laboratory of Automotive Safety and Energy, Tsinghua University, Beijing, China

e-mail: yeqiang@tsinghua.edu.cn



after re-construction cannot be done precisely. The innovation of this paper is as follows, one is introducing the value chain analysis to the research of EV business model; another is setting up the concept of re-construction of EV business model. In this paper, the existed value chain method is developed to analyse the internal reasons of the transformation of EV business model, the re-construction concept is projected to construct the new business models systematically. At the end of paper, one example of demonstration city is used to explain the re-construction method of EV business model. The main inadequacy of this paper is the lack of quantitative analysis, which may be the direction for improvement in the future.

**Keywords** Electric vehicle · Business model · Value chain · Re-construction · EV demonstration

## 1 Introduction

In the normal sense, the business model describes what value the company can provide the customers, and by achieving these value what sustainable elements of company's internal structure, partners network and relationship capital would be needed [1]. As for electric vehicles, there must be new business models other than CVs due to the difference on powertrain configuration, energy supply and etc. EV business model may be considered as a systematic solution, which including how to design and manufacture the cars meeting the market demand, and how to cut down the high cost of initial purchase and make convenient the later usage of EV, with the objective of getting break-even point or at least expected future earnings for Third-Party Operator (TPOs) and consumers. The value-added role of EV, such as V2G and V2H [2] still stuck in the concept, far away from application.

Value chain methodology [3] had been popularized since 1985 by Michael Potter, the professor of Harvard Business School. According to his theory, at least one value chain consisting of design, production, market, distribution and other value-creating activities, divided into primary activities and support activities, exist implicitly in most of enterprises (see Fig. 1), of which competitive advantage reflected in the difference of value chain. By upstream and downstream extension, enterprise value chain may transform to industry value chain.

The relationship between business model and value chain can be concluded into interdependence and interaction. Attached to the industry chain, business model comes into being based on value chain, with the inner force to chase margin. Also, the transformation of business model is the external performance of value chain, which be pushed forward changing in turn. Magretta [4] combined the innovation of business model with value chain in the theory that new business models are likely to promote the existing value chain innovation on two kinds of basic activities, one is manufacturing and the other is marketing.

**Table 1** Possible changes of value chain of EV industry

Value chain	Material	R&D	Parts	Aggregation	Distribution	Service
Vehicle OEMs		<input type="checkbox"/>	<input checked="" type="checkbox"/>	<input checked="" type="checkbox"/>	<input type="checkbox"/>	<input type="checkbox"/>
Parts OEMs	<input type="checkbox"/>	<input type="checkbox"/>	<input checked="" type="checkbox"/>		<input type="checkbox"/>	<input type="checkbox"/>
Power Suppliers		<input type="checkbox"/>	<input type="checkbox"/>	<input type="checkbox"/>	<input type="checkbox"/>	<input checked="" type="checkbox"/>
TPO			<input type="checkbox"/>	<input type="checkbox"/>	<input type="checkbox"/>	<input checked="" type="checkbox"/>
Finance Institute	<input type="checkbox"/>	<input type="checkbox"/>	<input type="checkbox"/>	<input type="checkbox"/>	<input type="checkbox"/>	<input checked="" type="checkbox"/>

Current value sectors   
  Possible value-added sectors in the future



**Fig. 1** Porter's value chain

**Fig. 2** The logic and process of analysis in this paper

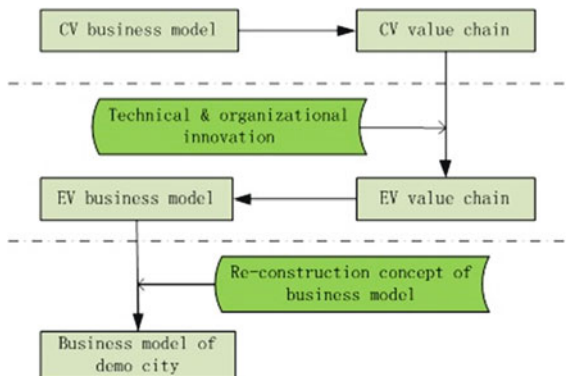
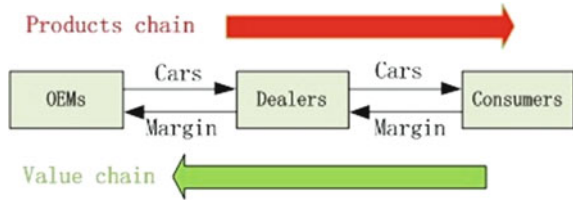


**Fig. 3** Typical business model of CV



The research mentality of this paper is as Fig. 2. Firstly, analyzing the traditional auto industry and business model of China to see what the value chain of CV is like. Secondly, discussing as the technical and organizational innovation of electric mobility happens, what changes will happen to the auto industry, especial the value chain of EV industry. Thirdly, introducing the concept of re-construction of business model to illustrate how to response the change of value chain. Finally, one example of demonstration city is used to explain the re-construction method of business model (Fig. 3).

## 2 Value Chain of Auto Industry

### 2.1 CV Business Model

The following figure shows a typical business model of CV, by which OEMs sell cars to consumers through the channel of auto dealers. After cars move from the OEMs to the consumers, margin transfers in the opposite direction. So the products chain and the value chain take shape along the business model.

### 2.2 Value Chain of CV Industry

The value chain of Chinese manufacture industry was described in the report of Srail & Shi [5], which divide the value chain of manufacture industry into several stages, such as R&D, Design, supply management, production, etc. Similar with manufacture industry, the value chain of auto industry also can be seen as composed of six stages, e.g. material industry, R&D, parts supply, car assembly, car distribution, and after-sales service, as Fig. 4. Parts supply and car assembly are still the core areas, but the value chain has begun to extend upstream to the research and preparation of new materials, and downstream to car distribution and after-sales service, all of which constitute the following diagram of a value chain that satisfying the characteristics of smiling curve, with profit relatively low at the middle of the curve and higher at the both ends.

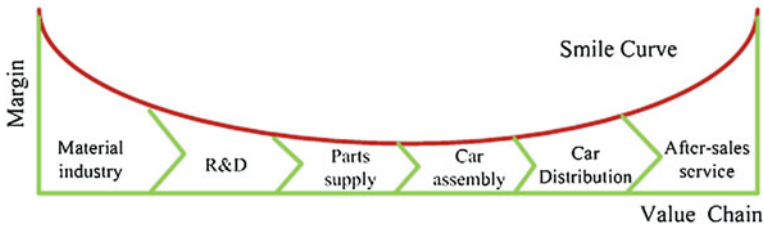


Fig. 4 Industry chain of auto industry

### 3 Value Chain of EV Industry

#### 3.1 Margin Variation of EV Industry

Margin is the core factor of value chain, whose change is the root of the movement of whole value chain. There, cost-benefit curve is used for illustrating how the margin varies in EV industry. There are three curves in Fig. 5, Line I, the red one, is the manufacture cost curve, Line II, the green one, is the manufacture margin curve, and Line III, the blue one, is the service margin curve. The cross point of Line I and Line II, point P, is the break-even point of EV OEMs, which indicates that after point P, OEMs begin to gain the margin. However, as more and more new participants come into the industry and share the benefit, the upward trend of average margin will be slowed down and finally exceeded by Line III at Q point, which indicates that the average margin of EV service providers exceed that of manufacturers and since then the focus of value chain will shift to the areas of service.

Now, the development stage of EV industry of China is still prior to the point P, with the barriers of especially high costs and inconvenient infrastructures. Despite of government subsidies, the specific new business models are also needed to help to cut down the EV possession costs.

#### 3.2 Possible Changes of Value Chain

With the gravity center of EV industry value chain changing, the margin space for participants has been expanded from the core business to more potential value-added business, which will promote the formation of new business models.

To most Chinese enterprises, just because the rare earth materials and precious metals for manufacturing power cells and permanent magnet motors are very scarce and expensive, and the capability of research and design is very important but in fact considerably weak, all of these will generate a huge profit. So, the vehicle OEMs and the parts OEMs of the manufacturing sector, which originally at the middle of value chain, have begun to extend their value-added business to the sectors of R&D, material industry and service. Moreover, power suppliers, TPOs

**Fig. 5** The cost-benefit curve of EV industry

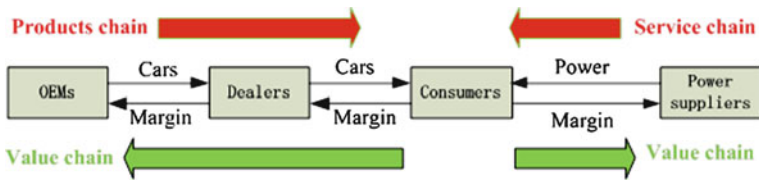
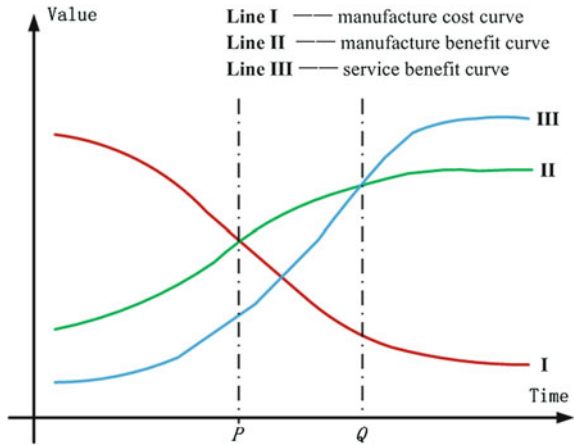


**Fig. 6** Typical EV business model

and finance institutions, which originally at the end of value chain, also have sufficient strength to extend their value-added business upstream in order to form the chain of monopolistic profit.

## 4 The Concept of Business Model Re-construction

The transformation of the value chain is just the base of the so called re-construction of business model, which may be the adjustment or repairment of original model, or even break the original model to create a new one.

### 4.1 Model

The following figure is the framework of a typical EV business model, consists of OEMs, dealers, consumers and power suppliers. With the consumers as the center, the products chain runs through the front end, but the service chain runs through the rear end, and the value chain extends to the both ends.

So, EV business model can be defined as a system consists of the members, the connections between members, and the streams flowing in the system, like the following formula:

$$\Omega = \{M, \vec{C}, \vec{S}\} \quad (1)$$

Members  $M$ , the collections of groups of the same attributes with different roles, such as OEMs, consumers, power suppliers, and etc.

Connections  $\vec{C}$ , a set of vectors standing for the relationships between members, the characteristics of connections will be defined in commercial contracts, e.g. the connections of consumers and dealers is based on the sales contract or lease contract.

Streams  $\vec{S}$ , the circulation of various substances in system, made difference not only at the direction but also at the size, e.g. among these the most important circulations are the products flow and cash flow, which constitute the products chain and value chain after continuously converging and branching.

## 4.2 Re-construction

The inner reasons of re-construction of business model are considered to be the technical innovation and organizational innovation. By technical innovation new products emerge and bring more profit margins. Then organization of business model will bound to innovate to fit the new technology, and the new mechanism will be set consequently.

According to the Eq. (1), the re-construction of business model consists of the following forms:

Organization re-construction, with the boundary extended, the new members participate in the collections, among which some members would have multiple identity.

Connection re-construction, as new members join, the new connections need to be set, or some original connections between old members may be adjusted.

Take the following Fig. 7 as the example. As we have seen, there are four sub-collections, such as aggregation, distribution, end-users and service, which are expanded from the four members in Fig. 6. Besides the nude EV and the battery, the production of vehicle motor and electric attachment also involves in aggregation. In vehicle distribution and after-sales service, the third-party operators will be needed for professional service. Due to expensive price, financial loans will help consumers to buy the electric vehicles. Consumers are no longer an individual, independent vehicle operators, such as taxi company, and special purposes vehicle users, such as touring cars company, possibly become the end-users. Services provided to EV users are not just the power supply, the mobile communication and navigation by mobile equipment operators also have a great profits margin.

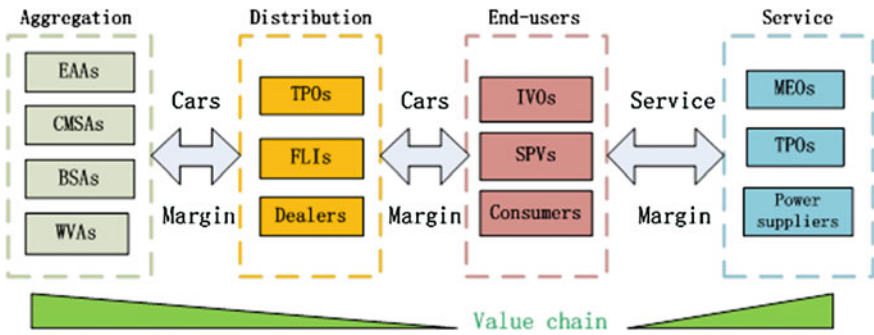


Fig. 7 EV industry chain and value chain after re-construction

The abbreviations used in Fig. 7 are as follows:

EAA	Electric Attachment Aggregator	IVO	Independent Vehicle Operator
CMSA	Car Motor System Aggregator	SPV	Special Purpose Vehicle users
BSA	Battery System Aggregator	FLI	Financial Lending Institutions
TPO	Third-Party Operator	MEO	Mobile Equipment Operator
WVA	Whole Vehicle Aggregator		

## 5 Example

Hangzhou City is the one of 25 cities for EV demonstration and the one of 6 cities for private purchase of new energy vehicles. By the end of 2011, there have been 200 electric taxis in practical run, which lead the EV demonstration of the China.

The business model plays the key role, as seen in Fig. 8. As the end-user, Hangzhou New Energy Taxi Company buys the nude EVs through the dealer from ZOTYE Auto Company, and leases the batteries from the TPO, Hangzhou Dayou Technology Company, from which the binded battery swap service given at the rents of mileage. In the future, the field of service would be extended to intelligent charger and communication and navigation.

The Hangzhou Model mainly brings three aspects of innovation. One is reducing the initial purchase costs by the model of vehicle-separate-from-battery, which means nude EV sold and battery leased separately. Second is introducing TPOs into EV distribution, who buy the batteries in large quantities and do the centralized maintenance and operation, which makes the battery leasing and recycling possible. Third is by setting joint ventures and subsidiary corporations, Hangzhou Electric Company has got involved in the fields of aggregation, distribution, end-user and service, with controlling the battery pack, purchase, usage and recycling, substantially has dominated the business model even EV industry chain and value chain.

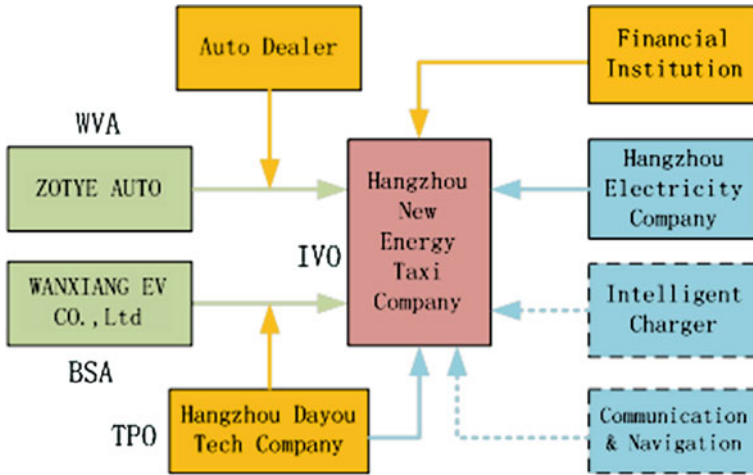


Fig. 8 Hangzhou business model for EV taxi

## 6 Conclusion

In this paper, the existed value chain method is developed to analyse the internal reasons of the transformation of EV business model, the re-construction concept is projected to construct the new business models systematically. At the end of paper, one example of demonstration city is used to explain the re-construction method of EV business model. The main inadequacy of this paper is the lack of quantitative analysis, which may be the direction for improvement in the future.

## References

1. Osterwalder A, Pigneur Y, Tucci C (2005) Clarifying business model: origin, present and future of the concept. *Comm Assoc Inform Syst* 16:1-25
2. Gómez SanRomán T, Momber I, et al (2011) Regulatory framework and business models for charging plug-in electric vehicles: infrastructure, agents, and commercial relationships. *Energy policy* 39:6360-6375
3. Potter ME (1998) *Competitive advantage: creating and sustaining superior performance*. A Division of Simon & Schuster Inc., New York
4. Magretta J (2002) Why business models matter. *Harvard Bus Rev* 5:3-8
5. Srai JS, Shi Y (2008) *Understanding China's manufacturing value chain*. University of Cambridge Institute for Manufacturing, Cambridge



**Part VIII**  
**Other**

# Research on Parameter Matching and Fuzzy Logic Control Strategies of EMT Hybrid Energy Storage System

Changle Xiang, Yanzi Wang, Weida Wang, Lijin Han  
and Donghao Zhang

**Abstract** Electro-mechanical transmission (EMT) is a transmission pattern of hybrid electric vehicles. This paper analyzes and calculates the required electric power of EMT. The requirement to the hybrid energy storage system of EMT is analyzed and calculated in this paper. Then according to the calculation results, the parameters of hybrid energy storage system consisted of batteries and supercapacitors for EMT are matched. Based on the analysis of required electric power, three fuzzy control strategies for different modes are proposed in this paper. The model of HESS and control block is built based on Matlab/Simulink. Simulation results indicate that the required electric power and energy is satisfied, and the control strategy proposed in this paper is feasible. The supercapacitors play an important role to diminish the impacts on batteries.

**Keywords** Batteries · Supercapacitors · Hybrid energy storage system · Parameter matching · Fuzzy control

Hybrid Electric Vehicles (HEVs) have been drawn significant attention in recent years. Electro-mechanical transmission (EMT) is one form of parallel-series

---

F2012-B08-008

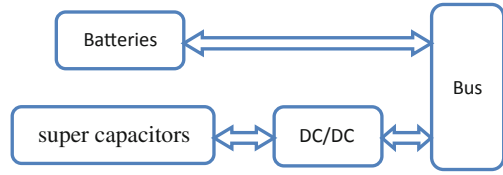
---

C. Xiang · Y. Wang · W. Wang · L. Han · D. Zhang (✉)  
National Key Laboratory of Vehicular Transmission, Beijing Institute of Technology,  
Beijing, China  
e-mail: wangyanzi\_bit@hotmail.com

C. Xiang  
e-mail: xiangchangle@bit.edu.cn

W. Wang  
e-mail: wangwd0430@163.com

**Fig. 1** Configuration of hybrid energy storage system



hybrid electric vehicles. It is a feasible method of driving heavy vehicles electrically. Through electrical and mechanical power flow transmission pathways, EMT transmits the power of engine. It can not only keep the engine working in the range of high efficiency, also improve fuel efficiency and dynamic property [1].

Because in some cases hybrid electric vehicles need to offer or store electrical energy, the research of energy storage system is a key issue for EMT. Battery has been used as energy storage component in hybrid electric vehicles for several decades [2]. Battery has high energy density, but the power density of battery is low. In the condition of rapid acceleration and brake, the high current will reduce the cycle life, efficiency and capacity of battery. In recent years, the appearance of supercapacitor solved the problem of high power electrical energy. Unfortunately, under present technology condition, the energy density of supercapacitor is much lower than battery, so it cannot be used as the independent energy storage system on vehicles. So the design of combining supercapacitors and batteries has been proposed to develop a hybrid energy storage system (HESS) to satisfy the need of both power and energy.

## 1 Configuration of Hess

There are two forms of HESS configuration, direct connection and indirect connection [3]. In direct connection configuration, there are no power electrical elements between batteries and supercapacitors, and the supercapacitors play an important role only when the voltage of DC bus changed rapidly. In indirect connection configuration, DC/DC converter is used on the base of direct connection configuration. Through the comparison, the chosen configuration of HESS is shown in Fig. 1. DC/DC converter is located between supercapacitors and bus, and the batteries are connected to the bus directly. The energy of batteries has high transfer efficiency, and the voltage of DC/DC converter is easy to be controlled.

## 2 Parameter Matching

The primary coverage of hybrid energy storage system parameter matching includes calculating power, capacitor and series number of batteries, and calculating the capacitor of supercapacitor cell and series number of supercapacitors.

**Table 1** The parameters of vehicle

$M$	$21 \times 10^3$ kg
$f_r$	0.013
$V_s$	15 km/h
$P_{aux}$	50 kW
$C_d$	0.6
$A_f$	$5.5 \text{ m}^2$
$S$	15 km

### 2.1 Electric Power and Energy of EMT

Before matching the parameters of HESS, the maximum required electric power and energy of HESS must be clarified. In some modes, the main power driving the vehicle is mechanical power supplied by engine, so the requirement of electric energy storage system is not great. In the electric driving mode, all the power coming from HESS, the electric demand is much larger than other driving mode, so the required electric power and energy must be calculated. Hybrid electric vehicle can recovery the electric energy when the vehicle is braking. So the electric power and energy in the braking mode should be calculated. In the accelerating mode, HESS will supply electric power to improve the acceleration performance of vehicles, so the required electric power in this mode should be calculated.

#### 2.1.1 Required Electric Power and Energy of Electric Driving Mode

The required electric power in electric driving mode can be calculated according to the Eq. (1) [4].

$$\rho_{jy} = \frac{vS}{1000} (Mgf_r + \frac{1}{2} \rho_a c_D A_f V_s^2) + p_{aux} \tag{1}$$

Where  $V_s$  is the required velocity in the pure electric driving mode;  $p_{aux}$  is the power of auxiliary system;  $f_r$  is coefficient of rolling resistance;  $\rho_a$  is air density;  $c_d$  is drag coefficient;  $A_f$  is front face area from HESS to ground.

The required electric energy in electric driving mode can be calculated as Eq. (2).

$$E_{jy} = \frac{P_{jy} S}{V_s} \tag{2}$$

Where  $P_{jy}$  is required power of pure electric driving mode;  $S$  is distance of pure electric driving mode;  $V_s$  is the required velocity in the pure electric driving mode.

Parameters of vehicle are shown in Table 1.

**Table 2** The maximum regenerative power of DC bus in brake mode

Speed (km/h)	6	11	7	3	9	4	6	4	2	1	9	7	5
Braking power of motor (kW)	199	398	597	675	675	675	558	683	808	829	736	689	698

The required power of electric driving mode according to Table 1 is 88.5 kW, and the required electric energy is 88.5 kWh.

### 2.1.2 Required Electric Power and Energy of Regenerating Brake Energy Mode

The brake performance requirement is that vehicle can reduce speed to 0 km/h from 85 km/h in 5 s. Table 2 refers to the braking power of motor when the vehicle is braking from 85 to 0 km/h in 5 s.

The maximum regenerative electric energy calculated according to Table 2 is 3154.4 kJ, 0.8763 kWh, and the peak power is 829 kW.

### 2.1.3 Required Electric Power and Energy of Accelerating Mode

The acceleration target is the vehicle speeds up to 32 km/h in 7 s. In this accelerating process, the electric power and energy of DC bus are shown in Fig. 2.

Figure 2a shows that the peak discharge power is 372.55 kW, and Fig. 2b shows that the maximum energy is 632.05 kJ. Compared with the brake mode, required discharge power and energy is relatively low.

## 2.2 The Parameters Matching of Battery Pack

### 2.2.1 Series Number of Batteries

In HESS, batteries are connected to DC bus directly, so the voltage of battery pack should be equal to the voltage of motor. The series number of battery pack can be calculated as Eq. (3):

$$n \geq \frac{U_m}{U_{bs}} \tag{3}$$

Where  $U_m$  is the rated voltage of motor, 500 V in this paper;  $U_{bs}$  is the rated voltage of single battery, 3.7 V.

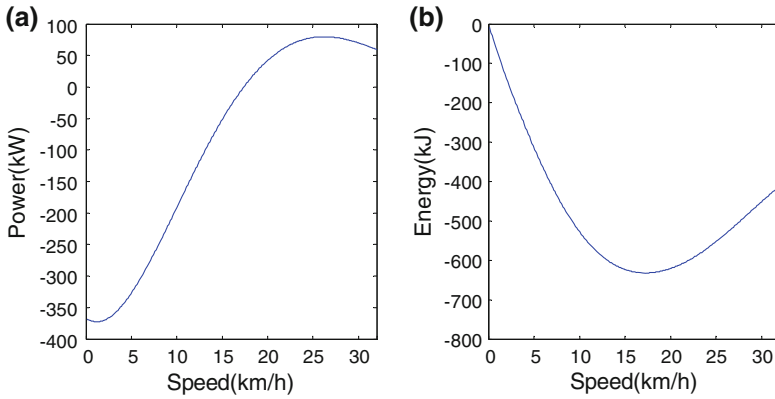


Fig. 2 The maximum required electric power of DC bus in accelerating mode

Table 3 The parameters of single battery

Rated capacity	35 Ah	Rated voltage	3.7 V
Mass energy density	≥135 Wh/kg	Volume energy density	≥225 Wh/L
Cycling performance	≥2500	Self-discharge	≤ 5 %
Temperature range	-20~55 °C	Mass	1080 ± 10 g

### 2.2.2 The Power of Batteries

The power of batteries must meet the requirement of power in electric driving mode, so the power of batteries  $P_{batt} \geq 88.5kW$ .

### 2.2.3 The Capacity and Parallel Number of Batteries

The capacity of batteries  $C_{batt}$  is determined by the distance of electric driving mode as Eq. (4):

$$C_{batt} \geq \frac{E_{jy}}{U_m \Delta SOC} \tag{4}$$

Where,  $\Delta SOC$  is effective SOC of battery, 0.8;  $U_m$  is the rated voltage of motor. If choosing the single battery with rated capacity  $C_{batt}$ , the parallel number  $m$  is:

$$m \geq \frac{C_{batt}}{C_{bs}} \tag{5}$$

The parameters of chosen single battery are shown in Table 3:

According to the parameters of chosen single battery, the calculating results are that series number  $n$  is 140, and parallel number  $m$  is 7, and the power of battery pack meets the required power.

## 2.3 The Parameters of Supercapacitor Pack

### 2.3.1 The Series Number of Supercapacitors

The supercapacitors are connected with bus through DC/DC convertor. The input and output of DC/DC are closer, and the DC/DC has the higher efficient [5]. So the voltage of supercapacitor pack should be closer to the minimum voltage of battery pack. The series number of supercapacitors  $p$ :

$$p \leq \frac{U_n}{U_{sc}} \quad (6)$$

Where  $U_n$  is the minimum voltage of batteries,  $U_n = n \times U_{bsn} = 420V$ ,  $U_{bsn}$  is the minimum voltage of battery cell;  $U_{sc}$  is the voltage of supercapacitor cell.

### 2.3.2 The Capacity of Single Supercapacitor

The main purpose of supercapacitor pack is store the regenerating energy, the capacity of supercapacitor cell can be calculated as following equation:

$$\frac{1}{2} \rho C (V_{Max}^2 - V_{Min}^2) + t * P_{batt} \geq E_b \quad (7)$$

Where,  $E_b$  is the maximum energy of one regenerating brake;  $p$  is series number;  $C$  is capacity of supercapacitor cell;  $V_{Max}$  is the maximum voltage of supercapacitor cell;  $V_{Min}$  is the minimum voltage of supercapacitor cell;  $P_{batt}$  is the power of batteries;  $t$  is brake time.

According to the above equations, the calculation results are series number of supercapacitors  $p$  is 155, and the capacity of supercapacitor cell is 3,000 F.

## 3 Fuzzy Control Strategies

The HESS of EMT may operate in different modes, based on the analysis above, the required electric power and energy is different for each mode. Consequently, three fuzzy control strategies are designed for different modes in this paper. The inputs of control block are the speed of vehicle, SOC of batteries, voltage of supercapacitors and required current of DC bus, and the output variable is recharge

current of batteries. In the light of the current of DC bus, one of the three fuzzy control strategies is chosen as followings:

- (1) If  $I_{BUS} > 0$ , choose mode 1;
- (2) If  $I_{BUS} < 0$ , choose mode 2;
- (3) If  $I_{BUS} = 0$ , choose mode 3;

### ***3.1 Mode 1—HESS Absorbs Electric Power (Charge HESS)***

When vehicle is braking, motors generate electric power and charge HESS. In brake process the current may be very high, so the charge current should be controlled to prevent the batteries from overcharging and the impact of high current. The input variables of this strategy are the speed of vehicle, SOC of batteries, voltage of supercapacitor pack and brake current from motor, and the output variable is recharge current of batteries. Every input and output is divided into three sub-sets, which are high, middle and low. The rules of the strategy are made according to the followings:

- (a) When SOC of batteries is lower, the recharge current is higher;
- (b) When the voltage of supercapacitors is higher, the recharge current of batteries is lower;
- (c) The recharge current of batteries should be held within the 1 C, the best recharge current is 0.3 C, When the brake current is higher, the recharge current of batteries is higher;
- (d) When the speed of vehicle is lower, the SOC of batteries should be maintained to a higher level.

### ***3.2 Mode 2—HESS Release Electric Power (HESS Discharge)***

When vehicle is accelerating, HESS may need to output electric power. According to analysis above, the required power in acceleration process is not as high as that in brake process, considering the efficiency losses of DC/DC converter, most of the output power should be provided by the batteries. This paper proposes a fuzzy control method to control the discharge current of batteries. The rules of the strategy are made according to the followings:

- (a) When SOC of batteries is lower, the discharge current of batteries is lower;
- (b) When the voltage of supercapacitors is higher, the discharge current of batteries is lower;



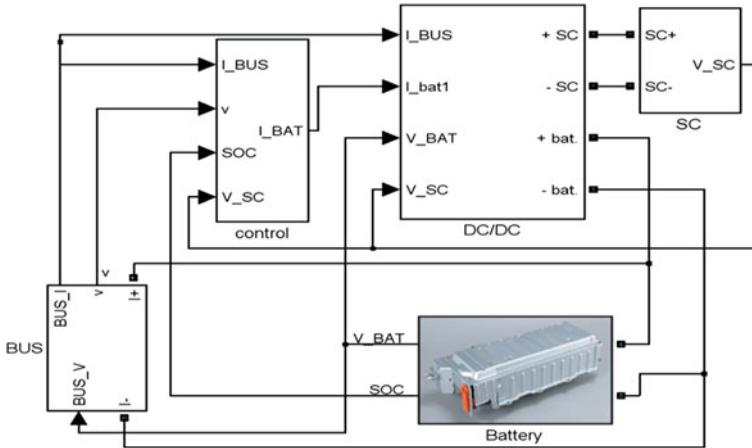


Fig. 3 The model in Matlab/Simulink

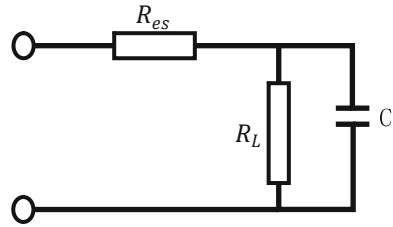
- (c) When SOC of batteries is low, the voltage of supercapacitors is higher and the required current is low, batteries can be recharged with 0.3 C current from supercapacitors;
- (d) The discharge current of batteries should be held within 2 C, and the best discharge current should be confined about 1 C or lower;

### 3.3 Mode 3—Electric Power Flow Between Batteries and Supercapacitors

According to the control strategy above, most of the discharge power comes from battery pack, but part of the recharge power flows into supercapacitor pack, so when there is no required electric power of the bus, the electric energy in supercapacitors should be transferred to batteries in an efficient way. According to the SOC of batteries, the voltage of supercapacitors and the speed of vehicle, this paper propose a fuzzy control strategy to choose the suitable recharge current of batteries. The rules of the strategy are made according to the followings:

- (a) When SOC of batteries is lower, the recharge current is higher;
- (b) When the speed of vehicle is higher, the voltage of supercapacitors should be confined into a lower level;

**Fig. 4** The model of supercapacitor



## 4 Simulation and Results

### 4.1 Model of HESS and Control Strategies

In order to verify the validity of the control strategy, a model is built based on Matlab/Simulink which is shown as Fig. 3.

The model is made up of five parts, bus, batteries, supercapacitors, DC/DC and control block. The bus part calculates the required electric power and bus current. If the bus current is positive, the electric power flows from bus to the HESS; if the bus current is negative, the electric power flows from HESS to the bus. Because the model establishing is beside the key point, so the models of battery pack, DC/DC and supercapacitor pack in this paper are established in a simple method. The battery model of Matlab/Simulink is adopted and the parameters of the model are determined according to the actual parameters of the chosen Li-ion batteries. The supercapacitors model is consists of capacitor C, series equivalent resistance  $R_{es}$  and leakage resistance  $R_L$ , as shown in Fig. 4.  $R_{es}$  characterizes the charge and discharge resistance, and  $R_L$  expresses the self-discharge characteristic of supercapacitor. The parameters of model can be calculated according to the properties of the chosen supercapacitor. The purpose of DC/DC convertor is electric power allocation between batteries and supercapacitors, and the DC/DC model neglecting the efficiency losses and structure.

The function of control block is calculating the charge and discharge current of batteries and supercapacitors according to the fuzzy control strategies proposed in this paper.

### 4.2 Simulation Results and Analysis

In this paper, part of motor power data obtained in practical tests of a heavy hybrid electrical vehicle adopting EMT is used as bus required electric power for simulation and to verify the matched parameters and the proposed control strategy. The simulation results are shown in Figs. 5 and 6. In Fig. 5, when DC bus power is positive, HESS releases electric power; when DC bus power is negative, HESS absorbs electric power.

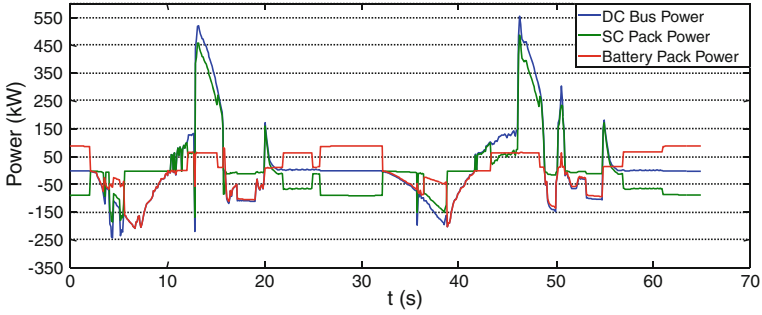


Fig. 5 Required electric power of DC bus and the responses of supercapacitors and batteries

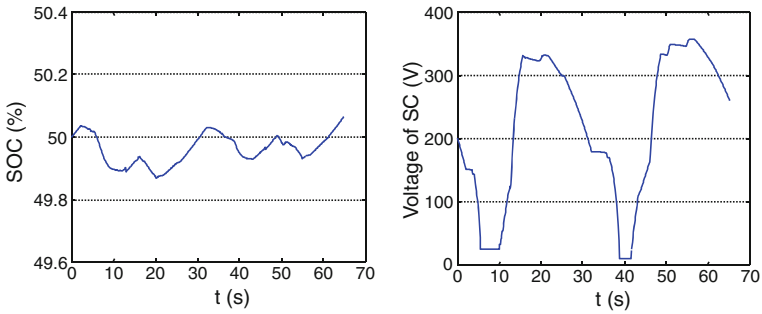


Fig. 6 Response curve of SOC and supercapacitor voltage

The simulation results indicate that:

- (1) HESS whose parameters are matched in this paper can provide enough electric power and energy for DC bus.
- (2) When DC bus releases electric power, because the electric power from DC bus is high, so supercapacitors recover most of the electric energy, and batteries recover energy with relatively stable recharged current;
- (3) When DC bus absorbs electric power, if the required electric power is within the compass of batteries output, batteries release most of the required energy, and the output of supercapacitors is supplement to batteries;
- (4) In some cases, the recovered electric energy can be transferred from supercapacitor pack to batteries with stable current;
- (5) The simulation results are consistent with the control strategy proposed in this paper.

## 5 Conclusion

In this paper based on calculating the required electric power and energy of EMT system, the parameters of HESS for EMT are matched. According to the characteristics of HESS's required electric power in different modes, three fuzzy control strategies are designed for different modes. The model of HESS and control strategies is built in Matlab/Simulink. Part of motor power data obtained in practical tests of a heavy hybrid electrical vehicle adopting EMT is used as bus required electric power to verify the matched parameters and the proposed control strategy. Simulation results show that the required electric power and energy is satisfied, and the control strategy is feasible.

## References

1. Wang W, Xiang C, Han L, Ma Y, Liu H (2011) Integrated control strategy of electro-mechanical transmission system. *J Mech Eng* 47(20):152–158
2. Chen Q (2009) *Advanced electric vehicle technology*. Chemistry Industry Press, Beijing
3. Yan X, Pan Y (2010) Design and analysis of the structure of ultracapacitor/Batteries hybrid system. *Power Electron* 44(5):75–77
4. Han L (2010) A study on performance matching and control strategy for power-split hybrid electric vehicles. Beijing Institute of Technology, Beijing
5. Marle-Francoise N, Gualous H (2005) 42 V power net with supercapacitor and battery for automotive applications. *J Power Sour* 143:275–283

# Cost-Effectiveness Analysis of CO<sub>2</sub> Reduction with Future Automobile Technologies in the Japanese Automotive Sector

Shuichi Kanari

**Abstract** The authors developed long-term scenarios for reducing CO<sub>2</sub> emissions by using CEAMAT. CEAMAT is an energy analysis model for considering long-term effects of future automotive technologies in the Japanese automotive sector. At first, future automotive data and demand of the automotive sector of the IEEJ2050 model were entered into CEAMAT, then open literature was reviewed, and interviews were conducted with relevant organizations. Secondly, the authors developed long-term scenarios for the Japanese automotive sector using CEAMAT. According to these scenarios, by the year 2050 the share of next-generation vehicles in use will increase by 43 % for passenger cars and 48 % for medium-sized and large trucks, and CO<sub>2</sub> emissions will be reduced by 47 % compared to the year 2005. Finally, calculations were made of the potential for integrated approaches of eco-driving and improving traffic flow to reduce CO<sub>2</sub> emissions. CEAMAT indicated that the integrated approaches could help reduce CO<sub>2</sub> emissions by 55 % compared to the year 2005.

**Keywords** CO<sub>2</sub> emissions reduction · Cost-effectiveness · Future automobile technologies

## 1 Introduction

Recently, international interest in energy security and the global environment is increasing. There have been studies on long-term technical strategies for conserving energy, diversifying energy sources, and reducing CO<sub>2</sub> emissions.

---

F2012-B08-009

---

S. Kanari (✉)  
Japan Automobile Research Institute, Tokyo, Japan  
e-mail: skanari@jari.or.jp

However, in the automotive sector, a method for evaluating technical strategies over the long-term has not yet been established. At the current time, various research organizations are estimating the energy savings and CO<sub>2</sub> emissions reduction potential of automobiles and associated costs, based on independently-developed methods and technical assumptions. However, these studies have not clarified the methodology and setting of assumptions. When estimating energy and environmental measures and policies, it is necessary to broaden the scope of investigations while giving these issues sufficient consideration.

This study was designed to formulate a method for evaluating future automobile technologies by creating a database of cost-efficiency information based on open literature and interviews with relevant organizations. The method and database is called cost and effectiveness assessment model for automobile technologies (CEAMAT). CEAMAT is used for quantitatively analyzing the cost-effectiveness of future technologies based on these results, and scenarios for reducing CO<sub>2</sub> emissions over the long term in the automotive sector were examined.

In regard to CO<sub>2</sub> emissions reduction potential resulting from eco-driving and traffic flow measures, an investigation was made into the methodologies for estimating the effects when applied nationwide to Japan, based on the results of existing research and surveys, then CO<sub>2</sub> emissions reduction scenarios were considered for the Japanese automobile sector for the year 2050.

## **2 Overview of the CEAMAT Model**

### ***2.1 Objects of CEAMAT Analysis***

Table 1 shows vehicle types and classes in CEAMAT. These were categorized to match the study area and the Japanese automotive sector (Table 1).

Table 2 shows the automobile technologies and fuels assumed for each of the categories. There are 14 technological categories that may be widespread by the year 2050, so those became the objects of the analysis.

### ***2.2 Model Structure***

The model of new vehicles in CEMAT Tank to Wheel consists of three sub models: a sub model for estimating fuel efficiency, a sub model for estimating vehicle price, and a sub model for estimating the number of vehicles sold for each technology. The sub models for estimating the fuel efficiency and vehicle price take into consideration the efficiency improvement effects of introducing future technologies into base vehicles, and incidental costs. The model for selection

**Table 1** Targeted vehicle types and classes

Passenger car	Truck	Bus
Middle (>2000 cc)	Large (GVW > 8 t)	Large (GVW > 8 t)
Small (≤2000 cc)	Middle (3.5t GVW ≤ 8 t)	Small (GVW ≤ 8 t)
Mini (≤660 cc)	Small (GVW ≤ 3.5 t)	
	Mini (≤660 cc)	

**Table 2** Automobile technology categories and fuel

Technology		Fuel path
GICEV	Gasoline internal combustion engine vehicle	Gasoline/ethanol
GICEHEV	Gasoline internal combustion engine hybrid vehicle	
DICEV	Diesel internal combustion engine vehicle	Diesel oil/BDF
DICEHEV	Diesel internal combustion engine hybrid vehicle	
HICEV	Hydrogen internal combustion engine vehicle	Hydrogen/gasoline
HICEHEV	Hydrogen internal combustion engine hybrid vehicle	
CNGV	Compressed natural gas vehicle	CNG
DMEV	Dimethyl ether vehicle	DME
LPGV	Liquefied petroleum gas vehicle	LPG
EV	Electric vehicle	Electricity
HFCV	Hydrogen fuel cell vehicle	Hydrogen
GICEPHEV	Gasoline internal combustion engine plug-in hybrid vehicle	Gasoline/electricity
DICEPHEV	Diesel internal combustion engine plug-in hybrid vehicle	Diesel oil/electricity
HFCPHEV	Hydrogen fuel cell plug-in hybrid vehicle	Hydrogen/electricity

based on technology uses a multinomial logit model to estimate the total costs using new vehicle fuel efficiency, future technology introduction, and number of models in the line-up as parameters.

### 2.3 Transportation Demand and Fuel Price Data

A scenario analysis with CEAMAT requires various types of data such as transportation demand, fuel costs, and average annual distance travelled per vehicle. However, CEAMAT does not have the built-in capability to make these estimates based on its data. The data used in this study were quoted from the long-term energy analysis model IEEJ2050 for all sectors in the world developed by the Institute of Energy Economics, Japan. The following figures show examples of automotive demand (Fig. 1) and fuel prices (Fig. 2).

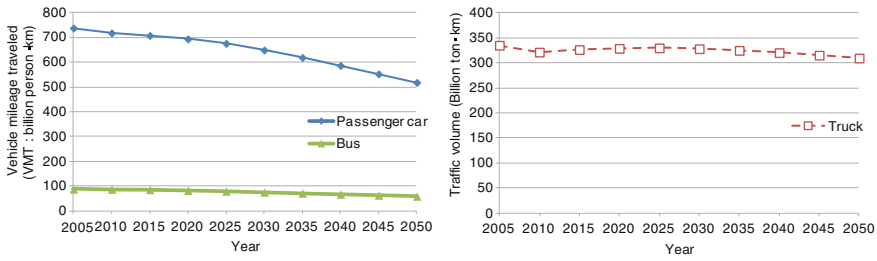


Fig. 1 Demand by road transport sector (left passenger vehicle, right truck)

### 2.4 Automotive Data

CEAMAT shows efficiency and prices of improved fuel efficiency in internal combustion engines (ICEs) and batteries in electric vehicles (EVs) as examples of automotive data.

#### 2.4.1 Effects and Prices of Improved Fuel Efficiency of ICEs

The objects of investigation of CEAMAT were the ICE technology’s factors shown in Table 3. However, there are many possible combinations. The technical strategy assessment model that was the object of this study was not suitable to evaluate numerous individual combinations. Therefore, based on these combinations, a price curve was established that could give additional prices for a fuel efficiency improvement ratio. It should be noted that the standard vehicles considered here were the average vehicles for the year 2000. Among the combinations of fuel efficiency improvement technologies, the one with the best price and fuel efficiency improvement ratio was used to make the price curve. Technology’s factors were examined for the engine, transmission, and peripherals. The effectiveness of fuel efficiency improvement technologies and price data were based on open literature [1, 2]. However, in order to use them to fit the situation in Japan, they were revised after interviews were conducted with relevant institutes.

Figure 3 shows the price curves for passenger cars and trucks used in CEAMAT. Trucks show less potential for improving fuel efficiency in the future than passenger cars. This may be due to differences between gasoline and diesel vehicles. In addition, because trucks have a higher vehicle rank than cars, their price per unit of fuel efficiency improvement is higher than for cars.

#### 2.4.2 Efficiency and Cost of EV Batteries

Figure 5 shows weights and prices of EV batteries. The analysis assumes that since the year 2010, all batteries used in passenger cars and trucks are lithium ion



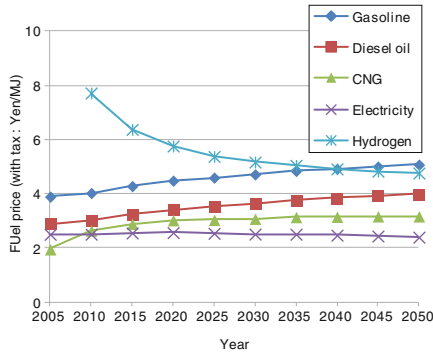


Fig. 2 Fuel prices

Table 3 Examples of improvement rates and prices of fuel efficiency enhancement technologies for ICEs

Improving FE technology	Passenger cars	Trucks
Gasoline direct injection (Stoichiometric)	○	
Gasoline HCCI	○	
Cam phasing	○	
Engine downsizing	○	○
EGR	○	○
Improved engine friction	○	○
Improved firing chamber	○	○
Other normal advance technologies	○	○
Turbo compound		○
Variable compression ratio		○
Valuable valve timing	○	○
2 stages turbo		○
After-treatment device		○

(Li-ion) batteries. These are considered technological advances and will lead to widespread use which will bring costs down. Scenarios for the performance and cost of Li-ion batteries were established based on NEDO’s road map [3] and on interviews with relevant institutes (Fig. 4).

NEDO’s scenario assumes that post-Li-ion batteries will be in widespread use from the year 2030. However, at the present time, there are no alternate materials that clearly appear to be at practical level so only Li-ion battery scenarios were used.

Compared with passenger cars, truck batteries are generally more expensive. This means that when viewed as a battery system, accessories are also added to the vehicle rank, which is larger than passenger cars, so this was reflected in the analysis.

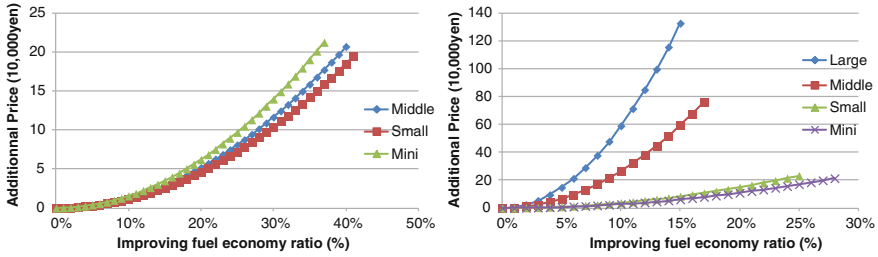


**Fig. 3** Improved fuel economy ratio and price curves of passenger cars and trucks (*left* passenger cars, *right* trucks)

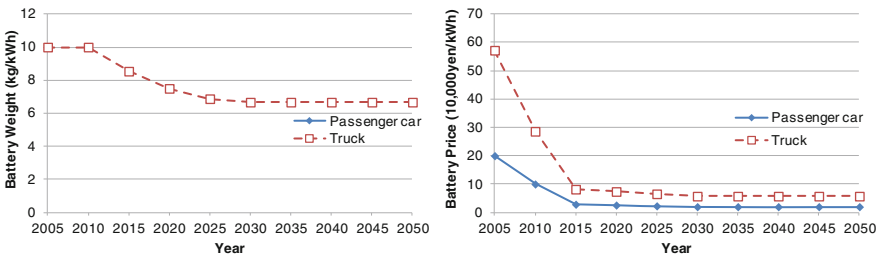


**Fig. 4** Weight and prices of EV batteries for cars and trucks

### 3 Scenario Analysis

#### 3.1 Fuel Economy and Price of New Vehicles

##### 3.1.1 New Small Passenger Cars

Figure 5 shows the fuel economy of small passenger cars. Conventional vehicles (GICEV, DICEV, HEV) will have improved fuel economy by the year 2030 as the fuel efficiency improvement technologies shown in Sect. 2.4.1 become popular. Next-generation vehicles such as EVs and HFCVs reflect improvements in battery efficiency, FC systems, etc., which improve the fuel efficiency of new vehicles.

Next, Fig. 5 shows the prices of new small vehicles. In the case of ICEV vehicles, the cost curve in Sect. 2.4.1 follows improvement in fuel efficiency, and estimated incidental costs are added to the calculations, so that vehicle prices increase until the year 2030. Decreased prices for next-generation vehicles such as EVs and HFCVs reflect the effects of technological advances, improved batteries and FC systems, and widespread use, but they are still more expensive than conventional vehicles.

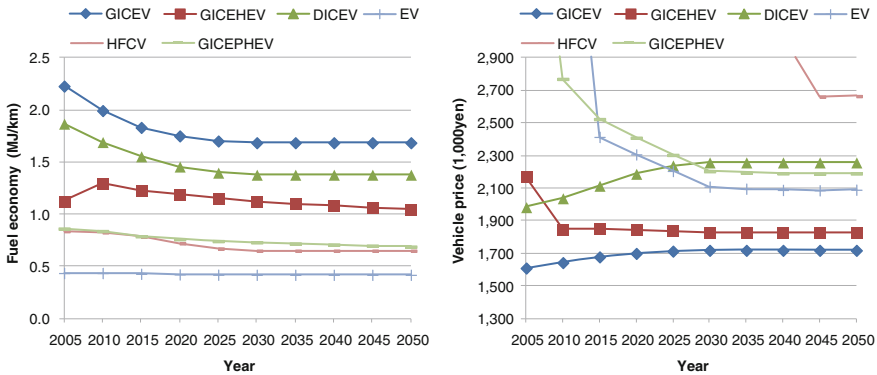


Fig. 5 Fuel economy and vehicle prices (new small passenger cars)

### 3.1.2 New Large Trucks

Figure 6 shows the fuel economy of new large trucks. The fuel economy will improve with the introduction of fuel efficiency improvement technologies by the year 2030, as with small passenger cars. Next-generation vehicles also reflect improvements in various technological elements, and fuel efficiency is also improved.

Next, Fig. 6 shows the prices of new large trucks. The basic trend is the same as with small passenger cars. The addition of fuel efficiency improvement technologies shown in Sect. 2.4.1 will increase vehicle prices, but the prices of next-generation vehicles reflect the effects of widespread use and technological advancements that reduce the costs of technology factors, which in turn lower vehicle costs. However, regarding EVs and HFCVs, large trucks travel long distances and must be equipped with large fuel storage systems for batteries, hydrogen tanks, etc., so their prices will remain higher than those of conventional vehicles.

## 3.2 Number of Vehicles in Use

Figure 7 shows the number of vehicles in use (passenger cars, and medium- and large-sized trucks) by type of technology. Basically, the same preconditions were set for compact and light trucks as for passenger cars. Since the number of vehicles in use structure by type of technology is similar to that of passenger cars.

The share of next-generation vehicles, especially GICEHEVs, increases up to 43 % by the year 2050. The reason for the estimated increases in next-generation vehicles is that advancements in technologies and fuel efficiency, as well as large market popularization, will reduce vehicle costs and bring such vehicles into wider use by consumers.

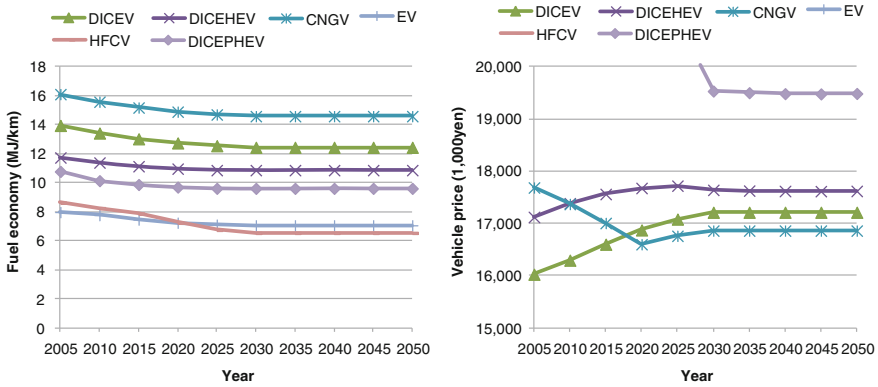


Fig. 6 Fuel economy and vehicle prices (new large trucks)

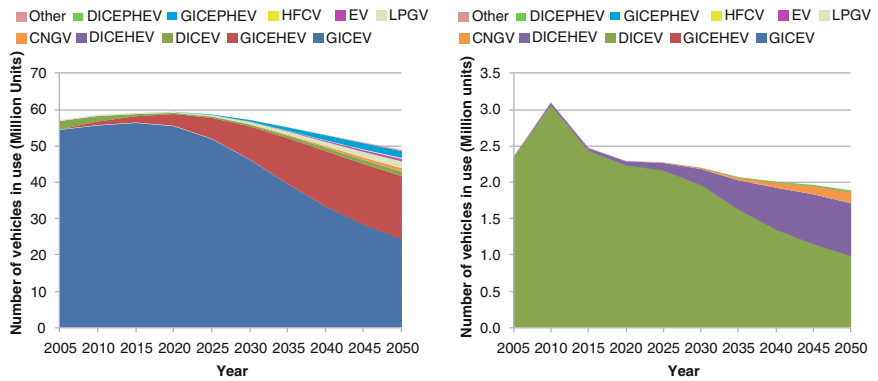


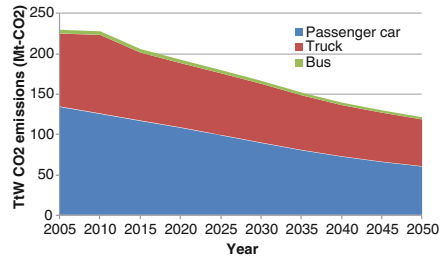
Fig. 7 Number of registered vehicles (left passenger cars, right medium and large sized trucks)

Regarding the number of medium and large size trucks in use, the share of next generation vehicles, especially DICEHEVs, increases up to 48 % by the year 2050. The reason for the estimated increases in next-generation vehicles is that, as with passenger cars, improvements in fuel efficiency resulting from advancements in technologies, as well as large market penetration, will bring vehicle prices down.

### 3.3 Average Fuel Economy of Vehicles in Use

Fuel economy for both using passenger cars and trucks has been revised based on fuel efficiency improvements in conventional vehicles and popularization effects of next-generation vehicles. As a result, compared to the year 2005, fuel economy improvement ratios for the year 2050 are 44 % for passenger cars, 31 % for small and light trucks, and 23 % for medium and large trucks.

**Fig. 8** CO<sub>2</sub> emissions in the automotive sector



### 3.4 Tank to Wheel (TtW) CO<sub>2</sub> Emissions

Figure 8 shows CO<sub>2</sub> emissions for all of Japan at the tank to wheel. In conjunction with the improved fuel efficiency of registered vehicles shown in Sect. 3.3 and the decreasing demand for transporting travelers and goods discussed in Sect. 2.3, the amount of CO<sub>2</sub> emissions in the automotive sector in the year 2050 will be reduced by 47 % compared to the year 2005. By type of vehicle, the CO<sub>2</sub> emissions reduction will be 55 % for passenger cars, 36 % for trucks (light to large), and 40 % for buses.

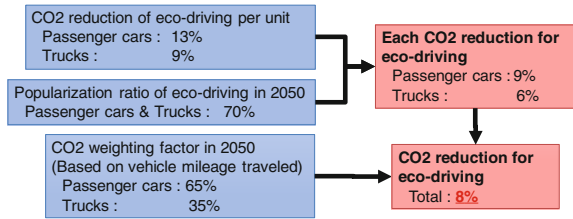
## 4 Effects of Integrated Approaches on CO<sub>2</sub> Emissions Reduction

This chapter examines the future CO<sub>2</sub> emissions reduction potential of eco-driving and traffic flow improvement measures. Furthermore, the results are entered into CEAMAT in order to examine scenarios for reducing CO<sub>2</sub> emissions in the automotive sector for integrated approaches.

### 4.1 Effects of Eco-Driving on Reducing CO<sub>2</sub> Emissions

Figure 9 shows the flow of estimating CO<sub>2</sub> emissions reduction effects of eco-driving. Studies conducted by nine organizations [4–13] estimated the per-vehicle CO<sub>2</sub> emissions reduction rate of vehicles equipped with eco-driving technologies is 13 % for passenger cars, and 9 % for trucks. Next, the future rate when eco-driving is implemented nationwide was set at 70 % for the year 2050, based on the results of a questionnaire that was administered by the Energy-saving ITS Study Group [14]. Finally, the effects of eco-driving differed between passenger cars and trucks, and the weighted coefficient of CO<sub>2</sub> emissions was set based on the annual distance traveled by passenger cars and trucks in Japan in the IEEJ2050 model. As a result, it was estimated that the CO<sub>2</sub> emissions reduction potential of eco-driving would be 8 % by the year 2050.

**Fig. 9** Flow for estimating the CO<sub>2</sub> emissions reduction effects of eco-driving



## 4.2 Effects of Traffic Flow Measures on Reducing CO<sub>2</sub> Emissions

Measures for traffic flow were defined into two main groups. The first group is measures for road improvements that are expected to have roughly the same effects as current measures. The second group is measures based on new technologies such as traffic signal control based on connections with autonomous driving and platooning in the ITS system, infrastructure, etc. that are expected to become widespread in the future.

This chapter examines two estimations. The first estimation is the potential to reduce CO<sub>2</sub> emissions by road improvements based on trends, etc., up to the present, and speed improvements. The second estimation is calculated CO<sub>2</sub> emissions reduction potential to introduce new technologies based on existing research and surveys.

### 4.2.1 Effect of Road Improvements on Reducing CO<sub>2</sub> Emissions

Figure 10 shows the flow of road improvements for reducing CO<sub>2</sub> emissions. First, future GDP was used to estimate future road project costs by extrapolating from the relation between past GDP data and road project costs [15]. Next, the relation between past road project costs and average speed [15, 16] was considered, then average improvement in speed due to road improvements was estimated. In the future scenario obtained in this way, the effects of improved average speed were reflected in the distribution of average speed and annual traveled distance derived from statistical values of the Ministry of Land, Infrastructure and Transport (MLIT) [16]. Then, using the relation between speed and the CO<sub>2</sub> emission base unit [17] created by the National Institute for Land and Infrastructure Management that was revised based on the year 2005 standards, estimates were made of CO<sub>2</sub> emission volume before and after road improvements in Japan. As a result, it appeared that the maximum improvement in speed based on road improvements in all of Japan would be about 4 km/h higher compared with the year 2005. This was calculated to be the equivalent of about 4 % CO<sub>2</sub> emissions reduction potential by the year 2050.

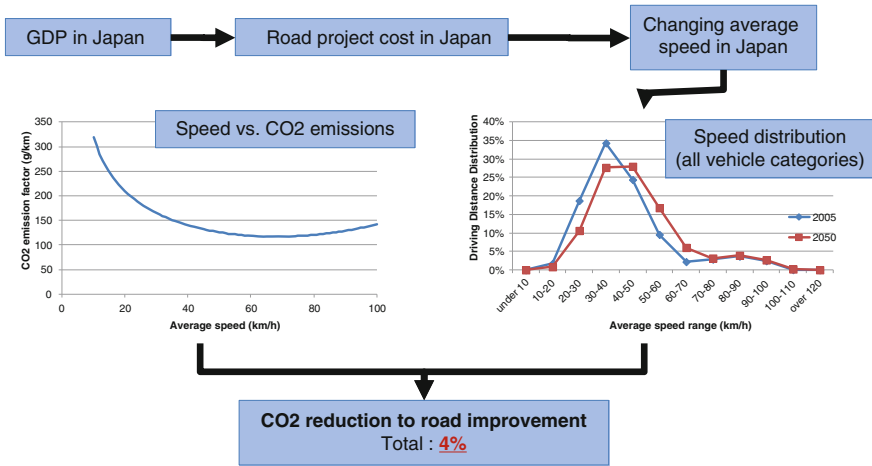


Fig. 10 Flow of estimating the effects of road improvements on reducing CO<sub>2</sub> emissions

### 4.2.2 Effects of Improved Traffic Flow Technologies on CO<sub>2</sub> Emissions Reduction

There are several existing studies about traffic flow improvement technologies, but all of them have examined the effects per vehicle, so there are cases where such things as the diffusion rate have not been considered and even in cases where the diffusion rate has been considered, most of them have involved short-term calculations for the year 2010–2030 [18, 19]. The results of one of these studies, by the Energy-saving ITS Study Group [14], targeted ITS technology up to the year 2050, and there were also clear bases for estimating the diffusion rate, etc., so those values were cited in the present study (Table 4). As a result, the potential for traffic flow improvement technologies to reduce CO<sub>2</sub> emissions is considered here to be approximately 4 % by the year 2050.

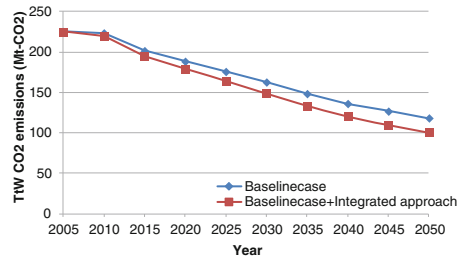
### 4.3 CO<sub>2</sub> Emissions Reduction Potential of Integrated Measures

Estimates were made of the CO<sub>2</sub> emissions reduction effects of eco-driving (Sect. 4.1) and traffic flow measures (Sect. 4.2). The results were entered into CEAMAT to estimate the CO<sub>2</sub> emissions volume for cases where the reduction effects of integrated approaches were added to the effects of fuel efficiency improvements in conventional vehicles and wider use of next-generation vehicles. As a result, in the baseline case that considered only fuel efficiency improvements in conventional vehicles and wider use of next-generation vehicles, there was a 47 % reduction in CO<sub>2</sub> emissions in the year 2050 compared to the year 2005, but when the effects of integrated approaches were added to the baseline case, it was found that CO<sub>2</sub> emissions could be reduced by up to 55 % (Fig. 11).

**Table 4** Effects of traffic flow improvement technologies on reducing CO<sub>2</sub> emissions

Item	CO <sub>2</sub> reduction (%)
Platooning	0.2
Traffic light control (only vehicle)	0.04
Traffic light control (link up with infrastructure)	2
Full route information	1.4
Predicting optimal starting time	0.1

**Fig. 11** CO<sub>2</sub> emissions with integrated approaches



## 5 Concluding Remarks

In this study, a database was created of the prices and effects of future automotive technologies then the database was used to construct a model called CEAMAT to perform cost-benefit analyses of automobile technologies. In addition, there was an examination of the CO<sub>2</sub> emissions reduction effects of an integrated approach involving eco-driving and traffic flow improvement measures. Finally, an investigation was made of long-term CO<sub>2</sub> emissions reduction scenarios in the automotive sector that included these effects.

With the above preconditions, it was found that by the year 2050, fuel efficiency improvement effects in conventional vehicles and the popularization of next-generation vehicles would result in a 47 % reduction in CO<sub>2</sub> emissions compared with the year 2005. Furthermore, when the effects of eco-driving and traffic flow improvements were added, then CO<sub>2</sub> emissions could be reduced by up to 55 % in the year 2050. These findings indicate the necessity of not only fuel efficiency improvement effects in conventional vehicles and the popularization of next-generation vehicles, but also integrated approaches that include the effects of such measures as eco-driving and traffic flow improvements.

## References

1. Air Resources Board (2004) Staff proposal regarding the maximum feasible and cost-effectiveness reduction of greenhouse gas emissions from motor vehicles, California Environmental Protection Agency
2. IEEP (2005) Service contract to carry out economic analysis and business impact assessment of CO<sub>2</sub> emissions reduction measures in the automotive sector



3. Storage Technology Division, Fuel Battery and Hydrogen Technology Development Department, NEDO (2008, 2009) NEDO road map for technological development of batteries for next-generation vehicles
4. Kato H, Kobayashi S (2010) Evaluation of eco-driving popularization effect using traffic flow simulation. *J Soc Autom Eng Jpn* 64:51–56
5. Sano M (2009) Analysis of the gap between on-road real fuel economy and certified fuel economy using e-Nenpi Data etc. In: Proceedings of society of automotive engineers of Japan, 2009
6. Sato S, Suzuki H, Miya M, Iida N (2009) Analysis of the effect of eco-driving on real-world emission. In: Proceedings of society of automotive engineers of Japan, 2009
7. Honda Motor Co. Ltd. (<http://www.honda.co.jp/news/2009/4091005.html>)
8. Ueki S, Saito A, Nagatomi Y, Takada Y (2008) Analysis of fuel economy improvement of commercial vehicles equipped with eco-drive support devices. In: Proceedings of the society of automotive engineers of Japan, 2008
9. Saito A, Takada Y (2008) The relationship between eco-driving patterns of light duty freight vehicles and the improvement of fuel economy in real traffic conditions. In: Proceedings of the society of automotive engineers of Japan, 2008
10. Kato H, Kobayashi S, Kondo Y, Matsuhashi K (2008) The contributing factors to improving fuel economy in eco-drive (Second report). In: Proceedings of the society of automotive engineers of Japan, 2008
11. Masuko T, Fujiwara H, Sambuichi H (2009) Analysis of the contributing factors to actual fuel economy by structural equation modeling. In: Proceedings of the society of automotive engineers of Japan, 2009
12. TNO (2006) Review and analysis of the reduction potential and costs of technological and other measures to reduce CO<sub>2</sub>-emissions from passenger cars
13. NESCAFE (2009) Reducing heavy-duty long haul combination and CO<sub>2</sub> emissions
14. Energy ITS Workshop (2009) Means for implementing energy ITS
15. Ministry of Land, Infrastructure, Transport and Tourism (2012) Roads in Japan (IR). [http://www.mlit.go.jp/road/ir\\_index.html](http://www.mlit.go.jp/road/ir_index.html)
16. Ministry of Land, Infrastructure, Transport and Tourism (2007) Road traffic census, 2005
17. Namikawa Y, Takai Y, Ohshiro N (2003) Calculation base of motor vehicle emission factors. Technical Note of National Institute for Land and Infrastructure Management
18. Strategic Committee for Popularizing Eco-friendly vehicles (2010) Strategies for popularizing eco-friendly vehicles
19. McKinsey & Company (2009) Scope of CO<sub>2</sub> emission reduction (for passenger cars) in the global road traffic sector aiming at a future low carbon society

# The Small-Signal Model Stability Analysis of Full-Bridge Buck Converter with Compensation Network

Lin Zhang, Dengmeng Fu and Haoxing Liu

**Abstract** Modelling and stability analysis of DC–DC switching converters is the key step to study, analyze and design switching power supplies. The equivalent circuit model in the continuous conduction mode (CCM) is presented in this paper. The DC/DC transfer functions are derived based on the main circuit model, the compensation network circuit model, and the PWM waveform generator circuit model. The analysis and simulation of the small-signal model are discussed based on it. Finally, DC/DC sample are tested with network analyzer. The results show that the modeling approaches taking converter parasitic parameters into account is feasible, which can help optimize and improve the performance of switching power supply design and efficiency. It has practical engineering value.

**Keywords** Voltage loop · Equivalent model · Compensation network · Buck converter · Loop stability analysis

## 1 Establishment of Transfer Function

### 1.1 Ordinary BUCK Converter LC Transfer Function

The work state in one cycle of Buck Converter can be expressed with two non-time-changed circuits [1], as shown in Fig. 1.

---

F2012-B08-014

---

L. Zhang (✉) · D. Fu · H. Liu  
United Automotive Electronic Systems (UAES) EH/EPE2, Beijing, China  
e-mail: lin.zhang2@uaes.com

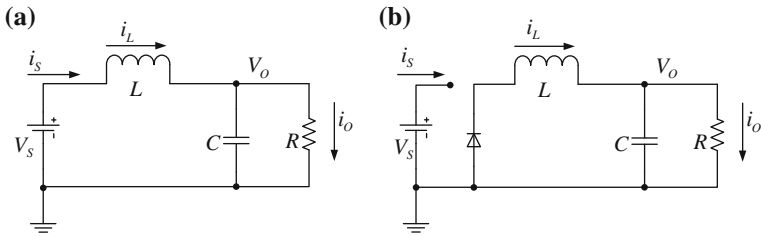


**Fig. 1** **a** Closed state of switch. **b** Open state of switch

(1) Establishment of differential equations

The state equation in switch conduction period is as follows:

$$\begin{cases} \dot{x} = A1 \cdot x + b1 \cdot V_s \\ y = C1 \cdot x \end{cases} \tag{1}$$

$$A1 = \begin{bmatrix} 0 & -\frac{1}{L} \\ \frac{1}{C} & -\frac{1}{R \cdot C} \end{bmatrix} \quad b1 = \begin{bmatrix} 1 \\ 0 \end{bmatrix} \cdot k \quad C1 = \begin{bmatrix} 0 & 1 \\ 1 & 0 \end{bmatrix} \tag{2}$$

where L is filter inductor, C is the filter capacitor, k is the transformer turns ratio, R is the load resistor.

The state equation in switch turn-off period is as follows:

$$\begin{cases} \dot{x} = A2 \cdot x + b2 \cdot V_s \\ y = C2 \cdot x \end{cases} \tag{3}$$

$$A2 = \begin{bmatrix} 0 & -\frac{1}{L} \\ \frac{1}{C} & -\frac{1}{R \cdot C} \end{bmatrix} \quad b2 = 0 \quad C2 = \begin{bmatrix} 0 & 1 \\ 0 & 0 \end{bmatrix} \tag{4}$$

(2) Average

The two segment linear state equation can be replaced by the average state equation, which is as follows:

$$\begin{cases} \dot{x} = A \cdot x + b \cdot V_{in} \\ y = C \cdot x \end{cases} \tag{5}$$

$$\begin{aligned} A &= d \cdot A1 + d' \cdot A2, & b &= d \cdot b1 + d' \cdot b2 \\ C &= d \cdot C1 + d' \cdot C2, & d' &= 1 - d \end{aligned} \tag{6}$$

Then:

$$A = \begin{bmatrix} 0 & -\frac{1}{L} \\ \frac{1}{C} & -\frac{1}{R \cdot C} \end{bmatrix}, \quad b = \begin{bmatrix} D \\ \frac{L}{0} \end{bmatrix} \cdot k, \quad C = \begin{bmatrix} 0 & 1 \\ D & 0 \end{bmatrix}$$

Imposed disturbance on above equations, and the disturbance is on the basis of the steady state. So ordering  $d = D$ , that is imposing disturbance on  $V_{in}$ ,  $D$ ,  $X$ ,  $Y$ , and separating the steady state and the transient state, then the steady state equation as follows:

$$A \cdot X + b \cdot v_{in} = 0, \quad Y = C \cdot X$$

The steady state value can be solved as follows:

$$X = -A^{-1} \cdot b \cdot v_{in}, \quad Y = -C \cdot A^{-1} \cdot b \cdot v_{in} \tag{7}$$

Imposed disturbance on (7)

$$\begin{aligned} v_{in} &= V_{in} + \hat{v}_{in} = D + \hat{d} \\ x &= X + \hat{x}, \quad y = Y + \hat{y}, \quad d' = D - \hat{d} \end{aligned}$$

Taking above into Eq. (7) can get:

$$\begin{aligned} \frac{d\hat{x}}{dt} &= A\hat{x} + b\hat{v}_{in} + [(A1 - A2)X + (b1 - b2)v_{in}] \cdot \hat{d} + (A1 - A2)\hat{d}\hat{x} \\ &+ (b1 - b2)\hat{d}\hat{v}_{in}\hat{y} = C\hat{x} + (C1 - C2)X\hat{d} + (C1 - C2)\hat{d}\hat{x} \end{aligned} \tag{8}$$

where,  $\hat{v}_{in}$ ,  $\hat{d}$ ,  $\hat{y}$ ,  $\hat{x}$  are the disturbance signals respectively.

(3) Linear

In order to get the linear state equation for description of the converter dynamic behavior, assuming that the disturbance signals is much smaller than the steady state, which is known a small signal assumes, that is:

$$\frac{v_{in}}{V_{in}} \ll 1, \quad \frac{\hat{d}}{D} \ll 1, \quad \frac{\hat{x}}{X} \ll 1, \quad \frac{\hat{y}}{Y} \ll 1$$

Ignore the second-order small signals  $\hat{d}\hat{x}$ ,  $\hat{d}\hat{v}_{in}$ , then

$$\begin{aligned} \frac{d\hat{x}}{dt} &= A\hat{x} + b\hat{v}_{in} + [(A1 - A2)X + (b1 - b2)v_{in}] \cdot \hat{d} \\ \hat{y} &= C\hat{x} + (C1 - C2)X\hat{d} \end{aligned} \tag{9}$$

The above equation is the state space average equations in the small signal disturbance, which is a linear non-time varying equation. It can be obtained

that the dynamic small signal characteristic equation of the converter in frequency form from the above equation.

$$\begin{cases} \hat{v}_O = G_{vs}\hat{v}_{in} + G_{vd}\hat{d} \\ \hat{i}_O = G_{is}\hat{v}_{in} + G_{id}\hat{d} \end{cases} \quad (10)$$

$$G_{vs} = \frac{D}{LCs^2 + \frac{L}{R}s + 1}, \quad G_{vd} = \frac{V_s D}{LCs^2 + \frac{L}{R}s + 1} \quad (11)$$

## 1.2 Phase-Shifted Full-Bridge Circuit Transfer Function

The basic idea of modeling the continuous working mode circuit to consider the conduction losses and the full bridge converter transformer leakage inductance is that the non-ideal device is equivalent to the ideal device and the parasitic device in series. For example, non-ideal power switching MOSFET is equivalent to the ideal switches and on-state resistance in series, the leakage inductance of the transformer primary winding resistor in series with the ideal transformer primary side, the secondary winding resistor in series with the secondary side of the ideal transformer.

### 1.2.1 The Average Modeling for Consideration of Conduction Losses of Full Bridge Converter

Figure 2 is the equivalent circuit of the full-bridge BUCK converter to consider the conduction losses.  $R_{ON\_P}$  is the on state resistance of the primary side MOSFET,  $R_{ON\_S}$  is the on state resistance of the secondary side synchronous rectifier,  $R_{T1}$  is the transformer primary winding resistance,  $R_{T2}$  is the transformer secondary winding resistance,  $R_L$  is the parasitic resistance of the filter inductor,  $R_C$  is the parasitic resistance of the filter capacitor.

The switch current of transformer primary side is about:  $i_s \approx I_L/n$ , and the average current of switch:

$$I_s = \frac{1}{T} \int_0^T i_L dt \approx \frac{1}{T} \int_0^{DT} \frac{i_L}{n} dt = \frac{D}{n} I_L$$

The RMS current of the power switch is:

$$I_{s_{rms}} = \sqrt{\frac{1}{T} \int_0^{DT} i_s^2 dt} \approx \frac{\sqrt{D} I_L}{n} = \frac{I_s}{\sqrt{D}} \quad (12)$$

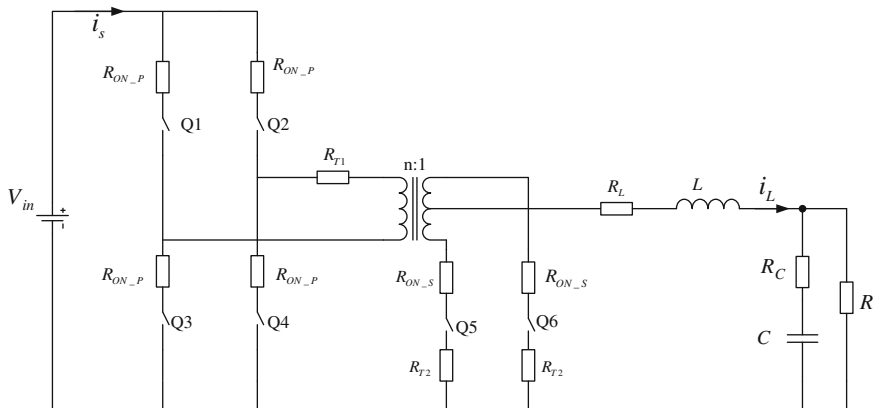


**Fig. 2** The equivalent circuit to consider the conduction loss

The average current of synchronous rectifier is:

$$I_{Q5} = \frac{1}{T} \int_0^T i_{Q5} dt \approx \frac{1}{T} \left( \int_0^{DT} I_L + \int_{DT}^{T/2} \frac{I_L}{2} dt + \int_{(1/2+D)T}^T \frac{I_L}{2} dt \right) = \frac{I_L}{2} \quad (13)$$

The RMS current of synchronous rectifier is:

$$I_{D3rms} = \sqrt{\frac{1}{T} \int_0^T i_{D3}^2 dt} \approx \frac{I_L \sqrt{2D+1}}{2} = \frac{nI_s \sqrt{2D+1}}{2D} = I_{D3} \sqrt{2D+1} \quad (14)$$

The power loss caused by on-stage resistor  $R_{ON}$  of power switch and resistor  $R_{T1}$  of transformer primary side:

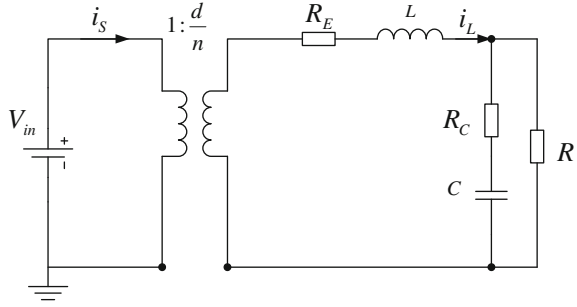
$$\begin{aligned} P_{ST1} &= (R_{on} + R_{T1}) I_{Srms}^2 = \frac{D(R_{on} + R_{T1})}{n^2} I_L^2 \\ &= \frac{4D(R_{on} + R_{T1})}{n^2} I_{D3}^2 = \frac{R_{on} + R_{T1}}{D} I_S^2 \end{aligned} \quad (15)$$

The power loss caused by on-stage resistor  $R_{ON\_S}$  of synchronous rectifier and resistor  $R_{T2}$  of transformer secondary side:

$$\begin{aligned} P_{DT2} &= (R_{ON\_S} + R_{T2}) I_{D3rms}^2 = (2D+1)(R_{ON\_S} + R_{T2}) I_{D3}^2 \\ &= \frac{(2D+1)(R_{ON\_S} + R_{T2})}{4} I_L^2 = \frac{n^2(2D+1)(R_{ON\_S} + R_{T2})}{4D^2} I_S^2 \end{aligned} \quad (16)$$

The average equivalent resistance that mapped to the inductance from the power switch branches in average model is:

**Fig. 3** The small-signal model of the full bridge converter considering the conduction loss



$$D_e \cdot \frac{2 \cdot R_{DS\_P} + R_{T1}}{n^2}$$

The average equivalent resistance that mapped to the inductance from the synchronous rectifier branches in average model is:

$$\begin{aligned} & \frac{D_e + 1}{2} \cdot (R_{DS\_S} + R_{T2}) \\ R_E := & D_e \cdot \frac{2 \cdot R_{DS\_P} + R_{T1}}{n^2} + \frac{D_e + 1}{2} \cdot (R_{DS\_S} + R_{T2}) + R_L \end{aligned} \tag{17}$$

Figure 3 shows the equivalent circuits taking the conduction losses of the full bridge converter into account, and the small signal transfer function can be derived as follows:

$$G_{ud}(S) := \frac{U_{in}}{n} \cdot \frac{1 + R_C \cdot C \cdot S}{L \cdot C \cdot \left(1 + \frac{R_C}{R}\right) \cdot S^2 + \left[(R_E + R_C) \cdot C + R_E \cdot R_C \cdot \frac{C}{R} + \frac{L}{R}\right] \cdot S + \frac{R_E}{R} + 1} \tag{18}$$

where,  $D_e$  is effective duty cycle,  $n$  is the ration of transformer,  $R_C$  is the parameter of LC filter capacitor.

### 1.2.2 The Average Modeling for Consideration of Transformer Leakage Inductor of Full Bridge Converter

The calculation formula of loss duty cycle is [3] (Fig. 4):

$$\begin{aligned} D_1 := & \frac{4 \cdot L_r \cdot D_e \cdot f_s}{n^2 \cdot R} \\ D := & D_e + D_1 = D_e \cdot \left(1 + \frac{4 \cdot L_r \cdot f_s}{n^2 \cdot R}\right) = \frac{n \cdot U_o}{U_{in}} \cdot \left(1 + \frac{4 \cdot L_r \cdot f_s}{n^2 \cdot R}\right) \end{aligned} \tag{19}$$

From the above, the effective duty cycle of transformer secondary side is less than the duty cycle of transformer primary side, and the bigger the loss duty cycle,

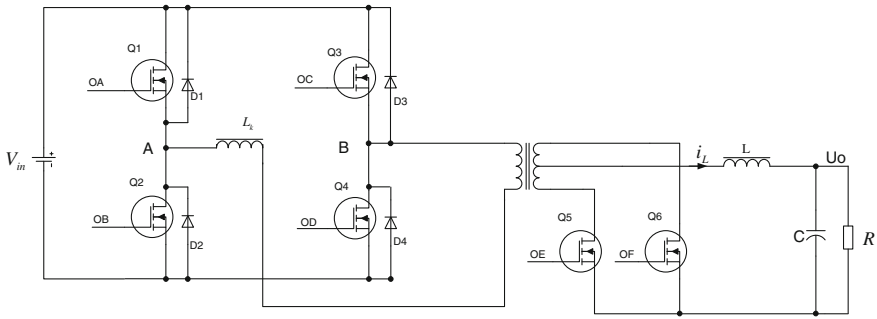


Fig. 4 The full bridge converter circuit for consideration of transformer leakage inductor

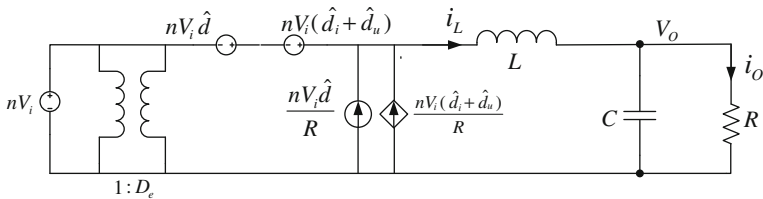


Fig. 5 The small-signal model of the full bridge converter considering the transformer leakage inductor

the less the effective duty cycle. So it should reduce the leakage inductor of transformer for reducing the loss duty cycle of the secondary side of transformer. The Fig. 5 is the equivalent circuit of full-bridge converter taking transformer leakage inductor of transformer into consideration. The small signal transfer functions are derived such as formula (20) [4].

$$G_{ud}(s) = \frac{V_i}{n} \cdot \frac{1}{s^2LC + s(L/R + R_pC) + R_p/R + 1} \tag{20}$$

where,  $R_p = \frac{4L_r f}{n^2}$ ,  $L_r$  is the leakage inductor of transformer.

### 1.2.3 The Average Modeling for Consideration of Transformer Leakage Inductor and Conduction Losses of Full Bridge Converter

The Fig. 5 is the equivalent circuit model of full-bridge converter taking transformer leakage inductor of transformer into consideration. The small signal transfer functions are derived such as formula (20).

Figure 6 is the equivalent circuit model of full-bridge converter taking transformer leakage inductor of transformer and conduction losses into consideration



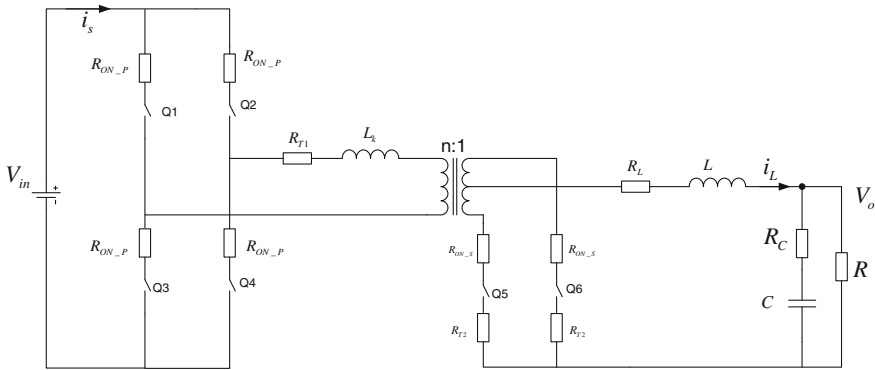


**Fig. 6** The full bridge converter circuit for consideration of transformer leakage inductor and conduction losses

[2]. The total equivalent resistor  $R_{E2}$  which is equivalent to the on-state resistance of transformer primary side MOSFET and synchronous rectifier in series with the inductor is as follows:

$$R_{E2} := \frac{2 \cdot \left(D_e + \frac{D_1}{3}\right) \cdot R_{DS\_P} + \left(D_e + \frac{2 \cdot D_1}{3}\right) \cdot R_{T1}}{n^2} + \frac{\left(\frac{D_e + 1}{2} + \frac{D_1}{3}\right) \cdot (R_{DS\_S} + R_{T2}) + R_L}{n^2} \quad (21)$$

Similarly, the transfer function of small signal model can be derived as follows according to the Fig. 3.

$$G_{ud}(S) := \frac{U_{in}}{n} \cdot \frac{1 + R_C \cdot C \cdot S}{L \cdot C \cdot \left(1 + \frac{R_C}{R}\right) \cdot S^2 + \left[(R_{E2} + R_P) \cdot \left(1 + \frac{R_C}{R}\right) \cdot C + R_C \cdot C + \frac{L}{R}\right] \cdot S + \frac{R_{E2} + R_P}{R} + 1} \quad (22)$$

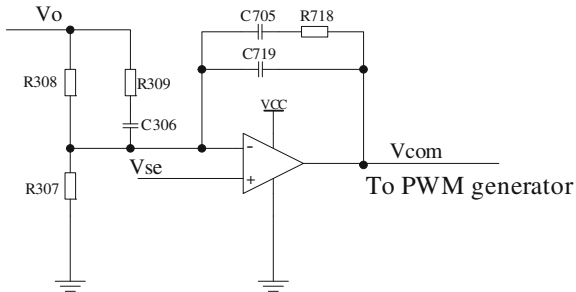
It is expressed as follows written in the form of second-order system.

$$G_{ud}(S) := \frac{U_{in}}{n \cdot \left(\frac{R_E + R_P}{R}\right)} \cdot \frac{1 + \frac{S}{\omega_{z1}}}{1 + 2 \cdot \xi \cdot \left(\frac{S}{\omega_0}\right) + \left(\frac{S}{\omega_0}\right)^2} \quad (23)$$

### 1.3 Compensation Network Transfer Function

It can be obtained using the node current equation in the frequency domain (Fig. 7):

**Fig. 7** Voltage loop compensation circuit



$$\frac{V_O - V_{SE}}{R_{308}} + \frac{V_O - V_{SE}}{R_{309} + \frac{1}{S \cdot C_{306}}} = \frac{V_{SE} - V_{COM}}{\frac{1}{S \cdot C_{719}}} + \frac{V_{SE} - V_{COM}}{R_{718} + \frac{1}{S \cdot C_{705}}} \quad (24)$$

It can be derived:

$$\begin{aligned} & \left( C_{719} \cdot S + \frac{C_{705} \cdot S}{1 + R_{718} \cdot C_{705} \cdot S} \right) \cdot V_{COM}(S) \\ &= \left[ \frac{1}{R_{308}} + \left( C_{719} \cdot S + \frac{C_{705} \cdot S}{1 + R_{718} \cdot C_{705} \cdot S} + \frac{C_{306} \cdot S}{1 + R_{309} \cdot C_{306} \cdot S} \right) \right] \cdot V_{SE}(S) \\ & - \left( \frac{1}{R_{308}} + \frac{C_{306} \cdot S}{1 + R_{309} \cdot C_{306} \cdot S} \right) \cdot V_O(S) \end{aligned} \quad (25)$$

Ordering:

$$\begin{aligned} a &:= C_{719} \cdot S + \frac{C_{705} \cdot S}{1 + R_{718} \cdot C_{705} \cdot S} \\ b &:= \frac{1}{R_{308}} + \left( C_{719} \cdot S + \frac{C_{705} \cdot S}{1 + R_{718} \cdot C_{705} \cdot S} + \frac{C_{306} \cdot S}{1 + R_{309} \cdot C_{306} \cdot S} \right) \\ c &:= \frac{1}{R_{308}} + \frac{C_{306} \cdot S}{1 + R_{309} \cdot C_{306} \cdot S} \end{aligned}$$

In the small-signal model, the reference input of the  $V_{SE}(s)$  is 0, so the transfer function  $V_{COM}$  to the converter output voltage is:

$$G_C(S) := \frac{c}{a}$$

It can be obtained on the simplification as follows:

$$G_C(S) := \frac{R_{308} + R_{309}}{R_{308} \cdot R_{309} \cdot C_{719}} \cdot \frac{\left( S + \frac{1}{R_{718} \cdot C_{705}} \right) \cdot \left[ S + \frac{1}{(R_{308} + R_{309}) \cdot C_{306}} \right]}{\left( S + \frac{1}{R_{309} \cdot C_{306}} \right) \cdot S \cdot \left[ S + \frac{C_{719} + C_{705}}{(R_{718} \cdot C_{705} \cdot C_{719})} \right]} \quad (25)$$

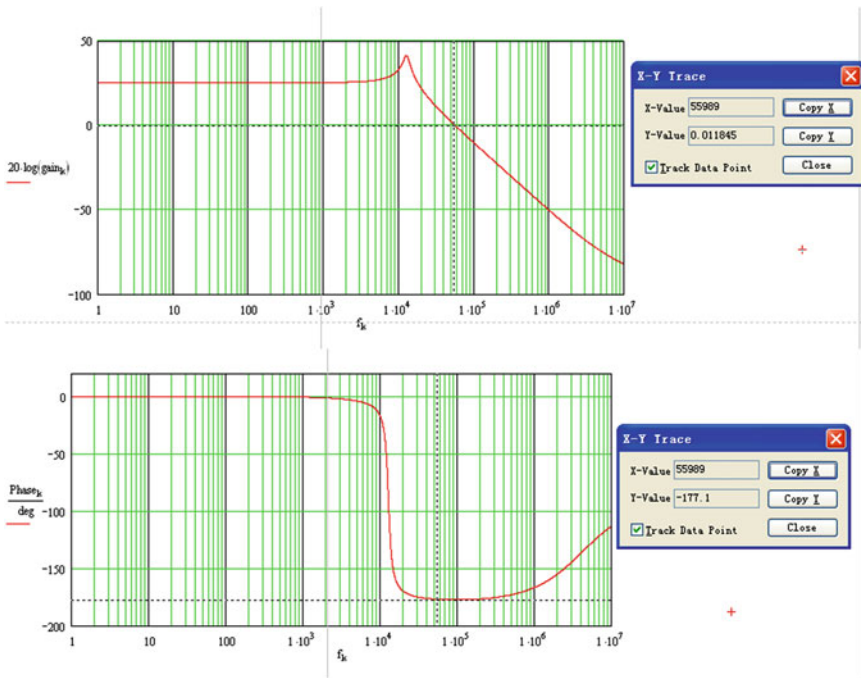


Fig. 8 The he main circuit Bode diagram considering the transformer leakage inductance and conduction losses

## 2 Stability Analysis

### 2.1 Stability Analysis for Main Circuit

Selecting one normal working condition, it can get the following Bode plot of the main circuit.

Figure 8 shows the crossover frequency of 55.9 kHz, the phase margin of 2.9°, from which the system relative stability is rather poor, so it is necessary for PI compensator.

### 2.2 The Effect to System Stability with Compensation Network

The Fig. 9 is the system Bode diagram by adding voltage loop feedback compensation net showing in Fig. 7, in which the parameter of capacitor and resistor is optimized and the working condition is the same as show in Sect. 2.1. From Fig. 9, it is shows that the crossover frequency is 38.9 kHz, the phase margin is 43.5°. The

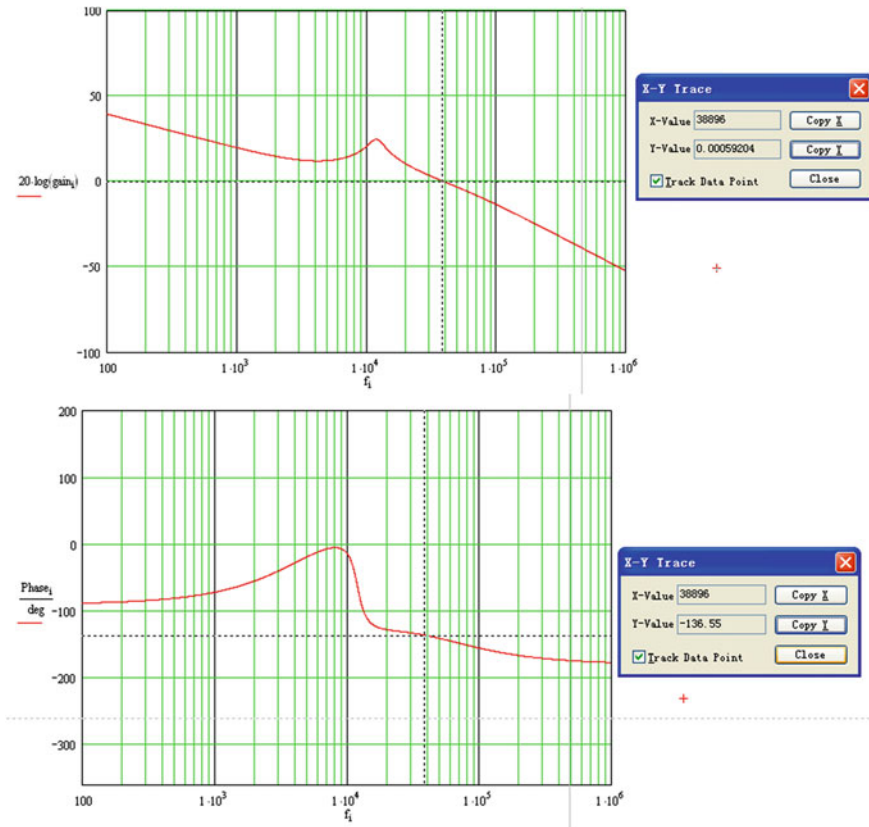


Fig. 9 The Bode diagram by adding the feedback compensation network

relative stability of system loop has been greatly improved comparing to the 2.9° of main circuit without compensation network.

In addition, this paper analyzes the stability characteristics of the DC/DC in all work conditions. The simulation results showed that the system with high relative stability and good dynamic response characteristics. In all work conditions, the lowest crossover frequency is 29.8 kHz, and the worst phase margin is 37.4°.

### 3 System Loop Stability Testing

In order to verify the correctness of the modeling approach and simulation results, the network analyzer is used to do the loop gain test with the DC–DC sample, the test results and the simulation results are compared in one diagram.

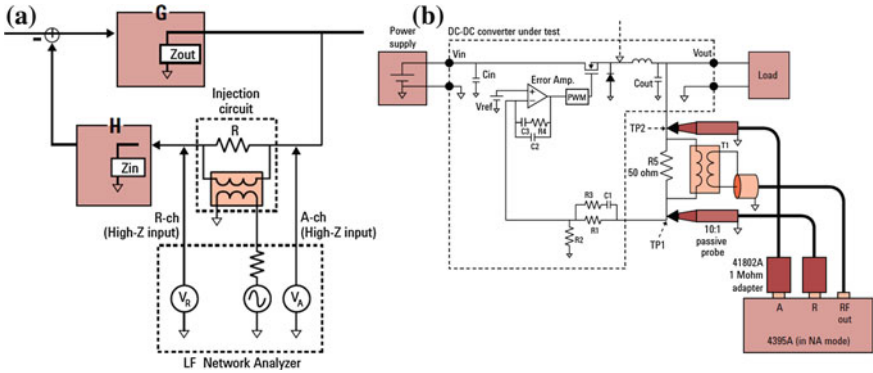


**Fig. 10** a Loop gain measurement method. b Configuration for measuring loop gain

### 3.1 Introduction of Test Methods

In this paper, the voltage loop test is used with Agilent’s network analyzer, with type of 4395A. The basic principle is injecting the analyzer’s source signal into the feedback loop via an injection circuit without breaking the loop. In the case of the DC–DC converter, the test signal is generally injected at the point just before the divider circuit on the feedback path by using the floating injection circuit that consists of a transformer and a resistor, as shown in Fig. 10a. By injecting the test signal at the point where  $Z_{in} \gg Z_{out}$  is satisfied and using the resistor  $R$  that satisfies  $Z_{in} \gg R \gg Z_{out}$ . The round transfer function  $-GH$  is measured with the ratio measurement  $A/R$  without disturbing the original loop characteristics. The transformer  $T1$  and the resistor  $R5$  are configured the signal injection circuit. The resistance value of  $R5$  should be sufficiently smaller than  $Z_{in}$ . In general, the resistance around  $50 \Omega$  is appropriate. The transformer should have an impedance that is not extremely smaller than the analyzer’s source output impedance,  $50 \Omega$ . In the measurement example shown in Fig. 10b, the source signal was injected with the 1:1 pulse transformer.

### 3.2 Measurement Results Analysis

In order to validate the calculation results for better comparison, test results and calculation results are plotted in the same graph with the same work conditions, such as input voltage, output voltage, output voltage, resistor and capacitor parameter and so on. The measurement results and calculation results show in Fig. 11.

The calculation results are consistent with the measurement result from the Fig. 11 in addition to the high-frequency and low frequency area. Because the excitation signal lower greatly through the transformer in low frequency and it is

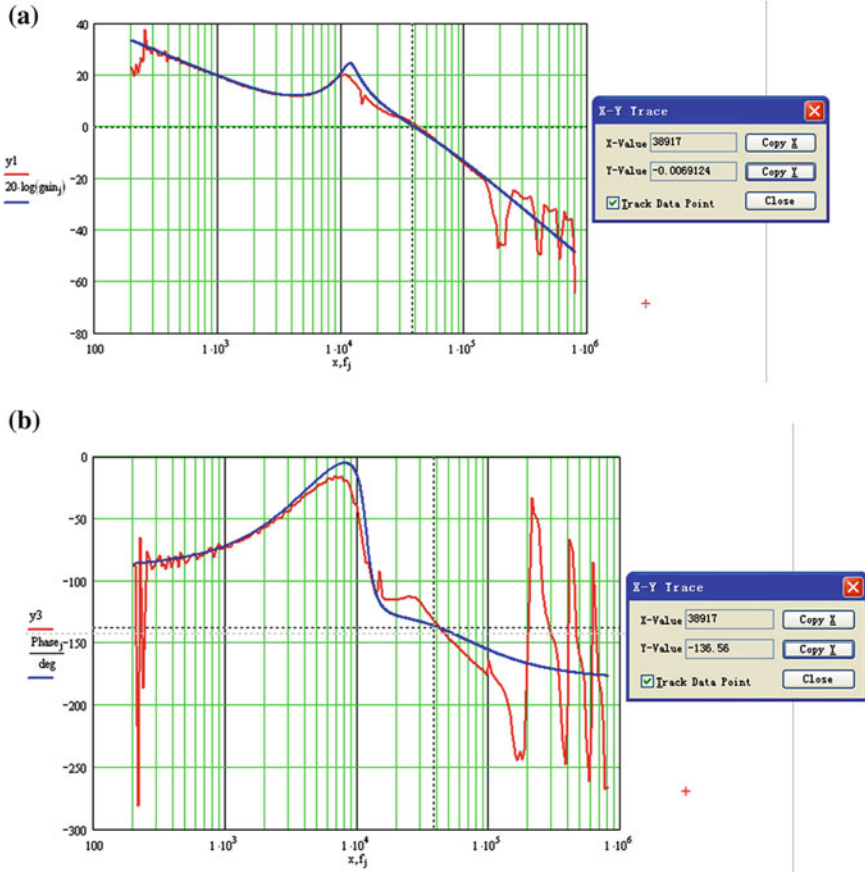


**Fig. 11** The comparison of Voltage loop gain for simulation and measurement results. **a** Amplitude-frequency characteristics. **b** Phase frequency characteristics. *Note* The red lines for the test results, the blue line for the simulation results

near the resonant frequency of the transformer due to non-ideal characteristics for the transformer in high frequency, so the modeling and analysis in this paper is validated. Overall, equivalent modeling method is correct in this paper, which is significant for optimization of the parameters of the compensation network and the main circuit base on it. It also plays an important role in further digital DC-DC design base on the modeling and analysis.

## 4 Conclusion

The main circuit model base on averaging method, the compensation network circuit model, and the PWM waveform generator circuit model are established in this paper, so the overall DC/DC transfer functions are derived. Finally, DC/DC sample are tested with Agilent's network analyzer. The modeling approaches taking leakage inductance of transformer and on-state resistors of power switches into account is feasible from the measurement results, which can help optimize the key parameters and improve the performance of DC/DC converter. It also plays an important role in further digital DC–DC design base on this.

## References

1. Cao X, Qiao K, Fu G (2011) The small signal model of buck converter with compensating network. Electrical switches, Novemb 2011
2. Lin A (2004) DC–DC switching converter modeling analysis and research. The doctoral thesis of Nanjing University of Aeronautics and Astronautics
3. Yuan J, Ma R, Fan P (2008) Research on phase-shifted full-bridge ZVS DC/DC converter with auxiliary branch. *Power Electron Technol* 42(5):23–25
4. Vlatkovic V (1992) Small-signal analysis of the phase-shifted PWM converter. *IEEE Trans Power Electron* 7:128–135

# The HV Safety Management Design of Battery System in Electric Vehicle

Tao Yan, Qi qian Jin and Fuquan Zhao

**Abstract** As the development of electric vehicle, we have to face the questions about HV safety. If the HV system, especially the battery system, is not designed properly, it will be impossible to make a safety car to the customer. Under certain circumstance, it may cause direct threatens to the people life. So it is very important to have a good analysis of the battery system safety design. This paper mainly pays attention to the safety solution of battery system in electric vehicle. From different levels, including battery cell design, battery system design and vehicle system safety design, we provide some safety concept. It will help a lot of the electric vehicle's safety.

**Keywords** Hazardous voltage in lock (HVIL) · Crash · Battery system · Battery management system (BMS) · Battery management unit (BMU)

## 1 Introduction

The battery system is a key component in electric vehicle, it provide power to propel the vehicle, however if not pay enough attention to the safety design, it will be very dangerous. And the accidents happen recently are mainly caused by the battery system. This paper mainly pay attention to this problem, aim to provide some design solutions.

---

F2012-B08-016

---

T. Yan (✉) · Qi qianJin · F. Zhao  
Geely Automobile Research Institute Ltd, Zhejiang, China  
e-mail: 94590998@qq.com



## 2 Battery System Analysis

To design a safe battery system, we need a detailed analysis of it. We will discuss it from three different ranks.

### 2.1 Battery Level

The battery system is mainly consists of hundreds of battery cells. For the battery cells, especially Li-ion battery, which becoming more and more intimate with our daily life, many test standards and methods have been published to verify the safety performance of it under abuse-use, such as over-charge, over-discharge, short-circuit. And it has made a great progress on the research [1].

The main solution to improve the cell safety ability can be described as below: Thermal closed film materials are used in the battery, as the battery inner temperature reaches a warning level, the battery separator film will close the chemical reaction, which will effectively reduce the over charge [2]; By adding flame retardant additives in the electrolyte, can effectively reduce battery short-circuit, which may cause security incidents; Research and development of new electrode materials, such as LiFePO<sub>4</sub>-instead of the currently widely used LiCoO<sub>2</sub> materials, can significantly improve the safety performance of the sub-battery.

### 2.2 Battery System Level

Besides battery cells, battery management system (BMS) paly the most important role in the battery system. To some extent, the other component including connecting wiring harness, HV accessories as contactors and fuses, crash monitor, cooling or heating systems, and electric control unit composed of BMS. The detailed battery system composition can refer to Fig. 1.

For the connecting wiring harness, special junction station is designed for specified project to improve the reliability. Also more and more fuses and contactors are embedded in the battery system to ensure the safety.

To make sure the battery system in a safe state, even when the charging mode, especially DC charging, we need the battery system to detect the battery signal by itself. Also, when the battery management system is failed, we need a method to make the contactors open.

One or more crash monitors are also embedded in the battery pack to detect the battery crash state, to cut off the HV contactor immediately. During this phase, a sophisticated algorithm should be designed to avoid the fault signal of the monitor.

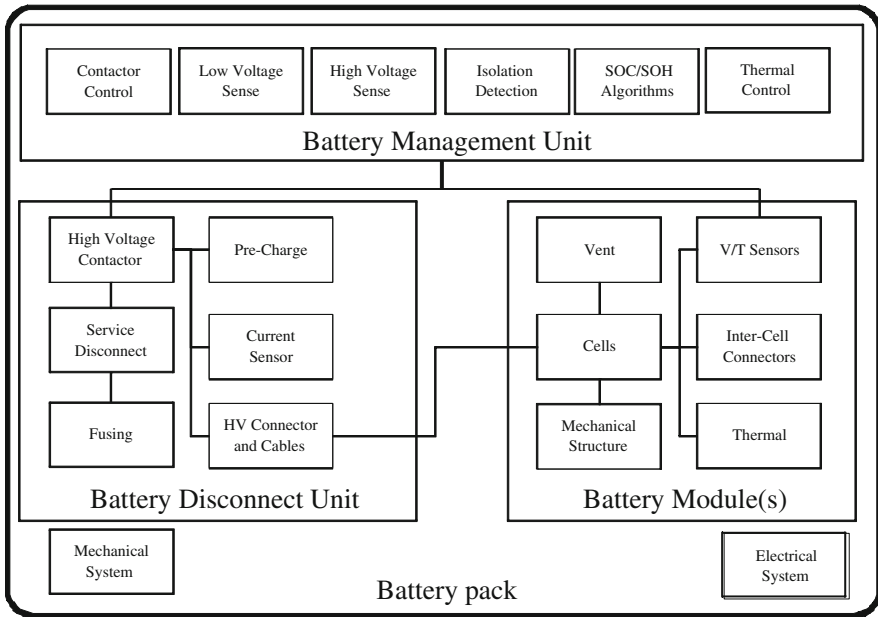


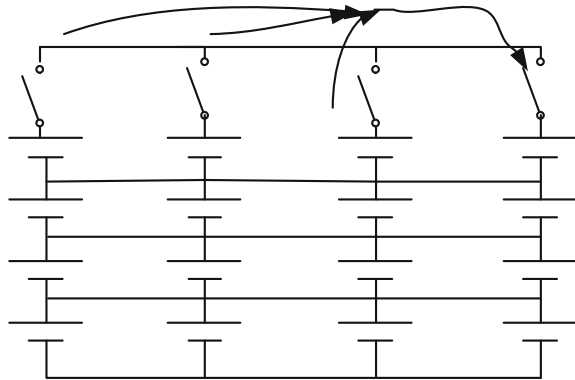
Fig. 1 Battery pack mainly component

For battery management system, the battery should keep the reliability of itself, it means when the battery detect the fault signals the battery system should have certain protection strategy to keep itself in a good state.

Such as, the temperature fault, when the battery cell temperature is higher than a set value, a warning signal will be triggered. Then the cooling system will make sense to keep the battery in a proper temperature. Also when the cell voltage is higher or slower than the warning value, the maximum charging power and maximum discharging power limit will be reduced to protect the cell from over discharge and over discharge.

Besides, the battery structure design is really very important. As most of the battery system are composed of hundreds of cells, which are in parallel or in series. When a cell is in a bad state such as in short, the cell will be charged by the cells adjacent, make the cell temperature will raise really quickly. The high temperature is a key problem of the battery safety. Even when a cell capacity is becomes lower, when charging or discharging, the cell will be over charging or over discharging easily. Under such situation, the whole battery system capacity will be lower and lower in a short time. So we need to separate the bad cell, when it is really in a bad state. Figure 2 just provides a solution, which by adding some switches; we can cut off the connection between bad state cell and the adjacent cells. Also some heat insulation structures and materials should be designed really carefully.

**Fig. 2** Battery cells in series and parallels



### 2.3 Vehicle Level

The battery system in an electric vehicle may have different operation mode in accordance with different driving mode, mainly including charging and discharging.

As in the battery system, there are different relays for different control aims. We can just divide the battery system safety to different ranks. For different rank, we find different solutions.

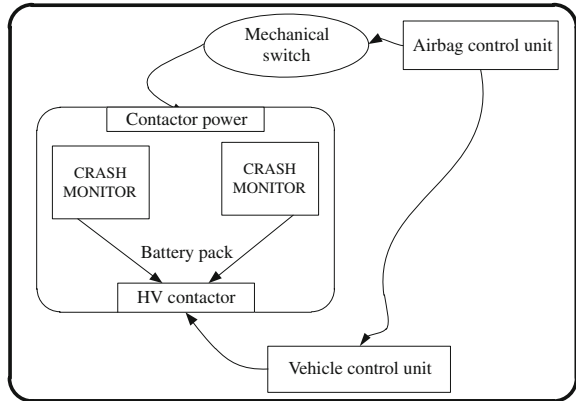
When the battery system is mounted on a vehicle, some extra problems will appear. Such as connection fault and insulation fault of the vehicle. So we should have some safety solution from vehicle level to make sure the safety of passenger and the battery system.

First of all, HVIL detection is essential, whatever the detection theory, it is just for all the HV connection is reliable. Otherwise, the HV contactor will never be closed. Also the insulation state between battery system and chassis should be detected continuously, to make sure the insulator resistance is in a safe value.

Second, the battery system should have certain protection action when receiving some emergency signals, as crash signal. As crash will be the most dangerous circumstance for the battery and the vehicle, in this case, we may have some redundant design both software and hardware. The main topology of the design is as Fig. 2 described. Of course, extra ECU like airbag control unit and vehicle control unit will be involved.

When the airbag control unit detect the crash happen, it will send an emergency signal to open a mechanical switch, which will cut off the HV of the battery from vehicle. As a redundant protection, the airbag control unit will also transmit a signal to Vehicle control unit via CAN bus, in case the mechanical switch is destroyed, the signal will be received by BMU, which will open the HV contactor too.

**Fig. 3** Vehicle safety control strategy



### 3 Results

By the analysis above, we just provide a better solution to design a more safe battery system.

First better cell is the most important; second we need a system level design, which include firmly structure design, cell over temperature protection equipment, effective temperature control system and active safety defend system.

Then from the vehicle control, we also add some redundant safety protection strategy to make sure the battery safety (Fig. 3).

### 4 Conclusion

From different level, we can have different protect solutions, however all the solutions just cannot make sure the safety of the electric vehicle. To make the electric vehicle as safe as traditional vehicle, we still have a lot of work to do.

Besides the realization of the different solution may need to find some product suppliers, which is also very difficult. Such as cell isolation device, crash switch and some other sensors are still unavailable in the market. In addition, to add more sensors and switches is a big challenge to the cost and space.

To different safety purpose and different project expectation, we may have different solutions. Of course the best solution will need more extra resources and costs more. Most of the case, we have to find a middle solution to a certain project.

### References

1. Liu C (2008) Study on the safety performance of Li-ion batteries [A]. Chinese Battery Industry
2. Chen Y-H (2006) Research of explosion mechanism of lithium-ion battery [J]. Chin Prog Chem 03:823-831

# The Free Piston Stirling Principle as Prime Mover for Alternant Hydraulic Propulsion Systems

Horia Abaitancei, Cristi Irimia, Gabriel Carciumaru, Ionut Tudor Soare and Sebastian Radu

**Abstract** The objective of the presented research work is the demonstration of the working principle as energy efficient and environmental friendly, low cost vehicle propulsion system of the free piston Stirling principle coupled with the alternant hydraulic transmission in order to use the alternant displacement of the Stirling principle, also to the hydraulic transmission and convert the alternant movement of the liquid using a free wheel based hydraulic motor. The design methodology considers the advantages of efficiency, noise and low emissions of Stirling principle, that can be further improved by a free piston solution and the advantages of a direct alternant energy transfer to the liquid column that is converted in a free wheel based hydraulic motor. An analytical and 1D multi-domain model is used in order to demonstrate the running principle, performance and parameter influences that allow the simulation of the combined Stirling principle with alternant hydraulic transmission integrated on a vehicle. For the heat transfer and flow simulation of the Stirling prime mover, 3D CFD software is used to simulated the temperature distribution. Experimentally the solution was demonstrated on a test rig and integrated on a ATV type demonstration vehicle equipped with the alternant hydraulic propulsion system. Flow, thermal and mechanical parameters

---

F2012-B08-020

---

H. Abaitancei (✉) · I. T. Soare · S. Radu  
Transilvania University of Brasov, Brasov, Romania  
e-mail: h.abaitancei@unitbv.ro

I. T. Soare  
e-mail: ionut-tudor.soare@unitbv.ro

C. Irimia  
LMS Romania, Brasov, Romania

G. Carciumaru  
World Machinery Works, Bacau, Romania

are measured to evaluate overall system performance. The former research work of the authors was focused on the demonstration and performance evaluation of the alternant hydraulic propulsion, being demonstrated its efficiency (up to 95 %), adaptability and low mass qualities. Main advantages of the Stirling principle may be improved by using a proper transmission. Coupling also the transmission based on the same alternant principle is a low cost, simple, efficient way to maintain the advantages of the Stirling energy conversion in the same time with an application of the hydraulic transmission that works also alternant in a more efficient way.

**Keywords** Vehicle · Propulsion · Stirling · Hydraulics · Simulation

## 1 The Technical Solution

The objective of the presented research work is the demonstration of the working principle as energy efficient and environmental friendly, low cost vehicle propulsion system of the free piston Stirling principle coupled with the alternant hydraulic transmission. The basic concept is, that primary energy converter and transmission have to be fitted and accorded one to each other, and functions have to be transferred from a system to the other in order to assure overall system efficiency.

The general concept is based on using the Stirling principle as primary energy source, able to convert the thermal energy resulting from fuel combustion. Fuel is still a very important high energy density carrier, at least for the foreseeable future, when significant measures for CO<sub>2</sub> reduction are stringent necessary.

The Stirling engine, considering the synthesis presented in [1], pp. 159–160, has as major advantages: continuous, external combustion is associated with low emissions and noise, free choice of the fuel, no combustion of lubrication oil, more simple injection system, potential for lower consumption due to improved cycle efficiency. The theoretical efficiency is affected by the continuous movement of the pistons in opposite to the discontinuous movement of the ideal cycle. Other factors that affect real to ideal cycle differences are isothermal processes, limited heat transfer in the regenerator, internal heat transfer. The disadvantages of the conventional Stirling engine are the costly heavy construction, where a significant contribution has the mechanical mechanism of fluid transfer and for gathering the rotational movement. Difficult control for load adjustment, large cooler areas, running up (30 s) and shut off (120 s) behaviour are factors considered also as disadvantages that limit the vehicle applications being necessary supplementary research, considering that proven applications in combined heat and power plants are working at 94 % efficiencies, with low asset and maintaining costs.

Analysing the disadvantages, it was considered that an improvement of the Stirling design would be the avoidance of the mechanical mechanism and direct energy transfer to the fluid power based transmission, the transfer of the load control, start up and switch off functions also to the fluid power transmission by

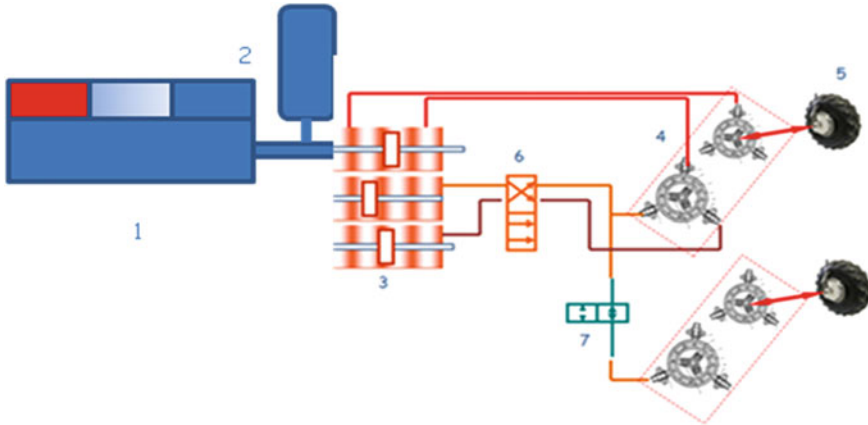


**Fig. 1** Working principle of the Stirling alternant hydraulic propulsion system

using an accumulator that would cumulate several functions: assist start up and switch off, assure control functions of power output, allowing the engine to run at constant parameter, allow a free control of piston movement, including constant volume run, allow brake energy recovery.

At transmission level the fluid power based option was chosen due to its advantages for power density, precise control, and simple layout for the propulsion when multiple hydraulic actuators have to be fed to obtain the propulsion functions of integral wheel actuation, considering running during cornering, synchronisation of wheel speed when excessive slip occurs. The typical disadvantage of lower efficiency has been considered to be improved by using alternant hydraulic solutions based on a liquid column that moves alternately and actuates a free wheel based mechanical translational to rotational displacement converter that propels the vehicle wheels. This configuration couples the translational movement of the Stirling engine pistons with the translational movement of the liquid column, avoiding normal forces that are associated with significant frictional losses at engine level.

The working principle of the Stirling-alternant hydraulic propulsion system is given in Fig. 1. The free piston Stirling engine 1 is driving the pistons of the hydraulic generator 3 that moves the liquid column in an alternant displacement to the freewheel motors 4 that propel the vehicle wheels 5. The hydraulic accumulator 2 has the role to adjust the energy delivered to the hydraulic pistons, to control the displacer movement of the Stirling engine and to store the energy recovered during the brake process. The directional control valve 6 assures a change in the succession process of the liquid column actuation, so that it is possible to change the rotational direction of the propelling wheel. The directional control valve 7 assures that the same flow is directed to the hydraulic motors for the case then road support is significant different for two or all four wheels.

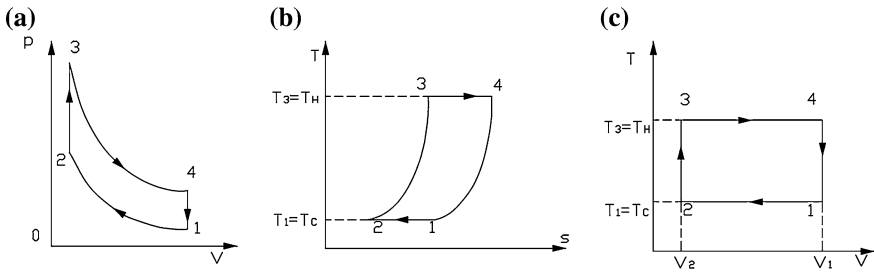


**Fig. 2** Ideal working cycle of the Stirling engine: **a** pressure Vs. volume; **b** temperature Vs. entropy; **c** temperature Vs. volume

Otherwise, the parallel connection of the hydraulic consumers allows the speed that is installed due to road resistance, so that a safe cornering is assured.

## 2 Simulation of the Stirling Hydraulic Propulsion System

The objective of the simulation work was to have a set of possibilities to evaluate the potential of the Stirling engine and to couple the model with the hydraulic one. At first level, the thermodynamic model was analysed, considering the basic thermodynamic equations that compose the cycle, two isochoric and two isothermal functions, presented in Fig. 2.

In order to have a general overview of the thermodynamic processes and the elementary influences on system performance basic analytical models were used, having the parameters named in Table 1.

The equation of mechanical work is given by the equation:

$$L = mR \left[ T_3 \ln \left( \frac{V_4}{V_3} \right) - T_1 \ln \left( \frac{V_1}{V_2} \right) \right] \tag{1}$$

The data identified for the working parameters in order to assure the system performance for vehicle propulsion are given in Table 2, having bolded the values considered for comparison.

It can be observed that a high potential for power density 163 kW/0.2 l working space at high efficiencies 55–60 % are theoretical possible. Considering the worst case efficiencies of fluid power propulsion of 80 %, overall propulsion efficiencies are in the range of 44 % significant above the actual performance of 25 % typical for vehicle propulsion systems.

The losses associated with the real model are cumulated and described by different authors that developed overall models for the Stirling engine. An overview on these models is given in (2). The equation confirmed by Beale [2], p. 99, also for free piston Stirling engines working in the temperature range 650–65 °C



**Table 1** Nomenclature of parameters for thermodynamic analysis

Physical parameter	Symbol	Units	Physical parameter	Symbol	Units
Pressure	p	(N/m <sup>2</sup> )	Volume of the regenerator	V <sub>reg</sub>	(m <sup>3</sup> )
Gas mass	M	(kg)	Temperature of the regenerator	T <sub>reg</sub>	(°K)
Volume of hot zone	V <sub>H</sub>	(m <sup>3</sup> )	Power	P	(kW)
Temperature of hot zone	T <sub>H</sub>	(°K)	Speed	N	(1/min)
Volume of cold zone	V <sub>C</sub>	(m <sup>3</sup> )	Mechanical work	L	(Nm)
Temperature of cold zone	T <sub>C</sub>	(°K)	Max./min. working volume	V1/V2	(m <sup>3</sup> )

**Table 2** Influences of running parameters on the output power for the ideal Stirling thermodynamic power

m kg	R J/(kg·K)	t <sub>1</sub> °C	t <sub>3</sub> °C	V <sub>1</sub> l	V <sub>2</sub> l	L J	η [-]	N 1/min	P kW
<b>0.05</b>	287	100	10	0.1	0.2	895.1996	24	1000	<b>15</b>
<b>0.1</b>	287	100	10	0.1	0.2	1790.399	24	1000	<b>30</b>
0.1	287	<b>100</b>	<b>10</b>	0.1	0.2	1790.399	24	1000	<b>30</b>
0.1	287	<b>500</b>	10	0.1	0.2	9747.729	63	1000	<b>162</b>
0.1	287	350	10	0.1	<b>0.15</b>	3956.529	55	1000	<b>66</b>
0.1	287	350	10	0.1	<b>0.2</b>	6763.73	55	1000	<b>113</b>
0.1	287	350	10	0.1	0.2	6763.73	55	<b>1000</b>	<b>113</b>
0.1	287	350	10	0.1	0.2	6763.73	55	<b>1500</b>	<b>169</b>

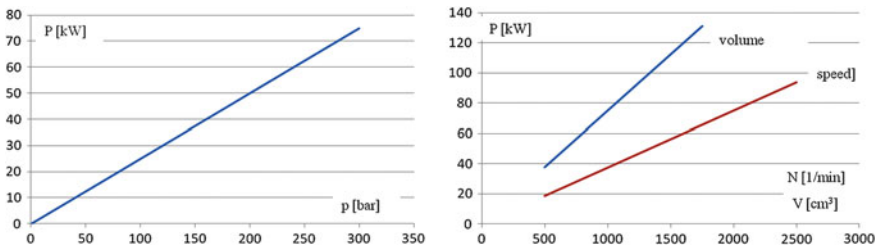


**Fig. 3** Influence of running and design parameters on Stirling engine power output

shows the influence of different design and working parameters and results are plotted in figure N for the power range used for conventional vehicles.

$$P[kW] = 0.015 \times p[bar] \times \frac{N[\frac{1}{min}]}{60} \times V[cm^3] \tag{2}$$

The manner how running and design parameters are influencing the output power is given in Fig. 3.

It can be observed that the cylinder volume has a more important influence on power than speed. Power density can be obtained with high pressure and speed. Also acceptable running and design parameters are supporting system performance

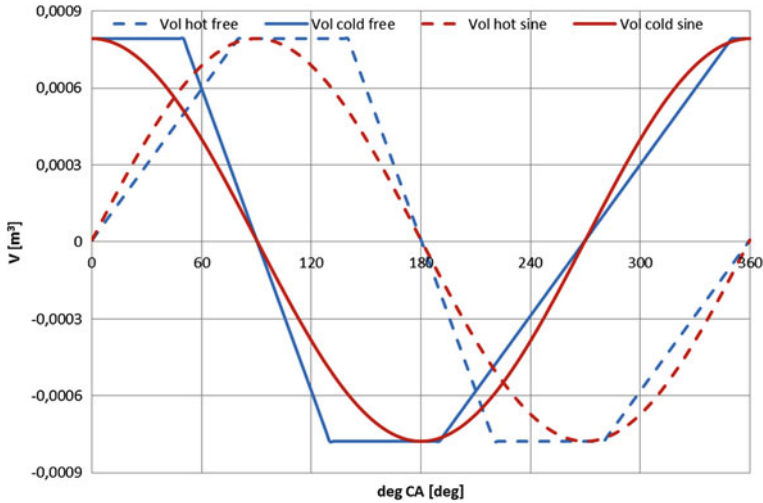


**Fig. 4** Displacer and power piston movement for conventional sin-function and free shape design

using a real model equation as it is the proposal of Beale [2]. In this case supplementary measures, as proposed, like free shape of piston displacement and direct power transfer to the hydraulic liquid improve system efficiency. Due to limited compressibility of hydrogen, a parameter study may be performed if the higher heat capacity of hydrogen can be compensated by higher working pressures of another fluid.

### 2.1 Energy Balance Model

In order to identify the influence of piston speed on cycle energy balance, a zero-dimensional time dependent model was build up. The model is based on the energy balance of a control volume associated to the working space. The internal energy of the trapped gas si changed due to external interactions: change of mechanical work at displacer and power piston level and heat exchange during heating and cooling. The equations resulting from the energy balance and integrated into the perfect gas equation, has as result the mathematical time dependency of the pressure (Eq. 3), as functions of the time dependent interactions. Main time dependent influences are given by the displacement of the piston.

$$P = \frac{M.R}{\frac{V_H}{T_H} + \frac{V_C}{T_C} + \frac{V_{reg}}{T_{reg}}} \tag{3}$$

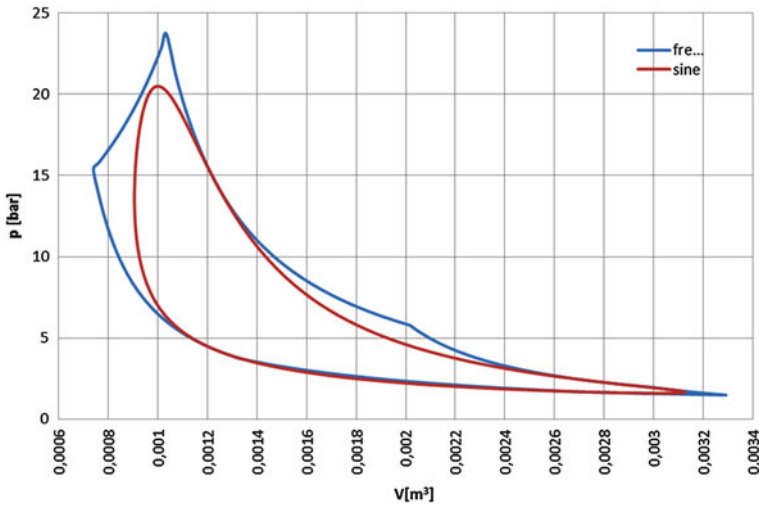


Fig. 5 Thermodynamic cycle of the Stirling engine for conventional and free shape piston displacement

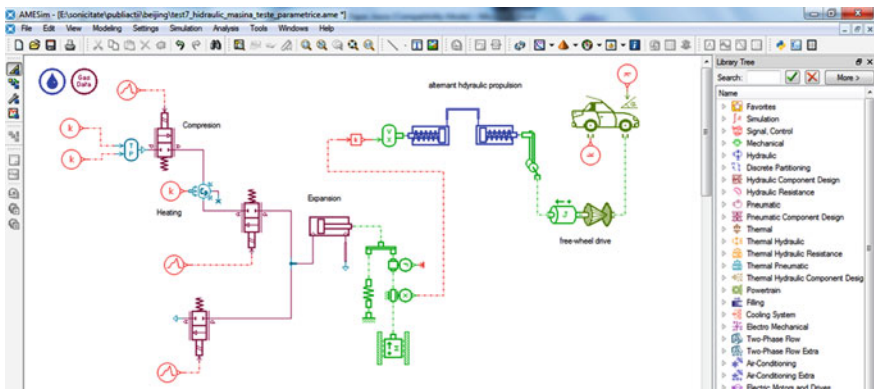


Fig. 6 Multi-domain model of the Stirling-alternant hydraulic propulsion system

Considering as reference, the sin-type displacement of the Stirling engine pistons having a 90° phase shift, a change of piston type of movement, as given in Fig. 4, has been applied. It can be observed, that only a small change of piston displacement, has a significant influence on the thermodynamic cycle, as can be observed in Fig. 5. The net mechanical work output in the case of conventional piston movement is 31.5 J and in the free displacement shape mode is 39.8 J, that mean an improvement of 21 %.

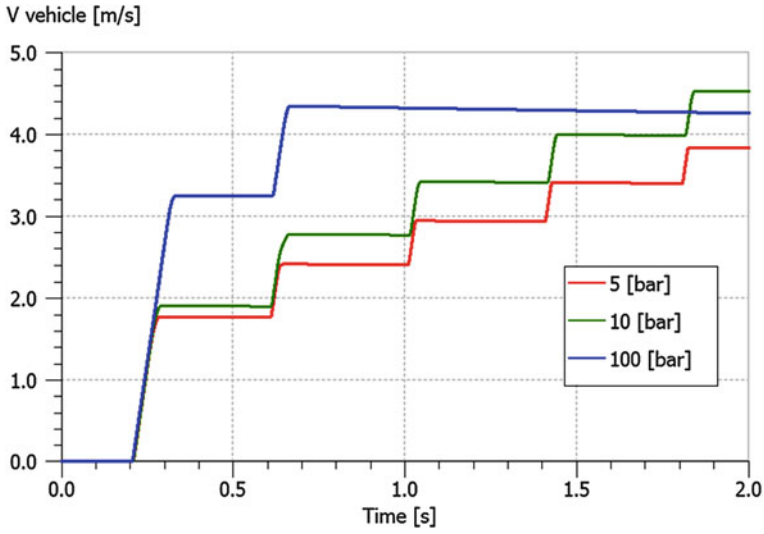


Fig. 7 Influence of Stirling engine working pressure on vehicle output speed-time dependency

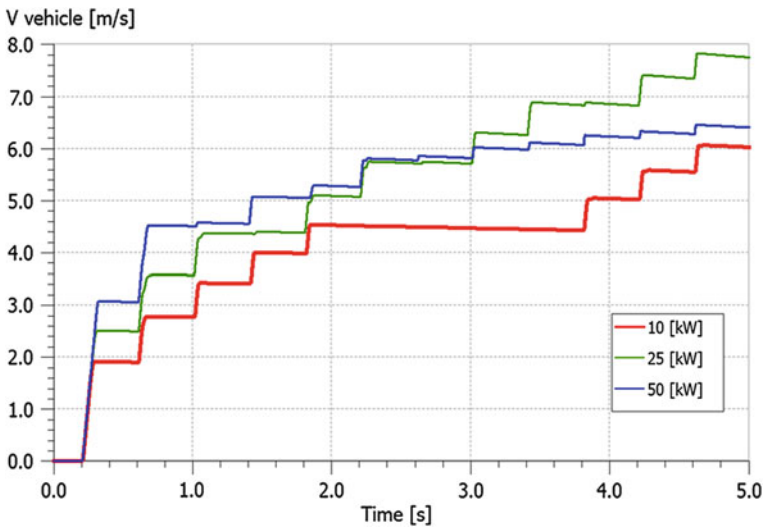


Fig. 8 Influence of added heat on vehicle performance

### 2.2 Multi-Domain Modelling and Simulation

For time-dependent analysis and coupling of the different subsystems from Stirling engine to the alternant hydraulic propulsion system coupled to a multi-domain analysis was performed using the model in Fig. 6.

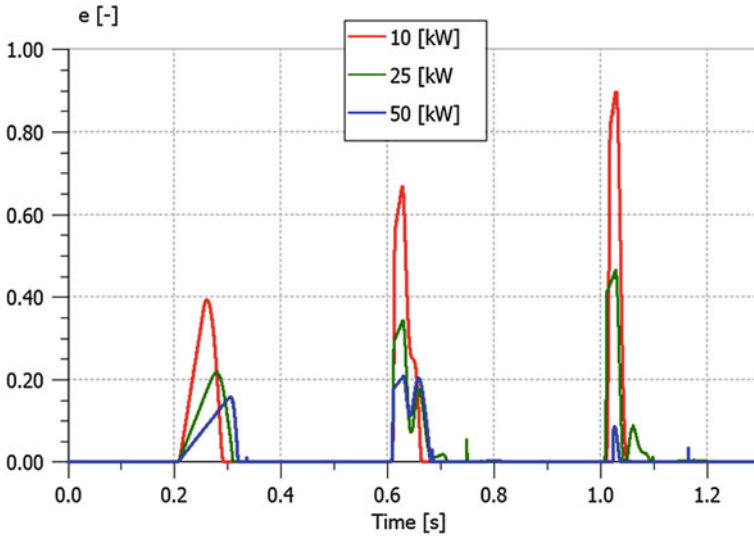


Fig. 9 Influence of time dependent power transfer on overall efficiency

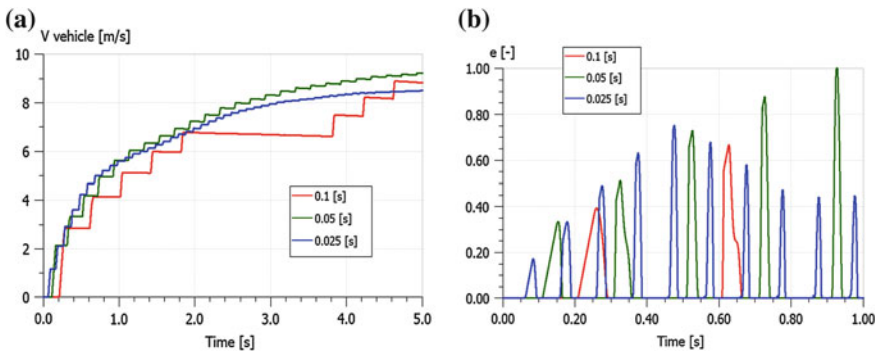
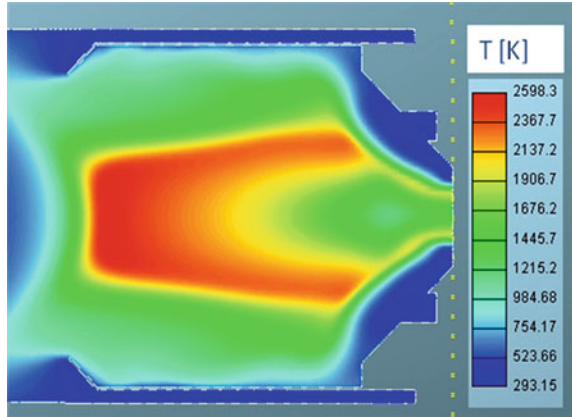


Fig. 10 Influence of actuation time on system performance: a vehicle speed; b efficiency

The model was build up considering the design structure indicated in [3, 4, 5] in order to allow a high flexibility of engine performance including directional control valves that can be actuated in a free manner, allowing the possibility of adjusting flow to the optimum heat transfer rate. The model of the Stirling-alternant hydraulic propulsion is based on the Stirling engine model composed of heat exchanger and pressure source with directional control valves, having the role of to assure the exposure of fluid to the heat exchange sources, the alternant hydraulic propulsion, based on two alternant moving cylinders maintained in a neutral position by mechanical springs, the translational-rotational movement device based on free wheel drive. The modelling parameters were adapted to an ATV type vehicle used also as demonstration vehicle, limited at 20 km/h (approximately 5 m/s).

**Fig. 11** Temperature distribution in a heater applicable to the Stirling alternant hydraulic propulsion system



**Fig. 12** The test rig and experimental vehicle to demonstrate the working principle of the Stirling alternant hydraulic propulsion system

Main influences of running parameters were analysed and studied bellow. Considering the influence of the working pressure of the Stirling engine on vehicle speed as objective parameter, Fig. 7, it can be observed that a higher pressure assures a rapid acceleration, but top speed remains limited. This capability is given by the induced pressure at working piston level—25 to 9 bar.

The added heating power has also a significant influence on system performance. Higher heat flows assure a very rapid start-up, but top speed is reached with a moderate amount of energy added to the system.

The analysis of the overall efficiency computed by dividing the output wheel power to the heat added to the working gas is plotted in Fig. 9. It can be observed that a medium amount of heat is transferred with increasing efficiency. It can be observed from the data in Figs. 8 and 9, that making available a great amount of energy is not necessary to be absorbed by the system. Also the data show that an impulsive energy transfer is very effective.

**Table 3** Comparison of computed and measured data for the Stirling alternant hydraulic propulsion system

	Gas pressure (bar)	Actuation pressure (bar)	Hydraulic pressure (bar)	Working Frequency (Hz)	Vehicle speed (m/s)
Computed	6	7	14.0	10	8
Measured	7	8	13.5	10	7
Error (%)	14	12.5	3.7	Adopted	14.28

A similar analysis is synthesised in Fig. 10, considering the actuation time as parameter. It can be observed that there it is an optimum time to expose the working fluid to heat transfer. A high energy transfer rate assures a smoother displacement of the vehicle.

In order to identify the possibility of achieve the necessary temperatures, a CFD 3D simulation was performed for a conventional heater based on natural gas as fuel, considering the simulation principles after [6]. The temperature distribution is presented in Fig. 11.

### 3 The Experimental Model

The experimental model of the Stirling alternant hydraulic propulsion system was developed at test rig level and vehicle level. The images of the test rig and of the vehicle are given in Fig. 12, and a comparison of computed and measured data is given in Table 3.

### 4 Conclusions

The analysis of the Stirling alternant hydraulic principle has been proven to be a system able to run, creating a set of possibilities to apply optimisation measures for both, the Stirling and the fluid power transmission principle. The free piston solution has the potential of a 21 % efficiency increase due to the free shape of the piston displacement curve. An additional 5 % improvement is expected due to the absence of the normal forces that induce piston friction. It has been proven that impulsive energy transfer is very efficient. The overall layout allows compensating current drawbacks of the Stirling engine like start/stop behaviour and control, due to the hydraulic accumulator.

## References

1. Pischinger S (2009) Alternative vehicle propulsion systems. Lecture Notes, Aachen
2. Martini WR (2004) Stirling engine design manual. University Press of the Pacific, Honolulu
3. Woods RL, Kent L (1997) Modeling and simulation of dynamic systems. Prentice Hall, New Jersey, Upper Saddle River
4. Abaitancei H (2010) Sisteme de recuperare hidraulica a energiei la bordul autovehiculelor. University Transilvania Publishing House, Brasov
5. LMS Amesim Tutorial Manual. Release 10
6. AVL Fire Tutorial Manual



# Design and Analysis of a Dual Power Supply with Super-Capacitor for EV

Ye Lu, Fen Liu, Xiaoyu Jia and Xiao Liang

**Abstract** Based on a systematic analysis of the dual power supply for electrical vehicle powertrain and on its control strategy, a simplified control algorithm which meets both continuous and heavy duty vehicular power needs was designed and integrated into the BDC control software. With this main component and super-capacitor module as a second assistant power source, and battery as the first primary one, a dual power supply system for short distance electric vehicle was designed and tested. Through rational design and selection of the energy sources and their parameters and optimal matching of powertrain energies in system level, the electric vehicle installing super-capacitors as an auxiliary power source can not only improve the electric vehicle performance, but also increase its vehicle range.

**Keywords** Design · Analysis · Dual power supply · Control strategy · Vehicle performance

---

F2012-B08-021

---

Y. Lu (✉) · F. Liu · X. Liang  
New Energy Vehicle Department, SAIC Motor Co. Ltd,  
Shanghai, People's Republic of China  
e-mail: bid\_ly@163.com

X. Jia  
Institute of Power Electronics, Zhejiang University,  
Hangzhou, People's Republic of China

## 1 Introduction

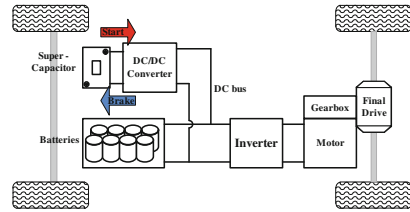
At present, no great breakthrough in the field of energy storage technology [1], which has been a key factor limiting the development of electric vehicles [2]. That is to say that battery is still one of the weakest components in electrical vehicle. Nevertheless, in electric vehicle, battery is the only energy and power source, it has to satisfy both the energy and the power demands as the same time in the vehicular application. Because the performance of electric vehicle is mainly depend on its electric power, the driving distance (range) of electrical vehicle on its energy stored, it is meaningful to improve the operate conditions for battery to ensure its reliable application in electric vehicle and to extend its cycle life, and to select the energy suitably for battery and the vehicle with an appropriate weight and cost. Otherwise, frequently and quickly variation of driving power to the battery will reduce its performance, inadequate battery capacity will led to the vehicle bulky. We need a multiple or a dual power supply to feed the vehicle demands both in energy and in power. Super-capacitor has high power density, which means that it can provide or absorb high peak power. Installing super-capacitors as an auxiliary power source to improve the performance of electric vehicle is a feasible and realistic solution [3, 4]. Peak instantaneous power can be provided through super-capacitors to avoid tremendous current discharge from batteries, during the starting, accelerating or climbing procedure. In that way, DC bus of the electric vehicle will not drop too much and the batteries will not be damaged by high current discharging as well. The braking energy can also be absorbed by super-capacitors so that the frequent charging and discharging of the batteries during the skid can be reduced. It is beneficial for batteries to extend the service life [5].

In this paper, we try to design a simple dual power supply system (DPSS) specialized for short distance EV, which is of low cost, compact, and light weighted.

## 2 Structure of Dual Power System

As we all know that battery and super-capacitor as energy storage components in electrical vehicle can both deliver energy outside (discharge), and accept energy from outside (charge). The battery is of high specific energy and super-capacitor is of high specific power. Generally speaking, for electric vehicle, the specific energy is the first consideration. For a given specific energy, more energy means more weight of battery. In the vehicle design process, engineers will have to weigh in many aspects such as performance, cost, and efficiency etc. Because of the limited specific energy, conflict between performance and cost are often arisen. Which will certainly led to vehicular overweight and over cost, if we target to the customer accepted vehicle performance and vehicle range. On the other hand, for two

**Fig. 1** Structure of battery and super-capacitor DPSS



energy sources, DPSS HEV application, specific energy becomes less important and specific power is the first consideration. Because sufficient power is needed to ensure vehicle performance, particularly during acceleration, hill climbing, and regenerative braking. Super-capacitor is characterized by much higher specific power, but much lower specific energy compared to the battery. By combining of super-capacitor, as an auxiliary power source, and battery as main energy source, a hybrid energy storage system or so-called dual power supply system is derived. In this DPSS powertrain, the vehicular specific energy and specific power requirements can be decoupled. Design work focuses on figuring out the battery that is optimized for specific energy and cycle life, and the super-capacitor that is best suitable for load leveling. Due to applying of super-capacitor, the high-current discharging from the battery to load and the high-current charging from load to the battery by regenerative braking is minimized, in the end the available energy, endurance, and life of the battery can be significantly increased.

### 2.1 Structure of Dual Power System

The structure and energy flow of battery and super-capacitor DPSS powertrain can be seen from Fig. 1.

Expressed in Fig. 1, DC BUS balances power and load in energy, power, and current etc. The dual power supply is composed of battery and DC/DC converter with super-capacitor. Vehicle load transfers driveline from wheel inverter. In the DC bus, the required inverter general input power becomes the load.

Figure 2 shows the energy flow of battery and dual power supply system. When electric vehicle drives normally, batteries provide power to the load through drive-line, Converter with super-capacitor decides whether charge or not according to its electricity state. When electric vehicle accelerating or high speed climbing, batteries provide a limited base power and super-capacitor provides the surplus peak power. When braking, the motor operating as a generator generates the power. The recovered energy is absorbed by super-capacitor or by super-capacitor and battery.

The energy sources or power supplies realizes a kind of hybridization of an energy source and a power source. The energy source, mainly battery has high specific power whereas the power source DC/DC converter with super-capacitor has high specific power. The power source can be charged form the battery during less demanding driving or regenerative braking.

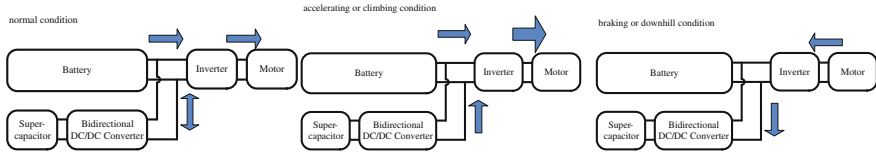


Fig. 2 Energy flow of battery and super-capacitor DPSS

### 2.2 Energy Source Battery

To act as a main energy storage container, battery should have to be chosen according to the requirements of the vehicle performance especially in vehicle range. In this way, balancing on its type, weight, cost, volume etc. would be a necessary. To match the former drivetrain, a Lithium Ion battery pack with rated capacity of 104.4 Ah, nominal voltage 72.6 V, DOD 0.8 is used. It is designed for a low speed, short distance electric vehicle with 1.5 C discharge and 1 C charge.

### 2.3 Power Source Super-Capacitor

Super-capacitor or ultra-capacitor is characterized by much higher specific power, but much lower specific energy compared to the battery.

The amount of energy stored in the super-capacitor is given by,

$$E = \frac{cv^2}{2}, \tag{1}$$

where C is the capacitance unit Farad and V is the terminal voltage unit volt.

When the measured terminal voltage equals to a predefined permitted maximum value, we will stop to charge the capacitor, and feed back a fully charged state signal. In this project, we use an 80 F super-capacitor module to fit the structure design.

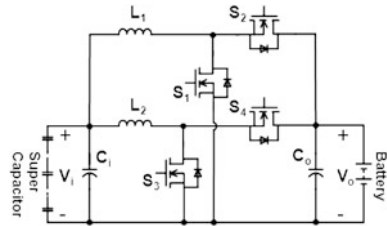
Besides, in later application, we use ‘Q = 1’ to represent that the super-capacitor is fully charged, and ‘Q ≠ 1’ not fully charged or discharging.

### 2.4 Power Converter-Bi-Directional DC/DC

To fix super-capacitors in parallel with batteries in electric vehicles, an energy transfer and control system known as bidirectional DC/DC converter is needed [5].

Figure 3 is the topology of this two directional interleaving and transformer parallel converter. The converter BDC works in two modes: one is buck with battery charging for the super-capacitor and the other is boost by capacitor discharging to the battery or bus. Correspondingly, energy and power flows to and from in between DC bus and super-capacitor in two converter modes.

**Fig. 3** Topology of BDC converter



In a practiced application, converter boost and buck efficiency comes the first. So a specifically designed BDC topology referencing to Fig. 3 with buck efficiency 0.98 and boost 0.96 is adopted.

### 3 Simplifying Control Strategy

#### 3.1 Generalization and Summarization of Control Strategy

The dual power supply electric vehicle is driven by the batteries as primary energy source and the super-capacitors as the assistant power source. Discarding of voltage variation, for dual power supply system, the relationship of battery, BDC with super-capacitor, and the load in power or in current can be simplified to as shown in Fig. 4. In the figure, current’s positive directions are defined and bus voltage variation is neglected.

The relationship of currents can be expressed as:

$$i_b + i_c = i_m, \tag{2}$$

where  $i_b$  is the battery discharge current,  $i_c$  is the super-capacitor boost current, and  $i_m$  is the total traction load current.

Analyzing of the power to-fro flowing directions or two power supply charge and discharge to the load combinations, we learnt that there are 12 flow states of dual power supply totally. Nevertheless, as a matter of fact, the 8 flow states depicted in Fig. 5 cover almost all of the power mode combinations for the short distance electric vehicle.

Within the state elements, state mark ‘’ is for the normal electric vehicle


operation and for the “stable state” operation too. In this state, the direction of arrows have a specific meaning that when targeting into the state, it stands for that the super-capacitor was fully charged ( $Q = 1$ ) and the super-capacitor is ready to assist the load peak power, and when leaving the state, it means that the super-capacitor must be charged preceded in other states ( $Q \neq 1$ ). With time elapsing, the battery’s energy in this state is depleting,

**Fig. 4** Defining of DPSS the positive currents

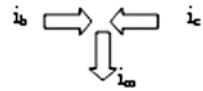
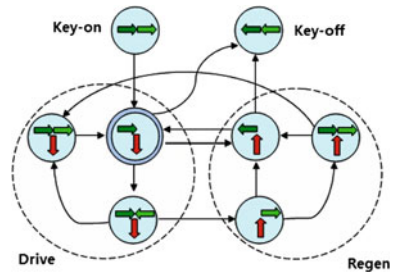


**Fig. 5** Flowchart of powering states of the DPSS powertrain



All other states are dynamic ones which shifting from one to others. Mark  represents a HEV acceleration and high speed cruising operation mode.

Subtracting from these 8 states, besides the two battery only powering states (EV) and two key on and off states, the remained 4 are states concerning to super-capacitor charge and discharge (HEV).

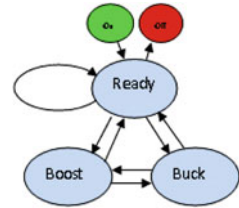
### 3.2 Control Strategy Realized Through BDC

For vehicle with independent Energy Management System, the control strategy for controller can be derived from Fig. 5. However, for this low cost short distance EV application, design a simplified solution based on economic and reliable rules is the best solution.

Figure 6 concerning three states of the BDC with super-capacitor is the adopted strategy for HEV operation. During operation, shifting from others to this stable state is of priority. Comparing this strategy of BDC HEV mode alone with battery operation in EV mode to the states of DPSS powertrain in Fig. 5, it is easily to find that BDC boost and buck operation modes are just coincide to the states concerning to the super-capacitor in Fig. 5. Naturally next, the work of design the control strategy for DPSS is focused on the scheduling of BDC mode shifting conditions. As expressed in Fig. 5, BDC ready state means the super-capacitor is fully charged and ready for power assistant. Boost state is a state in which super-capacitor discharge to the DC bus, acting with battery altogether discharge a peak current to the load, and buck state is the state in which super-capacitor is charged from the DC bus by battery or the regenerative braking energy.

In this project, shifting threshold from BDC ready state ( $Q = 1$ ) that the capacitor was fully charged to its boost state that the BDC with super-capacitor outputs power to vehicle load resulting super-capacitor lack of energy is set in this

**Fig. 6** Control Strategy of DPSS HEV mode



way: that when battery’s discharge power approaching to the preset peak power  $P_{bset}$  (less than maximum battery discharge power in electric vehicle  $P_{bmax}$ ) or the protect current  $k_1 * C$  (less than 1.5–2 C), BDC is forced to enter the boost operation mode. On the other hand, whenever the super-capacitor is short of energy ( $Q \neq 1$ ), it is programmed to charge from the battery or regenerative braking energy immediately. In this situation, BDC operates in buck mode and in a constant current operation [6]. Or programming the buck operation mode like boost one that when the battery preset charge power  $-P_{bsetc}$  or preset current  $-k_2 * C$  is measured, BDC starts to work at buck operation and in current limited charge operation. Where  $k_1 = 1$  and  $k_2 = 0.5$  are selected as the battery’s discharge and charge current coefficient.

### 4 Vehicular Design and Verification of DPSS

To design a DPSS applied for vehicle, the above mentioned type, parameter, and data of battery, super-capacitor, and BDC with control strategy are used. And the electric vehicle originally developed for short distant is utilized as a platform with its tested weight 1200 kg, top cruising speed 50 km/h, and vehicle range 90 km for DPSS study. Other main input data are: an inductive traction electric motor, normal power 7.5 kW, peak 12 kW; a suitable vector controller; Lithium Ion battery pack with rated capacity of 104.4 Ah, nominal voltage 72.6 V. Base on these technical specifications, this electric vehicle performance can be realized but with the battery having to stand for frequent 1.5–2 C charge or discharge current variation.

To test the method of design and analysis for DPSS, and to verify this DPSS function and performance, the key component BDC integrating the simplified HEV control strategy was specially developed. The DPSS is designed that the BDC has power converting capacity of normal power 3.5 kW, peak power 5 kW; preset current protect value in buck and boost mode can be adjusted according the specific requirements; and super-capacitor is of normal voltage 67.5 V and normal capacitance 80 F.

Figure 7 is the simplified designed DPSS powertrain principle (a) and its onboard recorded operation oscilloscope graphs (b) and (c). Where, we use a 48 V VRLA to instead of super-capacitor to verify the DPSS function first.

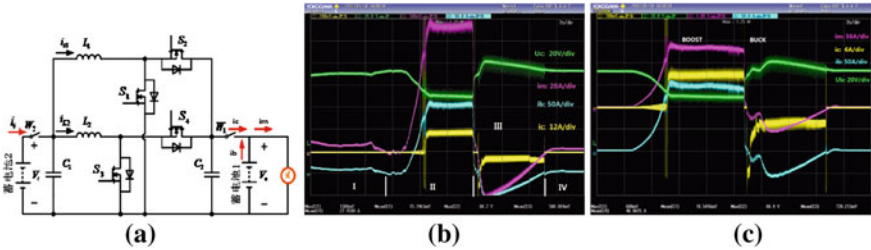


Fig. 7 The DPSS application circuit and its onboard operation oscilloscope graphs

Reading data from Fig. 7b and c, we find that there are four sections included: *I* Cruising speed section, *II* Acceleration section, *III* Regenerative brake section, and *IV* Vehicle idle section.

In section I, the super-capacitor was fully charged and ready to discharge current to assist battery for peak current. Battery follows the load requirement in current. In section II, the load (pink line  $i_m$ ) needs more current, when it exceeds or bigger than 130 A, the BDC starts to work in boost mode, the super-capacitor (discharge in preset current  $i_c$  yellow line), in conjunction with battery (current  $i_b$  in sky blue), discharge current to the bus. As a result, the maximum current draws from battery descending to a reasonable scale. While in section III, regenerative brake energy is stored both to battery and super-capacitor. The last section is vehicle idle one, where, only battery supplies the auxiliary vehicular power.

BUS voltage ( $U_c$  green line) starts from stable or continuous state, shift to dynamic peak drive operation state, transfer to regenerative state, and then stops at stable idle state.

Applying of the above DPSS design, the battery current is reduced from ‘former electric vehicle’ 164 to 150 A in vehicle acceleration, and braking energy is absorbed both by battery and super-capacitor quickly.

Because of the addition of BDC with super-capacitor, for leaving the vehicle performance unchanged, the maximum battery charge and discharge currents can be under controlled. By applying the BDC with super-capacitor module and working together with primary energy storage battery pack on a short distant electrical vehicle, the high current discharging from the battery and the high current charging to the battery by regenerative braking is minimized so that the available energy, endurance, and life of the battery can be significantly increased.

Standing on the vehicle development, when designing a new electrical vehicle by applying of a comparatively small battery mainly considering range and a BDC with super-capacitor assisting, the engineer can achieve his objective of good balancing among vehicle performance, volume and weight limitation, and battery or vehicle life cycle etc.



## 5 Summary and Conclusions

This paper is concerned with the design and analysis of dual power supply system for electric vehicle.

In this paper, DPSS powertrain principle and its critical components were analysed and key parameters introduced. Based on the simplified principle, a simple power flow control strategy for DPSS was summarized. Going a step further, in conjunction with BDC buck and boost operation, this simple control strategy was integrate with the BDC control arithmetic.

Developing of a high efficiency Bi-DC/DC integrating the simplified control strategy made the addition on conventional electric vehicle for hybrid operation easily. Through vehicle level verification on the DPSS powertrain and on the BDC with super-capacitor, and on BDC with lead acid battery, the powertrain and its design and analysis measure was proved to be correct and effective. The BDC shifting among different states correct and functions react properly.

Further study and verification on super-capacitor and on different platform are still needed.

## References

1. Wan P (1998) Key technologies for electric vehicle. Beijing Institute of Technology, Beijing
2. Qingsheng Shi, Chen, (2009) Key technologies research on energy management problems of pure electric vehicles. Degree thesis, Shandong University
3. Miller JM, Smith R (2003) Ultra-capacitor assisted electric drives for transportation. Electric machines and drives conference, 2003, IEMDC'03, vol 2, pp 670–676
4. Burke AF, Hardin JE, Dowgiallo EJ (2002) Application of ultracapacitors in electric vehicle propulsion systems. Proceedings of the 34th international power sources symposium, 1990, vol 6, pp 328–333
5. Orthzar M, Dixon J, Moreno J (2005) Power distribution control coordinating ultracapacitors and batteries for electric vehicles. American control conference, Jan 2005, vol 5, pp 4716–4721
6. Chan MSW, Chau KT Chan CC (2005) Effective charging method for ultracapacitors [J]. J Asian Electr Veh 3:771–776

# An Electrically Driven Chassis System Concept for Sub-Compact Vehicles with Integrated Close-to-Wheel Motors

Dr. Shih-Jen Yeh, Dr. Ingo Albers and Stephan Pollmeyer

**Abstract** Currently in the automotive sector both hybrid and completely electric drives are being discussed and developed. The comparatively compact design of electric motors permits considerably more flexible installation in the vehicle than is the case with conventional internal combustion engines. Thus, depending on the category of vehicle, in addition to classic placement in the conventional engine or differential installation space (conversion design), configurations with the motor positioned close to the wheel or integrated into the chassis are conceivable, permitting selective wheel drive, with elimination of the classic differential and driveshaft. On the one hand, close-to-wheel configurations involve increased system complexity, since they require more than an electric motor and a transmission, for instance. However, on the other hand they are particularly attractive with respect to space requirements, because they permit integration into the installation package that is required in any case for the chassis. The space thus saved in the middle of the vehicle can then be used for a comparatively large energy storage system or for additional electronic/electrical components. At the IAA 2011 in Frankfurt, in an early concept study, ZF presented a driven chassis system for the minicar and sub-compact segment, where the electric motors and the transmission are integrated close to the wheel in the chassis. In contrast to familiar close-to-wheel drives, in the concept presented, the unsprung mass is only slightly increased. The total system weight continues to be attractive, since the comparatively heavy side shafts and the differential are eliminated. The chassis system can be integrated into the floor assembly of a global sub-compact vehicle

---

F2012-B08-022

---

Dr. S.-J. Yeh (✉) · Dr. I. Albers · S. Pollmeyer  
ZF Friedrichshafen AG, Friedrichshafen, Germany  
e-mail: shih.jen.yeh@zf.com

platform with no significant changes in the vehicle body, and has the additional advantage that both standard-size wheel rims and conventional brakes can be used.

**Keywords** Electromobility · Driven chassis system · Chassis concept · Chassis system study

## 1 Background and Goals

The idea of a wheel hub drive has been discussed and elaborated for many years. However, as to date this fundamental concept has only been demonstrated at either a conceptual level or within relatively constrained application areas where no final application to a mass-produced passenger car was implemented. There are multifaceted and complex reasons for this fact: high mechanical stresses acting on the powertrain, significant efforts required on the electrical part and, with reference to the chassis, the concessions made in terms of comfort and driving safety due to the increased unsprung mass.

However, with a view to potential benefits such as new freedom in vehicle design and advanced driving dynamics by torque vectoring, wheel hub drives provide fresh impetus for on-going discussion on current electric vehicle technology.

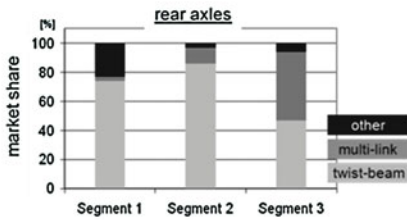
Consequently, ZF has focused on this subject again, having current state-of-the-art and comprehensive know-how on powertrain and chassis technology at hand within the company. As a result of these activities, the Electric Twist Beam (eTB) concept has been developed, which was presented at the 2011 IAA (*International Motor Show*).

The fundamental design of the eTB was targeted for vehicle segments 1 and 2. With a view to this constraint and supported by a high penetration within these market segments, a spring strut type axle (front axle) and a twist-beam axle (rear axle) are considered as possible axle designs. As suggested by package investigations, the latter clearly provides more favourable conditions in terms of integration of electric drives mounted close to the wheels. This is mainly due to the fact that no steering function is integrated, which in turn, when using the spring strut type axle, leads to compromises regarding kinematic design because of the narrow package situation.

The values of driving performance haven been chosen similar to typical values of the targeted vehicle segments. Consequently, the drive units were designed to deliver a peak performance of 60 kW and a wheel torque of 1,400 Nm (as a sum of the two drives).

■ Driving performance requirements

- slope 30% by  $a_{Fzq,rest} = 0.2 \text{ m/s}^2$
- $v_{max} = 150 \text{ km/h}$
- 0-100 km/h in < 11s

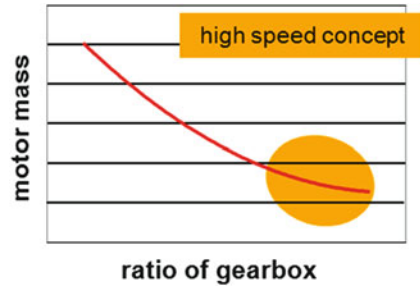


## 2 Concept Description

The two E-drive units consist of an electric motor and a fixed transmission, respectively. These functions have been integrated into the trailing arm of the twist-beam axle. The housings of the drive units are merged to a single element.

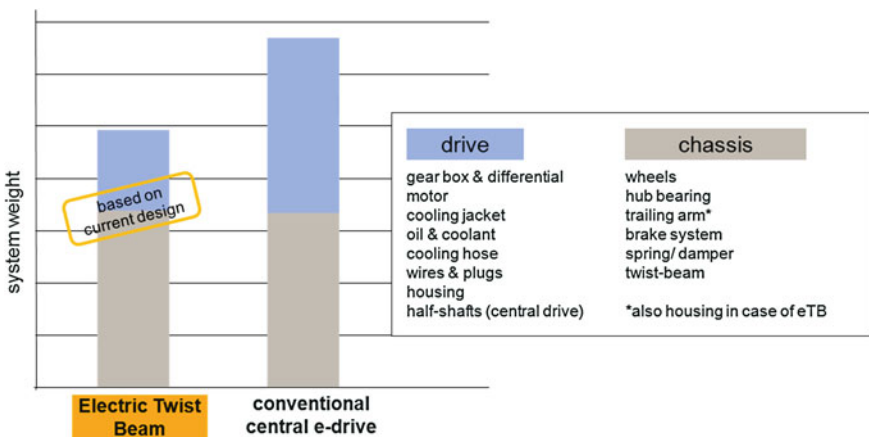


The selected high speed concept for the powertrain allows to meet the requirements of limited installation space as well as a low system weight. As commonly acknowledged, a higher transmission ratio provides the ground to design a more compact and light-weight electric motor which brings down the cost of the motor as well. The transmission was implemented by two gears with a fix transmission ratio.

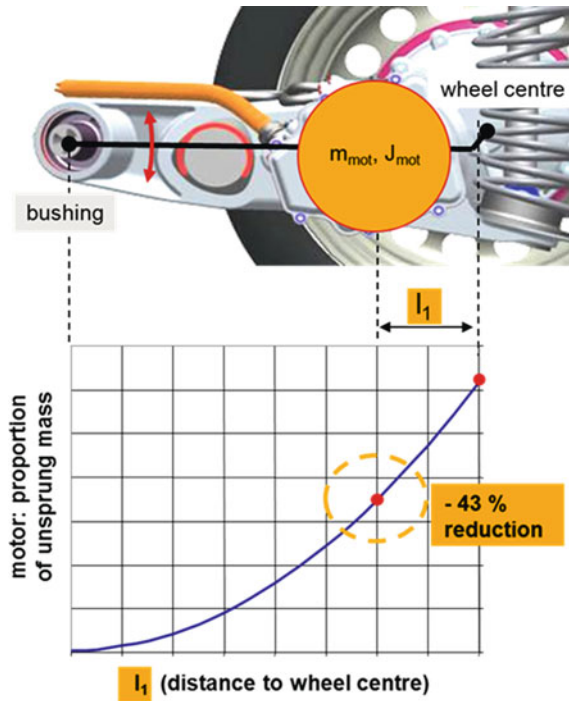


### 3 System Weight and Unsprung Mass

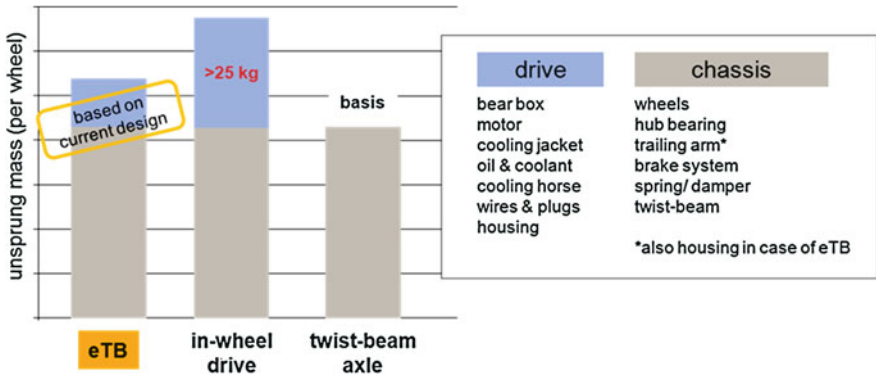
A significant advantage was achieved with a view to the system weight of the Electric Twist Beam resulting from a level of functional integration along the implementation of the high speed concept for the powertrain. As an example, no half-shafts and differential are needed in this design which obviously provides an important impact to the system weight. Moreover, the integration of the drive unit housing with the trailing arm results in further weight savings. Other components (e.g. wheel bearings) assume functions from the drive as well. When summing up all these effects, a significant reduction of the system weight could be achieved compared to a conventional central electric drive concept. The below figure shows a comparison of the conventional central drive unit to the electric twist beam concept in terms of system weight. It should be noted here that the entire conventional twist-beam axle must be taken into account for this comparison in order to have functionally equivalent systems.



In addition, the presented concept allows to reduce the impact on the unsprung mass as the positioning of the drive unit was identified as a key issue along with implementation of the high speed approach. Because of the offset between the motor axle and the wheel centre it becomes possible to relocate the motor towards the main bushing of the twist-beam axle.



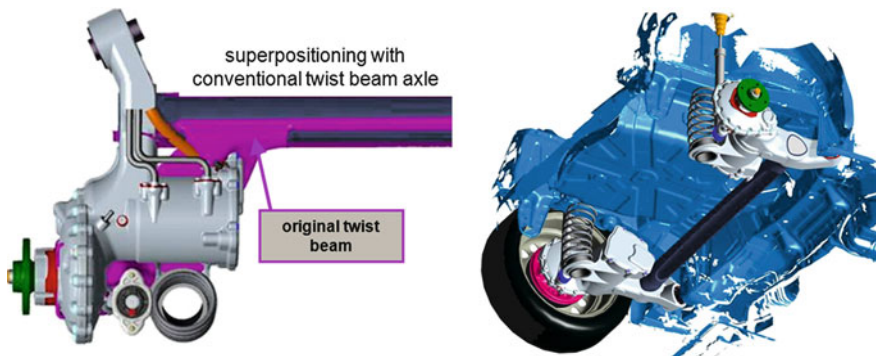
As a result of this geometric configuration, the moment of inertia introduced by the motor mass is reduced for a vertical wheel displacement. With respect to the wheel centre, the effect of reduced motor inertia corresponds to a small increase of the unsprung mass. The non-linear correlation between the length  $l_1$  (wheel centre to motor) and the contribution of the motor to the unsprung mass, the impact (compared to a motor positioned in wheel centre) can be reduced as much as 43 % with the selected motor location. Compared to a conventional in-wheel drive (gearless direct drive), the effects as described above will lead to a significantly lower influence of the unsprung mass.



### 4 Vehicle Integration and Gained Installation Space

During the design of the Electric Twist Beam, particular attention was paid to allow an easy integration within conventional car body. For this purpose, the system was built into the installation space of a typical vehicle from the targeted segment.

As depicted in the figure below, the Electric Twist Beam is almost neutral in terms of required installation space compared to a conventional twist beam axle. The bodywork attachment points can be left unaltered for almost all cases. Only the spring attachment was slightly moved towards the back to avoid geometric collisions with the electric motor. However, this attachment point is still located below the rigid longitudinal members of the body.



In conclusion, investigations on the installation space have revealed that the Electric Twist Beam concept has great potential to deliver an electrically-powered

rear axle within an existing vehicle platform which can be implemented in an easy, direct, and efficient way. Moreover, the Electric Twist Beam concept may offer inherent capabilities for future generations of vehicles to utilize the additional installation space gained from replacing the central E-drive. In such a way, other components or extra storage space might be possible to integrate.

## 5 Summary

Electric Twist Beam is an electric powertrain design with e-drives positioned close to the wheels where the electric powertrain and the chassis are merged. The concept was developed and elaborated for the vehicle segments 1 and 2. Significant advantages over traditional e-drive concepts are obtained in particular with a view to the gain in additional installation space as well as the feasibility of torque vectoring. The suggested functional integration combined with the high-speed concept provides the key to achieve a low system weight as well as low impact of the unsprung mass. Moreover, the Electric Twist Beam system may easily be applied to conventional vehicle bodies. In conclusion, the impact of these developments could be immense across a broad range of vehicle applications, facilitating a paradigm shift in the design for electrically-powered driving.





# Future Commercial Vehicle Powertrains: Contributions to Sustainable Transportation

Heimo Schreier and Lukas Walter

**Abstract** *Objective* Already for many years, fuel consumption and operating cost were the major technology drivers for commercial vehicles. Today, in order to achieve agreed CO<sub>2</sub> goals and to reduce the dependency on crude oil, governments are implementing CO<sub>2</sub> or fuel consumption legislation. Even more, reduction of fuel consumption and consequently low operating costs are continuously an important focus for manufacturers and owners of commercial vehicles. New powertrain technologies, which will further reduce fuel consumption, are able to combine these three drivers, to reduce CO<sub>2</sub> emission, to reduce the dependency on crude oil and to address the need of lower total cost of ownership of the owners of commercial vehicles. *Conclusions* The efficiency of commercial powertrains can be significantly increased in future. Several potentials for improvement are seen specifically in those technologies, which are able to provide a global optimum of the whole powertrain system, from engine to exhaust aftertreatment to cooling system up to transmission and the final drive. In total a fuel efficiency potential of 20 % is seen for long haul trucks. *Results* AVL has developed a whole line of technologies, which can be implemented to the commercial powertrain in the future to address the requirements above. The individual measures are the optimization of the balance between engine and aftertreatment systems, reduced engine friction by advanced thermal management systems, reduced parasitic losses of the auxiliaries in real life driving cycles, conversion of exhaust energy in driving power, application of new and advanced transmission technologies and shift strategies as well as degrees of electrification of the powertrain. Additionally, alternative fuels provide another field of CO<sub>2</sub> friendly technologies as well as

---

F2012-B08-024

---

H. Schreier · L. Walter (✉)  
AVL List GmbH, Graz, Austria  
e-mail: heimo.schreier@avl.com

reduced operating cost. Here specifically, the availability of local resources drive short term applications. This paper will compare the individual saving potentials of these technologies, will rate it against criteria like market readiness, cost efficiency and others. It will be demonstrated that major reductions in CO<sub>2</sub> emissions and operating cost are still possible by commercial vehicle powertrain measures.

*Methodology* To quantify the fuel saving potentials of the individual technologies AVL applied its proven seamless system simulation environment to analyze the whole vehicle system. Interlinked sub-models for all relevant vehicle, respectively engine sub-systems, are the core of this simulation environment. Where necessary, the individual models have been aligned with specific test bed and vehicle measurements. For some of the analyzed technologies the predicted fuel saving potential could already be confirmed by transient operation on test bed using prototype components. To analyze the cost efficiency for the individual technologies the predicted additional product costs have been rated against the saving in operational cost for the final vehicle owner. A return of investment calculation analysis has been made for each individual technology. To predict the market readiness of the individual technology, relevant boundary conditions like estimated development effort, components availability, established supplier base, development risk, etc. have been considered.

*Limitations* Basically the results of this study can be transferred to all commercial powertrain systems. However, the main focus of the study is on the long haul truck application since it has the most significant impact to total CO<sub>2</sub> emissions caused by the high mileage as well as the high absolute fuel consumption level of this vehicle category.

**Keywords** Commercial powertrain • Fuel efficiency • CO<sub>2</sub> reduction

## 1 Introduction

Commercial vehicles are the backbone of productivity and economic growth in many regions in the world. The sales numbers of commercial vehicles are heavily depending on trends of GDP. And, although initiatives are continuing to move more goods transport to ship and train, all predictions see a further significant growth of the number of the commercial vehicle population worldwide.

Thus, the topic of sustainable transportation by advanced commercial vehicles will become more important. This sustainability shall consider local transportation needs, conventional and CO<sub>2</sub> emissions as well as the area of dependency on crude oil as well as local resources. Technologies to reduce conventional emissions down to a “close to zero” level were already developed to series production. Thus, CO<sub>2</sub> is the main area for further emission reduction.

CO<sub>2</sub> legislation is progressing fast for passenger car transportation and light commercial vehicles. Considering transport efficiency as transported mass in relationship to the gross vehicle weight, commercial vehicles are by far more efficient methods of transportation than passenger cars. Additionally, for many

years, fuel consumption was a major buying factor of commercial vehicles. In the European market in the last 20 years, the fuel consumption of long haul transportation was reduced by more than 30 %.

Nevertheless, major legislation steps for fuel consumption or CO<sub>2</sub> emission reduction were already announced in major markets. With North America, Europe, Japan and China, soon approximately 80 % of the global production of commercial vehicles will be under the first steps of such legislation. Different to the conventional exhaust gas emission legislation, CO<sub>2</sub> or fuel consumption legislation qualifies not only to reduce the emission, but also to reduce the dependency on crude oil, as well as the total cost of ownership of commercial vehicles.

CO<sub>2</sub> reduction can be addressed by three main areas, the reduction of vehicle rolling and aerodynamic losses, the improvement of powertrain efficiency and the origin of fuels used for transportation. This paper will focus on the improvement of powertrain efficiency. The area of rolling and aerodynamic losses has been investigated in much detail, and solutions are already available. The implementation of these depends primarily on the cost impact on the vehicle as well as legislation.

Additionally, due to the fact that in most markets worldwide, long distance transportation of long haul trucks and long distance busses is responsible for the majority of the fuel used, most of the described results will address this vehicle class.

In all areas of powertrain losses, further significant reductions will be achieved. The line-up of such technologies reaches from further optimization of the trade-off between engine and aftertreatment system, improved charging systems, base engine friction reduction, to the control of the thermal management system, to use auxiliaries on demand, to optimize the engine torque curve and fuel consumption together with the transmission and rear axle to move operation to the fuel consumption best point, to implement a secondary thermal cycle to convert waste heat to driving power as well to store braking energy in electric systems.

With this long list of technologies all areas of energy losses are being addressed. It is a combination of engine, aftertreatment, cooling system and driveline technologies. Due to the intensive interaction of these systems, in order to find an optimum solution, it is required to optimize the powertrain as one system. All tools and methods need to be adapted to extend the boundary conditions to the whole powertrain.

Figure 1 shows the major energy flows in a commercial vehicle, with an estimated share of these.

## 2 Auxiliaries Power

As seen in Fig. 1, the overall share of losses due to the auxiliaries power seem to be comparably small. Nevertheless, due to the fact that such losses can be reduced by new advanced system optimization methodology, and can be implemented with

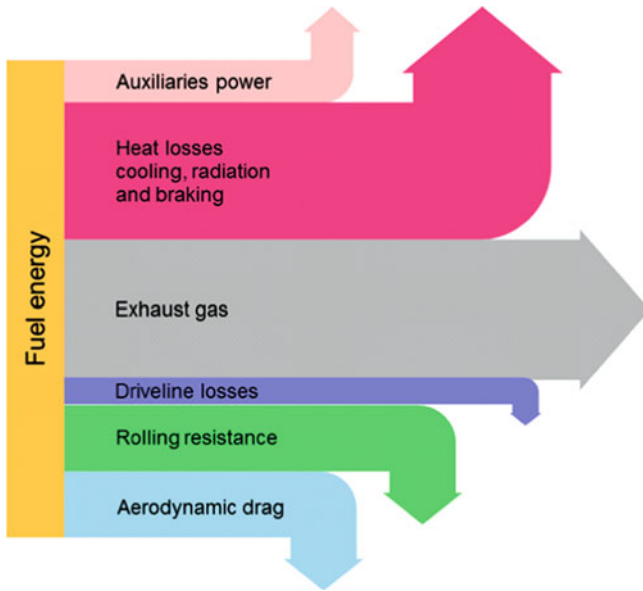


**Fig. 1** Energy flows

comparably low component cost and limited integration effort, the area of auxiliary losses will be addressed with high priority in the commercial vehicle industry.

Future emission legislation requires the combination of a number of emissions control systems. Especially the use of exhaust gas recirculation has a significant impact on the vehicle thermal management. High levels of exhaust gas recirculation requires significantly increased cooling power, and with this higher auxiliary power. Thus, further optimizing the strategy of all contributing systems in an overall system optimization, provides the potential to significantly reduce auxiliary power like cooling pump operation and fan operation. With this, fuel consumption reduction of up to 2 % can be achieved.

In addition, auxiliaries power losses can be significantly reduced by using auxiliaries exactly on demand. Measurements of AVL on typical long haul truck applications have shown that the operation of the following auxiliaries can be significantly optimized. The following systems were developed to operate on demand:

1. Multi step function or full variable cooling fan.
2. Multi step function or full variable cooling pump.
3. Variable flow oil pump.
4. Switchable piston cooling.
5. Air compressor deactivation.
6. Demand controlled hydraulic steering pump.

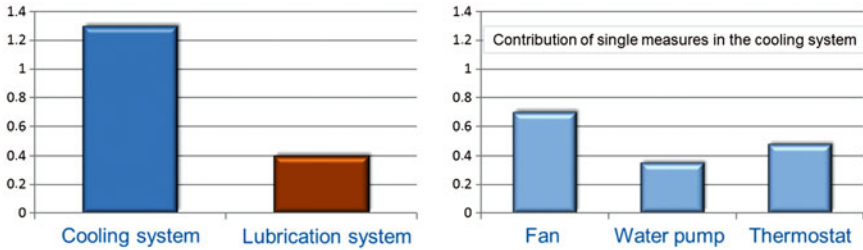


**Fig. 2** Potential of thermal management

The measures 1–4 need to be addressed with advanced thermal management strategies. Due to the significant interaction of the thermal flows in the engine, these measures need to be optimized in one thermal network. AVL has developed the Vehicle Thermal Management System (VTMS) layout and simulation platform, with which, such thermal management strategies can be developed and calibrated. This needs to be carried out in typical customer duty cycles of such vehicles. The VTMS platform considers the engine thermal network, combustion, powertrain losses, cooling and lubrication circuits, radiation and convection, air cooling and HVAC systems, all under real life cycle operating conditions. Advanced thermal management strategies considering road topology are being developed using this VTMS platform.

The potential for fuel consumption reduction using thermal management features can be seen in Fig. 2. This considers the potential of measures in the cooling and lubrication system, during a typical European driving cycle.

Strategies adapting to road topology will provide additional potential, but are not yet considered in the presented results.

Air compressor and hydraulic steering pump are both auxiliaries, which are laid out to operate due to specific and time limited events. Due to this, for most of the real life operating cycle the air compressor delivers compressed air only in 10 % of the driving time for highway driving and 40 % for city driving. For the rest of the time, the air compressor needs to idle, which results in significant losses.

Thus, comparing to conventional air compressor designs, a full decoupling of the air compressor would provide potential to reduce the fuel consumption by 1.3 %, whereas comparing to next generation air compressors with compressor power control, full decoupling would still provide 0.3 %.

The hydraulic steering pump is laid out to provide sufficient pressure for steering under vehicle stand-still conditions at low engine speeds. During driving the oil pressure requirements for the steering pump are significantly reduced. Due to the characteristics of the pump, the available pressure at increasing engine speeds is significantly higher than under engine idling conditions. Thus, the majority of the pressure potential needs to be released, which generates significant losses.

A controlled power steering pump will provide a fuel consumption benefit of up to 1 %, depending on the real life operating cycle.

### 3 Change of Engine Operating Range: Downspeeding

Due to fast further improvement of roads in many areas of the world, the average speed of long distance transportation is increasing. This improvement of the infrastructure allows implementing specific technologies, which are addressed to optimize the engine operation around a limited engine speed and torque range.

It is a global trend in the commercial vehicle industry to invest in technologies, which supports downspeeding of the engine operation. This means, that during regular driving, the vehicle is running under lower engine speeds, thus optimum fuel efficiency conditions. This downspeeding is a very effective and cost efficient way to reduce fuel consumption. This is especially true for long haul truck and long distance bus operation.

Figure 3 shows an engine map for engine speed and torque. In addition, there are lines of constant power and lines of constant fuel consumption difference to the base curve. Normal driving on a flat surface of a fully loaded 40 ton truck would require an engine power of approximately 110 kW. These 110 kW can be delivered at different engine speeds along the constant power curve, at different specific power levels.

In addition, the figure shows a typical operating range of such a truck as “occurrence times fuel consumption”. This shows, at which engine speeds and torques the most fuel is consumed. It can be seen, that the real life operating cycle represents a rather narrow window of engine speeds, with varying engine torque.

For most markets in the world, with a comparable infrastructure for long distance transportation, today's setup of engine, transmission and final drive this narrow band of engine speeds in a typical real life cycle would be in the range of 1300–1400 rpm.

Looking at the curves for differences in fuel consumption, it can be seen, that a significant improvement in fuel consumption can be expected, if the engine delivers the required power at lower engine speeds. Depending on the engine layout and calibration, there are fuel efficiency benefits of up to 5 % feasible, in case the full potential of such downspeeding can be achieved.

The limit for downspeeding is the driveability of the vehicle, mainly the number of down-shifts. It can be seen, that with current engine torque characteristics, the available power at lower engine speeds is significantly reduced. In order to keep the vehicle speed in the required range, the driver or the transmission control shifts to a lower gear when the truck runs on an inclination. A very large number of shifts in a real life driving cycle would reduce the driveability for the driver significantly due to frequent torque interruption and shifting.

One direction to improve this behavior would be to invest in transmission technology, which reduces the torque interruption to a minimum. The first improvement under this condition can be achieved, by using an automated manual transmission instead of a manual. With this, sophisticated shift strategies can be implemented, which are able to optimize fuel consumption. The next step are advanced automated transmissions, which are currently being developed. For

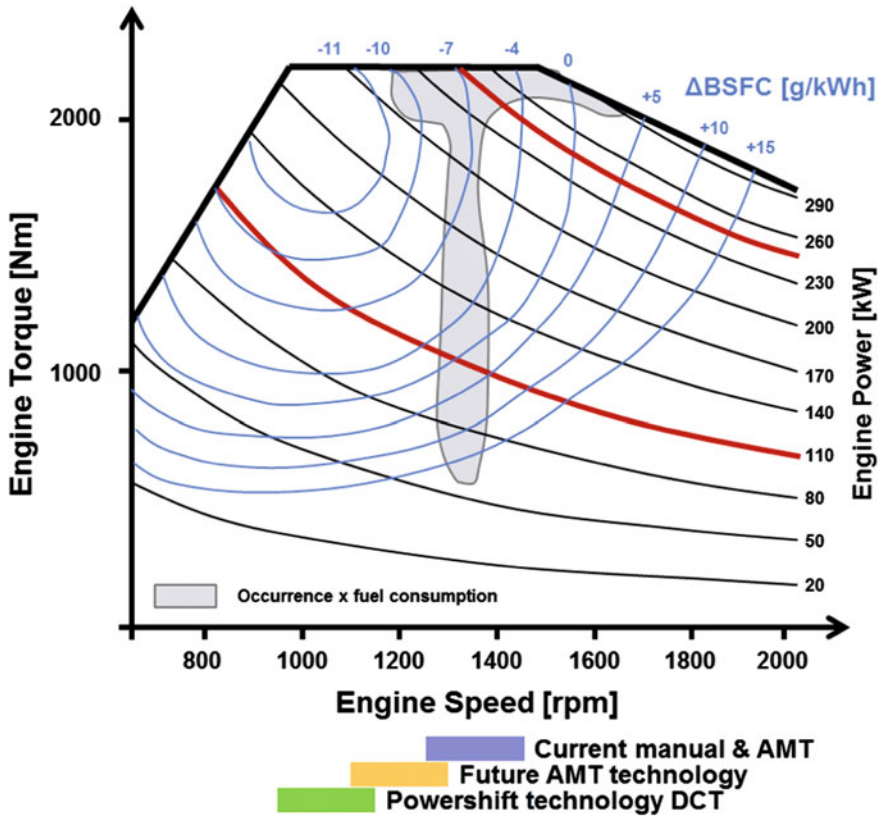


Fig. 3 Engine operating map

these, shift durations and torque management are already highly optimized, so that general operation is feasible within an engine speed range between 1100 rpm and 1300 rpm.

The full potential of downspeeding as described above can be gained by using a powershift transmission, which is capable of shifting without torque interruption. AVL developed in the past years such a transmission for long haul truck application, which uses double-clutch technology. Due to the unique design, this transmission can be packaged within the same spacing as state of the art automated manual transmissions. The main systems can be seen in Fig. 4.

In addition to the transmission technology, downspeeding can be also achieved or supported by shaping the torque of the engine. A high engine torque at low engine speeds will support downspeeding, as shifting does not become necessary. Current developments address this shaping of the torque curve by using new charging concepts.

Another promising technology to achieve such downspeeding is the use of an electric drive, to overcome such lack of power at lower engine speeds. This would

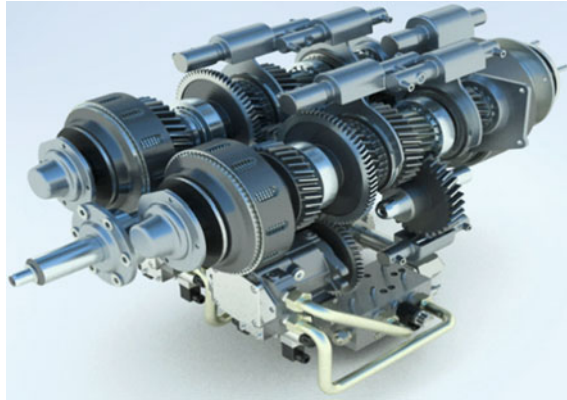


Fig. 4 AVL double clutch transmission for long haul truck application

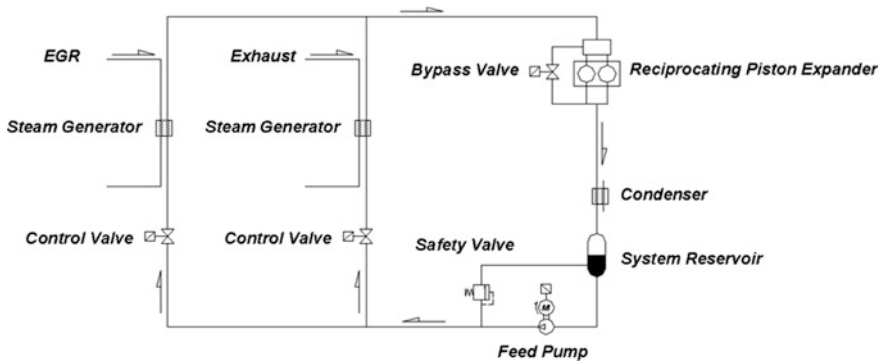


Fig. 5 Sketch of waste heat recovery system

mean using a hybrid system solution for long haul application. Research at AVL has shown that during a typical European real life operating cycle up to 80 % of the possible shifting needs can be overcome by adding electric power. These results were achieved using an optimized hybrid system, with reasonable cost and size limitations to the electric components. Thus, hybridization for long haul truck application would be able to support the gain of fuel efficiency due to downspeeding.

## 4 Waste Heat Recovery

A major area of research in the commercial vehicle industry is the recovery of exhaust energy to convert this to driving power. The focus is on the implementation of a secondary thermal cycle, the Rankine Cycle. AVL develops such



systems for already many years, using different layouts and applications. Figure 5 shows the system sketch of a typical waste heat recovery system.

Two key topics were addressed, the choice of the required operating fluid and the re-introduction of the produced power into the driveline.

The main operating fluids, which are currently being worked on are water, ethanol or similar and the refrigerant R245fa. For these, concerns for partly safety and partly implementation under real life conditions, are in the process of being solved.

For the re-introduction of the produced power, AVL did research on systems providing higher and lower rotational speeds, from turbine to piston expanders. The rotational speed is a key factor due to the size and cost of possible transmissions to reduce the rotational speed to the range of typical drivelines. Generally, it can be expected that systems providing lower rotation speeds will be used for mechanical introduction into the driveline, whereas solutions providing higher rotational speeds, may feed the produced power into an electric system.

Thus, in the future, waste heat recovery systems will likely be combined with hybrid systems. Still, due to the timeframe for implementation, mechanical re-introduction of the power of the waste heat recovery system will be the solution, which will be seen in series production at a much earlier time.

In order to gain the full benefit of the power generation in the Rankine cycle, it is required also using the transferred heat for cooling of exhaust gas recirculation.

AVL's research has shown that depending on the system configuration and the application, fuel efficiency gains of over 5 % are feasible within a typical long haul truck real life cycle operation.

## 5 Recuperation of Braking Energy

Braking energy can recuperated using mechanical, hydraulic or electric storage systems. For typical commercial vehicle operation with significant long haul share, electric storage is seen to be the most effective way to store the braking energy.

Depending on the real life operating cycle, recuperation of the braking energy can gain a fuel efficiency benefit of over 25 %. Even for long haul truck application, in a typical European real life operating cycle, 5 % of fuel efficiency gain due to recuperation of braking energy is feasible.

Electric recuperation of the braking energy can be achieved by using a hybrid system. The key factor to make a hybrid system a viable solution is the optimization of the component specification.

AVL's research has shown that an optimum can be found between the component sizes, their weight and performance, and that these can be balanced with the system cost.

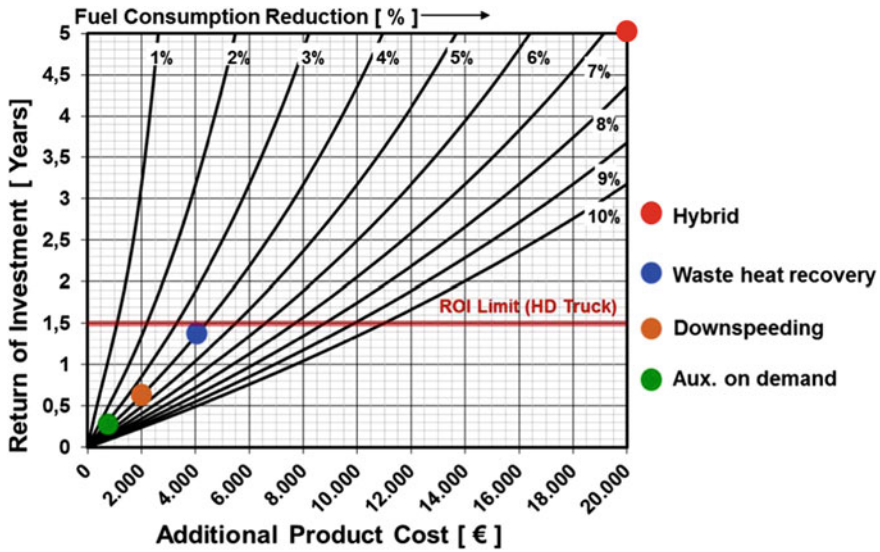


Fig. 6 Technology evaluation graph

## 6 Technology Implementation Timeline

There are three main drivers for the implementation of the described technologies. Similar to earlier conventional emission legislation, a strict fuel consumption or CO<sub>2</sub> legislation could be the driver. In addition, products providing the vehicle owner a green image will require such technologies. But, already in the past, the strongest driver for technologies to improve fuel efficiency was the total cost of ownership for the first vehicle owner. Due to the timing of CO<sub>2</sub> emission legislation, and the niche character of green image, the benefit in total cost of ownership will be driver for the implementation of the described technologies.

Figure 6 shows the relationship between the additional product cost due to a new technology, the fuel efficiency improvement and the return of investment period for the first vehicle owner. In addition, the described technologies are marked according to the legend.

The requirement of a return of investment period may differ from market to market. This is mainly depending on the usual period of use of the first vehicle owner. In order to evaluate the technologies, AVL has set a goal to achieve a maximum return of investment period of up to 1.5 years.

It can be seen, that most of the described technologies, once these are ready for series production, will significantly improve the total cost of ownership. Thus, this will remain the main driver for implementation in the future.

As discussed in the beginning of this paper, in order to optimize the fuel efficiency improvement using a combination of the above technologies, several

complex interactions need to be considered. Thus, sophisticated powertrain system optimization needs to be performed.

Nevertheless, according to AVL's research results, a total of over 20 % of fuel efficiency improvement by powertrain technologies will be gained within the next 10 years.